國立中山大學材料科學研究所

博士論文

以摩擦旋轉攪拌製程製作奈米細晶鎂基合金與複材之研發

Achieving Ultrafine Nano Grains in AZ31 Mg Based Alloys and Composites by Friction Stir Processing

研究生：張志溢 撰

指導教授：黃志青 博士

中華民國 九十六 年 十 月

Table of Content

Lists of Tables

Lists of Figures

Abstract

In this study, firstly, in order to achieve fine grains in solid solution strengthened AZ31 magnesium alloy by friction stir processing (FSP), various efforts have been made. It has found that with a newly designed cooling system, the microstructure of commercial AZ31 alloy can be refined dramatically by carefully controlling the FSP parameters. It is of scientific interest that nanometer grains have been observed in the resultant microstructure for the AZ alloy experienced by two-pass FSP. Besides, in order to modify the microstructure and mechanical properties, FSP is also applied to incorporate AZ31 Mg alloy with nano-ZrO_2 particles, nano-SiO_2 particles and different fractions of Al and Zn elements. The microstructure and mechanical properties of the modified alloy and composite samples are investigated and compared.

By one-pass FSP coupled with rapid heat sink from liquid nitrogen cooling approach, the ultrafine grain size in AZ31 Mg alloy is successfully achieved. The grain boundaries are well defined and the mean grain size can be refined to 100~300 nm from the initial 75 μm of commercial AZ31 Mg alloys sheets. The ultrafine grained structure can drastically increases the microhardness from the initial 50 up to 120 H_v, or an increment factor of 2.4 times. Furthermore, the nanometer grains can be even achieved by two passes FSP coupled with rapid heat sink. The resulting microstructure exhibits equiaxed grains ranging from 40 nm to 200 nm with an average grain size of less than 100 nm. The nanocrystalline grains can be characterized by the TEM observations and the diffraction rings in SAD patterns. The highest hardness point can reach ~150 H_v which is equal to triple of the AZ31 matrix, and the mean hardness also increases up to around 134 H_v.

Bulk Mg-AZ31 based composites with 10~20 vol% of nano-ZrO_2 particles and 5~10 vol% of nano-SiO_2 particles are also successfully fabricated by FSP. The average grain size of the resultant composites could be effectively refined to 2~4 μm, and it demonstrates much higher hardness values compared to commercial AZ31 billet. Moreover, for the Mg/ZrO_2 composite fabricated by one pass and subsequent cooling pass FSP, the recrystallized grain size could be further refined to 0.4 μm with the hardness value of 135 H_v. As for multi-element Mg base alloys fabricated by FSP, high fractions of Al and Zn elements can result in apparent grain refinement, this can be proved by the broadening of diffraction peaks. Multi-passes FSP can induce the appearance of intermetallic compounds, however, some of them are quasi-crystals with icosahedral point group symmetry. The average hardness of the resultant alloys reachs nearly 350 in H_v scale due to the generation of intermetallic compounds and grain refinement.

中文摘要

本研究之目標為致力於利用摩擦旋轉攪拌製程(FSP)對於固溶強化AZ31鎂合金進行改質以製備出奈米級細晶粒組織。在適當的製程參數下，利用本研究所設計出之新冷卻系統，可有效大幅度的將晶粒細化。而奈米細晶組織可在適當參數及有效新設計冷卻系統下，經二次道數後得到。此外，為了對鎂合金之微觀組織與機械性質進行改質，亦利用摩擦旋轉攪拌製程製備出添加奈米級ZrO_2與SiO_2顆粒之鎂基複合材料及鎂鋁鋅介金屬化合物合金以進行分析比較。

經由適當之製程參數與有效之液態氮冷卻系統，次微米級之極細晶粒可經一道摩擦旋轉攪拌製程得到。晶粒大小可從原始母材之 75 μm 大小細化至 100~300 nm，所得之再結晶粒具有明顯與清楚之晶界。其硬度值亦可提升至 120 H_v，達到原本母材(~50 H_v)的 2.4 倍。而本研究目標之奈米微細晶粒可在適當參數及有效冷卻系統下經二道次摩擦旋轉攪拌製程後得到。所得到之微細等軸再結晶粒大小分佈在 20 nm 至 200 nm 的範圍之間，其平均晶粒小於 100 nm，約為 80 nm。奈米晶粒可經由掃瞄式電子顯微鏡(SEM)與穿透式電子顯微鏡(TEM)的觀察下得到證明。於本實驗鎂基合金所得之極細晶粒組織最高硬度值硬度可達約 150 H_v 為原本母材之三倍值，而其平均硬度值為可提升至 134 H_v。

藉由摩擦旋轉攪拌製程可以成功製作出塊狀鎂基複合材料，經四道次的製程後，奈米級 ZrO_2 與 SiO_2 顆粒可有效的分散入鎂基材中。所製備之鎂基複合材料晶粒可細化至 2-4 μm，並可提升硬度值至兩倍以上。在更進一步利用已製備之 Mg/ZrO_2 複合材料，進行第二道次之 FSP 冷卻製程後，其晶粒大小可進一步細化至 0.4 μm 而其硬度值亦提升至 135 H_v 接近原始母材之三倍值。經摩擦旋轉攪拌製程所製備之鎂鋁鋅介金屬化合物，

具有明顯的晶粒細化效果，並有許多之介金屬化合物產生，可從其 XRD 繞射圖中有許多的結晶峰產生與繞射峰的寬化得到映證，而其其硬度值更可大幅提升至 350 H_v。

謝誌

本博士論文得以順利完成，最要感謝的就是恩師 黃志青教授在學業、研究及生活上的指導與照顧。吾師的學識淵博及待人處事的氣度皆讓學生深深的佩服，並成為我學習效法的典範。再多的言語也無法表達我對吾師的萬分感謝與敬意，老師，謝謝您。另外，要感謝口試委員 何扭今教授、高伯威教授、張六文教授、黃永茂教授及吳威德教授，在論文審查過程中，給予學生的教導與指正，由於你們的細心審查與寶貴意見，使本論文更加充實，在此對老師們致上我最由衷的謝意。

也感謝所上各實驗室的技術員，王良珠學姐、陳貴香女士、王國強先生、江宏達先生、古錦松學長、林明政先生、李秀月女士、施淑瑛小姐、行政上所辦的朱惠敏女士、顏秀芳女士、陳秀月小姐及熱心的華大哥。感謝您們在各項實驗及行政事務上的協助與幫忙。

在黃幫的大家庭裡，有太多人要感謝了，包括已畢業的木城學長、建超學長、凱琳學姐、佩汝學姐、鉉凱學長、英博學長、敬仁學長，感謝你們在學識與生活上的開導，博班的育誠學長、子翔同學、友杰、海明、炎暉、鴻昇、浩然、名哲學弟的協助，再次相見的宇庭、已畢業的致榮，及碩班的振偉、哲男、大豪，大學部的碩陽、逸志、柏佑學弟們帶給我美好的回憶與實驗室的新氣象。另外，也要感謝高、張幫的金福、文讀、小珠、小丁、惠君學長姐、宜珊、憲宗學弟，以及無法詳加記錄的諸位學長姐與學弟妹們，還有何幫的諸位，感謝你們的協助。

另外，也要感謝已經回到大陸的王軼農博士，在實驗上的指導。以及杜興蒿博士在實驗上的指導與討論，使我獲益良多，謝謝您。

最感謝的，莫過為我親愛的父母與家人，給予我關懷與支持，沒有你們不會有今天的我，給我全力的支持，使我無後顧之憂，得以完成學業，在此，把本論文獻給我的家人，感謝你們的支持與鼓勵。

要感謝的人事物太多了，謹以懷抱感恩的心，感謝上天，謝謝諸天地。

張志溢　　謹誌

於 中山大學材料科學所

2007.10

Chapter 1

Introduction

Magnesium alloys have gained increasing interest in transportation industries, because they can achieve considerable weight reduction of structures. Magnesium has the lowest density, 1.74 g/cm^3, among all light structural metals, such as Al, Mg and Ti. In addition, magnesium also has the advantage of recyclability, further decreasing the squander of natural resources. Based on the lower density and recyclability, magnesium alloys have gradually become the highly potential metallic materials.

Recently, many efforts have been made to produce ultrafine grained structural metallic materials. Fine grained materials are harder and stronger than those are coarsely grained because of having greater total grain boundary areas to impede dislocation motion and also being expected to exhibit superior mechanical properties, including high strength, high toughness and excellent superplasticity at high strain rates and low temperature [1,2]. Besides, fine grained Mg alloy possesses better ductility and formability near room temperature [3].

Metal matrix composites, MMCs, have arisen extensive researches, and numerous applications have been applied in automobiles, aircrafts, aerospace vehicles, and electronic components. Usually, metals or alloys of light weight and good ductility are adopted to serve as matrix, such as aluminum, magnesium, titanium or copper alloys. As for the reinforcement, ceramic materials with high temperature stability, high modulus, and high hardness, such as carbon fiber, glass fiber, the particulate of SiC, SiO_2, Al_2O_3 or TiB_2, are commonly introduced into the matrix. These ceramic materials should not dissolve or react with the metallic matrix.

Due to the particular mechanical and/or physical characteristics of the reinforcement, the composite properties may be significantly toughened, strengthened, modified or tailored. Better strength, stiffness, hardness, corrosion and wear resistance are commonly seen in the reinforced composite. On the other hand, MMCs can maintain the original characteristics of the matrix such as electric and thermal conductivity. Therefore, the composites with improved physical and mechanical properties will be used in higher temperature and stricter environment than that for pure metals or alloys without any reinforcement.

Friction stir welding (FSW) was invented at The Welding Institute (TWI) of UK in 1991 as a solid-state joining technique, and it was initially applied to aluminum alloys [4]. Now, the progress has been extended into Ti, Mg, Cu alloys and steel. Recently, friction stir processing (FSP) was developed by Mishra et al. [5,6] as a generic tool for microstructural modification based on the basic principles of FSW. In this case, a rotating tool is inserted in a monolithic workpiece for localized microstructural modification for specific property enhancement. FSP technique has been used to produce surface composite on aluminum substrate [6], homogenization of powder metallurgy aluminum alloy [7], microstructural modification of metal matrix composites [8] and property enhancement in cast aluminum alloys [9].

The success in fabrication of various nano-sized powders, wires or tubes has provided the new possibility in modifying the existing commercial materials in terms of their functional or structural characteristics. Except for few reports, the majority of achievements were focused on the polymer matrix modified by ceramic nano particles so as to significantly improve its mechanical or physical properties. The addition of nano powders in metallic alloys has been relatively much less addressed. The grain refining on pure solid solution AZ31 Mg alloys by other means are unable to reach nano-scale. Also, the efforts to grain

refinements on Mg alloys by FSP are less reported and the present progresses on pure Mg alloys are only in micro-scale.

In this study, the goals of grain refinement and high hardness value will be carried out by optimizing FSP process parameters and cooling facilities. Intensive efforts are made to refine the grains to nano-scale in Mg base alloys or composites by FSP. Also, the properties and the relationship between resulting grain size and parameters for the friction stir processing in AZ31 Mg alloy are systematically examined. The AZ31 Mg alloy is adopted as the matrix and nano-sized ZrO_2 and SiO_2 particulates as reinforcement to fabricate the Mg matrix composites. FSP is also applied on the dispersion of particulates by the complex plastic flow of AZ31 Mg matrix during the stirring process. Afterward, the examination and analyses of microstructures and mechanical properties of the resulting composites and modified AZ31 Mg alloy by FSP are conducted.

1.1 The developments and applications of magnesium alloys

After magnesium element was discovered by Davy in 1808, nowadays, magnesium alloys have become one of the most popular materials for structural utilization, especially in lots of areas of transportation vehicles because of the current global tend toward light-weight utilization and environmental consciousness. In order to achieve the light-weight goal, it is necessary to adopt the light metals in structural and non-structural components on the vehicles. Table 1-1 lists the comparison between the Mg alloys with many common materials. The advantages of magnesium and magnesium alloys are listed as follows, (a) Low density: Magnesium is the lightest engineering metal, with a density of 1.74, roughly 1/4 that of steel and 2/3 that of aluminum. (b) High specific strength: Mg alloys can reach required strength

with less material which can reduce the product thickness. (c) Good thermal conductivity: Mg has better thermal conductivity than equal weight polymeric materials. (d) Good damping and crash resistance: The damping capability of Mg is better than plastic and aluminum and the crash resistance is much superior to plastics. (e) Thin thickness: The thickness of Mg enclosures used for 3C procducts can be reduced to 0.5 mm (plastic ~ 1 mm) for sufficient strength. (f) Good castability: Mg can be easily die-cast into complicated shapes with minimum wall thickness. (g) Excellent electromagnetic shielding capabilities: A thin Mg wall can effectively shield electromagnetic wave. Mg is a better material than plastic to be used in the computer, consumer and communication (3C) electronic products. (h) Recyclabilty: Mg can be easily and economically recycled through proper re-melting procedures. This imposes a strong benefit over plastics.

Therefore, Mg alloys have potential to replace aluminum alloys or plastics on the application of the electronic products, or be the important structural materials according to the advantages mentioned above. Despite the numerous advantages, magnesium alloys exhibit poor workability due to the hexagonal closed-packed (HCP) crystal structure. Hence, the shaping of magnesium alloys needs to adopt the die casting, thixomolding [10] or thixocasting [11] for the present stage. The way to improve the workability of magnesium alloys will be essential in order to promote mass production of Mg alloys in many different engineering applications.

1.2 Properties of magnesium alloys

1.2.1 The classification of magnesium alloys

Alloying behavior of magnesium is notable for the variety of elements with which it will form solid solutions. Therefore, aluminium, zinc, lithium, cerium, silver, zirconium and thorium are examples of metals that are present in commercial Mg alloys [12]. Magnesium alloys are usually designed by two capital letters followed by two or three numbers. Table 1-2 [13] presents the standard four-digit ASTM designation system for magnesium alloys and their temper treatments. In this system the first two letters indicates the main alloying elements according to the following code: A for aluminium; C for copper; E for rare earths; F for iron; H for thorium; K for zirconium; L for lithium; Q for silver; Z for zinc and so on. The first latter is the element with greater quantity, and if they are equal in quality the letters are listed alphabetically. The two (or one) letters are followed by numbers which represent the nominal compositions of these main alloying elements in weight percent. For example, AZ31B-H24 means the alloy contains a nominal 3 wt% aluminum and 1 wt% zinc and is in the B modification, distinguishing form the same AZ31 that contains the different levels of impurity. The H24 designation indicates that the alloy is strain-hardened and partially annealed. The addition of solute elements in Mg alloys is generally helpful for improving its properties, such as casting capability and corrosion behavior. The effects of the various solute elements on the mechanical, corrosion and casting behavior are listed in Table 1-3 [14].

1.2.2 The characteristics of magnesium alloys

In recent years, an increasing resource shortage and environmental conditions require new ways of engineering. By using consistent lightweight construction within all areas of engineering new potentials can be created. Magnesium is the lightest metallic constructional material with a density approximately 1.74 g/cm^3 represents an attractive possibility for the lightweight construction. Therefore, the applications of magnesium and magnesium alloys gradual grow widely. The main applications of magnesium and magnesium alloys can be

divided into two categories: non-structural applications and structural applications. In the applications of structural materials, common cast magnesium alloys can be divided into several systems according to various alloy compositions:

(1) Mg-Al-X systems: The Mg-Al system has been the basis of the most widely used magnesium casting alloys. Most alloys contain 8-9% aluminium with small amounts of zinc.
    (a) Mg-Al-Zn series alloys: The addition of zinc causes some strengthening such as AZ91D which has good mechanical property, castability and corrosion resistance.
    (b) Mg-Al-Mn series alloys: Such as AM60, AM50 and AM20 which have good ductility.
    (c) Mg-Al-Si series alloys: Such as AS41 and AS21.
    (d) Mg-Al-RE (rare earth elements): Such as AE42 which has the improvements in creep resistance, ductility, and corrosion resistance.
(2) Mg-Zn-X systems:
    (a) Mg-Zn-Zr series alloys: The ability to grain refine Mg-Zn alloys with Zr led to the introduction of alloys, e.g. ZK51 and higher strength ZK61. They have high yield stress and good casting ability.
    (b) Mg-Zn-RE series alloys: Te alloys such as ZE33 and ZE41 show good creep resistance and are widely used for casting exposed to elevated temperature.
(3) Mg-Th-X systems: The addition of thorium also confers increased creep resistance to Mg alloys, and the ability for high working temperature.
    (a) Mg-Th-Zr series alloys: Such as HK31A and HK32.
    (b) Mg-Th-Zn series alloys: Such as HZ32A and ZH62A, the presence of zinc further increases the creep strength. Alloy ZH62A is also noted for its relatively high strength at room temperature.

(4) Mg-Ag-X systems: The alloys in this system possess high strength at elevated temperatures and good casting and welding capabilities.
   (a) Mg-Ag-RE series alloys: The most widely used alloy has been QE22 which has been used for a number of aerospace applications.
   (b) Mg-Ag-Zr series alloys: QK21A.

Most of all magnesium components are produced by die casting process. This process has high cycle times and good casting properties. Cast magnesium alloys have high strength and high productivity. But cast magnesium alloys common have the problem of the gas porosities which occur in the process and cause low ductility and insufficient fatigue strength. Wrought magnesium alloys offer crucial advantages like superior mechanical properties, opposite casting components weldability, possibility of a thermal treatment and an increased ductility. Because of high costs, a small deformation ratio and a severely limited alloy spectrum, therefore, there exists a requirement for technical breakthrough in the processings and new alloy systems. Some of the commonly used wrought magnesium alloys are listed below.

(1) Mg-Mn series alloys: Such as MA1.
(2) Mg-Al-Zn series alloys: Such as AZ31, AZ61 and AZ80, these alloys are of major industrial importance because of their combination of light weight, strength, castability and relatively good corrosion resistance for magnesium alloys. The alloys in these series could precipitate the β phase ($Mg_{17}Al_{12}$) in the matrix or on the boundaries to strengthen the alloys after solution and aging treatments.
(3) Mg-Zn-Zr series alloys: Such as ZK40A and ZK60A, these alloys have the characteristic of higher yielding strength and good castability, especially for the increased strength with about 0.7% zirconium for grain refinement.

The properties of different alloy systems can change by adding different alloying elements in Mg alloys according to different application demands, such as:

(1) Zinc (Zn) additions can improve castability and mechanical properties.

(2) The addition of yttrium (Y) and rare earth element into the magnesium alloys would impose superior creep resistance to the QE series alloys after fully hardened through the T6 thermal treatment [15].

(3) Silver (Ag) additions to magnesium alloys results in improving high temperature and creep properties.

(4) A small amount of Ca added into AZ series alloys could produce relatively smaller grain t to improve yield strength due to the presence of Al_2Ca and β-$Mg_{17}Al_{12}$ phases on the grain boundaries [16,17].

(5) Scandium (Sc) is a potential alloying element for improving the high temperature properties of magnesium alloys because of the high melting point of Sc (T_m = 1541^{o}C) or a lower diffusivity in Mg. Von Buch et al. [18] have developed the Mg-Sc-Mn alloys showing good creep resistance.

(6) Mg-Mn alloys system could add Sc, Gd, Y and Zr so as to develop creep-resistant magnesium alloys [19]. Mg-Gd and Mg-Sc alloy systems also show an improvement for the creep-resistant [15].

1.3 Grain refinements

Magnesium alloys are attractive for lightweight structural applications in the transportation industry because of their low density and high specific strength and stiffness [20]. However, the symmetry of the hexagonal close-packed (HCP) crystal structure has the

limiting number of independent slip systems, resulting in poor formability and ductility near room temperature [3]. Fortunately, this can be resolved by refining the grain size which can bring about sufficient room temperature ductility and even superplasticity at high strain rates and low temperatures [1,2].

Although the mechanical and physical properties of all crystalline materials are determined by several factors, the average grain size of the material generally plays a significant, and often a dominant, role. Thus, the strength of all polycrystalline materials is related to the grain size. The widely applied equation for the relation between grain size and strength or hardness, the Hall-Petch equation [21], as written in the form of

$$H = H_o + k_H d^{-1/2}, \quad (1)$$

or

$$\sigma = \sigma_o + k_\sigma d^{-1/2}, \quad (2)$$

where H and σ is hardness and flow-stress, respectively, d is the average grain size, and H_o, σ_o, k_H and k_σ are constants. It follows from Eq. (1) that the strength increases with a reduction in the grain size and this has led to an increasing interest in fabricating materials with extremely small grain sizes. Narutani et al. [22] has reported that the Hall-Petch relationship is also well followed for magnesium, and the k value is about 280~320 MPa • $\mu m^{1/2}$. Wu [23] and Lin et al. [24] also reported the k_H and k_σ are about 45~65 H_v • $\mu m^{1/2}$ and 300~350 MPa • $\mu m^{1/2}$, respectively. It is noticeable that the k slope, or called the grain size strengthening efficiency, of magnesium alloys is much higher than that of aluminum alloys (~68 MPa • $\mu m^{1/2}$), which means that the grain refinement of magnesium alloys has higher strengthening efficiency than aluminum alloys [25].

Magnesium alloys with refined grains could raise the strength and also improve the formability. In the study of AZ31 and ZK60, Bussiba et al. [26] suggested that magnesium alloys can possess better superplasticity at low temperatures or high strain rates with smaller grain size in the submicron scale. The grain refinement also affects the hardness value of magnesium alloys. Thus, the current research also focuses on producing high hardness magnesium material through effective grain refinement.

1.3.1 Grain size refinement techniques

In order to get good mechanical properties, different processes can be applied to refine the grain size, which would improve the mechanical properties such as strength, hardness, superplastic behavior, and so forth. The grain sizes of commercial alloys are generally tailored for specific applications by pre-determined thermechanical treatments in which the alloys are subjected in specified regimes of temperature and mechanical testing. However, the refining results of these usual produces are limited to the order of a few micrometers and can't be used to produce materials with submicrometer grain sizes. Therefore, the other specific grain refining techniques that may be used to fabricate ultrafine-grained (UFG) materials with grain sizes in the submicrometer range are developed.

Two basic and complementary approaches have been developed for grain refinement and these are known as the "bottom-up" and "top-down" approaches [27]. The "top-down" approach is dependent upon taking a bulk solid with a relatively coarse grain size and processing the solid to produce a UFG microstructure through heavy straining or shock loading. Unlike "bottom-up" approaches, these approaches can be readily applied to a wide range of pre-selected alloys and larger product sizes. Formally, the large strain is imposed on

the metal materials by severe plastic deformation (SPD) to gain fine grains via recrystallization or sub-grains by rearrangement of dislocations.

There are many different SPD processing techniques have been proposed, developed and evaluated. These techniques include rolling, equal-channel angular pressing (ECAP) [28-30], high-pressure torsion (HPT) [31], multi-directional forging [32,33], twist extrusion [34], cyclic-extrusion-compression [35,36], reciprocating extrusion [37,38], constrained groove pressing (CGP) [39], cylinder covered compression (CCC) [40], accumulative roll-bonding (ARB) [41,42]. All of these procedures are capable of introducing large plastic straining and significant microstructural refinement in bulk crystalline solids. Some of these techniques, such as ECAP, HPT, multi-directional forging and ARB are well-established methods for producing UFG materials.

Extrusion is the process by which a block of metal is reduced in cross section by forcing it to flow through a die orifice under a high pressure [43]. Semi-finished products of cylindrical bars or hollow tubes are most generally produced by extrusion. Lin and Huang [24,44] have extruded the AZ31 and AZ91 magnesium alloys, which are usually manufactured by thixomolding and casting, to refine the grain size from the initial average 75 μm to 1~5 μm via the occurrence of dynamic recrystallization during extrusion. These refined magnesium alloys can perform good superplasticity and higher room temperature tensile strength.

Rolling is the most widely used metalworking process because it lends itself to high production and close control of the final product. Rolling can be carried out at elevated temperatures (hot rolling), wherein the coarse-grained, brittle, and porous structure of the ingot or continuously cast metal is transformed into a wrought structure, with much finer

grain sizes. The rolling temperature plays an important role in rolling process. Rapid grain growth may be bought up by high rolling temperature that grains may not be effectively refined, while surface or edge cracking may take place at low rolling temperatures. Chang et al. [45] reported that grain sizes of AZ31 magnesium alloys could be refined from 13 μm to below 10 μm by rolling 2 mm thick plate to 0.5 mm for AZ31, and its thin sheet exhibited 300~325 MPa tensile strength. In addition, Kim et al. [46] also rolled AZ61 sheets with a thickness of 2.15 mm to 0.5 mm after nine passes at 648 K, and effectively refined grains from 16 μm to 8.7 μm.

In ARB process, the rolled material is cut, stacked and rolled again. In order to obtain the bulk material, the stacked sheets are bonded during rolling simultaneously (roll-bonding). Therefore, the achieved strain is unlimited in this process because repetition times are endless in principle. Fig. 1-1 illustrates the principle of ARB process. Perez-Prado et al. [47] reported that grain sizes of AZ31 and AZ91 alloys can be refined from 38 μm to 3 μm and 23 μm to less than 1 μm, respectively. Therefore, ARB process is also an efficient way for grain refinement and the homogeneity of the microstructure can be improved by increasing the number of rolling process.

The ECAP process, performed by pressing samples into equal-diameter channel with a different exit direction, is a shear deformation maintaining the same input dimension of the pressed (or extruded) materials. The detailed illustration is shown in Fig. 1-2 [48]. This process can impose severe plastic deformation on materials after several passes to induce micro-scaled grains [48] or even to submicro or nano-scaled extrafine grains [49]. Therefore, this process appears to be a powerful technique. Mabuchi et al. [50] refined the AZ91 alloy to 1 μm by ECAP after eight passes, and the resulting alloys also showed a high elongation of 661% at a low temperature of 473 K. Recently, Matsubara et al. [51] and Lin et al. [52] have

developed a two-stage extrusion plus equal channel angular pressing (ECAP) to fabricate the UFG Mg alloys. The original coarse grain size can be reduced to less than 10 μm after extrusion at 300^{o}C and it is further reduced to around 0.7 μm after subsequent 8-pass ECAP at 200^{o}C.

As for the "bottom-up" approach, UFG materials are fabricated by assembling individual atoms or by consolidating nanoparticulate solids. Examples of these techniques include inert gas condensation [53], electrodeposition [54], spray forming [55,56], ball milling with subsequent consolidation [57] and cryomilling with hot isostatic pressing [58], where cryomilling essentially denotes mechanical milling in a liquid nitrogen environment. In practice, these techniques are often limited to the production of fairly small samples that may be useful for applications in fields such as electronic devices but are generally not appropriate for large-scale structural applications.

The spray forming process is an inert gas atomization of a liquid stream into variously sized droplets which then are then propelled away from the region of atomization by fast flowing atomizing gas, as shown in Fig. 1-3 [55]. Droplets are subsequently deposited and collected by a substrate on which solidification takes place. Finally a coherent and near fully dense perform is produced. This process can produce bulk scale nano-grained materials via rapid solidification at a cooling rate about 10^2 ~10^3 K/s. Therefore, this process is very powerful tool, but it has an expensive issue related to patent. However, Chen and Tsao [56] reported that spray-formed AZ91-3.34 wt% Si alloys can possess finer structures and better workability than the as-cast counterpart.

Besides the refinement technologies mentioned above, there are still other methods to refine the grain size. Andrade et al. [59] used shock-wave deformation to refine Cu alloys to

0.1 μm at a high strain rate (~10^4 s^{-1}). Garces and Perez [60] conducted the physical vapor deposition (PVD) technique to obtain columnar grain structure of the diameter of 0.2 μm of the Mg-14wt%Ti–1wt%Al–0.9wt%Mn alloys. Although, there are numerous developed methods for grain refinement, most of them are limited to be applied. Some techniques are still in laboratory research trial, such as ARB process. Some are difficult to produce bulk materials, such as PVD method and most of the "bottom-up" approaches. Some are because of high production cost, such as spray forming. Thus, the traditional extrusion and rolling are still among the first choices to be adopted in industry because of the lower cost and higher feasibility.

1.4 Metal matrix composites

A composite is a combined material created by the synthetic assembly of two or more components - a selected filler or reinforcing agent and a compatible matrix binder – in order to obtain specific characteristics and properties. The criteria that a composite can be used is judged by the following points [61].

- It must be man-made.
- It must be a combination of at least two chemically distinct materials with a distinct interface separating the constituents.
- The separate materials forming the composite must be combined three dimensionally.
- It should be created to obtain properties which would not otherwise be achieved by any of the individual constituents.

Composite materials have long been designed to couple the weaker but more ductile

phase (e.g. polymers or metals) with the stronger but more brittle one (e.g. ceramics), so as to tailor the needed properties of the resulting mixed materials. Among them, metal matrix composites (MMCs) have attracted attention since 1970's. Metal matrix composites, in general, consist of at least two composites: one obviously is the metal matrix (in most case, an alloy is the metal matrix), and the second component is a reinforcement (in general, an intermetallic compound, an oxide, a carbide or a nitride). MMCs have several advantages that are very important for their use as structural materials. These advantages include a combination of the following properties [62]:

- High strength
- High elastic modulus
- High toughness and impact properties
- Low sensitivity to temperature changes or thermal shock
- High surface durability and low sensitivity to surface flaws
- High electrical and thermal conductivity
- High vacuum environment resistance

In addition to conductivity of MMCs, the most obvious advantages of MMCs are their resistance to severe environments, toughness, and retention of strength at high temperatures.

The reinforcements of the MMCs can be divided into two major groups, discontinuous and continuous. The continuous reinforcements, such as carbon fibers, glass fibers and silicon fibers, are in the form of continuous long fibers or short fibers. As for discontinuous reinforcements, the most prominent discontinuous reinforcements have been SiC, Al_2O_3 and TiB_2 in both whisker and particulate form.

Continuous fibers could improve the elastic modulus and ultimate tensile strength of composites significantly. Because continuous fibers have a large aspect ratio of axial length

to diametric width, such continuous fibers could effectively carry most of load so as to enhance the elastic modulus and strength of entire composites. From these viewpoints, continuous fibers seem to be perfect reinforcements, but they also suffer some disadvantages. The strength along the radial direction is greatly lower than that along axial direction, leading to an anisotropy problem [63]. This character will be unfavorable to some engineering applications. In order to improve this issue, most fibers are weaved into different directions to decrease anisotropy.

The composites reinforced by particulates or whiskers usually do not have a strong anisotropic character, sometimes can be almost isotropy. But discontinuous reinforcements would do not effectively share the load. Although particulates or whiskers reinforced MMCs would not have compatible elastic modulus and strength as the continuous fibers reinforced ones, the former can be processed by conventional methods such as extrusion, rolling and forging to meet the desired shapes.

It has long been known that the second phase inclusions or particles can inhibit grain growth in metallic materials. Therefore, one of the critical microstructure parameter is the particle interspacing L_s, which can be roughly estimated from [64]

, $$L_s = \langle r \rangle \left(\frac{2\pi}{3V_f} \right)^{1/2} \quad (3)$$

where <r> is the average particle radius and V_f is the particle volume fraction. Previous reinforcing ceramic particles in the 1980's usually measure around 10-50 μm in diameter, later improvements have lead to the smaller particles with uniform size distribution in the range of 0.5-5 μm. With the typical reinforcing particles of V_f=20% and <r>=10 μm in typical aluminum base composites, L_s will be around 30 μm. The resulting grain size after

casting would also generally be in this range. Further hot extrusion may refine the grain size down to around 5~10 μm, and toughening effects will only be moderately enhanced. With the abundant resources lately of the nano particles or nano carbon tubes (or wires) fabricated by various physical or chemical means, the reinforcements can be substantially smaller. If the reinforcement size is lowered to be submicron size or nano size, L_s can be reduced to submirco or nano range. It means that the grain size can be refined to submicron or nano grains. For example, Wang and Huang [65] ever added 1 vol% silica with 50 nm to 6061 aluminum alloy and extruded this composite to obtain 0.7 μm grain size.

1.4.1 Processing of metal matrix composites and magnesium matrix composites

There are various processes to produce particulates reinforced MMCs, but they could approximately be divided into solid-state and liquid-state methods.

1.4.1.1 Liquid-state methods

In principle, the liquid state route represents a very simple processing concept whereby particulates or whiskers are mixed into a light alloy melt, subsequently cast and then fabricated in a manner analogous to conventional unreinforced alloys. Sometimes, these particulates or whiskers may be manufactured into performs, and the melted alloy is subsequently introduced into performs. The related processes include the stir casting [66-68], squeeze casting [69-71], molten metal infiltration technique [72], semi-solid slurry stirring technique [73] and plasma spray [74]. Moreover, in order to uniform disperse these particles, Lan et al. [75] reported the use of ultrasonic non-linear effects to disperse nano-sized ceramic particles in molten metal to fabricated the nano-sized SiC particle reinforced AZ91D magnesium composites. This way could effectively disperse SiC particle and reduce severe

clustering occurrence. Detailed properties of composites by various processing routes are listed in Table 1-4.

1.4.1.2 Solid-state methods

The solid state method applies higher diffusion ability at elevated temperatures to sinter the entire composites and the metal matrix is remained to be the solid state during processing. The most typical solid state methods are the powder metallurgy (PM) [76-79] and diffusion bonding [80]. In addition, the PM process would generally be followed by a secondary processing such as extrusion, rolling, forging and superplastic forming to form final shapes of productions as well as to reduce the porosity. Detailed properties of composites made by the PM method are included in Table1-4.

It is known that many microstructure factors would influence the final performance of MMCs. Table 1-5 [81] presents a list of microstructural factors that influence mechanical properties and fracture in discontinuously reinforced MMCs.

The above mentioned metal based composites, either with the conventional reinforcements ~20 μm or the more advanced ones ~0.5 μm in dimension, have micro-range grain size. According to Eq. (3), when the reinforced particles are smaller, the resultant composite will have finer grain size. The success in fabrication of various nano-sized powders, wires or tubes has offered the new possibility in modifying existing commercial materials in terms of their functional or structural characteristics. At present, nano-sized composites were focused on the polymer matrix modified by ceramic nano particles so as to significantly improve its mechanical or physical properties [82-86]. It is less addressed about nano-sized particulates reinforced metal matrix composites except for few papers [75,79].

The nano-sized particulates reinforced metal matrix composites might be able to stabilize grain size to less than 200 nm and enhance the ductility at elevated temperatures.

Although the nano-sized particulates reinforced metal matrix composites could have a better properties, uniform dispersion of these nano-sized particles would be an extremely difficult task. Because of the high surface area ratio, nano-sized powders tend to cluster together, sometimes forming micro-sized aggregates. After secondary treatments, these aggregates will act as defect to form the initiation of crack to degrade the final performance. Methods in dispersing the nano powders have been limitedly disclosed, mostly still protected by patents.

1.5 Friction stir welding and friction stir processing

1.5.1 Introduction of friction stir welding (FSW)

Traditional welding methods can be divided into two categories. One is fusion welding, which fuses the edge of metals to the liquid state, and then solidifies to integrate these metals. There are many kinds of fusion welding technologies such as shield metal arc-welding (SMAW), tungsten inert gas arc-welding (TIG), electron beam welding (EBW) or laser beam welding (LBW), etc. Another is solid-state welding, which heats the metals to a softening state (not above melting point), and then applies a pressure to join two components by rapid diffusion at elevated temperatures. The methods of solid-state welding include the friction welding and superplastic welding [87]. The fusion welding always contains solidification structures, such as the inter-dendritic, eutectic phases, to influence the final properties after welding, and is sometimes subject to the phenomenon of pores. In addition, the fusion

welding also dissolves the precipitates to matrix to lower the original strength for some precipitation strengthening alloys, especially for highly alloyed 2000 and 7000 series aluminum alloys. The phenomena mentioned above are the disadvantage of fusion welding.

A novel and revolutionary welding technology, friction stir welding (FSW), was invented at The Welding Institute (TWI) of UK in 1991 as a solid-state joining technique, and it was initially applied to aluminum alloys [4]. The friction stir welding technique was also patented by TWI worldwide.

The basic concept of FSW is simple. A non-consumable rotating tool with a specially designed pin and shoulder is inserted into the abutting edges of sheets or plates to be joined and traversed along the line of joint. A schematic diagram of friction stir welding is shown in Fig. 1-4 [88]. In general, the pin is typically slightly shorter than the thickness of the workpiece. The pin is mounted in a shoulder that may be three times the diameter of the pin. The pin and shoulder are pressed against the workpiece, rotated at several hundred revolutions per minute, and advanced along the joining surface. The tool serves two primary functions: (a) heating of workpiece, and (b) movement of material to produce the joint. The heating is accomplished by friction between the tool and the workpiece and plastic deformation of workpiece. The localized heating softens the material around the pin and combination of tool rotation and translation leads to movement of material from the front of the pin to the back of the pin. As a result of this process a joint is produced in “solid state”. An entire process of friction stir welding is shown in Fig. 1-5.

1.5.2 Characteristics of friction stir welding

1.5.2.1 Microstructure of welding zone in friction stir welding

Based on the microstructural characterization of grains and precipitates in the FSW joint region, three distinct zones, the nugget zone (NZ) or termed as the stir zone (SZ) or dynamically recrystallized weld zone (DXZ), the thermo-mechanically affected zone (TMAZ), and the heat-affected zone (HAZ), have been identified as shown in Fig. 1-6. The part of base metal (BM) is the original metal materials, not undergoing any influence of welding process. The region between BM and TMAZ is HAZ. This zone experiences a thermal cycle with the occurrence of grain growth, but does not undergo any plastic deformation. The HAZ retains the same grain structure as the base metal. Beyond the nugget zone there is TMAZ which experiences both temperature and deformation during FSW. A typical micrograph of TMAZ is shown in Fig. 1-7 [89]. The TMAZ is characterized by a highly deformed structure. The base metal elongated grains were deformed in an upward flowing pattern around the nugget zone. Although the TMAZ underwent plastic deformation, recrystallization did not occur in this zone due to insufficient deformation strain. The part of DXZ is in the center location of welding zone. This DXZ has an apparent characteristic of fully recrystallized and equiaxed grains due to intense plastic deformation and frictional heating during FSW.

Generally, from the relation of the rotational direction of the pin tool and the direction of moving forward, the welding zone can be classified into the advancing side and retreating side, as shown in Fig. 1-8. The advancing side is on the position of the same direction of the rotational direction of the pin tool and forward direction. On the contrary, the retreating side is on the other position of the opposite direction of the rotation direction and forward direction.

In general, the difference of the transition region between DXZ and TMAZ is apparent

in aluminum alloys. However, there is no obvious difference between TMAZ and DXZ in the magnesium alloy. The microstructure in the TMAZ of Al alloy results from an insufficient heating temperature or strain for dynamic recrystallization during FSW. Mg alloys may experience dynamic recrystallization more easily than Al alloys, because Mg alloys have lower recrystallization temperature (about 523 K) than that of Al alloys [90]. Therefore, the deformed microstructure just outside the stir zone may be also dynamically recrystallized in Mg alloy. This may be the reason why the transition region between DXZ and TMAZ has roughly same microstructure as the nugget zone [91].

1.5.2.2 Recrystallization mechanisms

The fully recrystallized and equiaxed grains in DXZ comes from the occurrence of dynamical recrystallization due to the high strain and friction heat during the stirring process. Generally, the friction heat between the shoulder, pin and workpieces can provide enough energy to make the nugget zone to reach 0.6~0.8 T_m, and this temperature range is higher than the common recrystallization temperature (~0.5 T_m).

There were some possible mechanisms proposed for dynamic recrystallization process during FSW, such as discontinuous dynamic recrystallization (DDRX) [92-94] and continuous dynamic recrystallization (CDRX) [95,96]. The DDRX is characterized by nucleation of new grains at old high-angle boundaries and gross grain boundary migration [97]. On the other hand, mechanisms of CDRX have been proposed whereby subgrains rotate and achieve a high misorientation angle with little boundary migration. For example, mechanisms include subgrain growth [98], lattice rotation associated with sliding [99,100], and lattice rotation associated with slip [101].

Jata and Semiatin [95] were the first to propose CDRX as operative dynamic nucleation mechanism during FSW. They suggested that low-angle boundaries in the parent metal are replaced by high-angle boundaries in the nugget zone by means of a continuous rotation of the original low-angle boundaries during FSW. In their model, dislocation glide gives rise to a gradual relative rotation of adjacent subgrains. Su et al. [96] conducted a detailed microstructural investigation of FSW 7050Al-T651. Based on microstructural observations, they suggested that the dynamic recrystallization in the nugget zone can be considered a CDRX on the basis of dynamic recovery. Subgrain growth associated with absorption of dislocation into the boundaries is the CDRX mechanism. Repeated absorption of dislocations into subgrain boundaries is the dominant mechanism for increasing the misorientation between adjacent subgrains during the CDRX.

Alternatively, DDRX has been recently proposed as an operative mechanism for dynamic nucleation process during FSW. Su et al. [94] reported generation of recrystallized grains of 0.1 μm in a FSP 7075Al by means of rapid cooling behind the tool. Similarly, Rhodes et al. [92] obtained recrystallized grains of 25–100 nm in FSP 7050Al-T76 by using ‘‘plunge and extract’’ technique and rapid cooling. These recrystallized grains were significantly smaller than the pre-existing subgrains in the parent alloy, and identified as non-equilibrium in nature, predominantly high-angled, relatively dislocation-free. Thus, Rhodes et al. [92] and Su et al. [94] proposed that DDRX mechanism is responsible for the nanostructure evolution.

Although it is still a debating issue, the phenomenon of the nugget zone experiencing severe deformation and elevated temperature to result in fully recrystallized and equiaxed grain is of no doubt. Moreover, it is worth mentioning that this nugget zone exhibits a high fraction of high misorientation angles [95,102,103].

1.5.2.3 Onion rings in nugget zone

Besides the fully recrystallized and equiaxed grains with a high fraction of high misorientation angle, the onion rings are the most prominent features of nugget zone, as shown in Figs. 1-9 and 1-10. Krishnan [104] reported that the appearance of onion rings is attributed to a geometrical effect in that a transverse cross-section through a stack of semicylinders would appear like onion rings with ring spacing being wider at center and narrower towards the edge. He also thought that the formation of the onion rings is due to the process of friction heating due to the rotation of the tool and the forward movement extrudes the metal around to the retreating side of the tool. He qualitatively proved that the ring spacing would decrease with increasing rotation speed and decreasing advancing speed.

Mahoney et al. [105] reported that the onion ring structure within the stir zone is characterized by alternating bands of different grain size. Material flow probably leads to repetitive introduction of strain and strain rate into the material, which probably produces an alternation of three-dimensional ellipsoids with different grain sizes in the stir zone, as shown in Fig. 1-11. The alternation of the ellipsoids with different grain sizes generates an onion ring structure on the cross section perpendicular to the advancing direction. Park et al. [106] suggested that the formation of the elliptical nugget and that of the onion ring structure have their origin in shear deformation arising from the rotation of the threaded pin.

Yang et al. [107,108] reported that the precipitation-strengthening aluminum alloys (2024 and 2524) after FSW revealed the characteristic of banded microstructure. This bands consisted of band A containing a higher density of secondary particles and smaller grains and band B containing a lower density of secondary particles and larger grains. These banded

structure also affected performance of micro-hardness and mechanical characterization. For example, band A exhibited a higher value of micro-hardness and lower local-strain than band B, as shown in Fig. 1-12. In addition, they also pointed that these banded structure also affected the fracture behavior [109,110]. For some solid solution strengthening alloy, Chang [111] also found the similar but not apparent banded structure in the AZ31 Mg alloy after FSP. This similar banded structure was comprised by bands with larger grains and bands with smaller grains. The information of the formation of banded structure is limited and still needed to explore.

1.5.2.4 Materials flow behavior in nugget zone

The material flow during friction stir welding is quite complex depending on the tool geometry, process parameters and materials. Reynolds and coworkers [112,113] investigated the material flow behavior using a marker insert technique (MIT). Based on the observations, they suggested that the friction stir welding process can be roughly described as an in situ extrusion process wherein the tool shoulder, the pin, the weld backing plate, and cold base metal outside the weld zone form an ‘‘extrusion chamber’’ which moves relative to the workpiece. They concluded that the extrusion around the pin combined with the stirring action at the top of the weld created within the pin diameter a secondary, vertical, circular motion around the longitudinal axis of the weld.

In the study of the material flow of FSW 6061Al by means of a faying surface tracer and a pin frozen in place at the end of welding, Guerra et al. [114] reported that the material was moved around the pin in FSW by two processes. First, material on the advancing side front of a weld entered into a zone that rotates and advances simultaneously with the pin. The material in this zone was very highly deformed and sloughed off behind the pin in arc shaped

features. Second, material on the retreating front side of the pin extruded between the rotational zone and the parent metal and in the wake of the weld fills in between material sloughed off from the rotational zone. Further, they pointed out that material near the top of the weld (approximately the upper one-third) moved under the influence of the shoulder rather than the threads on the pin.

In the study of the material flow behavior during FSW of aluminum alloys by means of steel shot tracer technique and ‘‘stop action’’ technique, Colligan [115] suggested that not all the material in the tool path was actually stirred and rather a large amount of the material was simply extruded around the retreating side of the welding tool pin and deposited behind. Murr and co-workers [116,117] investigated the solid-state flow visualization in friction stir butt welding of 2024Al to 6061Al and copper to 6061Al. The material flow was described as a chaotic–dynamic intercalation microstructures consisting of vortex-like and swirl features.

Recently, Arbegast [118] suggested that the resultant microstructure and metal flow features of a friction stir weld closely resemble hot worked microstructure of typical aluminum extrusion and forging. Therefore, the FSW process can be modeled as a metalworking process in terms of five conventional metal working zones: (a) preheat, (b) initial deformation, (c) extrusion, (d) forging, and (e) post heat/cool down, as shown in Fig. 1-13. It is widely accepted that material flow within the weld during FSW is very complex and still poorly understood. It has been suggested by some researchers that FSW can be generally described as an in situ extrusion process and the stirring and mixing of material occurred only at the surface layer of the weld adjacent to the rotating shoulder.

1.5.2.5 Hardness variation in the weld zone

FSPed materials often possess equiaxed finer grains in the nugget zone. According to Hall-Petch relationship, finer grain size has higher hardness value. However, a number of investigations demonstrated that the change in hardness in the friction stir welds is different. Not all hardness profiles of FSPed materials follow the Hall-Petch relationship [119]. This is because of the different precipitation phenomenon. Aluminum alloys generally are classified into heat-treatable (precipitation-hardenable) alloys and non heat-treatable (solid-solution-hardened) alloys. FSW creates a softened region around the weld center in a number of precipitation-hardened aluminum alloys [116,120-124]. It was suggested that such a softening is caused by coarsening and dissolution of strengthening precipitates, such as Mg_2Si or $MgZn_2$, during the thermal cycle of the FSW. In the study of the hardness profiles associated with the microstructure in an FSW 6063Al-T5, Sato et al. [122] reported that hardness profile was strongly affected by precipitate distribution rather than grain size in the weld. In general, the mechanical properties of the FSWed precipitation-hardened alloys have been found to strongly depend on the volume fraction, size, and distribution of the strengthening precipitates and slightly on the grain size.

For the solution-hardened aluminum alloys, generally, FSW does not result in softening in the welds [125,126]. For 5083Al-O containing small particles, the hardness profile was roughly homogenous in the weld [126], whereas for 1080Al-O without any second-phase particles, the hardness in the nugget zone was slightly greater than that in the base material.

Sato et al. [126] reported that FSW created the fine recrystallized grains in the nugget zone and recovered grains in the TMAZ in 5083Al-O with the nugget zone and the TMAZ having slightly higher dislocation densities than the base material. Both small and large $Al_6(Mn,Fe)$ particles were detected in the nugget zone and the base material. They concluded

that the hardness profile could not be explained by the Hall–Petch relationship, but rather by the Orowan strengthening, namely, the hardness profile in the FSW 5083Al was mainly governed by the dispersion strengthening due to distribution of small particles. In this case, the interparticle spacing is likely to be much lower than the grain size.

It appears that excellent welds with no strength loss or other degradation of properties will occur in the FSW of aluminum or magnesium alloys where no reprecipitation or related aging/annealing effects occur. Therefore, the increase in hardness in the nugget zone of these materials can be explained by the Hall-Petch relationship, such as 1080Al and AZ31 Mg alloy [111]. The average hardness value in the nugget zone increases with decreasing grain size in the nugget zone.

1.5.3 Influence of welding parameters

The parameters influence friction stir welding include the welding materials, geometric shape of pin and shoulder, rotational speed, advancing speed, cooling rate, and tilt angle of working tool. Tool rotation rate (rotation per minute, rpm) and tool advancing speed (mm/min) are the most important parameters. Generally speaking, it could be explained in terms of the viewpoint of energy input for the entire welding process. Qualitatively speaking, increasing rotational speed and decreasing advancing speed could raise energy input per unit welding length. For example, Chang [111], Sato et al. [93] reported that the grain size in the nugget zone of Mg and Al alloys would gradually grow with increasing rotational speed on the same advancing speed due to raising maximum temperature or energy input per unit length. Hassan et al. [127] also reported that increasing advancing speed would result in smaller grain size in the nugget zone due to a lowered maximum temperature or reduced energy input. Except for lowering energy input, increasing the cooling rate is also an effective way.

The various the pin geometric shape of pin would result in different appearances of the nugget zone and material flow. A FSW tool consists of a shoulder and a pin as shown in Fig. 1-14. The tool has two main functions: (a) localized heating and (b) material flow. The generated heat is mainly from the friction between shoulder and workpiece during the process. After the first developed fixed pin tool, the evolvement of new tool geometry is significant. Complex featured tool, which is supposed to alter material flow, mixing and reduce process load, are designed by various researchers in the world. For example, Whorl^{TM} and MX Triflute^{TM} tools [128] developed by TWI are shown in Fig. 1-15 which are designed to reduce welding force, enable easier flow of plastically deformed material, facilitate the downward augering effect and increase the interface between the pin and the deformed materials, thereby increasing heating. However, Kwon and Shigematsu [129] also reported that applying a special pin with smaller contact area with the workpiece than screw type, as shown in Fig. 1-16(a), could achieve submicron grains of about 0.5 μm. It is a result of reducing the frictional area between the pin and workpiece to lower energy generation. In addition, many engineers designed various geometric shapes, as shown in Fig. 1-16(b), to result in different levels of material flow. It is hoped to improve the welding quality under the various welding form, such as, lap welding or butt welding.

1.5.4 Advantages and disadvantages of friction stir welding

Friction stir welding is considered to be the most significant development in metal joining in a decade and is a “green” technology due to its energy efficiency, environment friendliness, and versatility. FSW also has been so attractive and potential that many engineers and scientists spent great efforts on the related research. The process advantages result from the fact that FSW takes place in the solid phase below the melting point of the

welded materials which can avoid defects caused during solidification. The benefits therefore include the ability to join materials, which are difficult to fusion weld, such as the 2000 and 7000 series aluminum alloys. Other advantages listed as followed: (a) more environmental friendliness with no fume, no weld porosity and no spatter, (b) higher energy efficiency compared to fusion welding, (c) good welding qualities with low distortion, even in long welds, (d) excellent mechanical properties as proven by fatigue, tensile and bending tests, (e) the ability to apply in all positions, (f) the capability to make use of existing machine tool technologies, (g) no consumables or shielding gas required, (h) automation welds using robots. The key benefits of FSW are summarized on Table 1-6 [88].

Although FSW has the above advantages, it needs the various fixtures to fix the various forms of the workpieces. It means that extra cost is needed for the design and fabrication of the fixtures.

1.5.5 Friction stir processing (FSP)

Friction stir processing (FSP) was first proposed by Mishra et al. [5,6] as a generic tool for microstructural modification based on the basic principles of FSW. In this technique, a rotating tool is inserted in a monolithic workpiece for localized microstructural modification for specific property enhancement. Mishra [130] utilized the following unique features of FSW process to develop the friction stir process: (a) low amount of heat generated, (b) extensive plastic flow of material, (c) very fine grain size in the stirred region, (d) random misorientation of grain boundaries in the stirred region, (e) mechanical mixing of the surface layer, (f) large forging pressure and (g) controlled flow of material.

Friction stir processing is a technology similar to friction stir welding basically. FSW

and FSP have similar technologies but different goals. The goal of FSW focus on the jointing of metals, however, FSP emphasizes the modification of metals to be utilized on secondary process. This new process is a very potential technology to provide the opportunity to homogenize microstructure for subsequent forming operation and is emerging as a very effective solid-state processing technique.

1.5.6 Application of friction stir processing

1.5.6.1 Friction stir processing for grain refinement

During the FSP, the localized heating was produced by the friction generated between the rotating tool and the workpiece. The material undergoes intense plastic deformation at elevated temperatures, resulting in significant grain refinement via repeated dynamic recrystallization during this process. Thus, the dynamic recrystallization during FSP results in generation of fine and equiaxed grains in the nugget zone. A numerous researches for grain refinement by FSP have focused on aluminum related alloys. Table 1-7 [131-144] give a summary of the grain size values for various aluminum alloys under different FSP conditions. The typical recrystallized grain size in the FSP aluminum alloys can be refined to micro range. However, external cooling or special tool geometries are needed to obtain ultrafine-grained microstructures (average grain size < 1 μm) in FSPed aluminum alloys, as shown in Table 1-8 [145-147]. Su et al. [94] provided an example of ultrafine-grained 7075 Al with an average grain size of 100 nm by a mixture of water, methanol and dry ice to cool plate immediately behind the FSP tool. They progressively applied this cooling action to obtain large-area bulk of untrafine grained microstructure aluminum alloys by running multiple overlapping passes [148]. This idea provides an unlimited dream of applying FSP to fabricate a bulk ultrafine-grained alloy.

As for grain refinement, FSP has several advantages or potential advantages over other processing techniques: (i) It produces nanocrystalline with high-angle boundaries in a single step. No complex processing procedure is needed. (ii) It may be possible to control the resulting microstructures by changing the processing parameters and cooling rates. (iii) An entire sheet could be friction stir processed in a multipass overlapping sequence to obtain desired microstructure over a large area. (iv) The FSP technique can process any desired size thin sheet to nanostructure by running multipasses.

However, the researches of grain refinement by FSP mainly focus on Al based alloys. The similar studies on Mg alloys are much less than Al alloys due to the widespread and mainly use of all kinds of aluminum alloys as structural materials. Nevertheless, magnesium alloys are more and more attractive for lightweight structural applications because of their low density and high specific strength and stiffness. Although Mg alloy has poor formability and ductility near the room temperature due to limited number of independent slip systems, the shortage can be overcome by grain refinement which can bring about sufficient room temperature ductility and even superplasticity at high strain rates and low temperatures [1,2]. Thus, it is useful to develop grain refinement techniques for Mg alloys.

Table 1-9 [149-155] shows a summary of the grain size values for various magnesium alloys under different FSP conditions. Compared with the aluminum alloys, as shown in Table 1-8, the UFG microstructure Mg alloys are still not available. Because of higher grain boundary diffusion rate and lower melting temperature [64], Mg alloys with low content of alloying element are difficult to obtain UFG microstructure by SPD. Hence, ultrafine nano grained microstructure in pure or solution hardening Mg alloys still can not be obtained by SPD or FSP processes. However, it is interesting and worth paying efforts to develop the

ultrafine nano grains in AZ31 based alloys by FSP and this is also the main goal of this study.

1.5.6.2 Friction stir processing for superplasticity

Superplastic forming has several advantages over conventional forming operations, but typical forming rates (10^{-4}-10^{-3} s^{-1}) are slow for large volume production industries. Therefore, high strain rate superplasticity (HSRS) at or above 10^{-2} s^{-1} strain rate is needed to increase the utilization of superplastic forming.

The application of FSP to induce superplasticity has attracted extensive research efforts [89,140,141,156]. Compared to other processing techniques such as thermo-mechanical processing (TMP) [157], equal channel angular pressing (ECAP), torsional deformation under pressure, FSP is particularly attractive because it provides a very simple and effective approach to obtain a through thickness fine-grained microstructure for superplasticity. Conventional TMP, generally involving solution treatment, overaging, multiple pass warm rolling with intermittent reheating, and a recrystallization treatment [157], is complex, time-consuming, leads to increased material cost, and can only produce thin gage sheet. For ECAP, usually at least six processing passes, equivalent to an imposed strain of ~6, are necessary to create a fine-grained superplasticity microstructure [158]. By comparison, one-pass FSP can produce an estimated effective strain of >40 [159], resulting in a very fine 0.5–10 μm grain structure. High strain rate superplasticity has been induced by FSP in a number of aluminum alloys such as 7075Al [89,156], Al–Mg–Zr [140], 2024Al [141]. In addition, HSRS could also be found in AZ61/SiO_2 composite material [160].

Mishra et al. [5,89] demonstrated the feasibility of friction stir processing to produce a microstructure amenable to high strain rate superplasticity in a commercial 7075 aluminum

alloy. Charit and Mishra [141] also reported the success of high strain rate superplasticity on friction stir processed 2024 Al alloy. In addition, Dutta et al. [161] reported that overlapping passes of FSP can produce 80 mm wide sheets of reasonably homogenous 7075 Al alloy for punch stretching at 450^{o}C and a lower strain rate of 10^{-3} s^{-1}. This success meant that multiple overlapping passes of FSP could be applied on microforming or superplastic forming. Based on the above examples, FSP could be a potential process of TMP to refine grain size, and the alloys after FSP could exhibit good ductility at elevated temperatures.

1.5.6.3 Friction stir processing for fabrication of metal matrix composites

Mishra et al. [6] reported a novel technique for fabrication of surface composite by FSP. The method was that the SiC powders were firstly added into a small amount of methanol and mixed, and then applied to the surface of 5083 Al plates to form a thin SiC particle layer. The Al plates with a preplaced SiC particle layer were subjected to FSP after drying in air to form a surface composite. Hu [162] used 5083 Al plates with the deep holes filled Al_2O_3 powders to fabricate bulk aluminum based composites. Cavaliere [163] produced 2618/Al_2O_3/20p metal matrix composite by FSP successfully. This composite shows good strength and ductility values at room temperature because of very fine structure obtained by the FSP processing, revealing an increase in room temperature ductility compared to the unstirred material. In addition, Morisada et al. [164] successfully dispersed multi-walled carbon nanotubes (MWCNTs) into the AZ31 magnesium alloy using FSP. Distribution of the MWCNTs was changed on the basis of the travel speed of the FSP tool. The grain size of the AZ31/MWCNTs surface composites was smaller than that of the FSPed AZ31 without the MWCNTs. The addition of the MWCNTs appears effective for fabricating the composites consisting of fine matrix grains. Morisada et al. also fabricated AZ31/SiC [165] and AZ31/C_{60} [166] composites by FSP. The hardness values of composites can also be enhanced.

Moreover, Lee et al. [167] also produced AZ61/SiO_2 Mg based metal matrix composite by FSP successfully. The 5-10 vol.% nano-sized SiO_2 was incorporated into an AZ61 Mg alloy matrix to form bulk composites.

Except for the method of directly adding the reinforcement into the matrix, the method called "friction stir reaction processing" (FSRP) which is an extension of friction stir processing by adding particles into the weld to cause chemical reactions to form reinforcement was also conducted by Howard et al. [168]. Hsu et al. [169] also employed this similar method to fabricate Al based composites. They first utilized the powder metallurgy to fabricate Al-15Cu alloy without reaction, and applied the effect of high temperature and mixing material of the subsequent FSP to form the Al_2Cu intermetallic compound and disperse in the Al matrix. As stated above, FSP really could fabricate metal matrix composites by a suitable method to add the reinforcements into the matrix.

1.6 Motives of the research

Magnesium is the lightest of all metals used as the basis for constructional alloys. It is this property which entices industrial manufacturers to replace denser materials, not only steels, cast irons and copper base alloys but even aluminum alloys, especially for the lack of petroleum energy in the future. But Mg alloys usually cannot sustain heavy load at elevated temperatures greater than 250^{o}C except for a few QE or WE series Mg alloys. However, these series alloys are more expensive than the most commonly applied commercial AZ series Mg alloys. The creep properties of the later alloys are considered to be poor. The modification of commercial registered Mg alloys with the addition of ceramic particles might result in apparent improvement in creep properties. Although composites reinforced with nano-sized

particles, wires or tubes are very attractive, the uniform dispersion of nano-sized reinforcements is a critical and difficult task.

It is well known that fine-grain-sized alloys possess improved mechanical properties including higher strength, better ductility, and high superplasticity performance. A fine-grained material is also harder and stronger than one that is coarsely grained because it has greater total grain boundary areas to impede the dislocation motion. For many materials, the hardness, H, varies with grain size according to Hall-Petch relation. It means that reducing the grain size could increase the hardness of the material, especially for solution hardenable alloys.

Friction stir processing could result in the occurrence of materials plastic flow in the stirred zone to induce fully recrystallized grains with random misorientation boundaries. The entire process is under the solid state below the melting point. FSP could adjust the suitable pin rotational speed and advancing speed to control the amount of input energy. On the other side, FSP could also control the heating time by various cooling facilities, such as liquid nitrogen or ice water cooling. Based the features of FSP above, it would be possible to produce the fine grained high performance alloy or even nanocrystalline materials. Also, FSP provides a chance to uniformly disperse the nano-sized reinforcements utilizing the severe plastic flow in the stirred zone during processing.

Therefore, the current proposal will adopt a suitable method to add the thermally stable ceramic nano-sized powders into the light-weight Mg base alloys and uniformly disperse these nano-sized reinforcements by FSP. For the sake of grain refinement and high hardness value, optimal process parameters and cooling facilities are conducted. In this research, the work is designed as what summarized below:

(1) To refine the grain size to nano-scale (~100 nm) in magnesium base alloys or composites by suitable FSP parameters and cooling conditions.

(2) To enhance the hardness values of magnesium base alloys or composites up to triple (~150 H_v) of the base magnesium AZ31 alloy (~50 H_v).

(3) To develop magnesium base composites reinforced with nano-sized particles by friction stir processing.

(4) To modify magnesium base alloys by friction stir processing and to compare the difference between modified magnesium base alloys and magnesium base composites.

(5) To apply multiple FSP passes to disperse uniformly the nano particles, with higher FSP heat inputs initially to fabricate the composite, followed by subsequent FSP passes with lower heat inputs to refine the grain size to submicron or nano scale.

(6) To evaluate the microstructural characteristics using XRD, SEM and TEM.

Chapter 2

Experimental methods

In order to achieve ultrafine nano-scale grain sizes with triple hardness in Mg alloys. There are quite a few approaches tried to reach the goal. The effective approaches are summarized in the step flow chart in Fig. 2-1. The related total results are summarized in Table 3-8.

2.1 Materials

The AZ31 billets used in this study were purchased from the CDN company, Deltabc, Canada. The as-received alloy was fabricated through semi-continuous casting and has the form of extruded billet measuring 178 mm in diameter and 300 mm in length. The specimen of the as-received AZ31 alloy was cut into rectangular with 50 mm in width and 100 mm in length. For the different purposes, the thickness of the plate varies from 10 mm to 4 mm. The chemical composition of AZ31 alloys is listed in Table 2-1. This alloy is a solution hardened alloy with minimum precipitation. The as received alloys contained coarse grains around 75 μm (grain size measurement based on the linear line intercept method), as shown in Fig. 2-2, and did not exhibit any superplastic characteristics.

2.1.1 The materials for intrinsic reinforced Mg-Al-Zn alloys

The AZ31 billet was then warm rolled to 1 mm in thickness. Pure Al and pure Zn foils of 99.9% purity and 0.2 and 0.125 mm in thickness, respectively, were adopted for mixing with

the AZ31 stress. With the desired portions of Mg, Al, and Zn, the thin foil specimens were stacked as a sandwich and held vertically as shown in Fig. 2-3, ready for FSP. The alloys ratio was reached by stacking Mg sheets and Al, and Zn foils in the stirring position.

2.1.2 The extrinsic reinforcements for the Mg-AZ31 based composites

As for the reinforcements, the nano-sized ZrO_2 are particles, fabricated by Desunnao Company, Taiwan, were originally used as a kind of reinforcement for plastic materials. The ZrO_2 particles are 99% in purity, with a size in the range of 15-25 nm, or an average size around 20 nm, and a density of 5.89 g/cm^3. The XRD pattern of the ZrO_2 powder shown in Fig. 2-4(a) reveals the monoclinic structure. The different reinforcements, the nano-sized SiO_2 particles, also fabricated by Desunnao Company, Taiwan, were used for comparison. The particles are 99% in purity, with an average size around 20 nm and the density is 2.65 g/cm^3. The TEM and XRD photographs of these particles shown in Fig. 2-4(b) confirm the amorphous structure and an average size of 20 nm.

2.2 The set-up of friction stir processing

The simplified FSP machine is a modified form of a horizontal-type miller, with a 5 HP capability, as shown in Fig. 2-5.

2.2.1 The design of tool and fixture

There are several kinds of fixed pin tools used in this research. The largest one is 6 mm in diameter, 6 mm in length and 18 mm in shoulder diameter. The smallest tool has shoulder

diameter, pin tool diameter and length of 10, 3 and 3 mm, respectively. Smaller tool is conducted in order to reduce the heat generation caused by the shoulder and stirring pin during the process. All the tools have one fixed pin which has screw with a pitch distance of 1 or 0.8 mm. The material of the tool is SKH9, one kind of high speed steel. The details of the pin tools are listed in Table 2-2.

The back plate made by steel was used firstly in the experiments. In order to increase cooling effects, the copper made black plate was used in most experiments. The back plate is designed to contain three cooling channels with cooling liquid passing through them. The entire fixture design is shown in Fig. 2-6.

2.2.2 The special cooling condition during friction stir processing

In order to achieve ultimate fine grain size, optimal parameters and specific cooling system, such as liquid nitrogen, were applied. Firstly, the liquid nitrogen was added directly to chill the FSP specimen. Then, the black plate fixture, as shown in Fig. 2-6, was encircled to be a tank. The tank was filled with liquid nitrogen and the specimens are constantly contacted by liquid nitrogen. Therefore, with the accompanying of the liquid nitrogen cooling, the undesired heat causing grain growth could be eliminated more quickly. The finer recrystallized grain could be obtained without the long grain growth stage. However, the back plate fixture part is still not direct contacted and cooled by the liquid nitrogen. Hence, this cooling type is not efficient enough until the new effective cooling system is designed.

2.2.2.1 Newly designed effective cooling system

Based on extensive experimental experience, it is concluded that the primary heat

release during FSP is made from the bottom of the pin to the back plate beneath the sample. A newly designed cooling system is used, as shown in Figure 2-7. In order to transfer the heat generated between the tool and sample during FSP as quickly as possible, a thin copper mould and liquid nitrogen are used. Two tunnels are machined beneath the surface of the copper mould, and the liquid nitrogen can be immerged and flow through. The specimen was set and fixed direct on the thin copper mould and the whole system was also encircled and placed in the tank. Therefore, the liquid nitrogen can submerge the thin copper mould and flow through the tunnels.

2.2.3 The methods of adding nano-sized powders into AZ31 alloys

One or two deep shallow grooves ~6 mm depth, 1.25 mm wide and 100 mm length are cut on the rectangular samples of the AZ31 Mg alloy. The rectangular specimens of the AZ31 Mg alloy were sampled from the billet and were 55 mm in width, 130 mm in length and 10 mm in thickness. The appearance of the samples with one (1G) or two (2G) grooves is shown in Fig. 2-8. Then, these grooves were inserted with nano-sized ZrO_2 powders, in average, one groove is filled with 500 mg ZrO_2 powders. The AZ31 sample with grooves and inserted ZrO_2 powders was conducted multiple FSP to fabricate composites, as shown in Fig. 2-8(b) and (c). In order to prevent the nano-particles from being displaced out of the groove(s), surface “repair” was accomplished before FSP with a modified FSP tool that only has a shoulder without pin. The detailed procedure is shown in Fig. 2-9. In addition, the samples have the grooves inserted with nano-sized SiO_2 powders, with one groove filled with 100 mg SiO_2 powders, were prepared and the results are compared with those of the ZrO_2 containing composites.

2.2.4 The parameters of friction stir processing

2.2.4.1 FSP parameters for modified AZ31 alloys

The advancing speed of the rotating pin during FSP varies between 45 mm/min and 800 mm/min, with a variable pin rotation rate of 600 rpm (rotation per min) to 1800 rpm for pure AZ31 Mg alloys. The fixed pin tool with 6 mm in diameter and 6 mm in length was used. The shoulder diameter was 18 mm, and the applied tilt angle of the fixed pin tool was 3°. The AZ31 plate was 10 mm in thickness. In addition, a K-type thermocouple was inserted into the sample, as shown in Fig. 2-10, to measure the temperature variation during the entire FSP pass.

2.2.4.2 FSP parameters for fabricating intrinsic reinforced Mg-Al-Zn alloys

The fixed pin tool was 6 mm in diameter and 5 mm in length, with a pitch distance of 1 mm. The shoulder diameter was 16 mm, and the tilt angle of the fixed pin tool was 2^{o}. The pin rotation was set to be 1500 rpm, and the pin advancing speed was 20 mm/min. Most FSP experiments were conducted with air cooling, selected FSP runs were performed using copper clamping kits with water. Some selected FSP runs were even conducted using liquid N_2 to chill the specimens and the rotating pin. A special container was placed around the specimens so that the specimen and pin could be submerged in the liquid N_2, as shown in Fig. 2-3(c). For comparison, the $Mg_{70}Al_5Zn_{25}$ alloy system was also prepared by rapid quenching melt spinning with a cooling rate around 10^5 K/s. Melt spinning is a technique used for rapid cooling of liquids. A wheel is cooled internally, usually by water or liquid nitrogen, and rotated. A thin stream of liquid is then dripped onto the wheel and cooled, causing rapid solidification. This technique is used to develop materials that require extremely high cooling rates in order to form, such as metallic glasses. The schematic drawing of the melt spinning is

shown in Fig. 2-11 (a). The melt spinning process was conducted in our group and the picture of the facility is shown in Fig. 2-11 (b).

2.2.4.3 FSP parameters for fabricating extrinsic reinforced Mg-AZ31 based composites

The fixed pin tool with 6 mm in diameter and 6 mm in length was used. The shoulder diameter was 18 mm, and the applied tilt angle of the fixed pin tool was 2°. The plate was 10 mm in thickness. The FSP parameters of advancing speed of 800 rpm and pin rotation of 45 min/min were applied in the present experiment. The FSP was conducted for one to four passes (denoted as 1P to 4P), the advancing direction for the subsequent pass was in opposite direction to the previous pass (i.e. proceeding in a forward and then backward way).

2.2.4.4 FSP parameters for producing the ultrafine grained AZ31 alloys

A tool with shoulder diameter, pin tool diameter and length of 10 mm, 3 mm and 3 mm, respectively, was used to perform the FSP. The tool rotation rate of 800~1200 rpm was adopted and the advancing speed was 28~37 mm/min. A tool tilt angle 1.5^{o} was used. In order to obtain rapid heat sink during FSP, the newly efficient cooling system with liquid N_2 was conducted. The thin plate used in present study is 4 mm in thickness. Finally, Fig. 2-12 shows the experimental procedures for this research.

2.3 Microhardness measurements

A Shimadzu HVM-2000 microhardness machine with standard Vicker's diamond

indenter was used. The measurement condition is 200 g for 15 seconds along the transverse direction in transverse cross-sectional plane. The interspace between measurement positions is 500 μm and every measurement position is measured three times with the interspace of 200 μm along the vertical direction. The hardness value of every measurement position is the average value of three readings.

2.4 Mechanical tests

The tensile test was performed using in the Instron 5582 machine. The loading temperatures are set to be the room temperature. The strain rate is set to be $1x10^{-3}$ s^{-1} at room temperature. The loading direction is perpendicular to the welding line. The detailed size of the tensile sample is shown in Figs. 2-13. The gauge section of the perpendicular tensile sample is the nugget zone, so that the actual mechanical properties of the FSP nugget zone can be revealed.

2.5 The analysis of X-ray diffraction

The analysis of X-ray diffraction was performed using the Siemens D-5000 X-ray machine with a working voltage of 40 kV, and electron current of 30 mA. The analysis of X-ray diffraction was proceeded on the transverse cross-sectional plane.

2.6 Microstructure observations

2.6.1 Optical microscopy (OM)

The transverse cross-sectional planes of FSP samples are observed. The sample was cut by slow cutter followed by cold mounting. The samples to be cold mounted were ground with P800, P1200, P2000 and P4000 SiC papers and then polished with 0.3 μm and 0.05 μm Al_2O_3. After grinding and polishing, the samples were cleaned by methanol in an ultrasonic cleaner to obtain a clean and bright sample surface. The clean samples were etched by mixture of 5 g picric acid, 100 ml methanol, 5 ml acetic acid and 10 ml water to reveal the appearance, porosities and grain size of the nugget zone. Besides, the mixture of 5 g $NaNO_3$, 20 ml acetic acid and 80 ml water was also used to etch the clean samples to reveal the flow pattern of the nugget zone. The optical microscopy (OM) was undertaken using the Microphoto-FXL optical microscope manufactured by Nikon and the images were recorded by coolpix995 digital camera also manufactured by Nikon.

2.6.2 Scanning electron microscopy (SEM)

Due to the magnification limited of the optical microscopy, the FSPed AZ31 alloys which obtain ultra-fine grained microstructure have to be examined by SEM. JEOL JSM-6330 SEM was utilized to observe the ultra-fine grained microstructure here. Before observation, the transverse cross-sectional plane was polished to the stage using 0.05 μm Al_2O_3 and etched by mixture of 5 g picric acid, 100 ml methanol, 5 ml acetic acid and 10 ml water to reveal the appearance, porosities and grain size of the nugget zone.

The distribution of the nano-sized ZrO_2 particles in magnesium based composites made by FSP was also examined by JEOL JSM-6330 SEM. Before observation, the transverse cross-sectional plane was polished to the stage using 0.05 μm Al_2O_3. The clean samples were

observed on suitable magnification by secondary electron image (SEI) or back scattered electron image (BEI) and the recorded images were analyzed by Optimas® image analysis software. In addition, the fracture surfaces of tensile samples after tensile deformation were also examined using SEM.

In order to identify the constituent component and confirm the composition percentage of the intrinsic reinforced Mg-Al-Zn alloys, the samples were characterized by SEM with energy dispersive X-ray spectrometry (EDS).

2.6.3 Transmission electron microscopy (TEM)

The morphology of grains/subgrains and the dispersion of reinforcement phase in matrix and interface between the reinforcement and matrix were examined by TEM using a JEOL 3010 electron microscope operating at 200 kV. The specimens sampled from the nugget zone from the transverse cross-sectional plane were ground into thin foil by SiC papers and punched into a 3 mm disc for TEM microstructure characterizations. The 3 mm discs were electrically polished by twin-jet polisher using a solution of 22.32 g magnesium perchlorate, 10.6 g lithium chloride, 200 ml 2-butoxy ethanol and 1000 ml methanol electrolyte, the polisher applied a voltage of 90 V while keeping the electrolyte at about -40^{o}C. After the polishing finished, samples were taken out immediately and washed in ethanol and then soaked in ethanol for about 1 min, and then dried and stored in a dry environment to prevent oxidation.

As for the ultra-fine grain AZ31 Mg alloys with the nugget zone smaller than 3 mm in diameter, the TEM specimens are prepared by the advanced focus-ion-beam (FIB) technique. The focus ion beam instrument (SMI 3050) belongs to the dual-beam type of FIB, where one

beam can provide a second-electron image to observe the appearance of the sample, and another can provide the etching function by Ga^+ ion for the TEM specimen, cross-section image, and patterns, and so forth. The specimens, fixed on an aluminum holder and cleaned by nitrogen, were moved into the FIB chamber. The approximate 1 μm x 3 μm area was deposited with a carbon film to protect the damage from the Ga^+ ion during the process of preparation, as shown in Fig. 2-14. Then, the slope-etching was employed at the upper and under areas. At this moment, the archetype of the TEM specimen in the trapezoid shape was fabricated. The TEM archetype was retouched two parallel planes, and the thickness of the TEM specimen was thinned out less than 100 nm. Finally, the bottom part and both sides of the TEM specimen were cut. Then, the finished TEM specimens were moved on a carbon-coated Cu grid and examined by the TEM.

Chapter 3

Experimental results

3.1 Basic AZ31 alloy FSP trials

3.1.1 The appearance of the FSPed pure AZ31 alloy specimens

The appearances of the FSPed specimens are shown in Fig. 3-1. A hole can be seen on the specimens because the extraction of the fixed pin tool after the process. The volume of the hole is equal to the volume of the fixed pin. This shortage could be overcome by using the adjustable pin tool. Generally, semicircular rings are observed on the top surface of the stirred zone. The size of the semicircular features (XY plane in Fig. 3-2) is found to be related to the forward motion of the tool during one rotation cycle which also depends on processing parameters. The appearances of various FSPed specimens from the normal direction (ND) view (XY plane in Fig. 3.2) with different processing parameters are shown in Fig. 3-3. From Figs. 3-2 (a), (c), and (e), it can be seen that in the constant processing speed (90 mm/min), the spacing of the semicircular features decreases with increasing rotation rate which makes the appearances of the semicircular features smoother. In addition, from Figs. 3-3 (b), (d), and (f), in the constant rotating rate (800 rpm), the spacing of the semicircular features increases with increasing processing speed which makes the appearances of the semicircular features rougher. The spacing between the rings is roughly equal to the forward movement of the tool in one rotation. For the same period and processing speed, the increasing of rotating rate means the tool rotates more cycles in a fixed distance which shortens the spacing between each ring and makes the semicircular feature smoother. In addition, for the same processing

period and rotating rate, the tool rotates less cycles in a fixed distance when the processing speed increases. Therefore, ring spacing increases and the semicircular feature becomes rougher.

Figure 3-4 shows the cross-sectional views of the FSPed AZ31 alloy. It can be defined as the nugget zone, thermomechanically affected zone, and base metal. The feature of onion ring is contained in the nugget zone. The size of nugget zone is approximate equal to the size of pin. The pin tool with shoulder diameter, pin diameter, and pin length of 18, 6 and 6 mm, respectively, is used in present stage. The nugget zone is also called the dynamic recrystallized zone which experiences dynamic recrystallization. When the tool rotation, the material was stirred and forming a plastic material flow around the rotating pin and material is repeated in every rotation. Such material flow would lead to repetitive introduction of strain and strain rate into material, which probably produces an alternation of three-dimensional ellipsoidal surfaces, as shown in Fig. 1-10 (a). The alternation of the ellipsoids generates an onion ring structure in the nugget zone on the cross section perpendicular to the processing direction, as shown in Fig. 3-4. It also shows a region, named as TMAZ, which contains distorted grains between the nugget zone and base matrix in Figs. 3-4(c) and (d). The observed TMAZ region in Mg alloys is not as apparent as that in Al alloys. Although the TMAZ underwent plastic deformation, recrystallization did not occur in this zone due to insufficient deformation strain. Typically, the recrystallization temperature for Mg alloys is around 0.5-0.7 T_m (or around 250-400 ^oC) which is lower than 0.6-0.8 T_m or around 300-450^oC for Al alloys. Therefore, Mg alloys can experience more complete dynamic recovery and dynamic recrystallization easily than Al alloys.

3.1.2 The microstructure of the modified AZ31 alloy made by FSP

The as-received AZ31 alloys contained coarse grains around 75 μm, as shown in Fig. 2-1. AZ31 alloy can be considered as solid-solution alloy without precipitates. Microstructure characterization in this study was focused on the dynamically recrystallized nugget zone. The as-received AZ31 alloy with a coarser grain size turned to posses equiaxed and smaller grains in the nugget zone (i.e. dynamically recrystallized zone) after FSP. Figs. 3-5 and 3-6 show the typical grain structures of AZ31 alloy specimens after one-pass FSP. Compared to the as-received AZ31 alloy, the grain sizes of FSP AZ31 alloy specimens are obvious smaller and can be refined drastic from 75 μm to less than 8 μm under all conditions in this study, as shown in Table 3-1. The grain shape observed from different cross-sectional planes is consistently of the equiaxed fully recrystallized type. The grain sizes near the bottom region of the dynamically recrystallized zone are typically smaller. For example, the grain sizes in top, middle and bottom regions of the FSP AZ31 alloy specimens at 800 and 1400 rpm are 3.7/3.6/2.0 μm and 4.7/3.8/2.6 μm, respectively. The larger grain sizes in the top regime are due to the more severe temperature rise caused by the friction heat generated from the tool shoulder. The recrystallized grains would gradually increase with increasing rotational rpm speed as shown in Figs. 3-5 and 3-7. The higher rotation rate causes severer rotation actions which could produce more heat energy. More generated heat brings a larger driving force for grain growth and results in larger grains. With regard to the influence of the advancing speed, the lower advancing speed would result in inputting more heat energy. Figures 3-6 and 3-8 show the variation of recrystallized grain size in the nugget zone for different advancing speeds. It could be seen that the parameter of 45 mm/min advancing speed result in the biggest grain than all others under the same rotational speed of 800 rpm. On the other hand, the parameter of 800 mm/min advancing speed leads to the finest grains. From the experimental results, it is suggested that heat input increases with decreasing advancing speed and/or increasing rotational speed. The growth of the nucleated grains would be affected easily by the heat generated during the process.

3.1.3 The temperature of the stirred zone of modified alloys

The typical temperature profiles measured by the inserted thermocouple into the AZ31 alloys are shown in the Fig. 3-9. The temperatures measured during FSP varied from 250^{o}C to 450^{o}C, depending on the FSP rotation speed. Higher rotation rate can generate more heat energy during FSP and result in larger residual grains in the nugget zone. The temperature rise duration is about 150 s. Such temperatures are compatible to those experienced during our previous hot extrusion research [24,52]. And the resulting grain sizes can also be compared. In addition, the temperature profiles also varied with advancing speed, as shown in Fig. 3-10. With a higher advancing speed, the measured peak temperature is lower and temperature rise duration is shorter. This yields the lower and shorter heat history during FSP and results in finer grain sizes. The summary of temperature measurements with different parameters is listed in Table 3-2. From the temperature measurements, it can be shown that the rotation rate and advancing speed are important parameters which mainly affect the heat history during FSP and final residual microstructure in the nugget zone. These temperature results are also consistent with the grain size observations in OM, and the measured temperature ranges in this study are also consistent with the typical recrystallization temperatures which are around 0.5-0.7 T_m (or around 250-400^{o}C) for Mg alloys.

3.1.4 Hardness measurements

The typical microhardness readings, H_v, in the central cross-sectional zones of the FSP specimens are depicted in Fig. 3-11. For the AZ31 alloy, after FSP, the hardness could increase from ~50 H_v up to ~90 H_v due to grain refinement via dynamic recrystallizaiton. This hardness result is also consistent with the grain size observation in OM. After FSP, the

obvious increments in hardness of the nugget zone in AZ31 alloys were seen. It is unlike some precipitation hardening aluminum alloys which sometimes show drastic decreasing hardness values in the nugget zone after FSP. This is because that the precipitates of precipitation hardening alloys could dissolve into the matrix or form coarser precipitates during the thermal cycles of FSP, causing the decrement in hardness in the nugget zone. The typical microhardness readings, H_v, in the various zones of the FSP specimens are depicted in Fig. 3-12. Based on systematic hardness measurements of the base and FSP specimens, the Hall-Petch relationship is well followed (d, in μm), i.e.,

$$H_v = 40 + 72\, d^{-1/2}. \tag{4}$$

The average hardness values are also summarized in Table 3-3.

3.1.5 Grain orientations

With strong dynamic recrystallization occurred during FSP in the current AZ31 Mg, the equiaxed fine grains exhibit much lower texture intensities as compared with the as-extruded AZ31 specimens [24,170,171]. Figure 3-13(a) shows the computer simulated X-ray diffraction for completely random Mg. The $(10\bar{1}0)$ and (0002) peak heights are about half of the $(10\bar{1}1)$ peak height, all present within the 2θ of 30-40°. The XRD pattern for the transverse cross-sectional plane of the as-received billet is shown in the Fig. 3-13(b). The as-received billet basically exhibits nearly random grain orientation. The XRD diffraction patterns for the transverse cross-sectional plane of the as-received billet and its representative FSP specimens are shown in Fig. 3-14. The as-received billet exhibits basically nearly random grain orientation, reflecting its fully recrystallized coarse grained structure. As FSPed at a lower rotation speed of 800 rpm, the (0002) plane tends to lie on the transverse plane of

the FSP specimen (perpendicular to the pin travel direction and parallel to the onion back surface, as also observed by Park et al. [91]). With increasing rotation speed to 1400 or 1800 rpm, the $(10\bar{1}1)$ peak height increases slightly, but never approaching to the random case.

3.1.6 Brief conclusions of basic AZ31 alloy FSP trials

The relationship between processing parameters and the resulting grain size and temperature and mechanical properties for FSP in AZ31 Mg is systemically examined. In the views of grain refinement and hardness enhancement, FSP is a useful process to refine grain size in Mg alloy and fine grain size also results in obvious increment of hardness value which follows well to the Hall-Petch relationship. Based on experimental results, the most important parameters are rotation rate and advancing speed, which are also related to the amount of generated heat energy. Therefore, in order to get finer grain size with increment of hardness, lower rotation rate and higher advancing speed are both considered to apply during the FSP. In the above experiments, the finest recrystallized grain size can be refined from 75 μm to ~2 μm which is about 3% of the original billet grain size, and the hardness can be enhanced up to ~90 H_v which is 1.8 times of original base material (~50 H_v).

However, the means of only changing parameters in this step are not capable of producing extremely fine nano-scale microstructure with high hardness. The grain size can only be refined to micro-scale by the present step. Therefore, for the sake of achieving the goals of nano-scale grain size and triple of the hardness, more efforts and other specific approaches are needed. There are several improved ways which are considered to be carried on in the next steps. The flow chart is also shown in Fig. 2-1. The following steps are mainly classified into two ways. One is thought to reduce the generated heat or to accelerate heat conduction rate from the specimens. Another is trying to add reinforcements. With the help of

additional reinforcements combined with the base alloy, the hardness value can be further improved and the grain size can also be refined.

3.2 With reinforcements to enhance higher hardness values and finer grains

The severe plastic deformation and material flow in the stirred zone can be utilized to achieve surface or bulk alloy modification via mixing of other elements or second phases into the stirred alloys. The stirred materials can result in metal matrix composites [6,7,167] or intermetallic alloys [172] with much higher hardness and wear resistance. There are two primary approaches to reinforce the AZ31 Mg alloys for finer grains or higher hardness. One is intrinsic and the other is extrinsic method. The extrinsic method depends on adding other ceramic particles, such as SiO_2 or ZrO_2 particles, as the reinforcements. Then, the Mg-AZ31 based composites with nano-ZrO_2 and nano-SiO_2 particles can be fabricated by FSP. As for the intrinsic method, the existing solute elements of AZ31 Mg alloy, such as Mg, Al and Zn, are selected and combined together by FSP. During the repeating of heating and plastic deformation in the stirring action of FSP, there are several intermetallic compounds formed in situ as the reinforcements for the base material and the resulting materials will exhibit much more promising thermal and mechanical properties.

3.2.1 Intrinsic reinforcements for obtaining finer grains or higher hardness

3.2.1.1 The appearance of the FSPed specimens

Figure 3-15 shows the appearance of the FSPed specimens and the nugget zone of intermetallic alloys. It can be seen that the specimen consisted of several thin foil with

different elements. After FSP, all thin foils are combined together and the materials in the stir zone are mixed well. The stir zone for the multi-element intermetallic specimen was typically about the size of the rotation pin, namely 6 mm in width and 5 mm in depth, which is slight smaller than the dynamically recrystallized zone seen in the AZ31 Mg alloys (~7 mm in width and 6 mm in depth). It is conceivable that the intermetallic specimens are much harder and become less deformable during FSP.

3.2.1.2 Microstructure

The alloy composites vary in a wide range within $Mg_{37.5\text{-}80}Al_{5\text{-}25}Zn_{10\text{-}45}$. Figures 3-16 to 3-21 present some examples of the SEM micrographs using the backscattering electron image (BEI). For example, the microstructure of the $Mg_{70}Al_5Zn_{25}$ system with air cooling after three passes of FSP, as shown in Fig. 3-16, contains a fine grained darker Mg (measuring 0.1-2 μm) surrounded by lighter Al and nearly white Zn. The low melting Zn (T_m~ 420^{o}C) appears to have fully melted during FSP and is squeezed into a thin layer coating the Mg grains. There are a few large particles with distinct contrast in Fig. 3-16, typically around 5 μm in size. The composition determined by SEM energy dispersive spectrometry (EDS) is close to $Mg_3Al_2Zn_3$ (sometimes defined as the $Mg_{32}(Al,Zn)_{49}$) τ phase, with a cI162 space group and a cubic lattice constant of 1.42 Å when slowly cooled or with an icosahedral structure when rapidly quenched. For higher Al and Zn content, to compositions of $Mg_{50}Al_5Zn_{45}$ or $Mg_{37.5}Al_{25}Zn_{37.5}$, the τ particles occupy with higher volume fraction in the matrix, as shown in Figs. 3-17 and 3-18. With the cooling rate improved by copper clamping kits with a water cooling system, the microstructures also tend to be more homogeneous with smaller τ particles, as shown in Fig. 3-19. After ten FSP passes, the microstructure of $Mg_{37.5}Al_{25}Zn_{37.5}$ becomes more and more homogenous with much smaller τ particles, as shown in Fig. 3-20. Systematic SEM/EDS measurements for the white contrast phase have been conducted. It is

consistently found that the composition of this phase is close to $Mg_{49.2\pm1.8}Al_{17.2\pm1.5}Zn_{33.6\pm1.8}$, not far from the $Mg_3Al_2Zn_3$ τ phase, as determined by XRD and TEM diffractions. For comparison, the $Mg_{70}Al_5Zn_{25}$ alloy system was also prepared by rapid quenching melt spinning with a cooling rate around 10^5 K/s. The typical SEM/BEI micrograph is shown in Fig. 3-21. There is no apparent large intermetallic particle seen in the matrix. The whole specimen contains a homogenous and amorphous phase.

3.2.1.3 X-ray diffraction

The XRD patterns of the $Mg_{70}Al_5Zn_{25}$ system fabricated by FSP and melt spinning are compared in Fig. 3-22. There is no detectable crystalline peak for the melt spun amorphous specimen, but many crystalline peaks for the FSP counterpart. The typical XRD patterns of the $Mg_{70}Al_5Zn_{25}$, $Mg_{50}Al_5Zn_{45}$ and $Mg_{37.5}Al_{25}Zn_{37.5}$ alloys fabricated by FSP such are shown in Fig. 3-23. When the Al and Zn contents were low, the XRD patterns of the $Mg_{80}Al_{10}Zn_{10}$ system resembled those of the FSP AZ31 alloys. With much more Al and Zn in $Mg_{70}Al_5Zn_{25}$, $Mg_{50}Al_5Zn_{45}$ and $Mg_{37.5}Al_{25}Zn_{37.5}$, the XRD patterns in Fig. 3-23 are replaced by multiple phases, including the intermediate phases of $Mg_3Al_2Zn_3$ (in the form of either cubic or icosahedral crystal structure), Mg_2AlZn and Mg_4AlZn_{11}, and possibly some others. The diffraction peaks gradually declined and broadened with increasing FSP passes, suggesting the overall refinement of the microstructure. The peak broadening becomes more apparent in $Mg_{50}Al_5Zn_{25}$ or $Mg_{37.5}Al_{25}Zn_{37.5}$, as shown in Fig. 3-23. It appears that the increasing FSP passes and higher Al and Zn contents are promising means of refining grains to submicron- or nano-scales.

3.2.1.4 Hardness measurement

The typical hardness measurement results along the transverse cross-sectional plane are depicted in Fig. 3-24. The average H_v values in the various alloy systems and processes are also compared in Table 3-4. The hardness is seen to gradually increase with increasing Al and Zn contents (Fig. 3-24). The average hardness value approaches 350 H_v in the $Mg_{50}Al_5Zn_{45}$ and $Mg_{37.5}Al_{25}Zn_{37.5}$ systems after 3 passes without cooling system. However, the variation of hardness values with higher Al and Zn contents also slightly increases. Increasing the FSP passes would reduce the variation of H_v readings inside the nugget zone and the microstructure becomes more uniform. The hardness value of $Mg_{37.5}Al_{25}Zn_{37.5}$ after 10 passes shows minimum variation. This is due to the highly uniform microstructure in this system which can be seen in the Fig. 3-20. The hardness value of $Mg_{70}Al_5Zn_{25}$ fabricated by melt spinning could approach 264 H_v, but the hardness value of the same alloy system fabricated by FSP is only 164 H_v. The difference in hardness is originated from the different phase structures. It is obvious that a higher cooling rate is still necessary to generate fully or partially amorphous phase in the Mg-Al-Zn system.

3.2.1.5 TEM examination

TEM characterization on the $Mg_{37.5}Al_{25}Zn_{37.5}$ alloys, based on both diffraction patterns and TEM/EDS measurements, has revealed the abundant $Mg_3Al_2Zn_3$ phase. In addition to the large particles (~3-10 μm) seen from both the SEM and TEM micrographs, there are many submicron- or nano-sized intermetallic phases, as shown in Fig. 3-25. The diffraction and EDS analyses suggest that these are mostly the $Mg_3Al_2Zn_3$, Mg_7Zn_3, Mg_2AlZn phases. The intermediate $Mg_3Al_2Zn_3$ particles, defined as the τ phase, have been seen to possess either the cubic or icosahedral five-fold symmetry point group, the latter is shown in Fig. 3-25(c). Both phases have the composition close to $Mg_3Al_2Zn_3$, but would be formed upon slow or rapid cooling. During FSP, both phases have been induced, suggesting the cooling rate after the pin

stirring is within the overlapping region for these two phases. The grain sizes of the elemental Mg as seen in TEM micrographs are typically in the range of 0.05-1 μm, which are also smaller than those seen in SEM. It means that the Mg phase observed in the SEM/BEI micrographs is actually composed of several submicron or nano-sized grains. This result signified the good grain refinement efficiency of FSP. Meanwhile, there are also some nano-scaled intermetallic phases with sizes near ~10-100 nm dispersed inside the Mg grains.

3.2.1.6 Brief conclusions of in-situ formed intermetallic compounds reinforced Mg-Al-Zn alloys made by FSP

Bulk intermetallic compounds reinforced Mg-Al-Zn alloys with different fractions of AZ31 sheets, Al and Zn foils were successfully fabricated by friction stir processing. Multi-passes and high fractions of Al and Zn elements results in apparent grain refinement, proved by the broadening of diffraction peaks and from SEM results. Some intermetallic compound phases were generated after multi-passes FSP and some of them are quasi-crystals with icosahedral point group symmetry. The average hardness of the multi-element Mg base alloy made by FSP reached nearly 350 in H_v scale, especially in the $Mg_{50}Al_5Zn_{45}$ or $Mg_{37.5}Al_{25}Zn_{37.5}$ system, due to the generation of intermetallic compounds and grain refinement. The microstructure and hardness in the stirred zone become much more refined and uniform due to increasing FSP passes to ten.

Although the in-situ formed imtermetallic compound reinforced Mg-Al-Zn alloys can possess extremely high hardness and some nano-grains or particles, the original compositions of pure AZ31 alloy are shifted a lot. The applicable properties for in-situ formed imtermetallic compound reinforced Mg-Al-Zn alloys are also different with the AZ31 alloys. Therefore, using the extrinsic reinforcements for obtaining finer grains or higher hardness is

taken into consideration. The composition of particle reinforced Mg based metal matrix composites can remain closer to the original base alloy and not be shifted much. The applicable properties of this kind of composite are more comparable with the original base alloy.

3.2.2 Extrinsic reinforcements for obtaining finer grains or higher hardness

In order to refine grain size and enhance hardness value for the AZ31 Mg alloy, Mg-AZ31 based composites with nano-ZrO_2 and nano-SiO_2 particles are fabricated by FSP. The nano-ZrO_2 particles are of the monoclinic phase with an average size around 20 nm. The nano-SiO_2 particles are of the amorphous phase also with an average size around 20 nm. The shapes of nano-ZrO_2 and nano-SiO_2 particles both are granular. The XRD phase identification and TEM images of the particles are shown in Fig. 2-4.

3.2.2.1 The appearance of the FSPed composite specimens

The appearances of the Mg-based composites fabricated by FSP are shown in Fig. 3-26. It also shows a hole on each specimen because of the extraction of the fixed pin tool after the process. The volume of the hole is equal to the volume of the fixed pin. The cross-sectional views of the composite specimens are shown in Fig. 3-27. No sign of the grooves filled with nano-particles can be observed in the nugget zone. This result implies that the nano-particles placed in the grooves have been stirred into the Mg alloys matrix. Due to the combination of nano-particles with the matrix Mg alloy, the nugget zone of the composite specimen shows darker color. The nugget zone, also called dynamic recrystallized zone, experiences high strain and occurs dynamical recrystallization. TMAZ, as shown in Fig. 3-27(b), is a region containing distorted grains between the nugget zone and base matrix.

3.2.2.2 Microstructure of Mg matrix composites made by FSP

The OM observation is limited due to its depth of field and magnification. Therefore, SEM is conducted to characterize the composite specimens with the magnification greater than 1000 times and the observed results are analyzed by the Optimas® image analysis software.

Microstructure characterization in this study was mainly focused on the distribution and local clustering of the nano-ZrO_2 particles, as well as the matrix grain structures in the stirred zone that have undergone dynamic recrystallization. The frictional heating and severe plastic deformation are simultaneously introduced into the stirred material during FSP by the rotating tool. Therefore, it is expected that both the frictional heating and plastic strain would lead to the formation of dynamically recrystallized grains. These two effects would also help in dispersing the inserted nano-ZrO_2 and nano-SiO_2 particles in the stirred zones.

After one-pass (1P) FSP, the dispersion of the nano-particles within the central cross-sectional area of the friction stir zone (FSZ) is basically uniform, as shown in Fig. 3-28(a). The observed clustered particle size is frequently 0.1-2 μm, much larger than the individual nano-particle size (~20 nm). In addition, some local inhomogeneous areas of the particles can be found in the 1P FSP sample, as shown in Fig. 3-28(b). The clustered size of the particles after two to four passes (2P to 4P) appears to have further reduced, as shown in Fig. 3-28(c). It means that the composite made by FSP with further stirring passes; the clustering phenomenon could be eliminated gradually. The statistical measurements for the volume fraction of amorphous SiO_2 nano particles in matrix yield the values around 5 vol% and 10 vol% for the specimens with one groove (1G) and two grooves (2G), respectively. In

contrast, the volume fractions of the ZrO_2 nano-particles in matrix are estimated to be around 10 vol% and 20 vol% for 1G and 2G, respectively. The higher ZrO_2 content than the SiO_2 case is due to the fact that ZrO_2 particles are much heavier, leading the insertion of particles in the groove more efficient.

Figures 3-29 and 3-30 show the SEM/SEI images of the SiO_2 and ZrO_2 composites specimens with different volume fractions under different magnifications, respectively. The SEM/BEI images of ZrO_2 composite specimens with different volume fractions are also shown in Fig. 3-31. The bigger particles are the clustered ZrO_2 nano particles, as shown in Fig. 3-32. Because of the small atomic number difference between Mg and Si, it is difficult to distinguish SiO_2 particles from the Mg alloy matrix under SEM/BEI images, but it is much more readily for the ZrO_2/Mg composites. Meanwhile, with increasing FSP passes, the average grain size, d_g, of the AZ31 alloy matrix is also significantly reduced from around 75 μm in the initial billet to 2~4 μm in the 4P FSP samples. At higher magnifications, these clustered particles are generally located on the grain boundaries or triple junctions, and some are embedded inside the grains, as shown in Fig. 3-33. The summary of the clustered size of the particles and the average grain size of the AZ31 alloy matrix in the 4P FSP samples are listed in Table 3-5.

Provided that all of the nano-particles are individually and uniformly dispersed in the alloy, the theoretically estimated particle interspacing L_s ($=(d/2)(2\pi/3f)^{1/2}$, where f is the particle volume fraction) [64], and thus the approximate grain size d_g, should be less than 0.1 μm. It follows that a certain level of local clustering is inevitable, and not all nano-particles can restrict grain boundary migration. Note that the typical grain size of AZ31 alloy (without nano-particles) after the same 4P FSP was measured to be around ~6 μm. The grain size in the FSP composite samples with nano-particles can be refined to 2~4 μm, indicating that the

nano-particles or clusters in the matrix did play an effective rule in restricting grain boundary migration.

3.2.2.3 XRD results

Figure 3-34 shows the XRD patterns of the modified AZ31 Mg alloys with different advancing speeds. It could be seen that the (0002) peak in the FSPed AZ31 Mg alloy with a 90 mm/min advancing speed is significantly stronger than the $(10\bar{1}1)$ peak, as compared with the random Mg. It implies that the (0002) plane tends to lie on the transverse plane of the FSP specimen (or perpendicular to the pin travel direction). However, the XRD patterns of the FSPed AZ31 Mg alloy with 45 mm/min show random-like distributions despite in the modified AZ31 alloy or AZ31 composites, as shown in Figs. 3-34 and 3-35. It is suggested that the AZ31 Mg alloy is softer, and is easily to be affected by the heat generated during the process. As FSPed at a much lower advancing speed of 45 mm/min, the induced higher temperature rise results in more complete dynamic recrystallization, as well as more random orientation, almost approaching to the random pattern shown in Fig. 3-13(a).

The XRD patterns for the transverse cross-sectional plane of the ZrO_2 and SiO_2 FSP composites are presented in Fig. 3-34. It can be seen from Fig. 3-35(a) that in the Mg-AZ31/ZrO_2 composite there is no new phase except for a small amount of the ZrO_2 reinforcement phase (weak peaks) and the Mg matrix. This indicates that the crystalline ZrO_2 phase is very stable, no reaction between the ZrO_2 phase and Mg-AZ31 matrix occurred during FSP. However, some additional weak peaks, identified as Mg_2Si and MgO, can be found in the FSP Mg-AZ31/SiO_2 composite, as shown in Fig. 3-35(b). It is evident that the chemical reaction between the SiO_2 phase and Mg matrix has occurred during the FSP mixing. The reaction in the Mg - SiO_2 system can be described by the following reaction of

$4Mg + SiO_2 \rightarrow 2MgO + Mg_2Si$. Our previous study also confirmed the presence of the Mg_2Si and MgO phases in the Mg-AZ61/nano-SiO_2 composite fabricated by the FSP route [171].

3.2.2.4 Hardness measurements

The typical Vickers hardness readings, H_v, measured along the central cross-sectional zones of the FSP samples are depicted in Fig. 3-36. Compared with the AZ31 alloy without the ZrO_2 powders reinforcements, almost a double increment of the hardness, 105 H_v, was achieved for the present composites, especially for the 2G4P sample with ~20 vol% ZrO_2 particles, as seen in Table 3-6. After FSP, the scattering of H_v within the FSP nugget zone is considered to be relatively minor, implying that the pin stirring has efficiently dispersed the nano-ZrO_2 particles in a reasonably uniform manner, especially after more than one pass. In comparison, the SiO_2 containing composites show lower H_v, mainly a result of the lower particle volume fraction. For the AZ31 alloy without any ZrO_2 reinforcement, after four passes FSP, the H_v could also increase from ~50 for the AZ31 billet up to ~70, due to the grain refinement from ~75 μm down to ~6 μm via dynamic recrystallization. This hardness result is also consistent with the grain size observation in OM/SEM. The grain size in composites specimens could be refined to 2 μm, compared with the AZ31 alloy specimen (~6 μm) without any ZrO_2 or SiO_2 particle added into matrix.

3.2.2.5 Mechanical properties

All tensile samples were machined perpendicular to the processing direction from the central region of the FSP nugget. Table 3-6 also lists the tensile properties of the AZ31 FSP alloy and composites, taking the average from two or three samples. For the AZ31 billet without FSP, the room-temperature yield strength (*YS*), ultimate tensile strength (*UTS*), and

tensile elongation are ~100 MPa, 160 MPa, and 9%, respectively. After 4P FSP for the AZ31 billet, they are improved to ~120 MPa, 204 MPa, and 18%. The increase of *YS* and *UTS* as well as elongation for the FSP AZ31 sample was mainly contributed by the grain refinement. For the FSP composites, the *YS* and *UTS* were improved also by the nano-particle reinforcements, in addition to the apparent grain refinement. For example, the yield stress of the Mg-AZ31/ZrO_2 FSP composites was improved to 143 MPa in the 1G4P (~10% ZrO_2) and to 167 MPa in the 2G4P (~20% ZrO_2) samples. The ultimate tensile strength is also appreciably improved in parallel. The increment of *YS* and *UTS* for the SiO_2 containing composites was slightly lower, due to the lower particle volume fraction.

The differences in the fracture behavior after tensile tests between the FSP Mg-AZ31 alloy and the particle reinforced composites can be seen from the SEM fractographs in Fig. 3-37. The fracture surface of the FSP AZ31 alloy exhibits elongated uniform dimples, as shown in Fig. 3-37(a), which indicate the overall ductile fracture mode with a tensile elongation of 18%. In contrast, the fracture behavior of the present composite, for example, Mg-AZ31/10%ZrO_2, is very different, as shown in Fig. 3-37(b). Some dimples with the clusters of ZrO_2 particles, and some round and shallow small dimples in the matrix area can be seen on the fracture surface of the composite. The more shallow dimples indicate a relatively more brittle fracture mode with a tensile elongation of 6%.

3.2.2.6 Mg based composites with tetragonal phase nano-ZrO_2 particles fabricated by FSP

The tetragonal phase nano-ZrO_2 particles, yttria-stabilized zirconia (YSZ), with an average size around 40 nm are also chosen as the reinforcement here. The processing parameters and fabrication method are both the same as other AZ31/monoclinic phase ZrO_2

composites during FSP. The amount of added tetragonal phase ZrO_2 particles is also the same with the monoclinic phase ZrO_2 particles for 1G and 2G, respectively. The XRD patterns for the transverse cross-sectional plane of the tetragonal phase ZrO_2 FSP composites are shown in Fig. 3-38. It can be seen that there is also no new phase except for a small amount of the ZrO_2 reinforcement phase (weak tetragonal phase ZrO_2 peaks) and the Mg matrix. There is no reaction between the tetragonal phase ZrO_2 and Mg-AZ31 matrix during FSP which is the same as the previous monoclinic phase ZrO_2 results and also can be proven from the Mg-Zr phase diagram. From the phase diagram, there is no reaction occurring or intermetallic compound produced during the specific temperature period and composition range in the FSP process. Figure 3-39 shows the Vickers hardness readings, H_v, measured along the central cross-sectional zones of the FSP samples. It can be seen that average hardness values of both 1G4P and 2G4P tetragonal nano-ZrO_2 particles reinforced Mg AZ31 composites are higher than 1G4P and 2G4P Mg AZ31 composites which are reinforced by monoclinic phase nano-ZrO_2, respectively.

The mechanical properties, strength and especially toughness are enhanced by the presence of transformation toughened zirconia particles. The increasing hardness of Mg/tetragonal-ZrO_2 Mg composite is suggested to be induced by the transformation of the tetragonal zirconia particles. It is well-known that tetragonal phase zirconia is able to transform to the monoclinic phase if a stress field is developed around the particles [173]. Because of the volume expansion (> 3%) and shear strain (1-7%) developed in the transformed particles (Fig. 3-40), a resultant compressive stress is generated in the matrix which can prevent the crack from moving, thus accounting for the increase in hardness. Therefore, the increment of hardness in the Mg/tetragonal-ZrO_2 Mg composites is caused from the transformation toughened zirconia.

3.2.2.7 The XRD and hardness analysis for the Mg/tetragonal phase ZrO_2 composites after subsequent compression

Lee et al. [174] have proposed a route for improving mechanical properties of friction stirred Mg-Al-Zn alloys by subsequent compression along the normal direction which could improve the unfavorable texture by inducing deformation twins, thus raising the yield stress and hardness significantly. Therefore, the Mg/tetragonal phase ZrO_2 composite was chosen to be subjected to the subsequent compression along the normal direction. The XRD diffraction patterns of the 1G4P and 2G4P Mg/tetragonal phase ZrO_2 composites after 6% strain of subsequent compression along the normal direction are shown in Fig. 3-41. The grain orientations are changed after compression. Fig. 3-42 shows the hardness profiles for both 1G4P and 2G4P composites after 6% compression, respectively. After 6% compression, the hardness values for both 1G4P and 2G4P are slightly increased from 103 H_v and 113.5 H_v to 105 H_v and 120 H_v, respectively. Unlike the results of compressed pure AZ61 alloys in Lee's report [174], the increment of hardness after compression here is much smaller. This may because the grain sizes here are much smaller than previous reported AZ61 alloy. The activation of twins is more difficult and the effect of twins is less obviously.

3.2.2.8 Brief conclusions for Mg-AZ31 based composites with nano-ZrO_2 and nano-SiO_2 particles

After a series of systematic experiments on the Mg AZ31/ZrO_2 and SiO_2 composites, it can be concluded briefly as follows:

(1) Friction stir processing successfully fabricated bulk Mg-AZ31 based composites with 10 ~ 20 vol% of nano-ZrO_2 particles and 5 ~10 vol% of nano-SiO_2 particles. The distribution of the 20 nm nano-particles after four FSP passes resulted in satisfactorily uniform distribution.

(2) The average grain size of the AZ31 matrix of the 4P FSP composites could be effectively refined to 2 ~ 4 μm, as compared with the ~6 μm in the FSP AZ31 alloy (without particles) processed under the same FSP condition. The crystalline ZrO_2 phase is very stable, no reaction between ZrO_2 and Mg phases occurred during the FSP mixing.

(3) The hardness and tensile properties at room temperature of the AZ31 composites with nano-fillers were improved (up to H_V~105 for 2G4P monoclinic phase ZrO_2 reinforced composite), as compared with the AZ31 cast billet (H_V~50).

(4) Although after subsequent compression, the highest hardness value obtained in the present stage is about 120 H_v or an increment of 2.4 times which is still not reaching the triple goal. The refined grain sizes did not reach nano-scale, neither. Therefore, exploring other trials to produce nano-grain size AZ31 alloy by FSP is necessary.

3.3 Using lower heat generation for obtaining finer grain size and higher hardness

From the results of basic AZ31 alloy FSP trials, we know that the resulting microstructure is related to the heating history during FSP. We can obtain lower heat input by varying process parameters such as lower rotation rate and/or advancing rate. However, the effects are limited in certain circumstances. Thus, finding other approaches to fulfill the goal is necessary. For this reason, the approaches to lower the generated heat and to increase conduction or cooling rate are taken into consideration. There are several ways put in practice such as using a smaller tool and a thinner plate as well as applying an efficient cooling system.

3.3.1 The effects of tool size, plate thickness, and cooling method

The basic principle for friction stir processing is the repeating stirring action through the rotation tool during the entire process. The heat is mainly generated from the friction between shoulder/pin and the plastic deformed materials in every stirring action. Hence, the rotating tool is the main source of friction heat. Besides the decreasing rotation rate, using smaller tool is another effective way to lower the input heat energy.

In addition, to lower the input heat energy, accelerating the heat conduction rate or the cooling rate are both feasible for refining the resulting microstructures. Fig. 3-43 shows the variation of recrystallized grains in the nugget zone of the plates with different thicknesses. Under the same conditions and tool size, the thinner plate can possess finer resulting grain size after FSP. Shortening the distance between the rotation tool and the bottom back-up plate in the thinner specimen could increase the thermal conduction rate.

Other than the process parameters, cooling facility is also the method used for controlling the working temperature during FSP. The function of cooling facility is to accelerate the cooling rate, to repel the unnecessary heat immediately and to maintain the working temperature as low as possible during FSP. The applied cooling facility in this study is the copper made back plate containing three cooling channels with cooling water passing through them. Fig. 3-44 shows the microstructure of AZ31 alloy nugget zone after FSP with different back plates or cooling facilities. With a proper or more effective cooling facility, the finer resulting recrystallized grain size in the stirred zone would be yielded due to the less experienced heat history.

Furthermore, adding liquid nitrogen and keeping specimen contacting with the liquid nitrogen is a more effective way to cool the specimen and to bring out the friction heat. With the accompanying of the liquid nitrogen cooling, the undesired heat causing grain growth

could be eliminated more quickly. The finer recrystallized grain could be obtained without the long grain growth stage. Figure 3-45 shows the variation of recrystallized grains in the nugget subject to the different cooling conditions. The finest recrystallized grains could be ~0.55 μm in the bottom of the nugget zone of the liquid nitrogen cooled FSPed AZ31 alloy specimen. A summary of the recrystallized grain size for the different FSP parameters is presented in Table 3-7. The hardness profile of FSPed AZ31 alloy with liquid nitrogen cooling is shown in Fig. 3-46. Through liquid nitrogen cooling system, the resulting microstructure of nugget zone can possess finer grain size and higher hardness as compared with other approaches.

Other results by using the combination of smaller tool size, thinner plate, and liquid nitrogen cooling facility for the FSPed AZ31 Mg alloys are shown in Fig. 3-47. The finest grain size obtained at this stage is around 450 nm, as shown in Fig. 3-47, the SEM images of the specimen using 800 rpm, 90 mm/min, and a tool with shoulder diameter, pin tool diameter and length of 10, 3 and 3 mm, respectively.

3.3.2 The combination of composite and liquid nitrogen cooling methods

Since the cooling facility plays an important role for accelerating cooling/conduction rate which can result in finer grains, the combination of Mg/ZrO_2 composites and liquid nitrogen cooling facility are performed. The 2G4P Mg/monoclinic phase ZrO_2 composite is chosen because of finer grain sizes than other Mg-based composites. After the fabrication of 2G4P Mg/ZrO_2 composite, the subsequent FSP pass with liquid nitrogen cooling facility is performed. A smaller tool with shoulder diameter, pin tool diameter and length of 10, 3, and 3 mm, respectively, was used to perform the subsequent liquid nitrogen cooling pass. The pin rotation rate and advancing speed for the sequent pass was 800 rpm and 90 mm/min,

respectively.

Fig. 3-48 shows the resulting microstructure in the nugget zone for the Mg/ZrO_2 composite with subsequent cooling pass. The grain sizes can be further refined into submicro-scale and the average grain size is about 350~450 nm which is less than the finest grain size of all previous alloys and composites. The measured hardness value also increases to about 135 H_v which is also higher than all other composites in the present study, as shown in Fig. 3-49. Therefore, the improvement of cooling rate sure plays an important for producing finer grains during FSP.

Fig. 3-50 shows the TEM observations of the microstructure for the Mg/ZrO_2 composite with subsequent cooling pass. It can be seen that grain boundaries were pinned by the reinforced ZrO_2 particles in some small grains. There are also some nano-grains in the specimen. In addition, the corresponding selected area diffraction (SAD) pattern also exhibits diffraction rings indicating many small grains having random misorientations.

3.3.3 Brief conclusions

Based on above experiments, it can be concluded that using a smaller tool and a thinner plate as well as applying an efficient cooling system can produce finer FSPed microstructure. So far the recrystallized grain size of AZ31 Mg alloy after FSP is just around ~400 nm. The average hardness value can reach to around ~100 H_v for pure AZ31 alloy and ~135 H_v for Mg/ZrO_2 composite with the second cooling pass. However, the desire for much finer Mg grains by using the present cooling approach is difficult to achieve. Therefore, the need for another cooling design is emerged. The new designed cooling system has been applied as described below.

3.4 Ultrafine grained AZ31 Mg alloy made by FSP with new designed cooling system

Based on our previous experience, it is concluded that the primary heat releasing during FSP is made from the bottom of the pin to the back plate beneath the sample. In order to transfer the heat generated between the tool and sample during FSP as quickly as possible, a thin copper mould and liquid nitrogen are used. Two tunnels are machined beneath the surface of the copper mould, and the liquid nitrogen can be immerged and flow through. The detail of the newly designed cooling system is shown in Fig. 2-7. A constant tool rotation rate of 1200 rpm was adopted and the advancing speed was 28-33 mm/min. The thin plate used in present study is 4 mm in thickness. The tool with shoulder diameter, pin tool diameter and length of 10, 3 and 3 mm, respectively, are used here. In order to obtain rapid heat sinking during FSP, the newly efficient cooling system is carried out in the present stage.

3.4.1 Microstructure of ultrafine grained AZ31 alloy made by FSP

Figure 3-51 shows the macrograph of cross section containing the entire nugget zone for the single pass FSPed AZ31 alloy at the rotation rate of 1200 rpm and advancing velocity of 28 mm/min. The degree of refinement and the extent of homogeneity of the final FSP microstructure are the two aspects that are most noticeable. In Fig. 3-52, the grain structures in the AZ31 billets after one-pass FSP with the rotation rate of 1200 rpm and the advancing velocity of 28 mm/min, viewed at a low magnification, show a well-defined equaixed and highly homogeneous nature. Figures 3-53 and 3-54 show the microstructures with the advancing velocity of 28 and 33 mm/min at higher magnifications, respectively. All of these figures show that the recrystallized fine grains are distributed homogenously in the nugget

region. Compared with other SPD processes such as extrusion, accumulated roll bonding (ARB) or ECAP [45,47,52], the ultrafine grained (UFG) microstructure obtained in the present study has clearer grain boundaries and more uniform ultra-fine grain sizes without abnormal local grain growth. Such fine grains appear to be fully recrystallized and do not belong to subgrain structures with the "diffused" boundary nature. Figure 3-55 shows the grain size distribution of the 33 mm/min specimen, which is summarized from numerous SEM micrographs. It shows that the grains are mostly scattered from less than 100 nm to 500 nm, and more than 80% of the grains are refined within 300 nm. The average grain size is typically around 200-280 nm. The mean grain size of the obtained specimens can be refined to an ultrafine scale (100-300 nm) which is much finer than other SPD results and is also the finest microstructure obtained by FSP in pure AZ31 alloys to date. The dominated factors for the formation of ultrafine grain in the AZ31 Mg alloy by friction stir processing will be discussed in Chapter 4.

3.4.2 Hardness measurement

The ultra-fine grains lead to pronounced hardening, as demonstrated by the microhardness tests. The typical microhardness reading, H_v, in the UFG zone of the FSP specimens are depicted in Fig. 3-56. The highest H_v reaches 128, and the mean hardness values are scattered around 120 H_v, which is even higher than those observed in most FSP AZ31 based composites [164-166]. In the AZ31 matrix away from the nugget, H_v remains to be around 50, indicating that the ultrafine grain structure in the FSP nugget has strengthened the alloy by 2.4 times. Since there is no twin observed in such fine grains, the hardening is postulated to be a result of the UFG microstructure plus the retained matrix dislocations.

3.4.3 Brief conclusions

With proper control of the working temperature history, an ultrafine and uniform grained structure can be achieved. The grain boundaries are well defined and the mean grain size can be refined to 100~300 nm from the initial 75 μm by one single FSP pass. The ultrafine grained structure can drastically increases the microhardness from the initial 50 up to 120 H_v, or an increment factor of 2.4 times.

3.5 Nanocrystalline AZ31 Mg alloy made by new designed cooling system and subsequent second pass with lower heat input

In order to achieve further refined grain sizes in Mg AZ31 alloy by FSP, a concept of subsequent second pass with lower heat input parameters is newly proposed. Although the ultrafine grain size around 100~300 nm can be achieved through newly designed cooling system, the resulting recrystallized grains are still larger than 100 nm. Conducting the second pass with lower heat inputting parameters provides the possibilites for further grain refining to nano-scales. The thin plate with 4 mm in thickness is also used in the present study.

There are two ways applied here for the second pass to lower the heat input. One is to change the parameter with slower rotation speed, another is to use a smaller tool. In Fig. 3-57, the SEM/SEI images of the grain structures in the AZ31 alloy after two passes FSP with the same advancing speed of 37 mm/min but the rotation rate of 1200 rpm for the first pass and 800 rpm at the second pass. The tool with shoulder diameter, pin tool diameter and length of 10, 3 and 3 mm, respectively, are used in both two passes FSP here. These images all show well-defined equaixed grains and homogeneous distribution microstructure. The grain size distribution of this specimen is shown in Fig. 3-58 which is summarized from numerous SEM

micrographs. The average grain size can be further refined to around 120~240 nm and there are existing nano-grains. TEM images also confirm the existence of nano-grains, as shown in Fig. 3-59.

In Fig. 3-60, the SEM/SEI images of the grain structures in the AZ31 alloys after two passes FSP with the same rotation rate and advancing speed of 1000 rpm and 37 mm/min, respectively. However, the pin tool conducted for the second pass is smaller than for the first pass. The pin tool with 2 mm in diameter and 2 mm in length was used in the second pass. The shoulder diameter was 6 mm in diameter. The well-defined equaixed grains and homogeneous distribution microstructure are also shown in these images. The UFG/nano-grain microstructure obtained in the present study all has clear grain boundaries and more uniform ultrafine/nano-scale grain sizes without abnormal grain growth. Fig. 3-61 shows the grain size distribution of this specimen, which are summarized from numerous SEM micrographs. The resulting microstructure exhibits equiaxed grains ranging from 40 nm to 200 nm with an average grain size of less than 100 nm, clearly illustrating that a nanocrystalline structure is produced in the two-pass FSP. The average grain size is typically around 80-100 nm. The nano-grains also can be found under TEM observations. In Fig. 3-62, TEM images also show the existence of the nano-grains. In addition, the corresponding selected area diffraction (SAD) pattern, shown in Fig. 3-62(b), exhibits diffraction rings indicating many small grains having random misorientations, with no obvious signs of preferential orientations in the region of analysis. It is also the evidence of the large number of nano grains. In Fig. 3-63, the extremely fine nano-grains can be seen under the TEM observation.

The measured hardness values show that the highest H_v reaches 155 which is equal to triple of the AZ31 matrix and even higher than those observed in the FSP AZ31 based

composites. The mean hardness values are scattered around 134 H_v. In the AZ31 matrix away from the nugget, H_v remains to be around 50, indicating that the nano-grain structure in the FSP nugget has strengthened the alloy by 2.7 times. Since there is no twin observed in such fine grains, the hardening is postulated to be a result of the UFG microstructure plus the retained matrix dislocations.

Finally, the ultrafine grain AZ31 Mg alloy/composite which possesses nano-grains, less than 100 nm, and high hardness, triple of the base alloy, is achieved by friction stir processing. The resulting grain size and hardness at the FSP nugget bottom of all processes are summarized in Table 3-8. The nanostructure achieved here is extremely finer than other SPD results and also the finest microstructure produced by FSP in pure solid solution AZ31 Mg alloys to date.

Chapter 4

Discussion

4.1 Strain rates and temperatures during FSP

The material flow during FSP was driven by the rotating pin. The flow rate may be compatible to or lower than the rotation speed of the pin, since there would usually be a certain level of rotation lagging effect. By a simple linear assumption so that the average material flow rate, R_m, is about half of the pin rotational speed, R_p, the material flow strain rate, $\dot{\varepsilon}$, during FSP may be derived by the torsion typed deformation as

$$\dot{\varepsilon} = \frac{R_m \cdot 2\pi r_e}{L_e}, \tag{5}$$

where r_e and L_e are the effective (or average) radius and depth of the dynamically recrystallized zone. It is noted that all materials within the dynamically recrystallized zone would undergo the plastic flow, and such a zone appears to be an onion-like in shape. An effective radius, r_e, that can represent the average radius for all parts of the materials inside this zone, is assumed to equal about 0.78 (or $\pi/4$ [64]) of the observed zone boundary radius, r_b. Similar argument can also be applied to L. For a given R_p of 800 rpm (or 13.3 rps, rotation per second) with r_b ~3.5 mm and L_b ~6 mm, then $\dot{\varepsilon}$ can be calculated to be ~24 s^{-1}. The typical strain rates calculated for the current applied pin rotation speed from 180 to 1800 rpm are scattered within 5 to 50 s^{-1}, Fig. 4-1(a), or in the neighborhood of 10^0 - 10^2 s^{-1}, depending on the actual zone size measured in each FSP specimen. This strain rate range is slightly

higher than the processing strain rate previously adopted in our high-ratio extrusion experiments [24,170,171] (both ~10^{-2} – 10^{1} s^{-1}).

The temperatures measured during FSP varied from 250-450°C, depending on the FSP rotation speed, as shown in Fig. 4-1(b). Typical recorded temperature profiles are shown in Fig. 3-9. The temperature rise duration is about 150 s. Such temperatures are compatible to those experienced during our previous hot extrusion research. And the resulting grain sizes can also be compared.

4.2 Relationship between grain size and Zener-Holloman parameter of FSP Mg alloy

In calculating the temperature compensated strain rate parameter, or the *Zener-Hollomon* Z parameter, $Z = \dot{\varepsilon}\, exp(Q/RT)$, during dynamic recrystallization, the activation energy Q for Mg lattice diffusion is about 135 kJ/mol [175]. The relationship between the *Zener-Hollomon* parameter and the average recrystallized grain size (d, in μm) for the AZ31 alloy during FSP is established, as shown in Fig. 4-2(a), and is given quantitatively by

$$ln\, d = 9.0 - 0.27\, ln\, Z. \quad (6)$$

It should be noted that the ranges for d and Z in the current FSP study are still rather narrow, thereby the uncertainty is higher. Our previous analyses on the same AZ31 Mg alloys during warm extrusion or tensile loading [170,171] with wider ranges of d and Z have resulted in the same relationship but with slightly different constants, as

$$ln\ d = 6.0 - 0.17\ ln\ Z\ , \qquad (7)$$

as shown in Fig. 4-2(b). The current data on FSP still comfortably reside within the scattering band. In combining all the experimental data on the grain size and *Zener-Hollomon* parameter, it is found that the resulting grain sizes basically follow similar trends irrespective of the deformation path for extrusion, tension, or FSP.

4.3 The hardening mechanism of Mg based nano-ZrO_2 and nano-SiO_2 particles composites fabricated by friction stir processing

Predicting the overall mechanical properties of the composite is very important for material designs and applications. There have been many attempts to correlate the overall composite mechanical properties with the properties of the composite constitutes, for example, the self-consistent variation methods [176], mean-field theories [177], shear-lag theory [178], finite element method (FEM) [179] and the rule of mixtures (ROM) [180]. Among them, the simplest and intuitive method for estimating the effective mechanical properties in terms of constitutes is the ROM. Although the FEM gives satisfactory results for problems with the complex geometry and the nonlinearity of the materials properties, the ROM as a simple and fast solution for the simplified model is also useful, in which, the Voigt model based on the equal stain assumption and the Reuss model based on the equal stress assumption have been widely used.

However, most of the models are derived for elastic properties. In addition, the correlation between the effective hardness of the composite, which is the easiest mechanical property obtained by simple testing, and the hardness values of its constituent phases are not

well established. Therefore, there is still argument about the validity of the ROM for composites with hard particles, especially for plastic properties.

Figure 4-3 shows a schematic diagram showing (a) the iso-stress (Reuss) model and (b) the iso-strain (Voigt) model. The ROMs, such as the equal strain treatment which is an upper bound, Eq. (8) below, and the equal stress treatment which is a lower bound, Eq. (9) below, can be used for estimating the effective hardness $\overline{H}$ of the composite:

$$\overline{H}_{up} = f_h H_h + f_s H_s , \tag{8}$$

$$\overline{H}_{low} = (f_h / H_h + f_s / H_s)^{-1} , \tag{9}$$

where, H_h and H_s are the hardness values of the hard and soft phases, and f_h and f_s are the volume fractions of the hard and soft phases, respectively. The subscripts up and low in $\overline{H}$ represent the upper and the lower bounds of hardness, respectively.

More recently, the elastio-plastic finite element analysis (FEA) for the conventional unit cell model of the uniaxial compression of the composites with homogeneously distributed second particles has been carried out by Kim [181]. Combined with experimental results, the validity of the ROM in composites with hard particles had been confirmed. The FEA results fit better with the iso-strain model except for low volume fractions (<30%) of hard particles where the FEA results fit closely the iso-stress curve. This can be explained by the fact that the deformation of the soft matrix is larger than that of the hard particle. That is, as the compression proceeds on a composite with a high volume fraction of the hard particles, the distance between the particles is getting closer, the load is transferred to the adjacent particles along the loading direction and the hard particles can be deformed. On the other hand, for a low volume fraction of the hard particles, the deformation occurred mainly in the soft matrix

with little deformation of the hard particles. Such inhomogeneous deformation with the main deformation occurring in the soft matrix is much more apparent under the indentation of the composite than under the uniaxial compression. Figure 4-4 shows a schematic drawing of the load transfer direction in the indentation test. Because the loading direction is mainly normal to the indenter surface, the stress state might be similar to the 'iso-stress' condition rather than the 'iso-strain' condition.

The extreme case of this inhomogeneous deformation is the 'wet sand effect' [182], which means that only the soft matrix surrounding the hard particles deforms. In this case, it might be considered that the effective hardness of the particle reinforced composite is mainly related to the hardness of the soft matrix. This situation can be analyzed by using the following approximation of the 'iso-stress' case,

$$\overline{H}_{low} = H_h H_s /(f_h H_s + f_s H_h) \approx H_s / f_s \quad , \tag{10}$$

where $H_h >> H_s$ and $f_h << f_s$.

Equation (10) indicates that the effective hardness of the particle reinforced composite can be approximated to that of the soft matrix only when the hardness of the hard particle is much higher than that of the soft matrix ($H_h >> H_s$) and the volume fraction of the particles is much lower than that of the matrix ($f_h << f_s$). Otherwise, this approximation, Eq. (10), is not satisfied and should be modified.

In the present ZrO_2 and SiO_2 particle reinforced Mg-AZ31 composites fabricated by FSP, it is hardly possible to prepare the same state of the matrix in the real samples, regardless of the volume fraction of the same-sized particles. However, the hardness of the matrix without any particle can be roughly deduced from previous hardness results (d, in μm):

$$H_v = 40 + 72 d_g^{-1/2}. \quad (11)$$

The comparison of the hardness of the AZ31 matrix deduced from Eq. (10) is given in Table 4-1. The hardness H_v of the ZrO_2 and SiO_2 particles is ~900 and ~1000, respectively, much higher than that of the AZ31 matrix after FSP (H_v~76-90, depending on the refined grain size). The maximal volume fraction of the particles is ~20%. Therefore, it is considered that the approximation of Eq. (10) is satisfied for the present case. The prediction results, as shown in Table 4-1, approximately match the experimental ones, especially in the case of lower volume fractions. Our present results confirm that the effective hardness of the particle reinforced composite can be approximated to that of the soft matrix when the hardness of the hard particle is much higher than that of the soft matrix and the volume fraction of the particles is much lower than that of the matrix.

As can be seen in Table 3-5, the average grain size of the FSP composites is smaller than that of the un-reinforced FSP Mg-AZ31 alloy. The finer grain structure in the composites could result from the SiO_2 or ZrO_2 particle addition. It is well recognized that the second phase particles will influence the stress and strain distribution during plastic deformation, and thus particles will strongly affect the dynamic recrystallization (DRX) process. Generally, particles could be classified into two size groups according to their effects on RX. Particles larger than 0.1-1 μm will stimulate the RX process, while particles smaller than 0.1 μm will hinder DRX process [183].

As for the present composites, the behavior of the second phases might be much more complex since their size and distribution will change during FSP. During the first FSP, the particles will be dispersed inhomogeneously, some large size particle clusters will occur unavoidably. However, the particles will be dispersed more and more homogeneously with

increasing FSP passes, and the large size particle clusters will change into smaller ones gradually (to an average size of 180-300 nm, as listed in Table 3-5). Simultaneously, stress concentration around the second phases (particle clusters) will produce a large strain gradient in the adjacent magnesium matrix because of the dislocation pile-up against the second phases during the FSP deformation. Nucleation of dynamic recrystallization is stimulated in these zones. While the nuclei grows, small second phases will hinder grain boundary migration due to the Zener pinning. The second phase pinning on grain boundaries could be observed clearly in Figs. 3-29, 3-30 and 3-50. In other words, the second phases play a different role in DRX during FSP according to their changing size. At the beginning of FSP, while the second phase is large, the strain energy in the matrix around it is high. These kinds of places are preferential sites for nucleation of DRX. While the second phase changes into small particles due to the mechanical breaking with increasing FSP passes, the new nuclei has already been produced in the matrix. Then, the small particles act as obstacles for grain growth. Therefore, relatively fine magnesium grains are generated in the present composites during the multiple FSP passes. If the FSP heat input is lowered by lowering the pin rotation and raising the advancing speed, the resulting grain size can be further lowered.

In this study, it is clear that the softest AZ31 Mg alloy can be hardened by the inclusion of nano fillers through FSP, from H_v~50 up to H_v~105. If the harder AZ91 alloy is in use, H_v is expected to be raised from the original 65 to over 120, based on the prediction of H_s/f_s in Eq. (10). The hardened bulk section or surface layer would greatly improve the wear resistance that is vital for practical applications.

4.4 Mechanisms for forming ultrafine grain in AZ31 Mg alloy made by FSP

Some previous works have demonstrated that the inability in preparing UFG microstructures in pure Mg or Mg alloys with low content of alloying elements by SPD, such as ECAP [27]. This is reasonable from the physical point of view. Since the lattice and grain boundary diffusion rates of Mg at the working temperatures, for example, 300°C, are 4.7×10^{-17} m^2/s and 2×10^{-20} δ m^3/s (where δ is the grain boundary width), respectively [175]; both are much higher than the values of 1.8×10^{-17} m^2/s and 1.1×10^{-21} δ m^3/s for Al counterparts [175]. The achievement of ultrafine and uniform grain structures need to be accomplished by the combination of a high degree of SPD and the sufficiently rapid heat release. To make clear the mechanism for the formation of UFG, the relationship between *Zener-Hollomon* parameter, Z, and the average recrystallized grain size, d in μm, can be used because the recrystallization process proceeds during the course of FSP. First, the strain rate and working temperature of the nugget region experienced during FSP need to be determined.

The material flow strain rate, $\dot{\varepsilon}$, during FSP may be estimated by the torsion typed deformation as shown in Eq. (5) where R_m is the average material flow rate (assumed to be about half of the pin rotational speed, namely 1200/2 rpm), r_e and L_e are the effective (or average) radius and depth of the dynamically recrystallized zone. An effective radius, r_e, that can represent the average radius for all parts of the materials inside this zone, is assumed to equal about 0.78 (or π/4 [64]) of the observed zone boundary radius (1.7 mm in the current case). Similar argument can also be applied to L_e (~0.78x3 mm). Thus, $\dot{\varepsilon}$ can be calculated to be ~36 s^{-1}. From the previous results, the relationship between Z and d in μm for the AZ31 alloy during FSP can be estimated as: $ln\ d = 9.0 - 0.27\ ln\ Z$, where $Z = \dot{\varepsilon}\exp(Q/RT)$ and Q is the activation energy for lattice diffusion (135 kJ/mol [175]) and RT has its usual meaning. In this case, with the average grain size ~0.3 μm and the strain rate ~36 s^{-1}, the working temperature can be calculated to be ~200°C. Note that the heating history during FSP in Mg alloys without rapid cooling design is typically a heating stage from RT to ~400°C

over 30 s, followed by a cooling stage to RT over 100 s, as monitored by the inserted thermal couples. In the present FSP case under effective rapid cooling, the heat generated during FSP can be conducted away quickly, as reflected by the calculated low working temperature of 200°C.

Watanabe et al. [184] reported that the grain size after dynamic recrystallization, d_{rec}, was dependent on the initial grain size, d_{init}. They proposed that initial grain size and the *Z*-parameter of Mg alloys could be related by the following empirical equation (d, in μm):

$$(d_{rec} / d_{init}) = 10^3 \times Z^{-1/3} = 10^3 \times \{\dot{\varepsilon} \times \exp(Q / RT)\}^{-1/3} \quad . \qquad (12)$$

Using the initial grain size of 75 μm and the estimated working temperature of 200°C, the achievable grain size after dynamic recrystallization based on Eq. (12) will be about 250 nm, consistent with the current experimental result. Here, precipitates that are often helpful to stabilize the microstructure (the Zener pining) are not available because the $Mg_{17}Al_{12}$ precipitates in the AZ31 alloy dissolve into the matrix above 200°C [185]. Therefore, the low working temperature in the current case is critical in achieving the UFG microstructure for the AZ31 alloy. It is known that one-pass FSP can only produce ultrafine grained structures along the weld line. In order to achieve a wider area with such microstructures, it is necessary to proceed overlapped multiple FSP using robot control. Experimental trials in the laboratory using multiple FSP passes under liquid N_2 cooling ensure the same fine grain structures. It is meaningful to scale up the current processing route for possible engineering applications.

4.5 Capability for further grain refining with subsequent second pass with lower heat inputs

The material flow strain rate during FSP may be estimated by Eq. (5) where R_m is assumed to be about half of the pin rotational speed, namely 1000/2 rpm, and r_e and L_e are the effective (or average) radius and depth of the dynamically recrystallized zone. An effective radius, r_e, that can represent the average radius for all parts of the materials inside this zone, is assumed to equal about 0.78 (or $\pi/4$ [64]) of the observed zone boundary radius (1.17 mm in the current case). Similar argument can also be applied to L_e (~0.78x2 mm). Thus, $\dot{\varepsilon}$ can be calculated to be ~31 s^{-1}. From the relationship between Z and d in μm for the AZ31 alloy during FSP: $ln\ d = 9.0 - 0.27\ ln\ Z$, where $Z = \dot{\varepsilon}\exp(Q/RT)$. In this case, with an average grain size of ~0.1 μm and a strain rate of ~31 s^{-1}, the working temperature can also be calculated to be ~150°C. In the present FSP case under effective rapid cooling and combination of second pass with lower heat input, the heat generated during FSP can be less and conducted away quickly, as reflected by the calculated even lower working temperature of 150°C.

Because of either grain coarsening or grain refinement is occurring during deformation. It appears that the change in grain size is dependent on the initial grain size and deformation temperature. Hence, Takara et al. [186] recently proposed that the critical grain size, d_{crit} in μm, above which grain refinement would occur during deformation, could be given by the following empirical equation for AZ31 alloy:

$$d_{crit} = 650Z^{-0.2} = 650\{\dot{\varepsilon}\times\exp(\frac{Q}{RT})\}^{-0.2}, \quad (13)$$

where Z is the Z parameter (= $\dot{\varepsilon}\times\exp(Q/RT)$), $\dot{\varepsilon}$ is the strain rate, Q is the activation energy for lattice diffusion (135 kJ/mol [175]) and RT has its usual meaning. By utilizing Eq. (13), it is possible to consider the optimal initial grain size for the required process condition

such formed shape, processing speed, and temperature. Using the strain rate 31 s^{-1} and the estimated working temperature of 150^{o}C, the critical grain size for further grain refining based on Eq. (13) will be about 150 nm, which is smaller than initial grain size (~0.3 μm) in this case. Hence, in the present initial grain size, strain rate, and working temperature, the grain refining process is capable of carrying on. However, lower heat input, rapid cooling system and low working temperature play the key roles for obtaining nano-grains in the AZ31 alloy.

4.6 The mechanism of the nanocrystalline structure evolution for AZ31 Mg base alloy during two-pass FSP

In the past decade, severe plastic deformation (SPD) approaches, such as equal channel angular extrusion (ECAE) [51,52], accumulative roll bonding (ARB) [47] and high-pressure torsion (HPT), have been applied to the grain refinement of Mg alloys on bulk materials. Twinning and dynamic recrystallization (DRX) were found to be responsible for grain refinement for most processes. But in most of these cases, the grain size of the final refinement structure is in the micrometer or submicro-meter range. It is not clear what dominates the grain refinement mechanism if grain size can be further divided into the nanometer scale by SPD. So it is of interest from both the scientific and the practical points of view to investigate the strain induced grain refinement mechanism in the Mg system by using FSP, which, in Al alloy systems, has been proven to be able to produce a nanocrystalline structure in the nugget regions [94].

Under the cooling system with liquid nitrogen, the generated heat from the input of works can be conducted rapidly away by effective heat sink, therefore the effect of heat on

the growth of the resulted microstructure can be decreased significantly as compared to air cooling. In this study, the newly designed cooling system has demonstrated efficient cooling and thus favors to the refinement of resulting microstructure during FSP. Furthermore, it is interested to observe that FSP pass is an important parameter to determine the scale of the resultant microstructure for the tested alloy. Figure 4-5 shows the TEM images of the microstructure for the one-pass FSPed AZ31 alloy, which shows that the microstructure can be only refined to submicron scale, with the mean grain size of 100~300 nm. Besides the submicro-scale fine grains, some clear subgrains and dislocation walls can also be observed in the resultant microstructure.

However, followed by subsequent second pass with a lower heat input, the two-pass FSPed AZ31 alloy can produce a nano-scale microstructure (fine grains with an average size of less than 100 nm). Figure 4-6 shows the typical microstructure observed in the two-pass FSPed AZ31 alloy in the as processed condition, together with a select area diffraction (SAD) pattern. The pattern exhibits rings, indicating that there were many small grains with random misorientations in the selected regions. Figure 3-61 shows the grain size distribution of the FSPed specimens, which is summarized from numerous SEM micrographs. The resulting microstructure exhibits equiaxed grains ranging from 40 nm to 200 nm with an average grain size of less than 100 nm, clearly illustrating that a nanocrystalline structure is produced in the two-pass FSPed AZ31 alloy.

The foregoing observations demonstrate that for AZ31 alloy, during friction stir processing, the severe plastic deformation in the processed region under the high strain rate results in a progressive refinement of coarse grains into a nanometer regime. First, we characterize the microstructure of the two-pass FSPed samples. Figs. 4-7(a), (b), and (c) show that clear nanometer grains have formed within a highly deformed subgrain along the

boundary or the triple-connected point of the recrystals. This clean nanometer grain implies the elimination of strain even through there is still high strain in the surrounding area. The only possible way to generate such clean nanometer grains within a highly deformed area is DRX. Fig. 4-7(d) is another TEM micrograph taken from this region. The "clean" and strain-free equiaxed grains can only be the result of recrystallization.

Dynamic recrystallization is generally acknowledged to happen within temperature ranges from 0.5–0.6 to 0.9–0.98 T_m [187,188]. For pure Mg, 0.5 T_m corresponds to 193^{o}C; the DRX temperature for AZ31D, therefore, could be even lower than this temperature. Moreover, Kaibyshev et al. [189] even claimed that DRX occurred at room temperature, which corresponds to 0.3 T_m in pure Mg when the strain is quite high. During the FSP process, the rapid rotation of work pin generates severe plastic deformation and strain at the nugget region. The high strain in the sample will decrease the DRX temperature. As mentioned above, the Mg alloy has a low melting point and therefore a low recrystallization temperature. The heavy plastic deformation at high strain rates during the FSP also leads to the generation of heat. The combination of heat and heavy plastic deformation leads to the occurrence of DRX for recrystallized grains.

Generally, there are two types of dynamic recrystallization (DRX) discussed in the literature: (i) continuous DRX and (ii) discontinuous DRX. During continuous DRX, new grains develop via a gradual increase in misorientation between subgrains. In contrast, during discontinuous DRX, new grains exhibiting large-angle boundaries evolve; for example, dynamic nucleation followed by grain growth from migration of high-angle boundaries. It is worth mentioning that the development of nanostructures with high-angle grain boundaries via continuous DRX during severe plastic deformation (SPD) process, which result in qualitative changes in properties, is a rather difficult task. For example, equal channel angular

pressing (ECAP), which currently offers maximum potential for scaling, can reduce the grain size to 0.5–1.0 μm in aluminum alloys, but requires a strain of >4.0 [190,191].Generally it takes >8 ECAP passes to achieve very-fine grains exhibiting high grain-boundary misorientations [192]. In the past decade, severe plastic deformation (SPD) approaches have also been applied to the grain refinement of Mg alloys on bulk materials. But in most of these cases, the grain size of the final refinement structure is in the micrometer or submicro-meter range.

But, how the nanocrystalline structure is achieved for the two-pass FSPed AZ31 alloy? Based on the published papers, the assumption of the occurrence of discontinuous DRX is reasonable for the current study. The difference between FSP and the previously reported severe plastic processes, may lie in the strain rate. Wang et al. [193] have reported that strain rate plays an important role in refining grains into the nanometer region during the SPD processes. The strain rates of ECAP and HPT are too low to induce enough twinning activity and to form nanometer grains. However, in FSP, the strain rate is estimated to be about 10^0 - 10^2 s^{-1}. It is believed that a complex stress state and strain components with very-large strain gradients will be induced by the high strain rate. Furthermore, large amounts of dislocations are also introduced to accommodate the strain incompatibility. The complex stress state, complicated strain patterns and dislocation configurations, and high density of geometrically necessary dislocations provide the necessary conditions for the occurrence of discontinuous DRX process, which is beneficial in allowing copious nucleation.

However, a notable feature of this study is that dislocation walls and subgrains can be observed in the one-pass FSPed samples, as shown in Fig. 4-5. This suggests that the continuous DRX plays a dominant role in the evolution of microstructure. As what we have known, nuclei form preferentially in regions where the local degree of deformation is highest,

such as grain boundaries, deformation bands, inclusions, twin intersections and free surfaces. Due to the paucity of the "site" for nucleation originating from the coarse microstructure of first-pass FSPed samples, more dislocation walls even subboundaries form to accommodate the high strain incompatibility. Therefore, continuous DRX may be dominant process for the first-pass FSPed samples. Due to the rapid cooling, these microstructual features can be remained in the first-pass FSPed samples. Then during second-pass FSP, the remained high-density dislocation walls and submicro-scale subgrains as well as recrystallzed grains all can become the "site" for the nucleation of recrystals. Then under the high strain rate of FSP, the discontinuous DRX may be dominant, which results in the formation of copious nuclei. It should be mentioned that discontinuous DRX process can significantly refine the grains, but the newly formed grains will be subject to growth process which is controlled by volume diffusion under the condition of severe plastic deformation. Then the working temperatures are crucial for the refinement of the resulted microstructure of the FSPed AZ31 alloy. However, in this current study, under the cooling system with liquid nitrogen, the generated heat from the input of works can be conducted rapidly away by effective heat sink, therefore, the working temperature is decreased significantly. Thus, nanocrystalline microstructure can be remained.

On the basis of microstructure observation, the evolution of the nanostructure can be described as follows: (i) In the first-pass stage of FSP, submicro-sale grains are introduced in the processed sheet via continuous dynamic recrystallization (ii) In the second-pass stage of FSP, copious nuclei form via discontinuous dynamic recrystallization (DDRX) due to the existence of submicro-sale grains, subgrains and a high density of dislocation walls (iii) The growth of the recrystallized grians is limited due to the effective heat sink from the liquid nitrogen cooling system. This fundamental understanding of the nanocrystalline evolution makes it possible to control the final microstructure, including grain size, grain-boundary

structure, and dislocation density, by changing the processing parameters and cooling rate.

Based on the above discussions, the process and mechanism of nanocrystallization of AZ31 alloy during the FSP with subsequent second pass can be proposed. Fig. 4-8 is a schematic diagram showing the process. A two type recrystallization mechanism is proposed. During the first pass, the continuous recrystallization is preferable, in which a lot of dislocation walls and subgrains as well as recrystals is remained. During the second-pass FSP, discontinuous DRX process is chosen due to the combining effects from low heat input, high total strain, high strain rate and copious sites for nucleation.

Chapter 5

Conclusions

There have been numerous efforts in processing metallic alloys into fine-grained materials. The current study applied the simple and feasible one single pass or subsequent second pass FSP on the commercial AZ31 magnesium billet to result in ultrafine grained microstructures. Numerous approaches were tried using FSP in order to achieve ultrafine nano-scale grain sizes with higher hardness in the AZ31 magnesium alloys. After systematical and numerous experiments are conducted and analyzed, the results can be concluded as follows:

(1) The resulting microstructure after FSP is mainly affected by processing parameters. Besides, the cooling condition is also a very important factor. After systemical examinations, the relationship between the resulting grain size and the applied working strain rate and temperature for the friction stir processing in the AZ31 Mg alloy is concluded. To rationalize the relationship, the Zener-Holloman parameter is utilized, and it was found that the relationship of $ln\ d = 9.0 - 0.27\ ln\ Z$ is followed. The temperature rise during FSP is traced, and the maximum temperature can reach 250-450^{o}C, depending on the FSP pin rotation speed. The temperature duration also depends on advancing speed. X-ray diffraction results show that, in the FSP dynamically recrystallized zone, the (0002) basal plane tends to lie on the transverse plane at lower pin rotation speeds, and approaches to nearly random orientation at higher rotation speeds.

(2) As for in-situ formed intermetallic compounds reinforced Mg-Al-Zn alloys, friction stir process was used to fabricate bulk multi-element Mg base alloys with different fractions of AZ31 sheets, Al and Zn foils. Multi-passes and high fractions of Al and Zn elements results in apparent grain refinement, proved by the broadening of diffraction peaks and from SEM results. After multi-passes, some intermetallic compound phases were generated. Some intermetallic compounds are quasi-crystals with icosahedral point group symmetry. The average hardness of the multi-element Mg base alloy made by FSP reached nearly 350 in H_v scale, especially in the $Mg_{50}Al_5Zn_{45}$ or $Mg_{37.5}Al_{25}Zn_{37.5}$ system, due to the generation of intermetallic compounds and grain refinement. With increasing FSP operation to 10 passes, the microstructure and hardness in the stirred zone become much more refined and uniform.

(3) As for Mg based composites reinforced by extrinsic reinforcements, friction stir processing successfully fabricated bulk Mg-AZ31 based composites with 10~20 vol% of nano-ZrO_2 particles and 5~10 vol% of nano-SiO_2 particles. The distribution of nano-particles after four FSP passes resulted in satisfactorily uniform distribution. The average grain size of the AZ31 matrix of the 4P FSP composites could be effectively refined to 2~4 μm, as compared with the ~6 μm in the FSP AZ31 alloy (without particles) processed under the same FSP condition. The crystalline ZrO_2 phase is very stable, no reaction between the ZrO_2 and Mg phases occurred during the FSP mixing.

(4) The hardness properties at room temperature of the AZ31 composites with nano-fillers were improved (up to H_v~105), as compared with the AZ31 cast billet (H_v~50). The hardened bulk section or surface layer would greatly improve the wear resistance that is vital for practical applications. The effective hardness of the present particle reinforced composites can be approximately predicted by the iso-stress model when the hardness of

the hard particle is much higher than that of the soft matrix and the volume fraction of the particles is much lower than that of the matrix.

(5) The ultrafine grain size in solid solution hardened AZ31 Mg alloy is successfully achieved by one-pass FSP coupled with rapid heat sink. With proper control of the working temperature history, an ultrafine and uniform grained structure processed by FSP can be achieved. The grain boundaries are well defined and the mean grain size can be refined to 100~300 nm from the initial 75 μm by one single FSP pass. The ultrafine grained structure can drastically increases the microhardness from the initial 50 up to 120 H_v, or an increment factor of 2.4 times. The low working temperature is critical in achieving UFG AZ31 alloy. The estimated high strain rate and low working temperature during FSP with rapid heat sink also agree self-consistently with the achieved ultrafine grains.

(6) The finest grain size ever found in solid solution hardened AZ31 Mg alloy can be achieved by two passes FSP coupled with rapid heat sink. However, the subsequent second pass has lower heat input than first pass. The resulting microstructure exhibits equiaxed grains ranging from 40 nm to 200 nm with an average grain size of less than 100 nm, clearly illustrating that a nanocrystalline structure can be achieved by described two-pass FSP. The nanocrystalline grains can be shown in the TEM observations and the diffraction rings also can be seen in SAD patterns. The highest hardness point can reach ~150 H_v which is equal to triple of the AZ31 matrix, and the mean hardness increase up to around 134 H_v from initial 50 H_v. The process and mechanism of nanocrystallization of AZ31 alloy during the FSP with subsequent second pass is proposed as a two-type recrystallization mechanism.

References

1. C.C Koch, D.G. Morris, K. Lu, A. Inoue, Mater. Res. Soc. Bull., 24 (1999), p. 54.

2. S.X. McFadden, R.S. Mishar, R.Z. Valiev, A.P. Zhilyaev, A.K. Mukherjee, Nature, 398 (1999), p. 684.

3. P.G. Patridge, Met. Rev., 118 (1967), p. 169.

4. W.M. Thomas, E.D. Nicholas, J.C. Needham, M.G. Church, P. Templesmith and C.J. Dawes: The Welding Institute, TWI, International Patent Application No. PCT/GB92/02203 and GB Patent Application No. 9125978.8, 1991.

5. R.S. Mishra, M.W. Mahoney, S.X. McFadden, N.A. Mara, A.K. Mukherjee, Scripta Mater., 42 (2000), p. 163.

6. R.S. Mishra, Z.Y. Ma, I. Charit, Mater. Sci. Eng., A341 (2002), p. 307.

7. P.B. Berbon, W.H. Bingel, R.S. Mishra, C.C. Bampton, M.W. Mahoney, Scripta Mater., 44 (2001), p. 61.

8. J.E. Spowart, Z.Y. Ma, R.S. Mishra, in: K.V. Jata, M.W. Mahoney, R.S. Mishra, S.L. Semiatin, T. Lienert (Eds.), Friction Stir Welding and Processing II, TMS, 2003, pp. 243–252.

9. Z.Y. Ma, S.R. Sharma, R.S. Mishra, M.W. Manohey, Mater. Sci. Forum 426–432 (2003), p. 2891.

10. 葉峻轍，工業材料，186 期 (2002)，p. 82.

11. 范元昌、蘇健忠、翁震灼、陳俊沐，工業材料，186 期 (2002)，p. 131.

12. G.V. Raynor, in The Physical Metallurgy of Magnesium and Its Alloys (Pergamon Press, London, 1957).

13. T. Lyman, H.E. Boyer, P.M. Unterwesier, J.E. Foster, J.P. Hontans, H. Lawton, in Metals Handbook (ASM International, Metals Park, Ohio, 1975).

14. R.W. Cahn, P. Hassen, E.J. Kramer, in Materials Science and Technology Structure and Properties of Nonferrous Alloys, VCH, New York, 1996.

15. B.L. Mordike, Mater. Sci. Eng., A324 (2002), p. 103.

16. Q.D. Wang, W.D. Chen, X.Q. Zeng, Y.Z. Lu, W.J. Ding, Y.P. Zhu, X.P. Xu, M. Mabuchi, J. Mater. Sci., 36 (2001), p. 3055.

17. P. Li, B. Tang, E.G. Kandalova, Mater. Lett., 59(2005), p. 671.

18. F. Von Buch, J. Lietzau, B.L. Mordike, A. Pisch, R. Schmid-Fetzer, Mater. Sci. Eng., A263 (1999), p. 1.

19. J. Grobner, R. Schmid-Fetzer, J. Alloys and Compounds, 320 (2001), p. 296.

20. K.U. Kainer, von Buch F. In: Kainer KU, editor. Magnesium alloys and technologies. DGM. (2003) 1.

21. R.E. Reed-Hill, R. Abbaschian, in Physical Metallurgy Principles (PWS Publishing Company, 20 Park Plaza, Boston, 1994).

22. T. Narutani, J. Takamura, Acta Mater., 39 (1991), p. 2037.

23. 吳信輝，“電子束或電弧銲接鎂合金之微織構與機性分析”國立中山大學碩士論文 (2003).

24. H.K. Lin, J.C. Huang, Mater. Trans. JIM, 43 (2002), p. 2424.

25. G. Nussbaum, P. Sainfort, G. Regazzoni, Scripta Mater., 29 (1989), p. 1079.

26. A. Bussiba, A. Ben Artzy, A Shtechman, S. Ifergan, M. Kupiec, Mater. Sci. Eng., A 302 (2001), p. 56.

27. Y.T. Zhu, T.C. Lowe, T.G. Langdon, Scripta Mater., 51 (2004), p. 825.

28. R.Z. Valiev, N.A. Krasilnikov, N.K. Tsenev, Mater. Sci. Eng., A 137 (1991), p. 35.

29. V.M. Segal, V.I. Reznikov, A.E. Drobyshevskiy, V.I. Kopylov, Russian Metall., 1 (1981), p. 99.

30. V.M. Segal, Mater. Sci. Eng., A197 (1995), p. 157.

31. A.P. Zhilyaev, G.V. Nurislamova, B.K. Kim, M.D. Baro, J.A. Szpunar, T.G. Langdon,

Acta Mater., 51 (2003), p. 753.

32. G.A. Salishchev, O.R. Valiahmetov, R.M. Galeev, J. Mater. Sci., 28 (1993), p. 2898.

33. O. Sitdikov, T. Sakai, A. Goloborodko, H. Miura, R. Kaibyshev, Mater. Trans. 45 (2004), p. 2232.

34. V.N. Varyutkhin, Y.Y. Beygelzimer, S. Synkov, D. Orlov, Mater. Sci. Forum, 503-504 (2006), p. 335.

35. J. Richert, M. Richert, Aluminum 62 (1986), p. 604.

36. M. Richert, Q. Liu, N. Hansen, Mater. Sci. Eng., A 260 (1999), p. 275.

37. H.S. Chu, K.S. Liu, J.W. Yeh, Metall. Mater. Trans., A 31 (2000), p. 2587.

38. H.S. Chu, K.S. Liu, J.W. Yeh, Scripta Mater., 45 (2001), p. 541.

39. D.H. Shin, J.J. Park, Y.S. Kim, K.T. Park, Mater. Sci. Eng., A 328 (2002), p. 98.

40. X. Zhao, T.F. Jing, Y.W. Gao, J.F. Zhou, W. Wang, Mater. Lett., 58 (2004), p. 2335.

41. Y. Saito, N. Tsuji, H. Utsunomiya, T. Sakai, R.G. Hong, Scripta Mater., 39 (1998), p. 1221.

42. Y. Saito, H. Utsunomiya, N. Tsuji, T. Sakai, Acta Mater., 47 (1999), p. 579.

43. G.E. Dieter, in Mechanical Metallurgy (McGraw-Hill Book Company, Singapore, 1988)

44. 林鉉凱，“析出型 AZ91 鎂合金低溫超塑性之研究”，國立中山大學碩士論文 (2001).

45. T.C. Chang, J.Y. Wang, C.M. O, S. Lee, J. Mater. Prod. Technol., 140 (2003), p. 588.

46. W.J. Kim, S.W. Chung, C.S. Chung, D. Kum, Acta Mater., 49 (2001), p. 3337.

47. M.T. Perez-Prado, J. A. del Valle and O. A. Ruano, Scripta Materialia, 51 (2004), p. 1093.

48. Y. Iwahashi, Z. Horita, M. Nemoto, T.G. Langdon, Acta Mater., 45 (1997), p. 4733.

49. 痩忠義，“超細晶鋁之機械性質”，國立中山大學博士論文 (2003).

50. M. Mabuchi, H. Iwasaki, K. Yanase, K. Higashi, Scripta Mater., 36 (1999), p. 681.

51. K. Matsubara, Y. Miyahara, Z. Horita, T.G. Langdon, Acta Mater., 51 (2003), p. 3073.

52. H.K. Lin, J.C. Huang, T.G. Langdon, Mater. Sci. Eng., A 402 (2005), p. 250.

53. H. Gleiter, Prog. Mater. Sci., 33 (1989), p. 223.

54. U. Erb, A.M. El-Sherik, G. Palumbo, K.T. Aust, Nanostruct. Mater., 2 (1993)

55. S. Spangel, E.M. Schulz, A. Schulz, H. Vetters, P. Mayr, Mater. Sci. Eng., A 326 (2002), p. 26.

56. C.Y. Chen, C.Y.A. Tsao, Mater. Sci. Eng., A 383 (2004), p.21.

57. C.C. Koch, Y.S. Cho, Nanostruct. Mater., 1 (1992), p. 207.

58. D.B. Witkin, E.J. Lavernia, Prog. Mater. Sci., 51 (2006), p. 1.

59. U. Andrade, M.A. Meyers, K.S. Vecchio, A.H. Chokshi, Acta Mater., 42 (1994), p. 3183.

60. G. Garces, P. Perez, P. Adeva, J. Alloys Compounds, 333 (2002), p.219.

61. K.K. Chawla, in Composite Materials (Springer-Verlag, New York, 1987).

62. M. Taya, R.J. Arsenault, in Metal Matrix Composites (Pergamon Press, First edition, 1989).

63. D. Hull, T.W. Clyne, in An Introduction to Composite Materials (Cambridge University Press, Second edition, 1996).

64. A.J. Ardell, Metall. Mater. Trans., 16 A (1985), p. 2131.

65. T.D. Wang, J.C. Huang, Mater. Trans. JIM, 42 (2001), p. 1781.

66. R.A. Saravanan, M.K. Surappa, Mater. Sci. Eng., A 276 (2000), p. 108.

67. A. Bochenek, K.N. Braszczynska, Mater. Sci. Eng., A 290 (2000), p. 122.

68. M. Manoharan, S.C.V. Lim, M. Gupta, Mater. Sci. Eng., A 333 (2002), p. 243.

69. L. Hu, E. Wang, Mater. Sci. Eng., A 278 (2000), p. 267.

70. M.Y. Zheng, K. Wu, M. Liang, S. Kamado, Y. Kojima, Mater. Sci. Eng., A 372 (2004), p. 66.

71. M. Zheng, K. Wu, C. Yao, Mater. Sci. Eng., A 318 (2001), p. 50.

72. B.Q. Han, D.C. Dunand, Mater. Sci. Eng., A 277 (2000), p. 297.

73. Q.C. Jiang, X L. Li, H.Y. Wang, Scripta Mater., 48 (2003), p. 713.

74. H.K. Kang, Scripta Mater., 51 (2004), p. 1051.

75. J. Lan, Y. Yang, X. Li, Mater. Sci. Eng., A 386 (2004), p. 284.

76. D.M. Lee, B.K. Suh, B.G. Kim, J.S. Lee, C.H. Lee, Mater. Sci. Technol., 13 (1997), p. 590.

77. H.Y. Wang, Q.C. Jiang, Y. Wang, B.X. Ma, F. Zhao, Mater. Lett., 58 (2004), p. 3509.

78. Q.C. Jiang, H.Y. Wang, B.X. Ma, Y. Wang, F. Zhao, J. Alloys and Compounds, 386 (2005), p. 177.

79. S.F. Sassan, M. Gupta, Mater. Sci. Eng., A 392 (2005), p. 163.

80. P.L. Ratnaparkhi, J.M. Howe, Scripta Metall., 27 (1992), p. 133.

81. S.M. Lee editor, in Handbook of Composite Reinforcements (VSH publisher, 1993).

82. P.M. Ajayan, O. Stephan, C. Colliex, D. Tranth, Science, 265 (1994), p. 1212.

83. M. Narkis, A. Ram, F. Flashner, J. Appl. Polymer Sci., 22 (1978), p. 1163.

84. B. Poulaert, J. Jossi, Polymer, 24 (1983), p. 841.

85. S. Balabanov, Krezhov, J. Physics. D: Appl. Physics, 32 (1999), p. 2573.

86. M.T. Connor, S. Roy, T.A. Ezquerra, Phys. Rev. B, 57 (1998), p. 2286.

87. 王振欽，“銲接學”，登文書局，1985。

88. R.S. Mishra, Z.Y. Ma, Mater. Sci. Eng. R, 50 (2005), p. 1.

89. Z.Y. Ma, R.S. Mishra, M.W. Mahoney, Acta Mater., 50 (2002), p. 4419.

90. S.E. Ion, F.J. Humphreys, S.H. White, Acta Metall., 30 (1982), p. 1909.

91. S.H.C. Park, Y.S. Sato, H. Kokawa, Scripta Mater., 49 (2003), p. 161.

92. C.G. Rhodes, M.W. Mahoney, W.H. Bingel, M. Calabrese, Scripta Mater., 48 (2003), p. 1451.

93. Y.S. Sato, M. Urata, H. Kokawa, Metall. Mater. Trans., A 33 (2002), p. 625.

94. J.Q. Su, T.W. Nelson, C.J. Sterling, J. Mater. Res., 18 (2003), p. 1757.

95. K.V. Jata, S.L. Semiatin, Scripta Mater., 43 (2000), p. 743.

96. J.Q. Su, T.W. Nelson, R. Mishra, M. Mahoney, Acta Mater., 51 (2003), p. 713.

97. F.J. Humphreys, M. Hotherly, the Recrystallization and Related Annealing Phenomena, Pergamon Press, New York, 1995

98. R.H. Bricknell, J.W. Edington, Acta Metall., A 22 (1991), p. 2809.

99. S.J. Hales, T.R. McNelley, Acta Metall., 36 (1988), p. 1229.

100. H. Gudmundsson, D. Brooks, J.A. Wert, Acta Metall. Mater., 39 (1991), p. 19.

101. K. Tsuzaki, X. Huang, T. Maki, Acta Mater., 44 (1996), p. 4491.

102. D.P. Field, T.W. Nelson, Y. Hovanski, K.V. Jata, Metall. Mater. Trans., 32 A (2001), p. 2869.

103. H.G. Salem, Scripta Mater., 49 (2003), p. 1103.

104. K. N. Krishnan, Mater. Sci. Eng., A 327 (2002), p. 246.

105. M.W. Mahoney, C.G. Rhodes, J.C. Flintoff, R.A. Spurling, W.H. Bingel, Matall. Mater. Trans., 29 A (1998), p. 1955.

106. S.H.C. Park, Y.S. Sato, H. Kokawa, Metall. Mater. Trans., 34 A (2003), p. 987.

107. B.C. Yang, J.H. Yan, M.A. Sutton, A.P. Reynolds, Mater. Sci. Eng., A 364 (2004), p. 55.

108. M.A. Sutton, B.C. Yang, A.P. Reynolds, J.H. Yan, Mater. Sci. Eng., A 364 (2004), p. 66.

109. M.A. Sutton, A.P. Reynolds, B.C. Yang, R. Taylor, Mater. Sci. Eng., A 354 (2003), p. 6.

110. M.A. Sutton, A.P. Reynolds, B.C. Yang, R. Taylor, Eng. Fract. Mechanics, 70 (2003), p. 2215.

111. 張志溢，“摩擦旋轉攪拌製程對 AZ31 鎂合金晶粒細化之研究”，國立中山大學碩士論文 (2004)。

112. A.P. Reynolds, Sci. Technol. Weld. Joining, 5 (2000), p. 120.

113. T.U. Seidel, A.P. Reynolds, Metall. Mater. Trans., 32 A (2001), p. 2879.

114. M. Guerra, C. Schmidt, J.C. McClure, L.E. Murr, A.C. Nunes, Mater. Charact., 49 (2003), p. 95.

115. K. Colligan, Weld. J., 78 (1999), p. 229.

116. Y. Li, L.E. Murr, J.C. McClure, Mater. Sci. Eng., A 271 (1999), p. 213.

117. Y. Li, L.E. Murr, J.C. McClure, Scripta Mater., 40 (1999), p. 1041.

118. W.J. Arbegast, in: Z. Jin, A. Beaudoin, T.A. Bieler, B. Radhakrishnan (Eds.), Hot Deformation of Aluminum Alloys III, TMS, Warrendale, PA, USA, 2003, p. 313.

119. H. Liu, H. Fujii, M. Maeda, K. Nogi, J. Mater. Sci. Lett., 22 (2003), p. 1061.

120. G. Liu, L.E. Murr, C.S. Niou, J.C. McClure, F.R. Vega, Scripta Mater., 37 (1997), p. 355.

121. S. Benavides, Y. Li, L.E. Murr, D. Brown, J.C. McClure, Scripta Mater., 41 (1999), p. 809.

122. Y.S. Sato, H. Kokawa, M. Enmoto, S. Jogan, Metall. Mater. Trans., 30 A (1999), p. 2429.

123. Y.S. Sato, H. Kokawa, M. Enmoto, S. Jogan, T. Hashimoto, Metall. Mater. Trans., 30 A (1999), p. 3125.

124. Y.S. Sato, H. Kokawa, M. Enmoto, S. Jogan, T. Hashimoto, Metall. Mater. Trans., 32 A (2001), p. 941.

125. Y. Li, E.A. Trillo, L.E. Murr, J. Mater. Sci. Lett., 19 (2000), p. 1047.

126. Y.S. Sato, S.H.C. Park, H. Kokawa, Metall. Mater. Trans., 32 A (2001), p. 3023.

127. A.A. Hassan, P.B. Prangnell, A.F. Norman, D.A. Price, S.W. Willams, Sci. Technol. Weld. Joining, 8 (2003), p. 257.

128. W.M. Thomas, E.D. Nicholas, S.D. Smith, in S.K. Das, J.G. Kaufman, T.J. Lienert (Eds.), Aluminum 2001-Proceedings of the TMS 2001 Aluminum Automotive and Joining Sessions, TMS, 2001, p. 213.

129. Y.J. Kwon, I. Shigematsu, N. Saito, Scripta Mater., 49 (2003), p. 785.

130. R.S. Mishra, Adv. Mater. Process, 161 (2003), p. 43.

131. C.G. Rhodes, M.W. Mahoney, W.H. Bingel, R.A. Spurling, C.C. Bampton, Scripta Mater., 36 (1997), p. 69.

132. B. Heinz, B. Skrotzki, Metall. Mater. Trans., 33 B (6) (2002), p. 489.

133. L.E. Murr, G. Liu, J.C. McClure, J. Mater. Mater. Lett., 16 (1997), p. 1081.

134. G.S. Frankel, Z. Xia, Corrosion, 55 (1999), p. 139.

135. S.H. Kazi, L.E. Murr, in: K.V. Jata, M.W. Mahoney, R.S. Mishra, S.L. Semiatin, D.P. Field (Eds.), Friction Stir Welding and Processing, TMS, Warrendale, PA, USA, 2001, p. 139.

136. H.G. Salem, A.P. Reynolds, J.S. Lyons, Scripta Mater., 46 (2002), p. 337.

137. R. Braun, Litynska-Dobrzynska, Mater. Sci. Forum, 396-402 (2002), p. 1531.

138. A. F. Norman, I. Brough, P.B. Prangnell, Mater. Sci. Forum, 331-337 (2000), p. 1713.

139. K.A.A. Hassan, A.F. Norman, P.B. Prangnell, Mater. Sci. Forum, 396-402 (2002), p. 1549.

140. Z.Y. Ma, R.S. Mishra, M.W. Mahoney, R. Grimes, Mater. Sci. Eng., A351 (2003), p. 148.

141. I. Charit, R.S. Mishra, Mater. Sci. Eng., A 359 (2003), p. 290.

142. I. Charit, R.S. Mishra, M.W. Mahoney, Scripta Mater., 47 (2002), p. 631.

143. I. Charit, Z.Y. Ma, R.S. Mishra, in: Z. Lin, A. Beaudoin, T.A. Bieler, B. Radhakrishnan (Eds.), Hot Deformation of Aluminum Alloys III, TMS, 2003, pp. 331-342.

144. P.S. Pao, E. Lee, C.R. Feng, H.N. Jones, D.W. Moon, in: K.V. Jata, M.W. Mahoney, R.S. Mishra, S.L. Semiatin, T. Lienert (Eds.), Friction Stir Welding and Processing II, TMS, Warrendale, PA, USA, 2003, p. 113.

145. I. Charit, R.S. Mishra, in: Y.T. Zhu, T.G. Langdon, R.Z. Valiev, S.L. Semiatin, D.H. Shih, T.C. Lowe (Eds.), Ultrafine Grained Materials III, TMS, 2004.

146. Y.S. Sato, Y. Kurihara, S.H.C. Park, H. Kokawa, N. Tsuji, Scripta Mater., 50 (2004), p. 57.

147. D.C. Hofmann, K.S. Vecchio, Mater. Sci. Eng., A 402 (2005), p. 234.

148. J.Q. Su, T.W. Nelson, C.J. Sterling, Scripta Mater., 52 (2005), p. 135.

149. F.Y. Hung, C.C. Shih, L.H. Chen, T.S. Lui, J. Alloys Compd., 428 (2007) 106.

150. N. Afrin, D.L. Chen, X. Cao, M. Jahazi, Mater. Sci. Eng., A (2007), doi:10.1016/j.msea.2007.03.018.

151. J.A. Esparza, W.C. Davis, E.A. Trillo, L.E. Murr, J. Mater. Sci. Lett., 21 (2002), p. 917.

152. D. Zhang, M. Suzuki, K. Maruyama, Scripta Mater., 52 (2005), p. 899.

153. P. Cavaliere, P.P. De Marco, Mater. Sci. Eng., A 462 (2007), p. 393.

154. S.G. Lim, S.S. Kim, C.G. Lee, C.D. Yim, S.J. Kim, Metall. Mater. Trans., 36 A (2005), p. 1609.

155. Y.S. Sato, A. Sasaki, A. Sugimoto, A. Honda, H. Kokawa, Mater. Sci. Forum, 539-543 (2007), p. 3775.

156. Z.Y. Ma, R.S. Mishra, Acta Mater., 51 (2003), p. 3551.

157. J. Xianggang, C. Jiangzhong, M. Longxiang, Acta Matell. Mater., 41 (1993), p. 2721.

158. M. Furukawa, Y. Iwahashi, Z. Horita, M. Nemoto, T.G. Langdon, Mater. Sci. Eng., A 257 (1998), P. 328.

159. P. Heurtier, C. Desrayaud, F. Montheillet, Mater. Sci. Forum 396–402 (2002), P. 1537.

160. C.J. Lee, J.C. Huang, P.J. Hsieh, Scripta Mater., 54 (2006), p. 1415.

161. A. Dutta, I. Charit, L.B. Johannes, R.S. Mishra, Mater. Sci. Eng., A 395 (2005), p. 173.

162. 胡哲明，“摩擦攪拌製程之應變率對奈米氧化鋁粉均勻分佈與機械性質的影響”，國立中山大學碩士論文 (2004).

163. P. Cavaliere, Composite Part A: applied sci. manufact., 36 (2005), p. 1657.

164. Y. Morisada, H. Fujii, T. Nagaoka, M. Fukusumi, Mater. Sci. Eng., A 419 (2006), p. 334.

165. Y. Morisada, H. Fujii, T. Nagaoka, M. Fukusumi, Mater. Sci. Eng., A 433 (2006), p. 50.

166. Y. Morisada, H. Fujii, T. Nagaoka, M. Fukusumi, Scripta Mater., 55 (2006), p. 1067.

167. C.J. Lee, J.C. Huang, P.J. Hsieh, Scripta Mater., 54 (2006), p. 1415.

168. S.M. Howard, B.K. Jasthi, W.J. Arbegast, G.J. Grant and D.R. Herling, in: K.V. Jata, M.W. Mahoney, R.S. Mishra and T. Lienert (Eds.), Friction Stir Welding and Processing

III, TMS, 2005, pp. 139-146.

169. C.J. Hsu, P.W. Kao, N.J. Ho, Scripta Mater., 53 (2005), p. 341.

170. Y.N. Wang, C.J. Lee, H.K. Lin, C.C. Huang, J.C. Huang, Mater. Sci. Forum, 426-432 (2003), p. 2655.

171. C.C. Huang, J.C. Huang, I.K. Lin, Y.M. Hwang, Key Eng. Mater., 271-274 (2004), p. 289.

172. C.I. Chang, C.J. Lee, C.H. Chuang, H.R. Pei, J.C. Huang, Adv. Mater. Res., 15-17 (2007), p. 387.

173. L. Plazanet, D. Tetard, F. Nardou, Comp. Sci. Techn., 59 (1999), p. 537.

174. C.J. Lee, J.C. Huang, X.H. Du, Scripta Mater., 56 (2007), p. 875.

175. H.J. Forst, M.F. Ashby, in: Deformation-Mechanism Maps. Oxford: Pergamon Press; 1982. p. 21 and p. 44.

176. P. Leble, M. Dong, E. Soppa, S. Schmauder, Scripta Mater., 38 (1998), p. 1327.

177. O.B. Pederson, Acta Metall., 31 (1983), p. 1795.

178. V.C. Nardone, K.M. Prewo, Scripta Metall., 20 (1986), p. 43.

179. M. Dong, S. Schmauder, Acta Mater., 44 (1996), p. 2465.

180. R. Hill, Phys. Soc. Lond., A 65 (1952), p. 349.

181. H.S. Kim, Mater. Sci. Eng., A 289 (2000), p. 30.

182. Z.C. Zhong, X.Y. Jiang, A.L. Greer, Philos. Mag., 76 (1997), p. 505.

183. N. Hansen, D.J. Jensen, in: T. Chandra (Eds.), Recrystallization'90, TMS, Australia, 1990, pp. 79-88.

184. H. Watanabe, H. Tsutsui, T. Mukai, H. Ishikawa, Y. Okanda, M. Kohzu, K. Higashi, Mater. Trans., 42 (2001), p. 1200.

185. T.B. Massalski, H. Okamoto, P.R. Subramanian, L. Kacprzak (Eds.), Binary alloy phase diagrams, ASM International, Materials Park, OH, 1990, p. 2444.

186. A. Takara, Y. Nishikawa, H. Watanabe, H. Somekawa, T. Mukai, K. Higashi, Mater.

Trans., 45 (2004), p. 2377.

187. C.M. Sellars, Phil. Trans. R. Soc. Lond., A 288 (1978), p. 147.

188. H.J. McQueen, J.J. Jonas, Appl. Met., 3 (1984), p. 233.

189. R. Kaibyshev, O. Sitdikov, Z. Metallkd., 85 (1994), p. 738.

190. R.Z. Valiev, R.K. Islamgaliev, I.V. Alexandrov, Prog. Mater. Sci., 45 (2000), p. 103.

191. M. Furukawa, Z. Horita, M. Nemoto, T.G. Langdon, in: R.S. Mishra, S.L. Semiatin, C. Suryanarayana, N.N. Thadhani, T.C. Lowe (Eds.), Ultrafine Grained Materials, TMS, Warrendale, PA, 2000, p. 125.

192. S.D. Terhune, Z. Horita, M. Nemoto, Y. Li, T.G. Langdon, T.R. McNelley, in: T. Sakai, H.G. Suzuki (Eds.), Proceeding of the Fourth International Conference on Recrystallization and Related Phenomena, JIM, Sendai, Japan, 1999, p. 515.

193. K. Wang, N.R. Tao, G. Liu, J. Lu, K. Lu, Acta Mater., 54 (2006), p. 5281.

Table 1-1 Comparison among Mg alloy, Al alloy, Ti alloy, steel and plastics.

Material	Cast Mg	Wrought Mg	Steel	Cast Al	Wrought Al	Ti	Plastics (PC/ABS)
Alloy/ Grade	AZ91	AZ31 -H24	Galva- nized	A356-T6	6061-T6	Ti-3Al	Dow Pulse 2000
Process/ Product	Die cast	Sheet	Sheet	Die cast	Extrusion		Injection molding
Density (g/cm^3)	1.81	1.77	7.80	2.76	2.70	4.2	1.13
Elastic Modulus (GPa)	45	45	210	72	70	140	2.3
Yield Strength (MPa)	160	220	200	186	275	925	53
Ultimate Tensile Strength (MPa)	240	290	320	262	310	1000	55
Elongation (%)	3	15	40	5	12	16	5 at yield and 125 at break
Melting Temp. (^oC)	598	630	1515	615	652	1600	143 (softening temp.)

Table 1-2 The standard four-part ASTM designation system of alloy and temper for the magnesium alloy [13].

	First part	Second part	Third part	Fourth part
Statement	Indicates the two principal alloying element	Indicates the amount of the two principal elements	Distinguishes between different alloys with the same percentage of the two principal alloying elements	Indicates condition (temper)
Method	Consists of two code letters representing the two main alloying elements arranged in order of decreasing percentage (or alphabetically if percentage are equal)	Consists of two numbers corresponding to rounded-off percentage of the two main alloying elements and arranged in same designation in first part	Consists of a letter of the alphabet assigned in order as compositions become standard	Consists of a letter followed by a number (separated from the third part of the designation by a hyphen
Example	A- Al E- rare earth H- Th K- Zr M- Mn Q- Ag S- Si T-Sn W- Y Z- Zn	Whole numbers	Letters of alphabet except I and O	F- as fabricated O- annealed H10 and H11-strain hardened H23, H24 and H26-strain hardened and partially annealed T4- solution heat treated T5- artificially aged only T6- solution heat treated and artificially aged

Table 1-3 The effect of separate solute addition on the mechanical properties [14].

Alloying element	Melting and casting behavior	Mechanical and technological properties	Corrosion behavior I/M produced
Ag		Improves elevated temperature tensile and creep properties in the presence of rare earths	Detrimental influence on corrosion behavior
Al	Improves castability, tendency to microporosity	Solid solution hardener, precipitation hardening at low temperature (< 120°C)	Minor influence
Be	Significantly reduces oxidation of melt surface at very low concentration (< 30 ppm), leads to coarse grains		
Ca	Effective grain refining effect, slight suppression of oxidation of the molten metal	Improve creep properties	Detrimental influence on corrosion behavior
Cu	System with easily forming metallic glasses, improves castability		Detrimental influence on corrosion behavior, limitation necessary
Fe	Magnesium hardly reacts with mild steel crucibles		Detrimental influence on corrosion behavior, limitation necessary
Li	Increases evaporation and burning behavior, melting only in protected and sealed furnaces	Solid solution and precipitation hardening at ambient temperatures, reduce density, enhances ductility	Decreases corrosion properties strongly, coating to protect from humidity is necessary
Mn	Control of Fe content by precipitating Fe-Mn compound, refinement of precipitates	Increases creep resistivity	Improves corrosion properties due to iron control effect
Ni	System with easily forming metallic glasses		Detrimental influence on corrosion behavior, limitation necessary
Rare earth	Improve castability, reduce microporosity	Solid solution and precipitation hardening at ambient and elevated temperatures; improve elevated temperature tensile and creep properties	Improve corrosion behavior
Si	Decreases castability, forms stable silicide compounds with many other alloying elements, compatible with Al, Zn and Ag, weak grain refiner	Improve creep properties	Detrimental influence
Th	Suppresses microporosity	Improves elevated temperature tensile and creep properties, improves ductilities, most efficient alloying element	
Y	Grain refining effect	Improves elevated temperature tensile and creep properties	Improves corrosion behavior
Zn	Increases Fluidity of the melt, weak grain refiner, tendency to microporostiy	Precipitation hardening, improves strength at ambient temperatures, tendency to brittleness and hot shortness unless Zn refined	Minor influence, sufficient Zn content compensates for the detrimental effect of Cu
Zr	Most effective grain refiner, incompatible with Si, Al and Mn, removes Fe, Al, and Si from the melt	Improves ambient temperature tensile properties slightly	

Table 1-4 Mechanical properties of magnesium matrix composites by various processing means.

Magnesium matrix composites	Processing	D (μm)	d (μm)	E (GPa)	$\sigma_{0.2}$ (MPa)	UTS (MPa)	Hardness (HV)	Elongation (%)	Reference
Pure Mg; 30 vol% SiC	casting + extruded	20	40	59	229	258	57	2	[66]
Pure Mg; 4.3 vol% SiC	casting	--	25	45	112	191	--	0.057	[68]
ZK51A; 15 vol% SiC_w (whiskers with diameter of 0.3~1 μm and lengths of 15~50 μm)	squeeze casting	--	--	58	305	325	--	1.2	[69]
AZ91; $Al_{18}B_4O_{33}$(whiskers with diameter of 0.5~1 μm and lengths of 10~30 μm)	squeeze casting + 250°C annealing 100 hours	--	--	71	270	368	--	0.96	[70]
AZ91; 20 vol% SiC with $Al(PO_3)_3$ binder (whiskers with diameter of 0.1~1 μm and lengths of 30~100 μm,)	squeeze casting	--	--	85	220	355	175	1.38	[71]
AZ91; 20 vol% SiC without $Al(PO_3)_3$ binder (whiskers with diameter of 0.1~1 μm and lengths of 30~100 μm,)	squeeze casting	--	--	77	202	314	174	1.29	[71]
Pure Mg; 30 vol% Y_2O_3	casting	--	0.33	--	268	363	--	15	[72]
Pure Mg; 30 vol% Y_2O_3	casting + extruded	0.88	0.33	65	344	455	--	0	[72]
AZ91; 10 vol% TiC	semi-solid slurry stirring	--	5	--	--	214	83	4	[72]
AZ91; 5 wt% SiC	ultrasonic	--	0.03	--	--	--	135	--	[75]

**D: grain size, d: particle size

Table 1-4 Mechanical properties of magnesium matrix composites by various processing means.

Magnesium matrix composites	Processing	D (μm)	d (μm)	E (GPa)	$\sigma_{0.2}$ (MPa)	UTS (MPa)	Hardness	Elongation (%)	Reference
AZ91; 10 vol% SiC	PM + extrusion	17.2	8	58	271	360	--	3	[76]
AZ91; 10 vol% SiC	PM + extrusion	24	30	58	243	350	--	3	[76]
AZ91; 10 vol% SiC	PM + extrusion	28.2	50	58	236	350	--	2	[76]
Pure Mg; 10 vol % TiB_2	PM	--	10	--	--	--	45 HB	--	[77]
Pure Mg; 20 vol % TiB_2	PM	--	10	--	--	--	66 HB	--	[77]
Pure Mg; 30 vol % TiB_2	PM	--	10	--	--	--	90 HB	--	[77]
Pure Mg; 10 vol % B_4C	ball milling + PM	--	6	--	--	--	44 HB	--	[78]
Pure Mg; 20 vol % B_4C	ball milling + PM		6	--	--	--	133 HB	--	[78]
Pure Mg; 0.5 wtl% Al_2O_3	PM	61	0.05	42.5	169	232	44 HV	6.5	[79]
Pure Mg; 2.5 wt% Al_2O_3	PM	31	0.05	44.5	194	250	70 HV	6.9	[79]

**D: grain size, d: particle size

Table 1-5 Microstructure-mechanical property and fracture correlations for metal matrix composites [81].

Microstructure condition	Mechanical property response
Addition of reinforcement	Increase in strength, modulus, fatigue life, creep properties, abrasion resistance, impact strength, high temperature strength, decrease in ductility (elongation to failure), and fracture toughness
Reinforcement type	In general, fibrous reinforcements give higher mechanical properties than particulate at equal volume fraction. Particulate reinforcement, however, gives higher elongation to failure and fracture toughness.
Reinforcement orientation	Fibrous reinforcement aligned along test axis gives approximately 25% higher strength than particulate or transverse fibrous reinforcement. Fatigue and creep properties are improved in aligned fibrous composites. Ductility and fracture toughness is generally lower in the aligned material.
Reinforcement distribution	Banding and or clustering enhances crack initiation and growth, and hence lowers strength, ductility, and toughness.
Particle size	Mp effect on modulus; strength properties decrease with particle size increase
Aspect ratio	Influence modulus, strength, fracture toughness, ductility and fracture mechanism
Interface condition	Strong bonding increases modulus and strength but decreases ductility. Can be embrittled as a of excessive result of excessive precipitation and/or diffusion of alloying ingredients or impurities to interface
Matrix phases	Normal precipitate phases increase yield and ultimate strength. Impurity particles and preferential precipitation decrease strength, fracture toughness, fatigue, creep, and ductility
Heat treatment	Heat treatment increases mechanical properties; however, overaging minimizes the benefits. Precipitation kinetics can be altered by the addition of reinforcement; hence time and temperature for peak aging may differ
Secondary processing	Secondary processing affects microstructure and hence mechanical properties. Extrusion aligns fibrous reinforcements but induces banding or reinforcements-free areas. Rolling homogenizes microstructure, giving higher properties, but can damage matrix-reinforcement bonds and lead to overaging. Material must be heat-treated to regain properties.

- These comments assume well-bonded reinforcements.

Table 1-6 The key benefits of friction stir welding [88].

Key benefits of friction stir welding		
Metallurgical benefits	Environmental benefits	Energy benefits
Solid phase process Low distortion of workpieces Good dimensional stability and repeatability No loss of alloying elements Excellent metallurgical properties in the joint area Fine microstructure Absence of cracking Replace multiple parts joined by fasteners	No shielding gas required No surface cleaning required Eliminate grinding wastes Eliminate solvents required for degreasing Consumable materials saving, such as rugs, wire or any other gases	Improved materials use (e.g., joining different thickness) allows reduction in weight Only 2.5% of the energy needed for a laser weld Decreased fuel consumption in light weight aircraft, automotive and ship applications

Table 1-7 A summary of grain size in nugget zone of FSP aluminum alloys

Material	Plate thickness (mm)	Tool geometry	Rotation rate (rpm)	Advancing speed (mm/min)	Grain size	Ref.
7075Al-T6	6.35	-	-	127	2-4	[131]
6061Al-T6	6.3	Cylindrical	300-1000	90-150	10	[120]
Al-Li-Cu	7.6	-	-	-	9	[95]
7075Al-T651	6.35	Threaded, cylindrical	350, 400	102, 152	3.8, 7.5	[89]
6063Al-T4, T5	4	-	360	800-2450	5.9-17.8	[93]
6013Al-T4, T6	4	-	1400	400-450	10-15	[132]
1100Al	6	Cylindrical	400	60	4	[133]
5054Al	6	-	-	-	6	[134]
1080Al-O	4	-	-	-	20	[126]
5083Al-O	6	-	-	-	4	[126]
2017Al-T6	3	Threaded, cylindrical	1250	60	9-10	[135]
2095Al	1.6	-	1000	126-252	1.6	[136]
Al–Cu–Mg–Ag–T6	4	-	850	75	5	[137]
2024Al-T351	6	-	-	80	2-3	[138]
7010Al-T7651	6.35	-	180, 450	95	1.7, 6	[139]
7050Al-T651	6.35	-	350	15	1-4	[96]
Al–4Mg–1Zr	10	Threaded, cylindrical	350	102	1.5	[140]

2024Al	6.35	Threaded, cylindrical	200-300	25.4	1-3.9	[141]
7475Al	6.35	-	-	-	2.2	[142]
5083Al	6.35	Threaded, cylindrical	400	25.4	6	[143]
2519Al-T87	25.4	-	275	101.6	2-12	[144]

Table 1-8 A summary of ultrafine-grained microstructures produced via FSP in aluminum alloys

Material	Plate thickness (mm)	Tool geometry	Special cooling	Rotation rate (rpm)	Advancing speed (mm/min)	Grain size (μm)	Ref.
2024Al-T4	6.5	Threaded, cylindrical	Liquid nitrogen	650	60	0.5-0.8	[121]
1050Al	5.0	Conical pin without thread	N/A	560	155	0.5	[129]
7075Al	2	N/R	Water, methanol, dry ice	1000	120	0.1	[94]
Cast Al-Zn-Mg-Sc	6.7	Threaded, cylindrical	N/A	400	25.4	0.68	[145]
1100Al	1.5	Threaded, cylindrical	N/A	500	720	0.8	[146]
6061Al-T6	3.2	Threaded, cylindrical	Submerged in water	1000	76	0.2	[147]

Table 1-9 A summary of grain size in nugget zone of FSP magnesium alloys

Material	Plate thickness (mm)	Tool geometry	Rotation rate (rpm)	Advancing speed (mm/min)	Grain size (μm)	Ref.
AZ61	6.3	Threaded, cylindrical	1220	90	14	[91]
AZ31B-H24	3.1	Threaded, cylindrical	1500-2800	120	3.1-8.4	[149]
AZ31B-H24	4.95	Adjustable pin tool	500-1000	60-180	8.5-10.2	[150]
AZ31B	6.4	Threaded, cylindrical	800, 1000	60	25	[151]
Mg-Al-Ca-RE-Mn	2	Threaded, cylindrical	1500	1500	0.8-1	[152]
AM60B	2.5	Threaded, cylindrical	700	90	2.5	[153]
AZ31-H24	4	-	1200-1600	100-200	13	[154]
AZ31B	2	Threaded, cylindrical	500	720	2.9	[155]

Table 2-1 Chemical composition of the AZ31 (in wt%)

	Mg	Al	Zn	Mn	Si	Fe	Cu	Ni
AZ31B	Bal.	3.02	1.01	0.3	0.0067	0.0028	0.0031	0.0001

Table 2-2 The dimensions of the tools

Tool diameter (mm)	Shoulder diameter (mm)	Pin size		
		Diameter (mm)	Length (mm)	Pitch distance (mm)
20	18	6	6	1
16	16	6	6	1
10	10	3	3	0.8
6	6	2	2	---

Table 3-1 The recrystallized grain size of the modified AZ31 Mg alloy made by FSP

(a) Using the different rotational speeds under the same advancing speed of 90 mm/min

	AZ31 billet	600 rpm	800 rpm	1000 rpm	1200 rpm	1400 rpm	1800 rpm
Average grain size (μm)	75	2.9	3.1	3.6	3.7	3.7	7.7

(b) Using the different advancing speeds under the same rotational speed of 800 rpm

	AZ31 billet	45 mm/min	90 mm/min	200 mm/min	400 mm/min	800 mm/min
Average grain size (μm)	75	5	3.1	2.6	2.3	2

Table 3-2 Summary of the measured temperature during FSP

AZ31 alloy	Max. temperature
600 rpm, 90 mm/min	365 ^{o}C
800 rpm, 90 mm/min	385 ^{o}C
800 rpm, 200 mm/min	379 ^{o}C
800 rpm, 400 mm/min	318 ^{o}C
1000 rpm, 90 mm/min	413 ^{o}C
1400 rpm, 90 mm/min	422 ^{o}C
1800 rpm, 90 mm/min	417 ^{o}C

Table 3-3 Summary of the H_v hardness in the 1P FSP processed AZ31 alloys

AZ31 alloy	Average H_v
As-received	~50
600 rpm, 90 mm/min	76
800 rpm, 90 mm/min	75.9
1000 rpm, 90 mm/min	75
1400 rpm, 90 mm/min	68.7
1800 rpm, 90 mm/min	58.6

Table 3-4 Summary of the H_v hardness in the FSP processed intermetallic alloys after multi-passes under different cooling methods. The melt spun alloy is also included for comparison

Alloy system	Cooling	FSP passes	Average H_v
AZ31	Air cooling	3	60 ± 2
$Mg_{80}Al_{10}Zn_{10}$	Air cooling	3	133 ± 7
$Mg_{70}Al_5Zn_{25}$	**Melt spinning, cooling rate 10^5 K/s**	**--**	**265 ± 10**
$Mg_{70}Al_5Zn_{25}$	Air cooling	3	164 ± 9
$Mg_{70}Al_{15}Zn_{15}$	Air cooling	3	187 ± 23
$Mg_{60}Al_{20}Zn_{20}$	Air cooling	3	216 ± 16
$Mg_{80}Al_{10}Zn_{10}$	Liquid N_2 cooling	3	--
$Mg_{70}Al_{15}Zn_{15}$	Liquid N_2 cooling	3	216 ± 23
$Mg_{60}Al_{20}Zn_{20}$	Liquid N_2 cooling	3	244 ± 7
$Mg_{60}Al_{15}Zn_{25}$	Air cooling	3	227 ± 10
$Mg_{50}Al_5Zn_{45}$	Air cooling	3	306 ± 43
$Mg_{50}Al_{20}Zn_{30}$	Air cooling	3	240 ± 18
$Mg_{37.5}Al_{25}Zn_{37.5}$	Air cooling	3	340 ± 47
$Mg_{37.5}Al_{25}Zn_{37.5}$	Water cooling	3	341 ± 25
$Mg_{37.5}Al_{25}Zn_{37.5}$	Water cooling	10	316 ± 8

Table 3-5 Summary of the average cluster size of nano-particles and the average grain size of AZ31 matrix in the 4 passes FSP composites

Materials	AZ31 after 4P	AZ31/ZrO_2 (~10%)	AZ31/ZrO_2 (~20%)	AZ31/SiO_2 (~5%)	AZ31/SiO_2 (~10%)
Average grain size (μm)	~ 6	~ 3	~ 2	~ 4	~ 3
Particle cluster size (nm)		~ 200	~ 180	~ 300	~ 260

Table 3-6 Comparison of the mechanical properties of AZ31 alloy and AZ31-based composites

Materials	*Hardness, H_v*	*YS*, MPa	*UTS*, MPa	*El*, %
AZ31 billet	50	100	160	~ 9
AZ31 after 4P FSP	69	120	204	~ 18
~10 vol% ZrO_2 (1G4P)	98	143	232	~ 6
~20 vol% ZrO_2 (2G4P)	105	167	255	~ 6
~5 vol% SiO_2 (1G4P)	78	-	-	-
~10 vol% SiO_2 (2G4P)	87	128	258	~ 6

YS: yield strength; *UTS*: ultimate tensile strength; *El*: elongation.

Table 3-7 A summary of the recrystallized pure AZ31 grain size for the different FSP parameters

(a) On the different cooling condition under the same rotational speed of 800 rpm, these FSPed thinner specimens are 7 mm in thickness

	Without liquid N_2 cooling	With liquid N_2 cooling system	
Advancing speed	90 mm/min	45 mm/min	90 mm/min
Average grain size	2.7 μm	2.4 μm	1.6 μm

(b) On the different cooling condition and plate thickness under the same rotational rate and advancing speed of 800 rpm and 90 mm/min, respectively

Sample	Average grain size in the bottom ultrafine grain area
10 mm plate FSPed one pass	~2 μm
7 mm plate FSPed one pass	~1.5 μm
7 mm plate FSPed one pass with liquid N_2 cooling	~550 nm
4 mm plate FSPed one pass with liquid N_2 cooling (smaller pin tool, pin size: 3mm in diameter and length and shoulder: 10 mm in diameter)	~450 nm

Table 3-8 Grain size and hardness at the FSP nugget bottom

	FSP process condition	d (μm)	H_v
AZ31 alloy	As received billet	75	50
	800 rpm, 90 mm/min, 10 mm plate, pin size: 18/6/6, no special cooling	2	76
	800 rpm, 90 mm/min, 7 mm plate, pin size: 18/6/6, no special cooling	1.5	--
	800 rpm, 90 mm/min, 7 mm plate, pin size: 16/6/6, liquid N_2 cooling	0.55	88
	800 rpm, 90 mm/min, 4 mm plate, pin size: 10/3/3, liquid N_2 cooling	0.45	92
	1200 rpm, 28 mm/min, 4 mm plate, pin size: 10/3/3, new designed cooling system with liquid N_2	0.35	110
	1200 rpm, 33 mm/min, 4 mm plate, pin size: 10/3/3, new designed cooling system with liquid N_2	0.25	120
	Two pass FSP. 1^{st} pass: 1200 rpm, 37 mm/min; 2^{nd} pass: 800 rpm, 37 mm/min, 4 mm plate, pin size: 10/3/3, new designed cooling system with liquid N_2	0.18	125
	Two pass FSP. 1000 rpm, 37 mm/min, 4 mm plate, pin size for 1^{st} pass: 10/3/3; 2^{nd} pass: 6/2/2, new designed cooling system with liquid N_2	0.08	134
AZ31/ZrO_2 Composite (monoclinic)	ZrO_2 1G4P, 800 rpm 45 mm/min, 10 mm plate, pin size: 18/6/6, no special cooling	3	98
	ZrO_2 2G4P, 800 rpm 45 mm/min, 10 mm plate, pin size: 18/6/6, no special cooling	2	105
	ZrO_2 2G4P, 800 rpm 45 mm/min, 10 mm plate, pin size: 18/6/6, no special cooling. Subsequent pass: 800 rpm 90 mm/min, pin size: 10/3/3, liquid N_2 cooling	0.4	135

* 10/3/3 represents the pin tool with shoulder diameter, pin diameter and length of 10, 3 and 3 mm, respectively.

	FSP process condition	d (μm)	H_v
AZ31/ZrO_2 Composite (tetragonal)	ZrO_2 1G4P, 800 rpm 45 mm/min, 10 mm plate, pin size: 18/6/6, no special cooling	-	103
	ZrO_2 2G4P, 800 rpm 45 mm/min, 10 mm plate, pin size: 18/6/6, no special cooling	-	113.5
	ZrO_2 1G4P, 800 rpm 45 mm/min, 10 mm plate, pin size: 18/6/6, no special cooling With subsequent 6% compression	-	105
	ZrO_2 2G4P, 800 rpm 45 mm/min, 10 mm plate, pin size: 18/6/6, no special cooling With subsequent 6% compression	-	120
AZ31/SiO_2 Composite (amorphous)	ZrO_2 1G4P, 800 rpm 45 mm/min, 10 mm plate, pin size: 18/6/6, no special cooling	4	78
	ZrO_2 2G4P, 800 rpm 45 mm/min, 10 mm plate, pin size: 18/6/6, no special cooling	3	87
Mg-Al-Zn intermetallic compound alloy	$Mg_{70}Al_5Zn_{25}$, 3P, 1500 rpm 20 mm/min, pin size: 16/6/5, air cooling	-	164±9
	$Mg_{50}Al_5Zn_{45}$, 3P, 1500 rpm 20 mm/min, pin size: 16/6/5, air cooling	-	306±43
	$Mg_{37.5}Al_{25}Zn_{37.5}$, 3P, 1500 rpm 20 mm/min, pin size: 16/6/5, air cooling	-	340±47
	$Mg_{37.5}Al_{25}Zn_{37.5}$, 3P, 1500 rpm 20 mm/min, pin size: 16/6/5, water cooling	-	341±25
	$Mg_{37.5}Al_{25}Zn_{37.5}$, 10P, 1500 rpm 20 mm/min, pin size: 16/6/5, water cooling	-	316±8

* 10/3/3 represents the pin tool with shoulder diameter, pin diameter and length of 10, 3 and 3 mm, respectively.

Table 4-1 The experimental hardness and predicted hardness used by the iso-stress model in the present composites. The initial hardness for the AZ31 billet is ~50

Particle and its volume fraction in composite	Measured hardness of composite, H_v	Hardness of matrix*, H_v	Predicted hardness of composite, H_v
~10 vol% ZrO_2	98	82 (d_g~3 μm)	96
~20 vol% ZrO_2	105	90 (d_g~2 μm)	112
~5 vol% SiO_2	78	76 (d_g~4 μm)	80
~10 vol% SiO_2	87	82 (d_g~3 μm)	96

* The matrix hardness is calculated by the equation $H_v = 40 + 72 d_g^{-1/2}$.

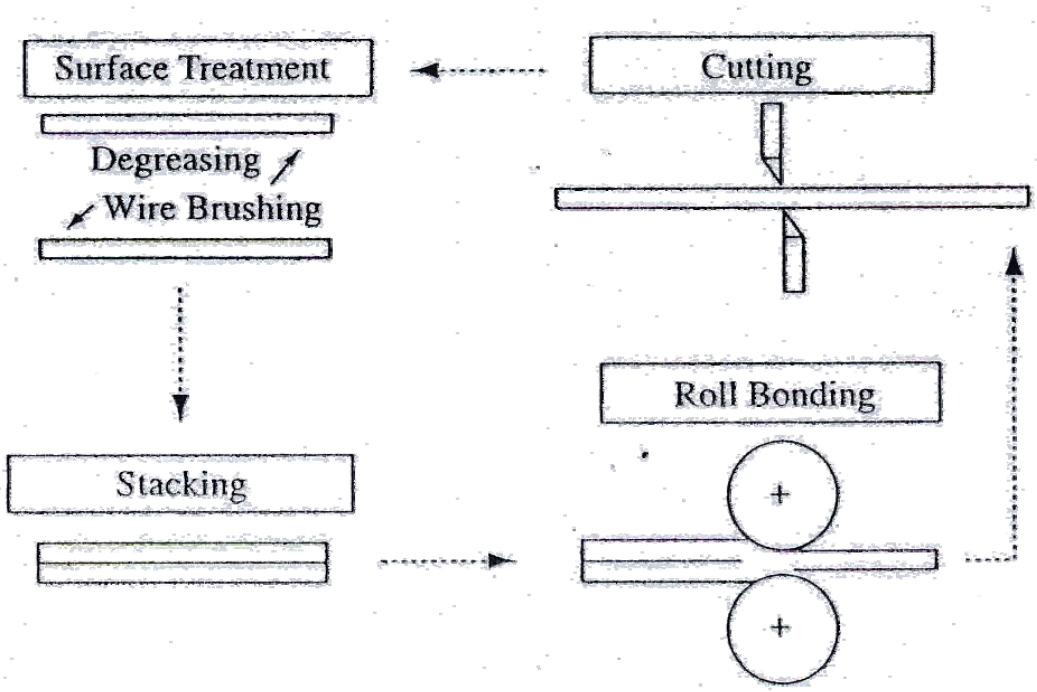

Figure 1-1 Schematic illustration of the ARB facility.

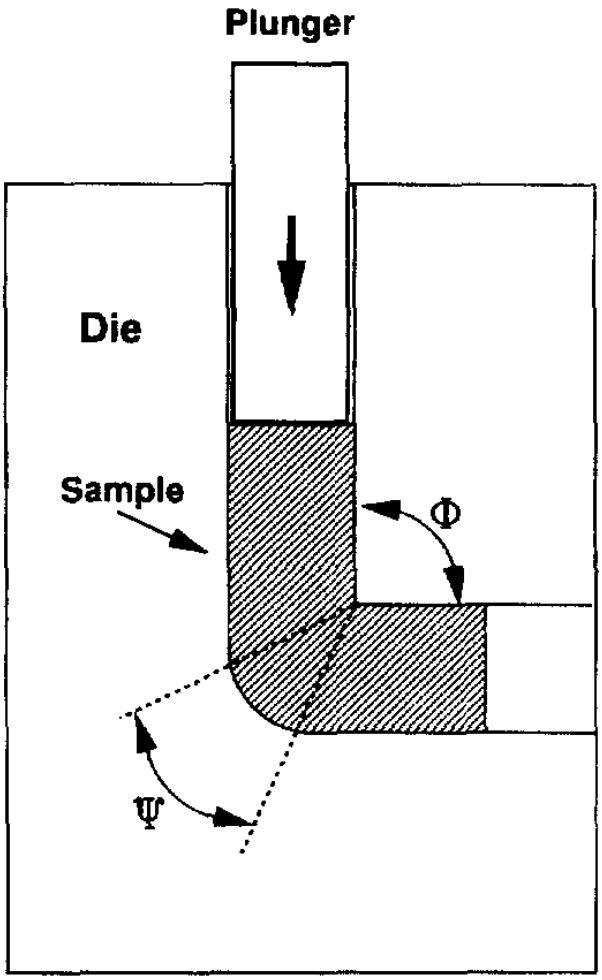

Figure 1-2 Schematic illustration of the ECA pressing facility [48].

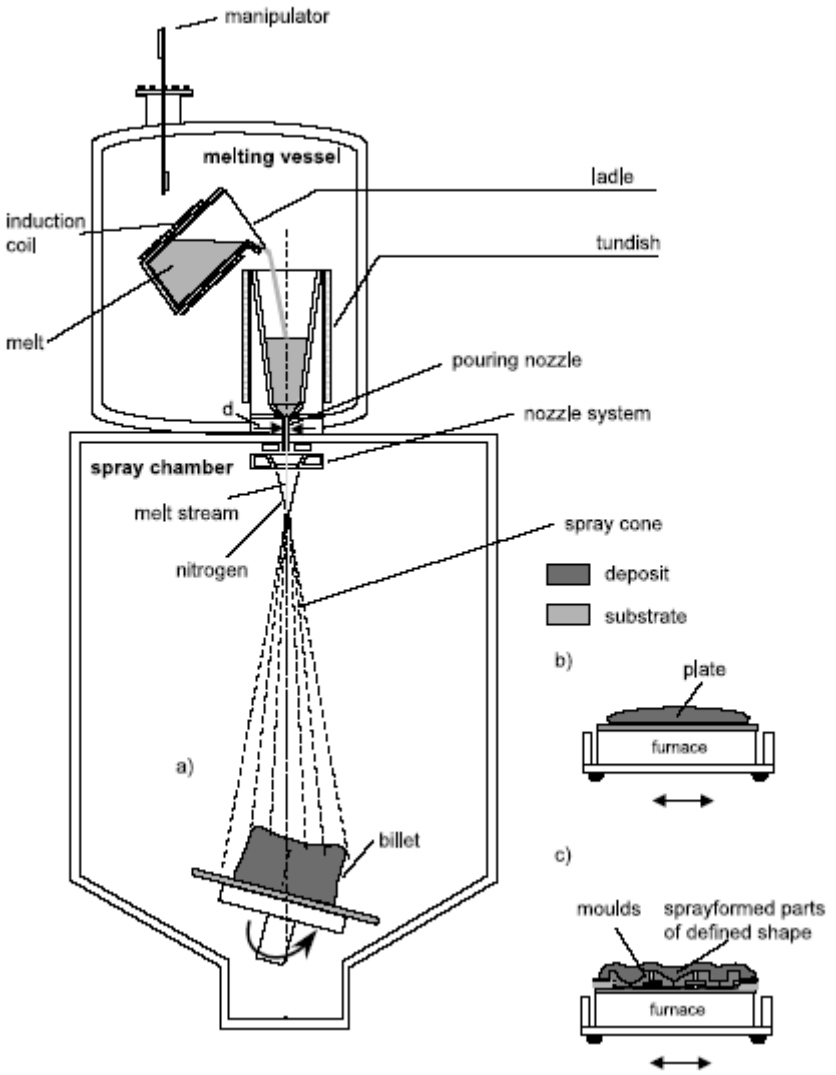

Figure 1-3 Schematic illustration of the spray forming facility [55].

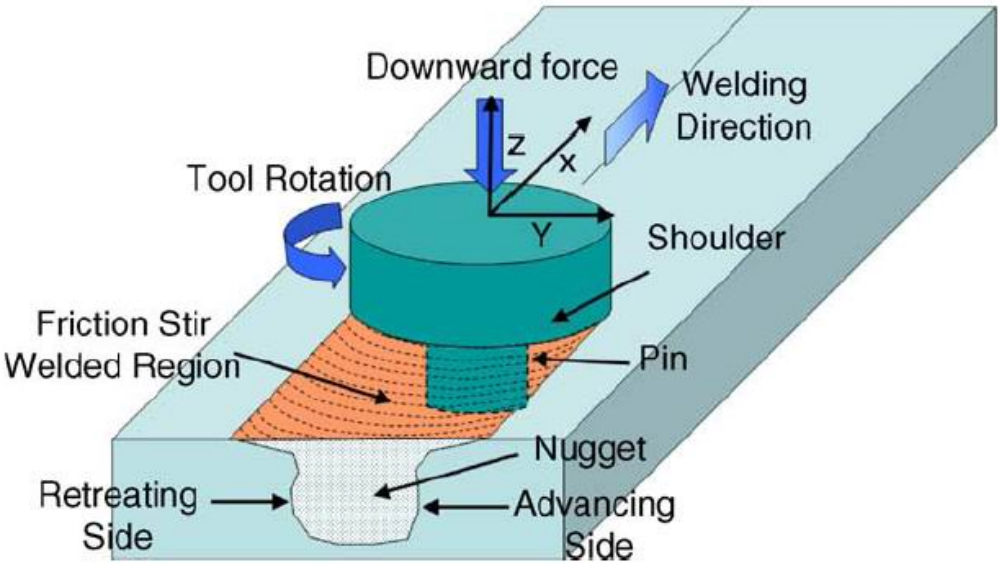

Figure 1-4 Schematic diagram of friction stir welding [88].

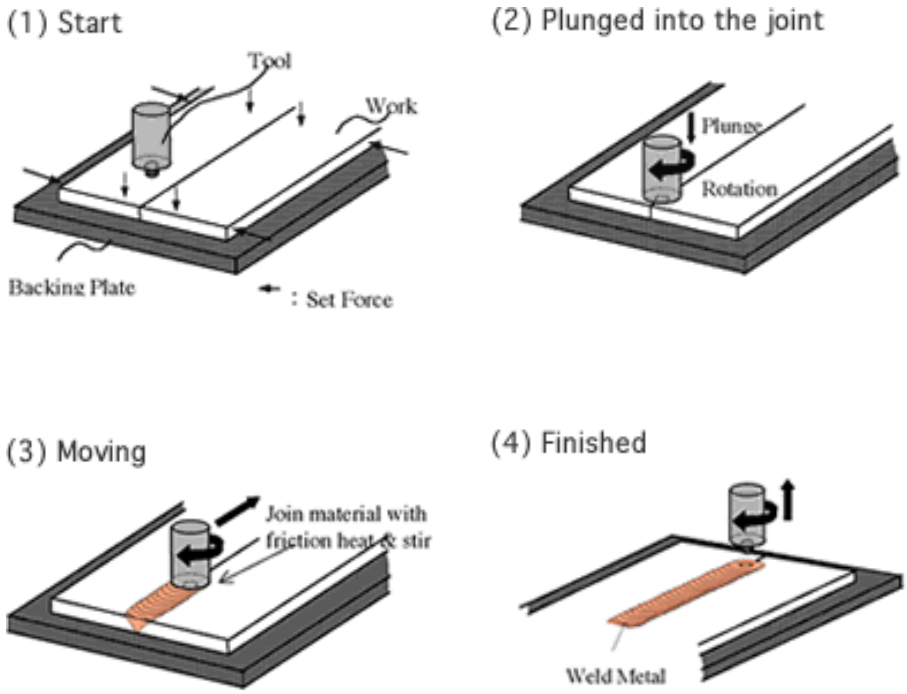

Figure 1-5 Schematic diagram of entire friction stir welding.

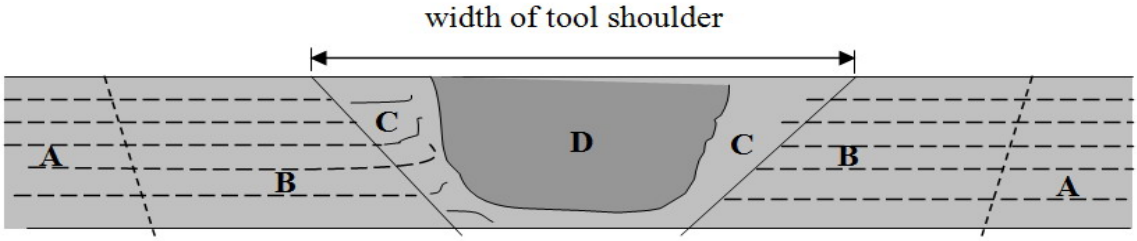

(A) Base metal, BM : This region not undergoing any influence of welding process

(B) Heat affected zone, HAZ：This region experiencing heat influence of welding process

(C) Thermomechanically affected zone, TMAZ：This region experiencing high deformation and undergoing heat influence of welding process

(D) Stirring zone, SZ or dynamically recrystallized weld nugget zone, DXZ：This region experiencing high strain and occurring dynamical recrystallization

Figure 1-6　Schematic illustration of the welding zone in friction stir welding.

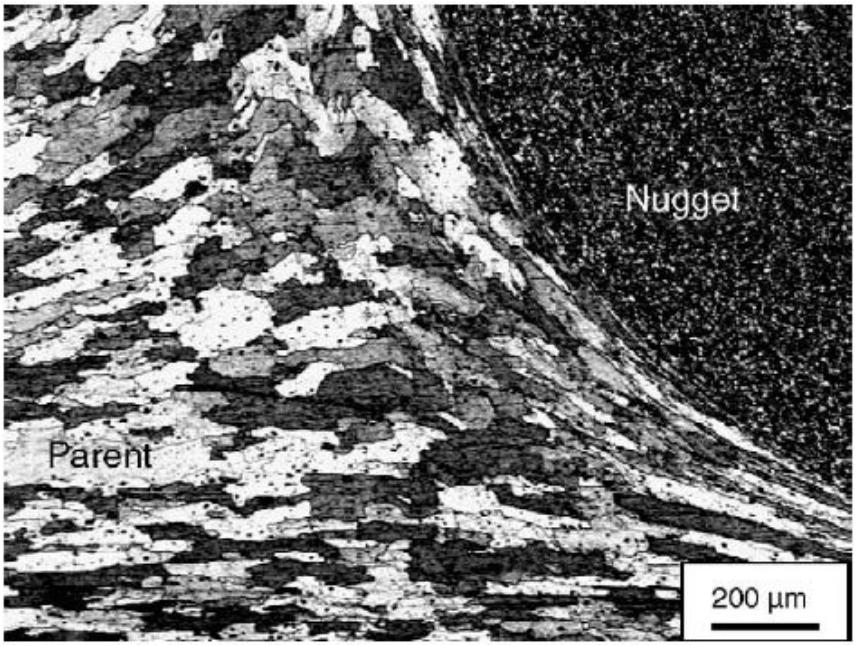

Figure 1-7 Microstructure of thermo-mechanically affected zone in FSP 7075Al [89].

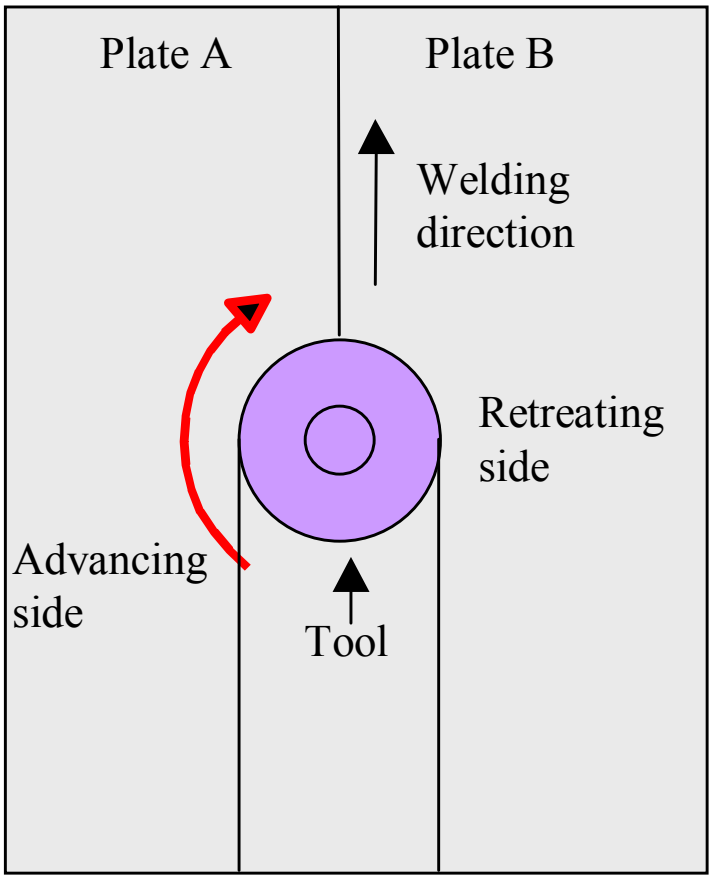

Figure 1-8 Illustration of advancing side and retreating side.

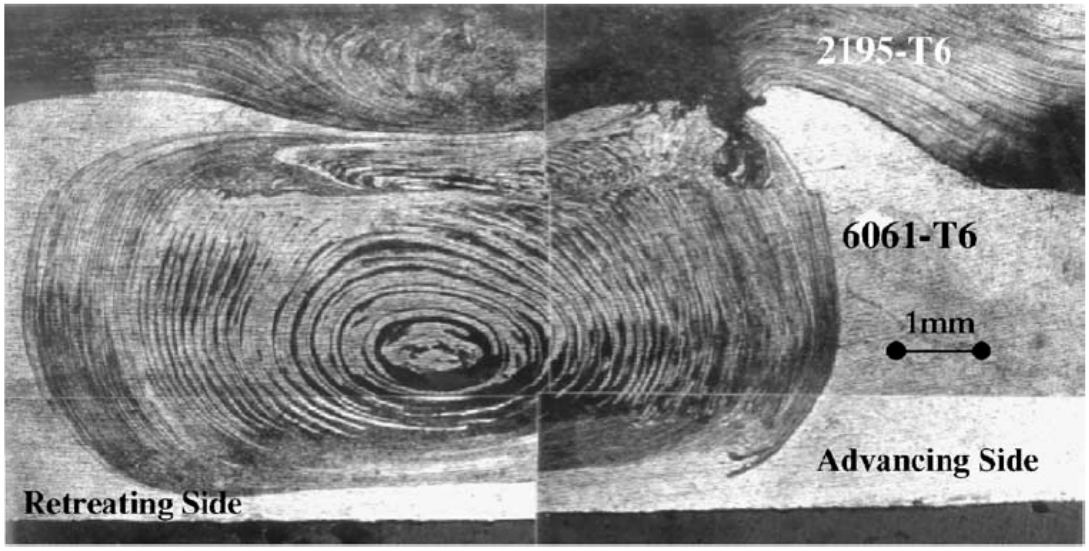

Figure 1-9 Typical onion ring in the nugget zone [104].

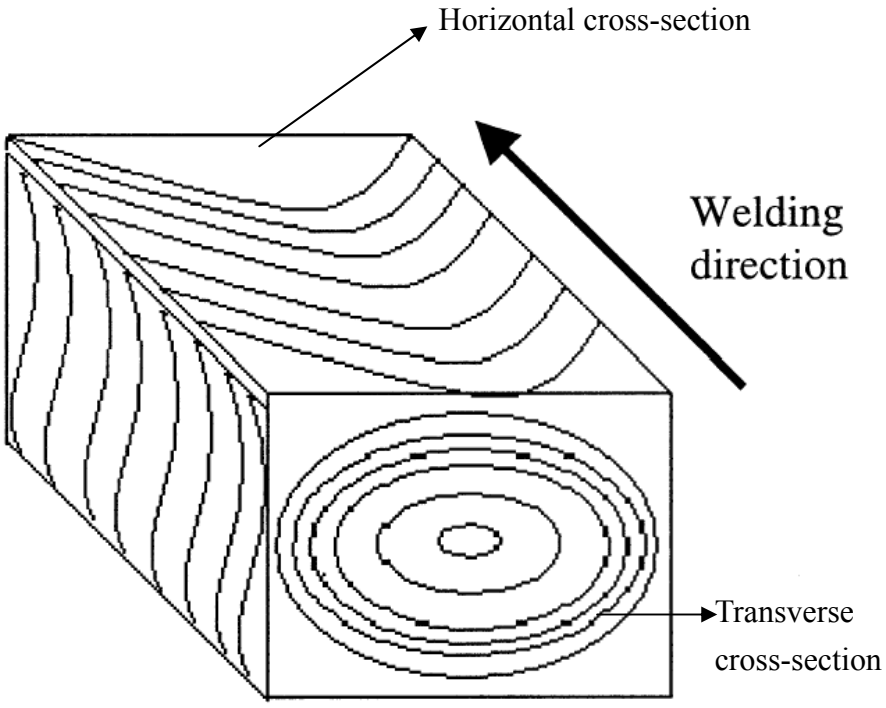

Figure 1-10 Three-dimensional drawing of the onion rings in the nugget zone [104].

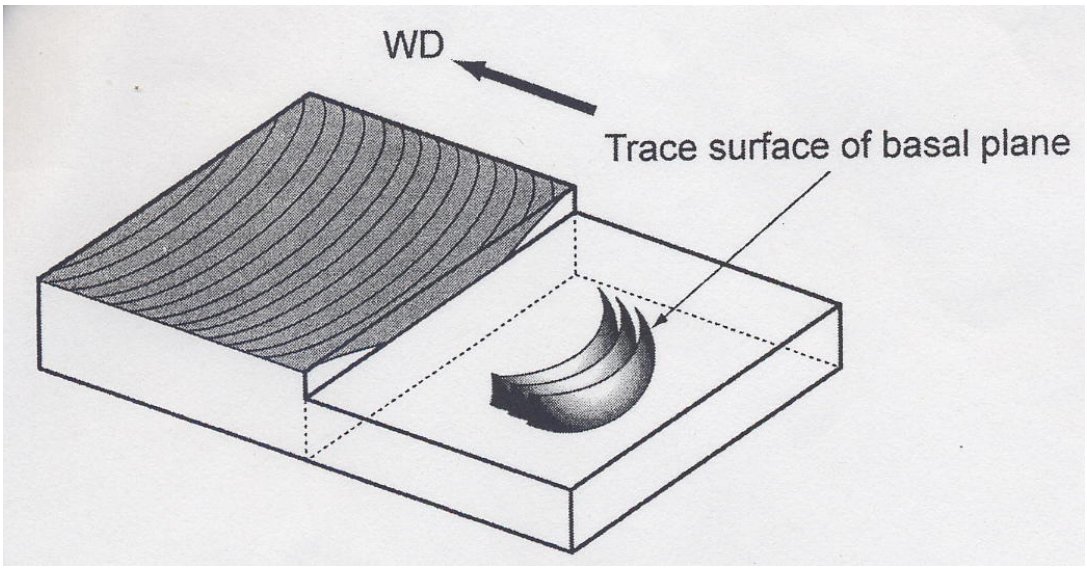

(a)

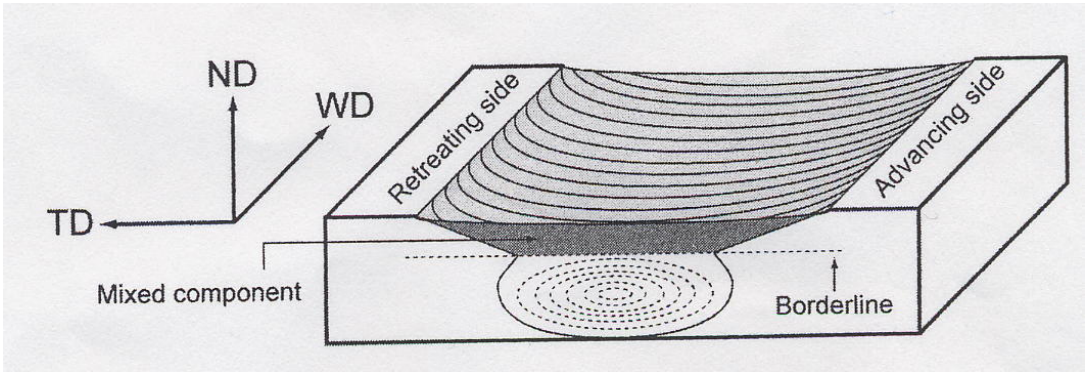

(b)

Figure 1-11 Schematic illustration of (a) trace surface of basal plane produced below the borderline with an onion shape and (b) its transverse cross section [106].

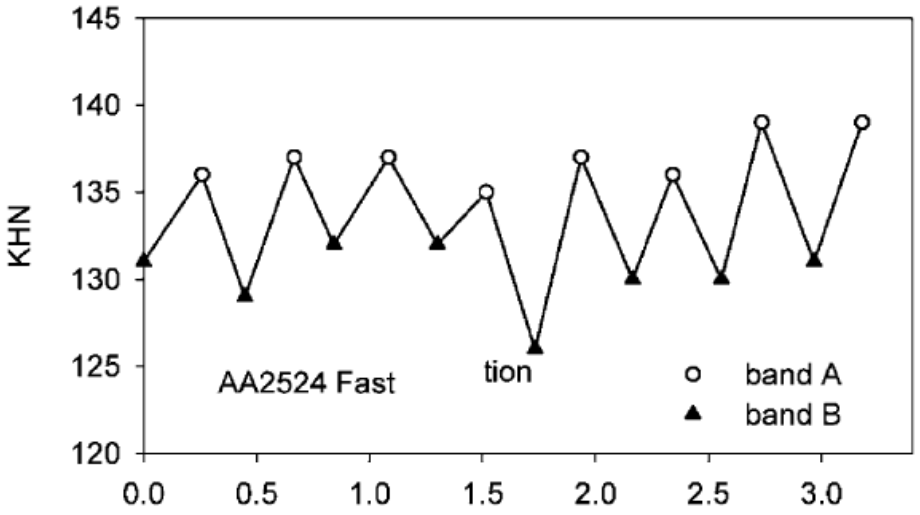

(a) Micro-hardness

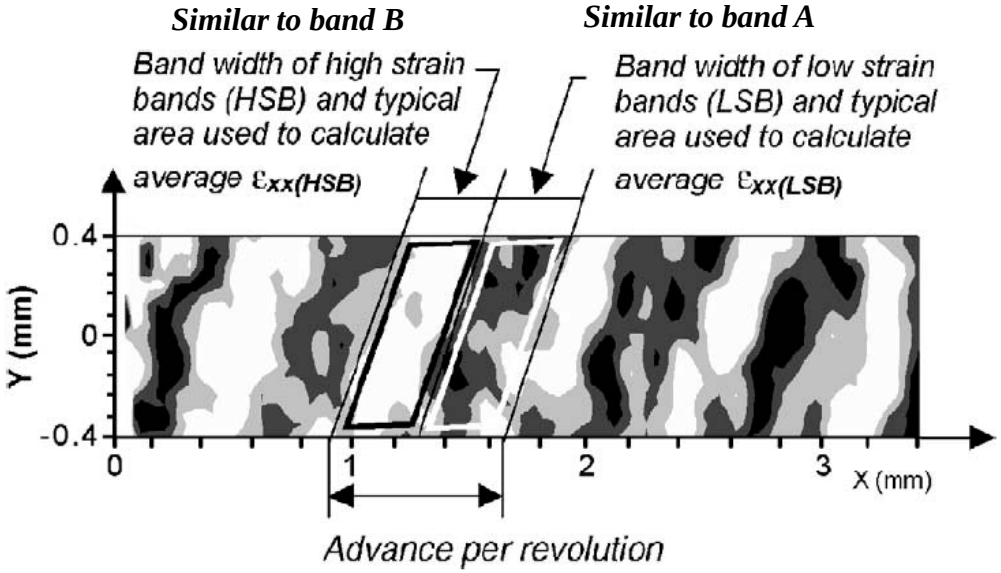

(b) Strain field map in banded microstructure

Figure 1-12 Micro hardness and strain field map in the banded microstructure [109,110].

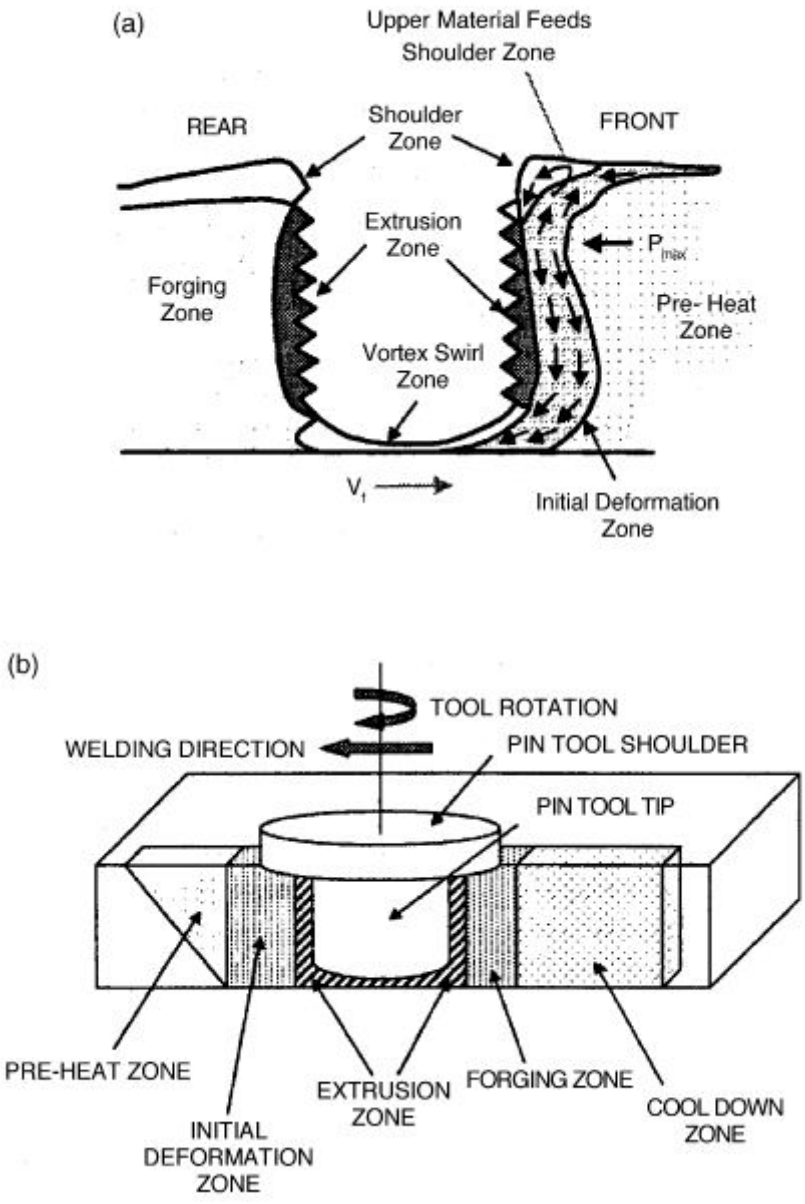

Figure 1-13 (a) Metal flow patterns and (b) metallurgical processing zones developed during friction stir welding [118].

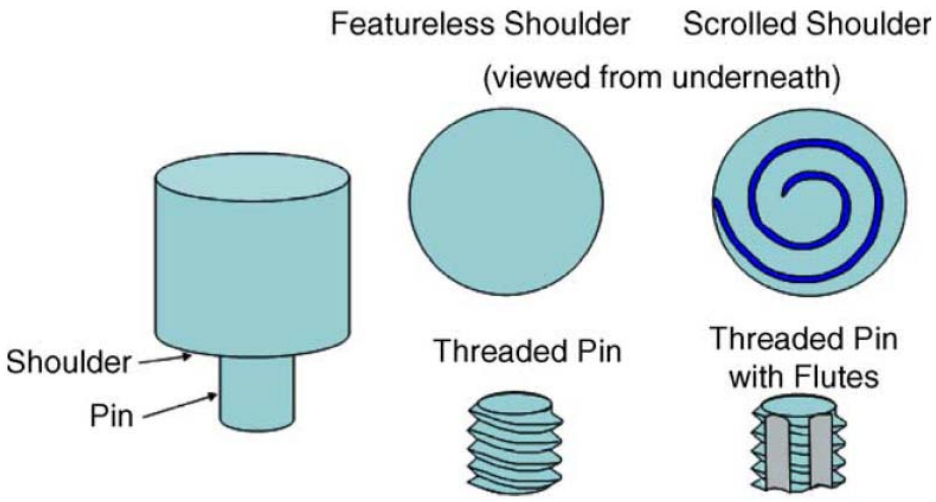

Figure 1-14 Schematic drawing of the FSW tool [88].

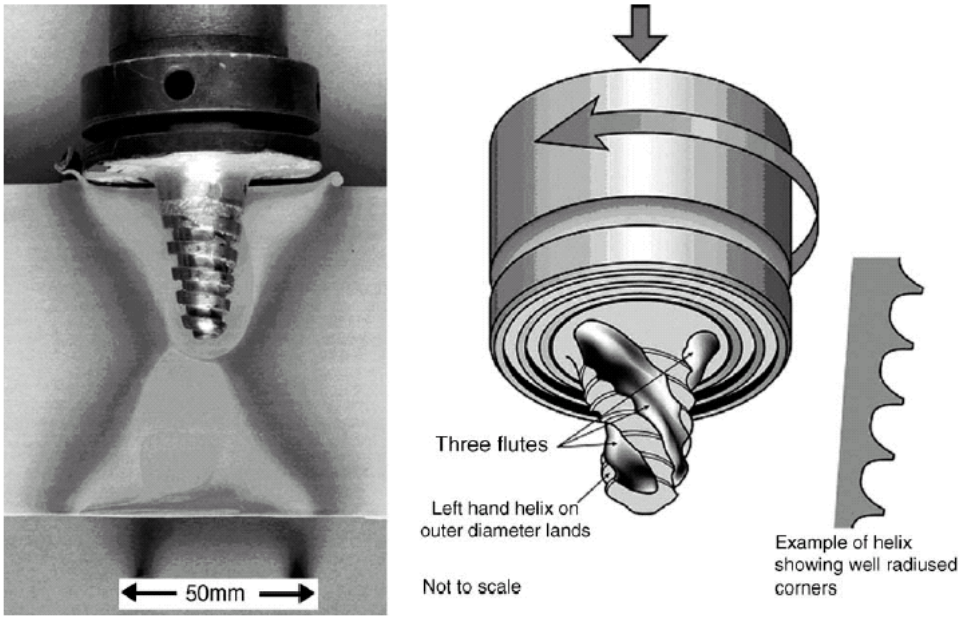

Figure 1-15 Worl™ and MX Triflute™ tools developed by The Welding Institute (TWI), UK [128].

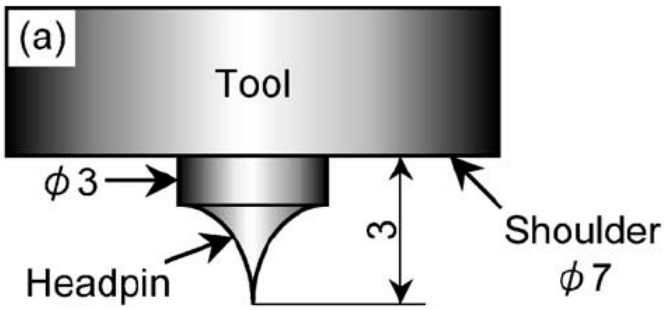

(a) Smaller contact area of headpin

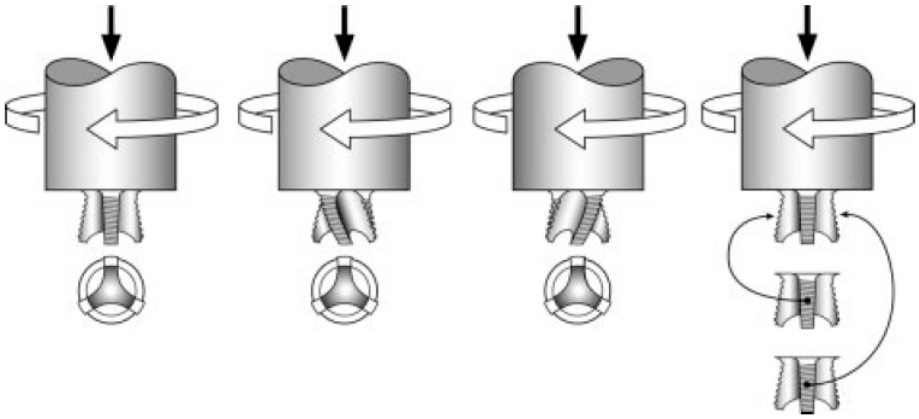

(b) Flared-triflute type probes

Figure 1-16 Illustration of the different probes, (a) smaller contact area of headpin and (b) flared-triflute type probes [128,129].

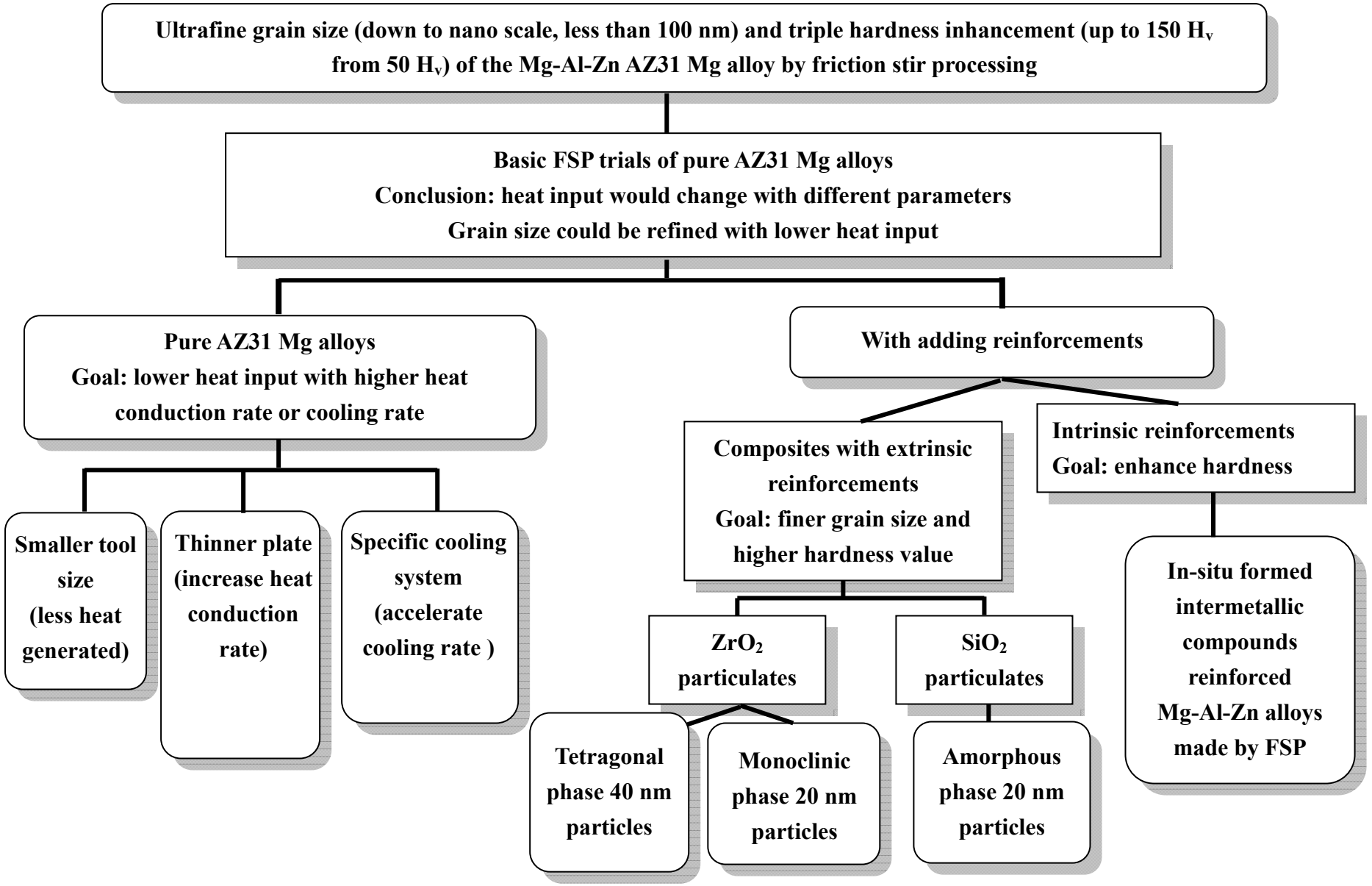

Figure 2-1 The flow chart for progressive improvement of grain size and mechanical properties.

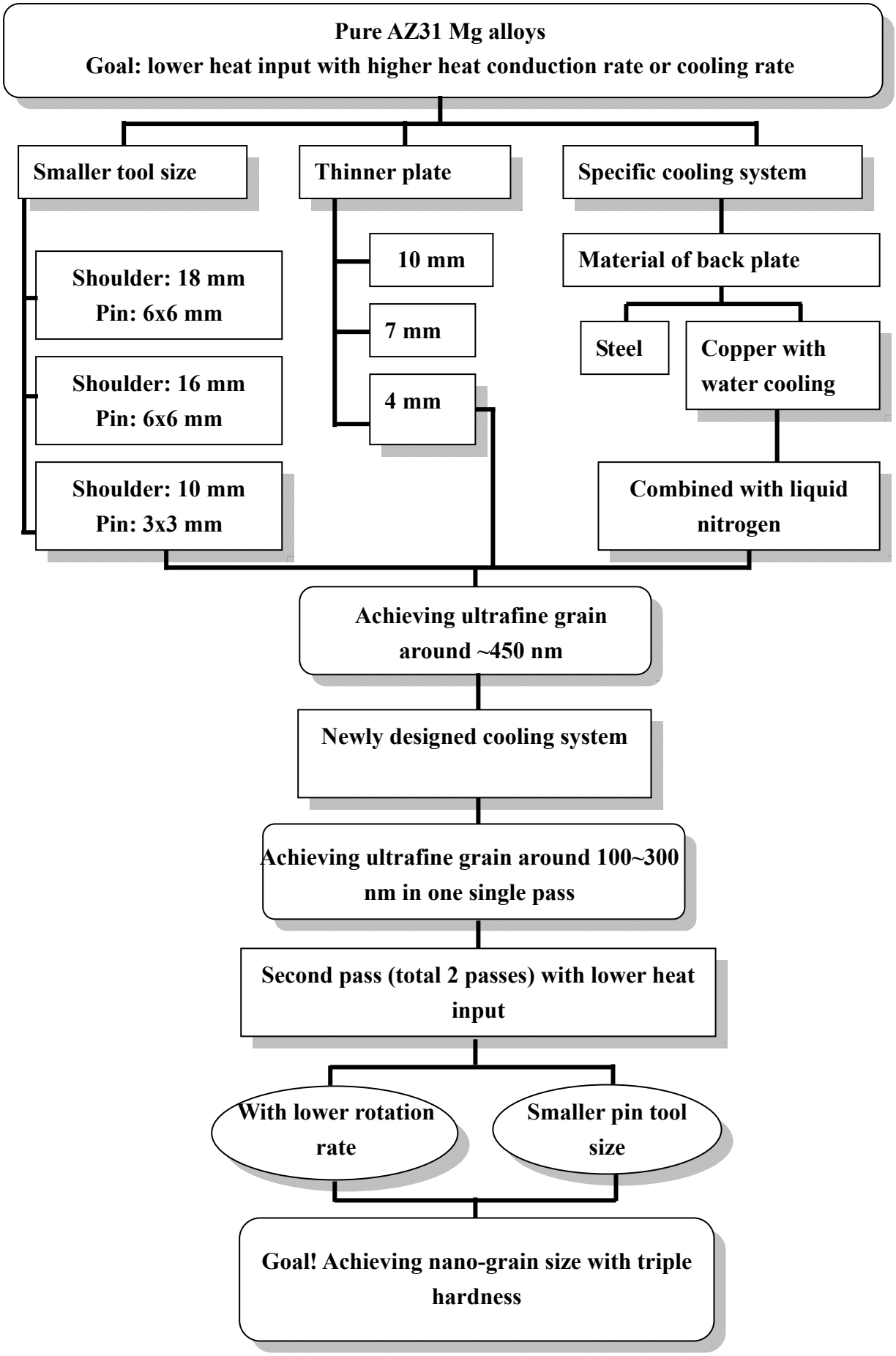
Pure AZ31 Mg alloys
Goal: lower heat input with higher heat conduction rate or cooling rate
Smaller tool size
Thinner plate
Specific cooling system
Shoulder: 18 mm
Pin: 6x6 mm
Shoulder: 16 mm
Pin: 6x6 mm
Shoulder: 10 mm
Pin: 3x3 mm
10 mm
7 mm
4 mm
Material of back plate
Steel
Copper with water cooling
Combined with liquid nitrogen
Achieving ultrafine grain around ~450 nm
Newly designed cooling system
Achieving ultrafine grain around 100~300 nm in one single pass
Second pass (total 2 passes) with lower heat input
With lower rotation rate
Smaller pin tool size
Goal! Achieving nano-grain size with triple hardness

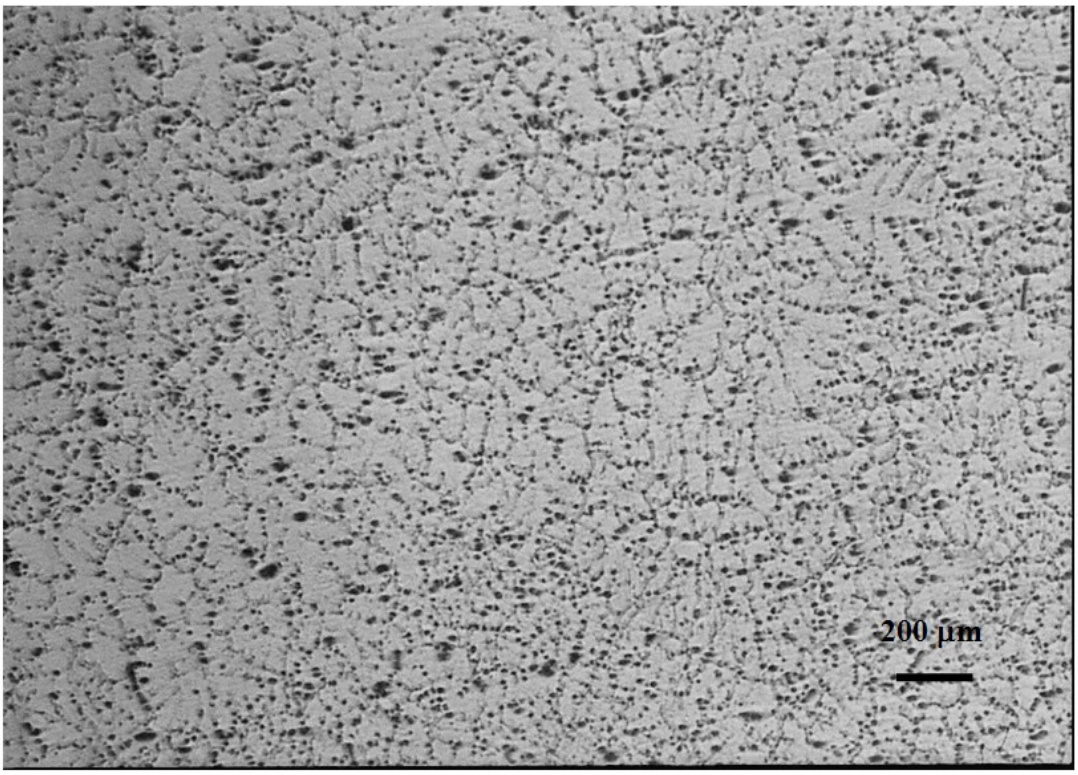

Figure 2-2 The microstructure of the as-received AZ31 billet.

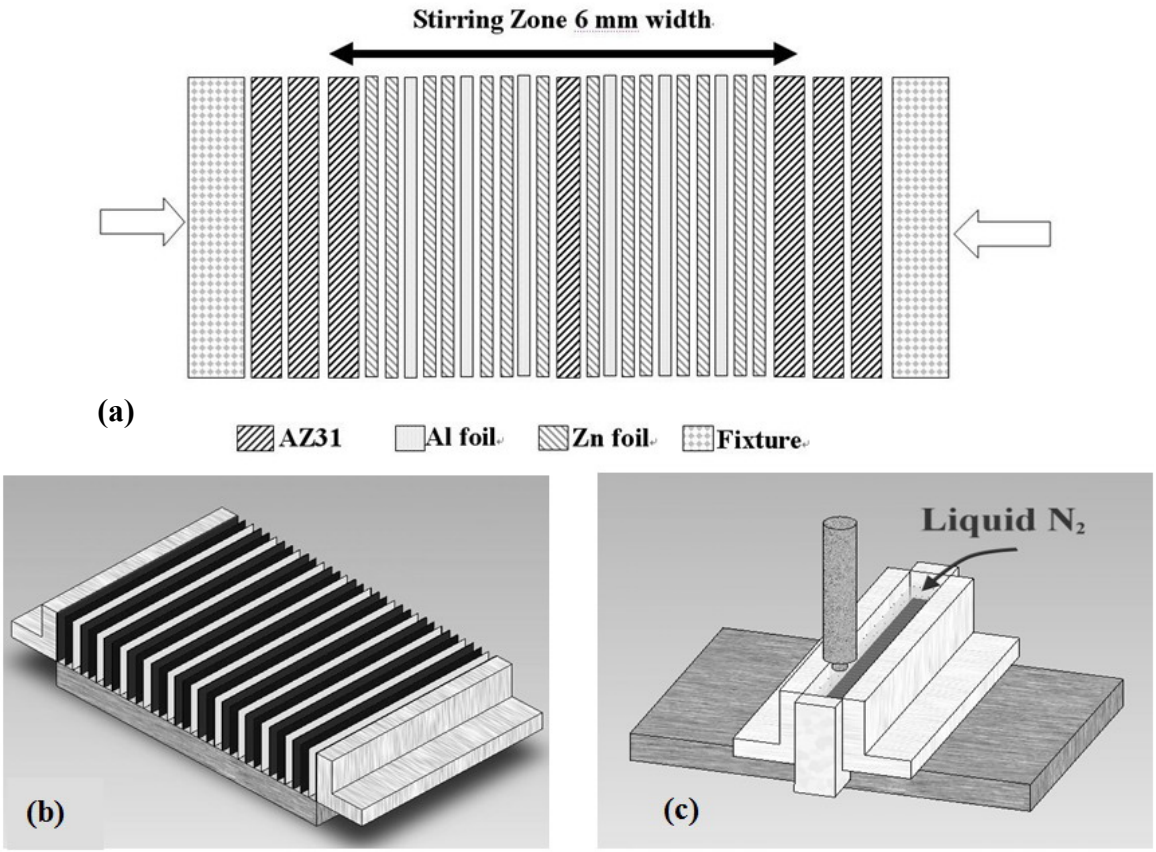

Fig. 2-3 Schematic illustration of (a)(b) the stacked AZ31 Mg alloy sheets with pure Al and pure Zn foils, and (c) the fixture used for liquid N_2 cooling.

(c)

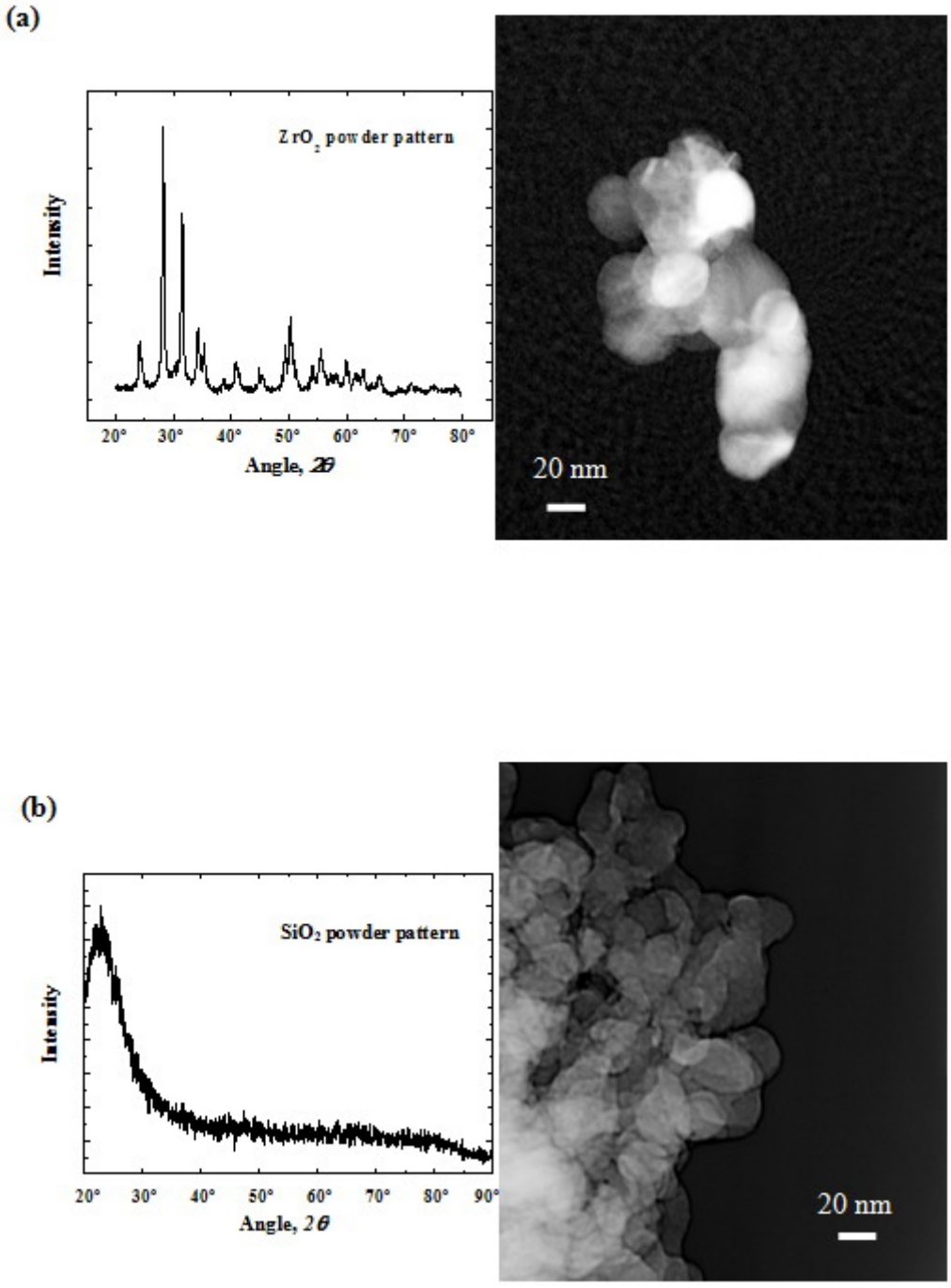

Figure 2-4 The XRD patterns and TEM micrographs of (a) the monoclinic ZrO_2 particles and (b) the amorphous SiO_2 particles, both with an average diameter ~20 nm.

Figure 2-5 The appearance of the horizontal-type miller.

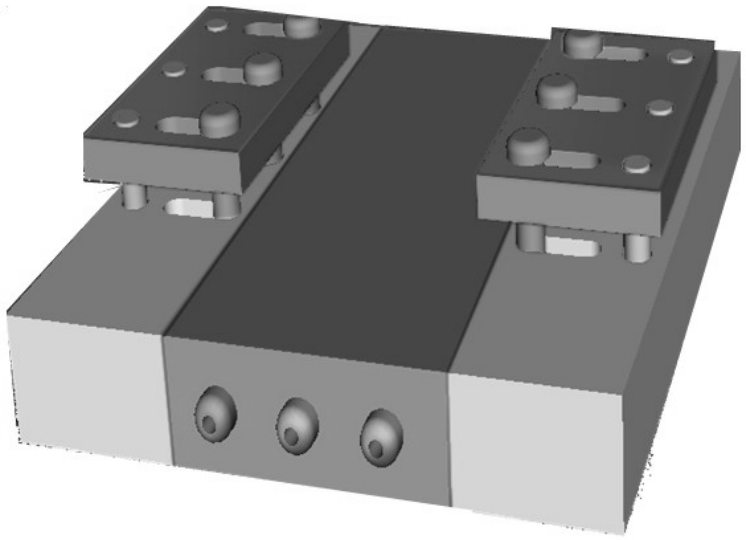

Figure 2-6 Schematic illustration of the fixture design only with water cooling.

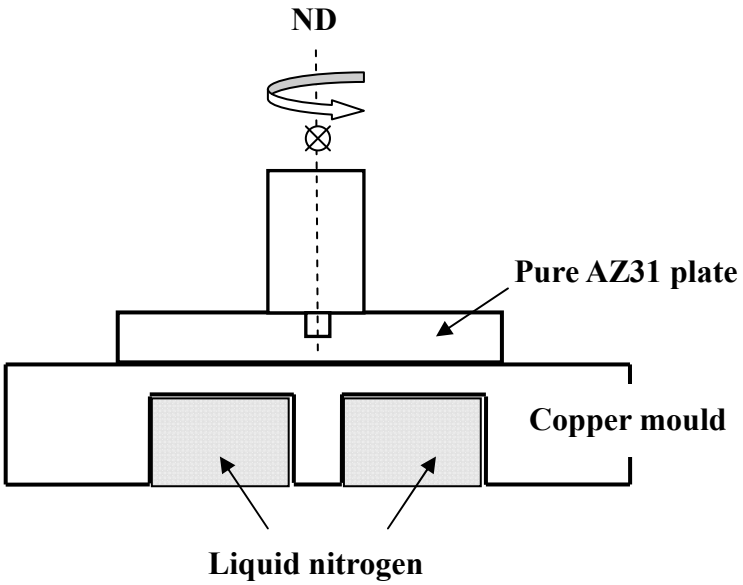

Figure 2-7 Schematic drawing of the newly designed cooling system with liquid nitrogen cooling.

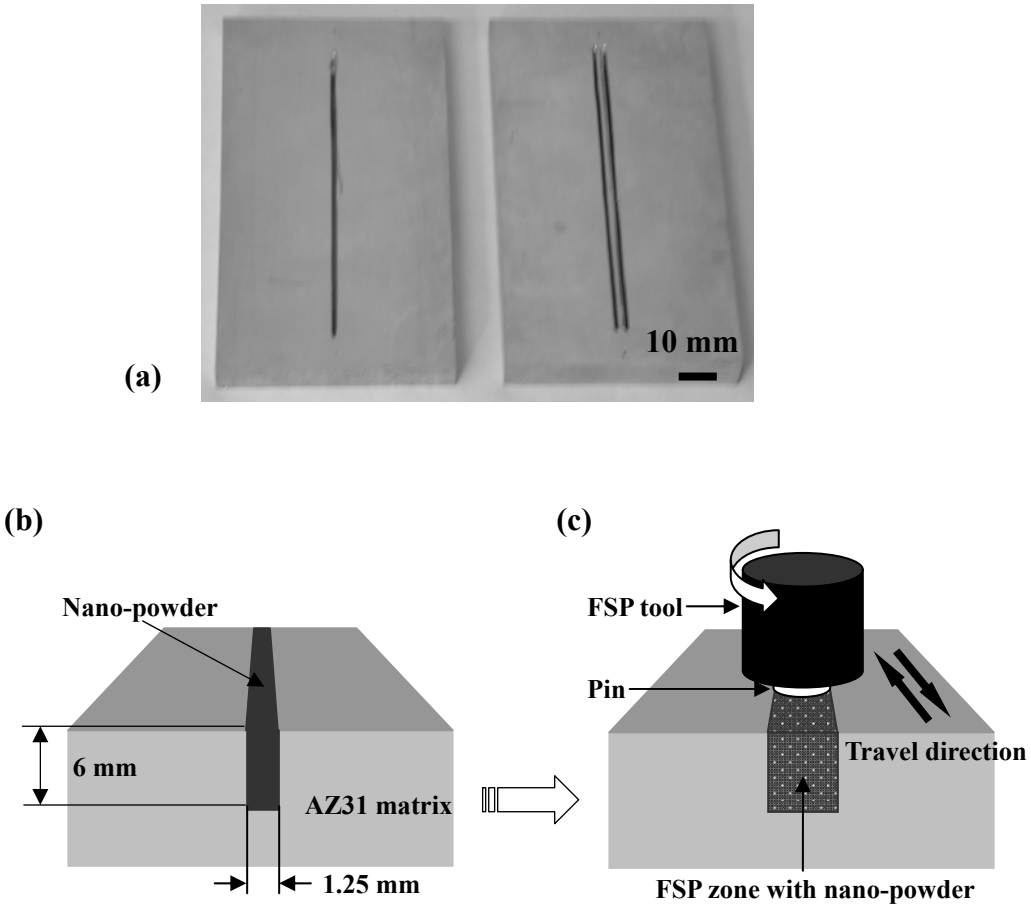

Figure 2-8 Schematic drawings of the friction stir processing in fabricating the Mg-AZ31/nano-particles composites: (a) appearance of cut deep grooves and (b) cutting groove(s) and inserting nano particles and (c) conducting multiple FSP to fabricate composites.

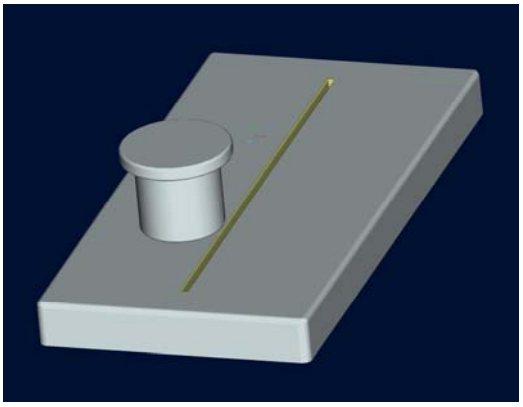

(1) To insert nano-sized ZrO_2 powders into grooves

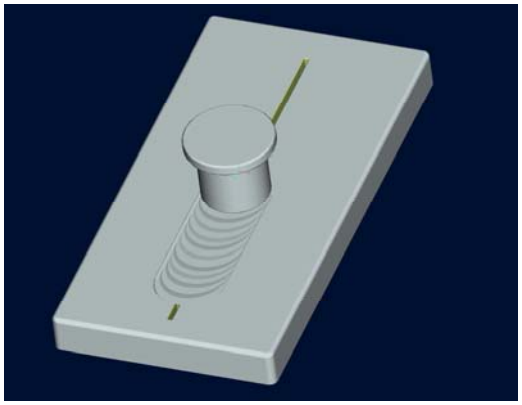

(2) To repair the surface by the tool without the fixed pin

(3) The true appearance after surface repair

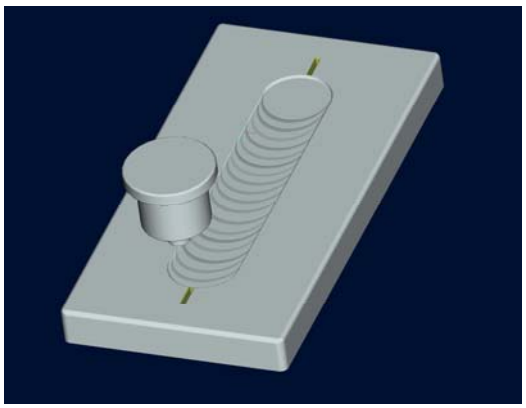

(4) Friction stir processing by tool with fixed pin

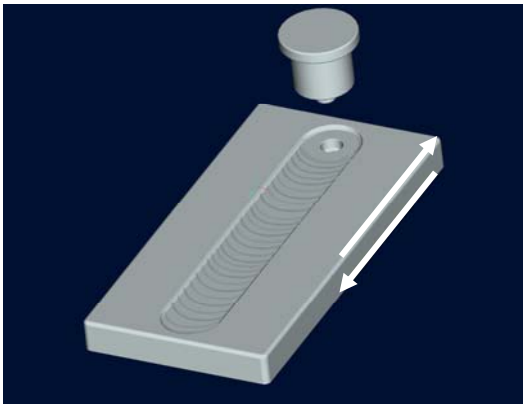

(5) Over multi-passes with opposite direction

Figure 2-9 Schematic illustration for the surface repair method for fabricating Mg base composites by FSP.

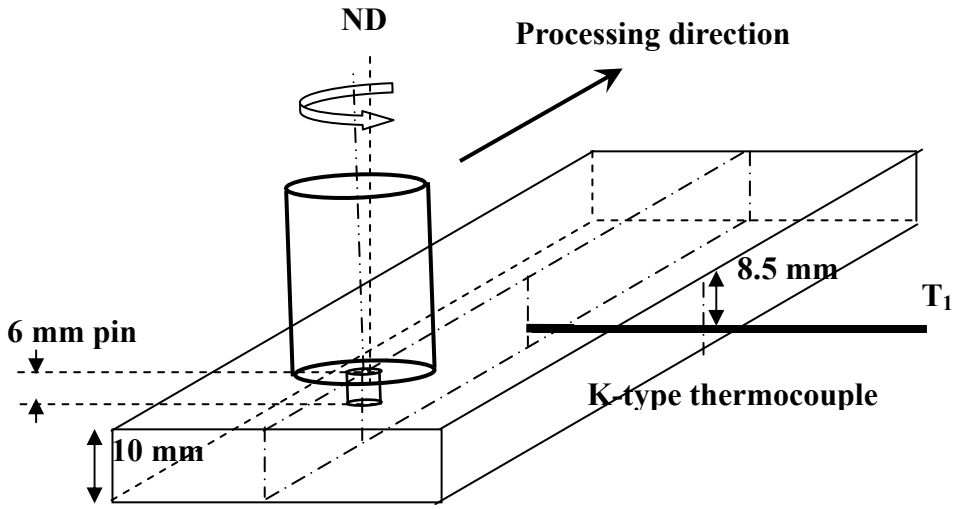

Figure 2-10 Schematic illustration of the position for the K-type thermocouple inserted in the sample.

(a)

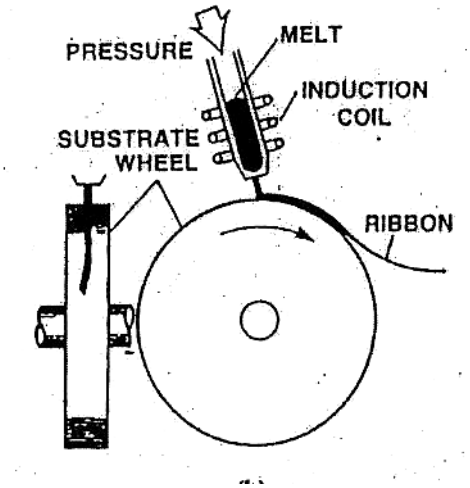

(b)

Figure 2-11 (a) Schematic diagram of the chill block melt spinning. (b) Photography of the melt spinning device.

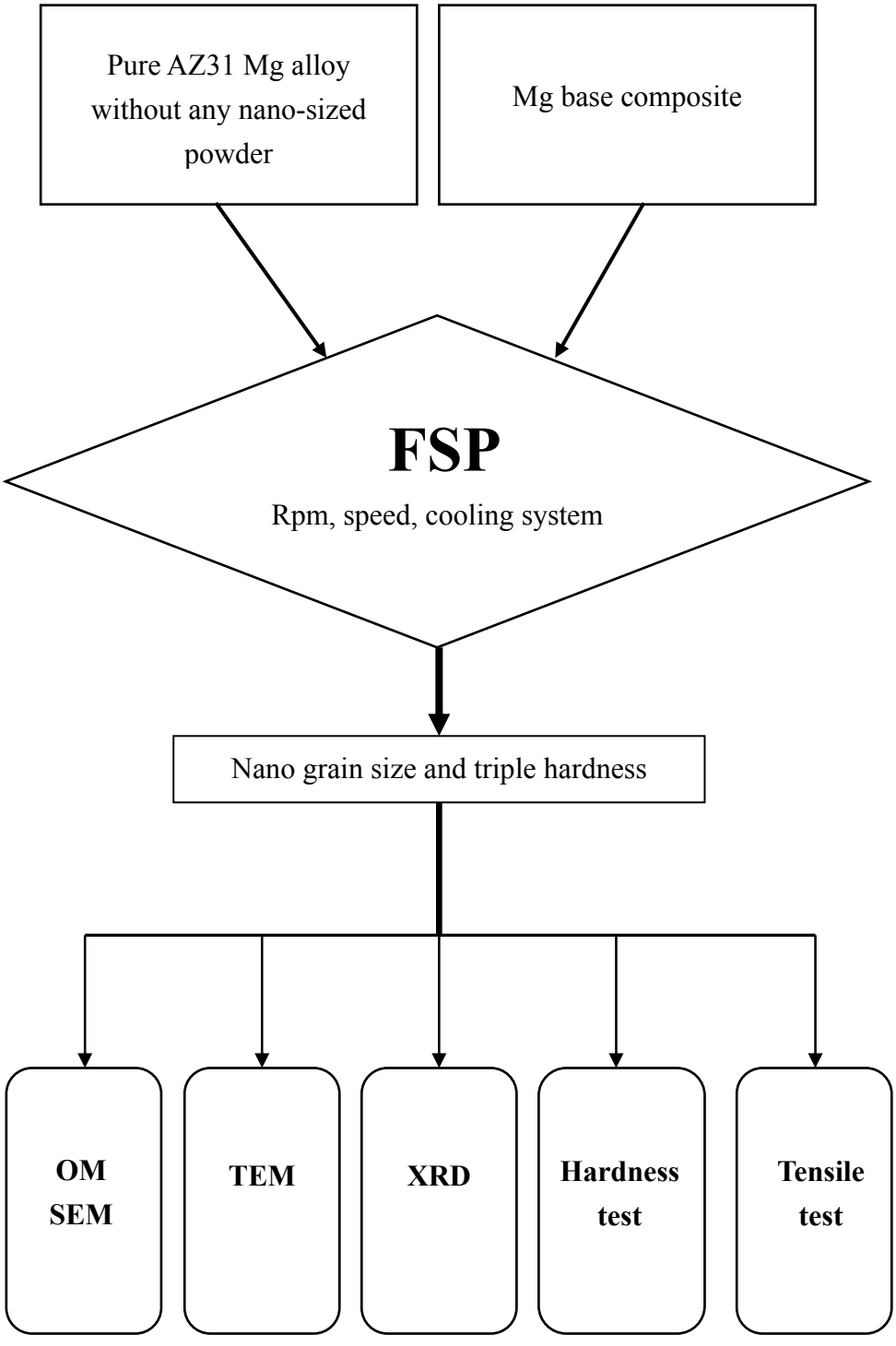

Figure 2-12 The experiment flowchart for this research.

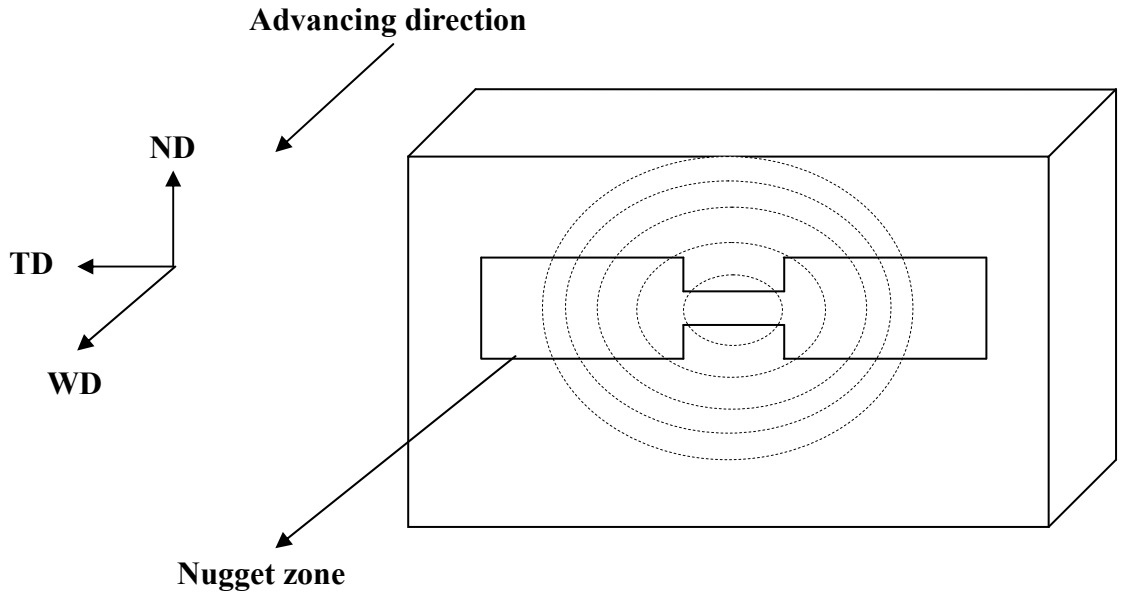

(a) Schematic illustration of the sampling for tensile sample perpendicular to the pin advancing direction.

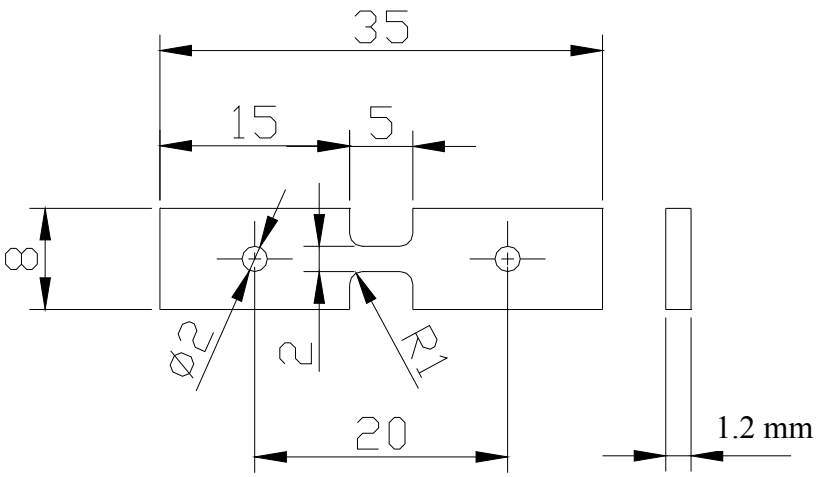

(b) The geometry and dimension of the tensile sample perpendicular to the pin advancing direction.

Figure 2-13 Schematic illustration for the sampling and dimension of the tensile sample perpendicular to the pin advancing direction.

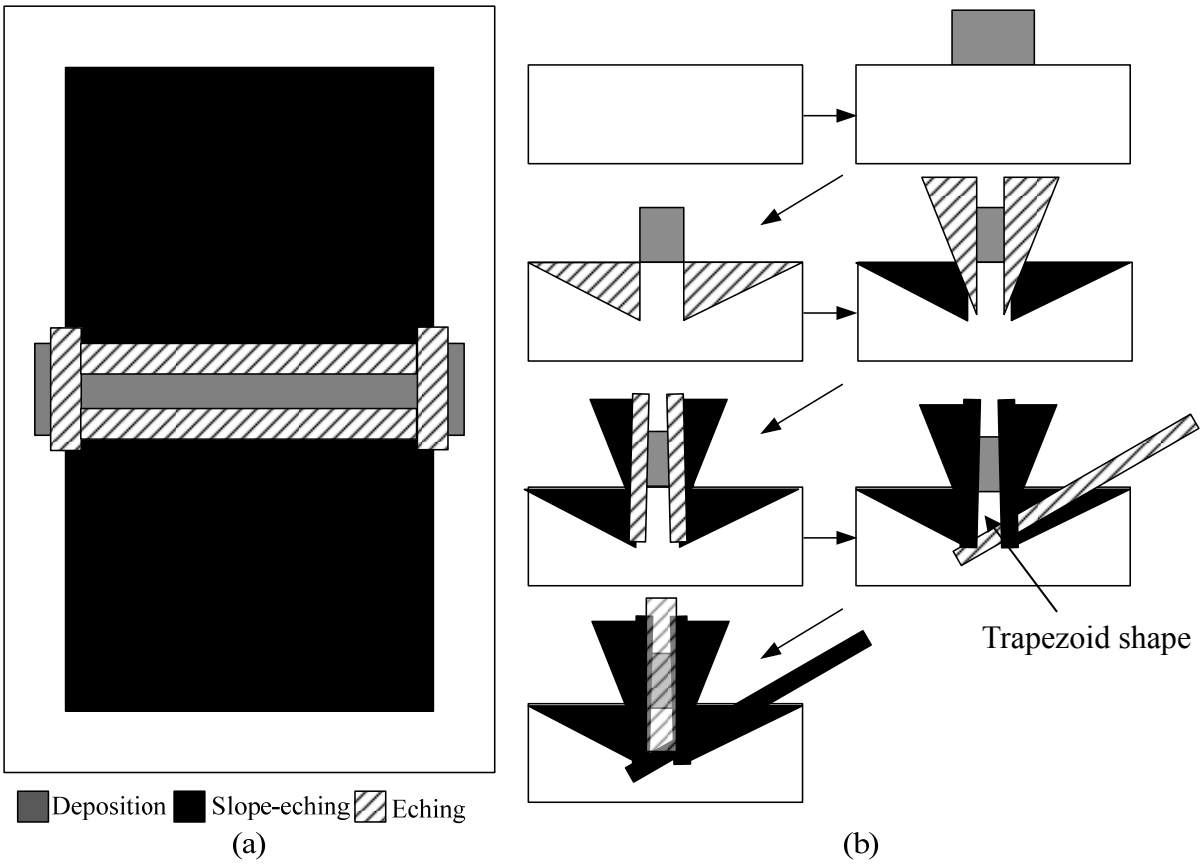

Figure 2-14 Schematic illustrations of (a) Top-view and (b) Side-view of preparation of TEM-specimen by focus ion beam (FIB).

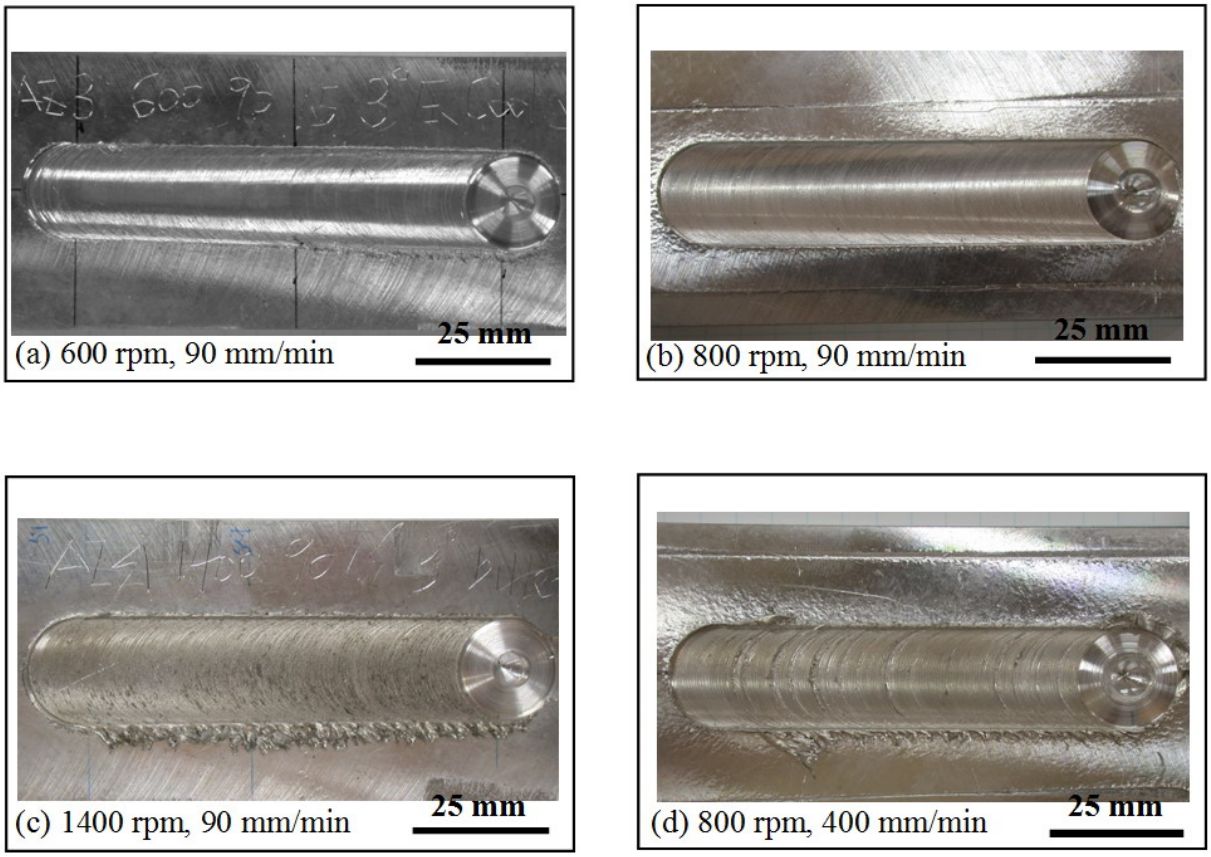

Figure 3-1 The appearances of the FSPed pure AZ31 alloys.

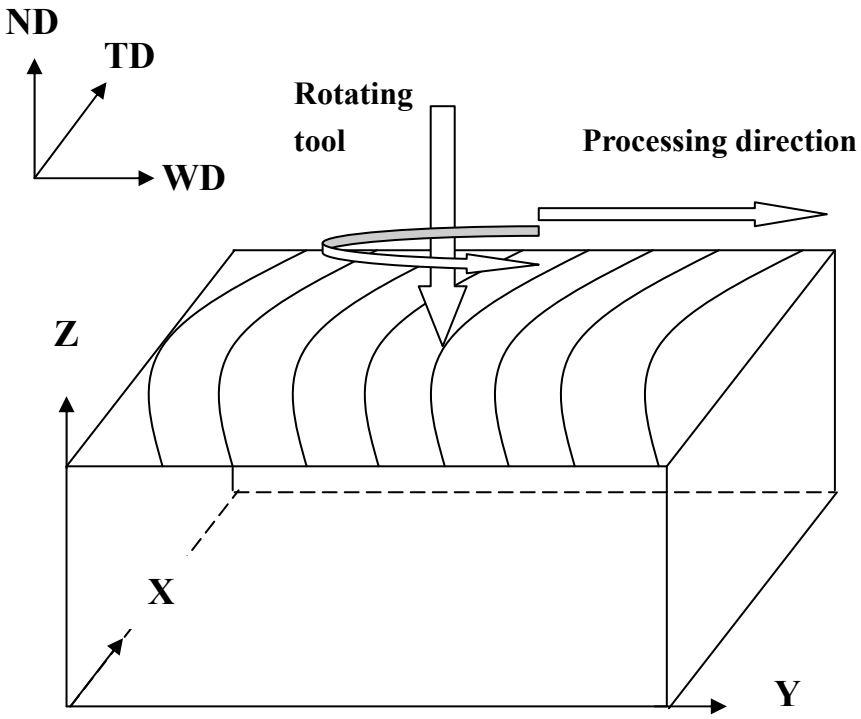

Figure 3-2 Schematic illustration for sampling positions.

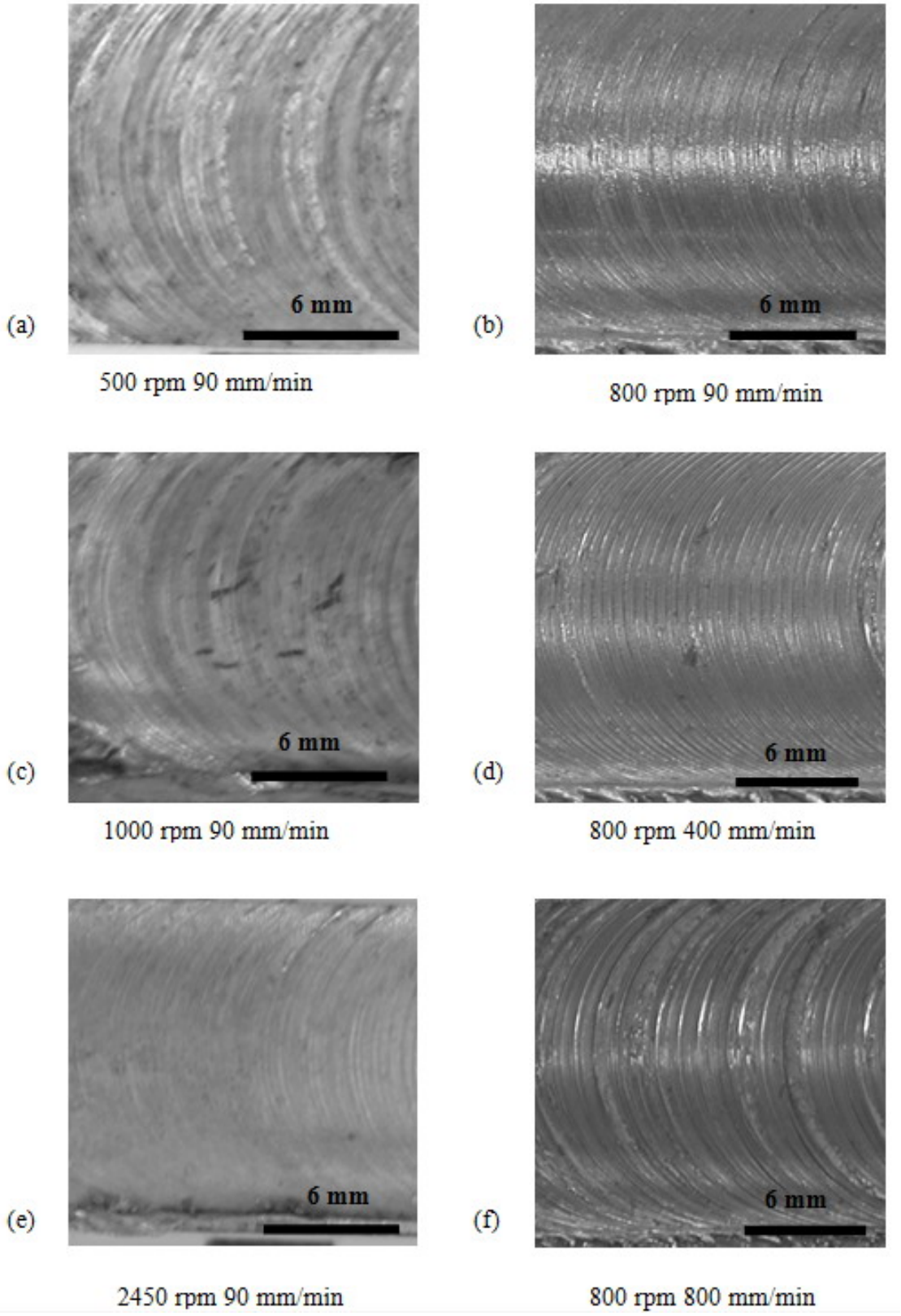

Figure 3-3 The semicircular appearances of various FSPed specimens with different processing parameters.

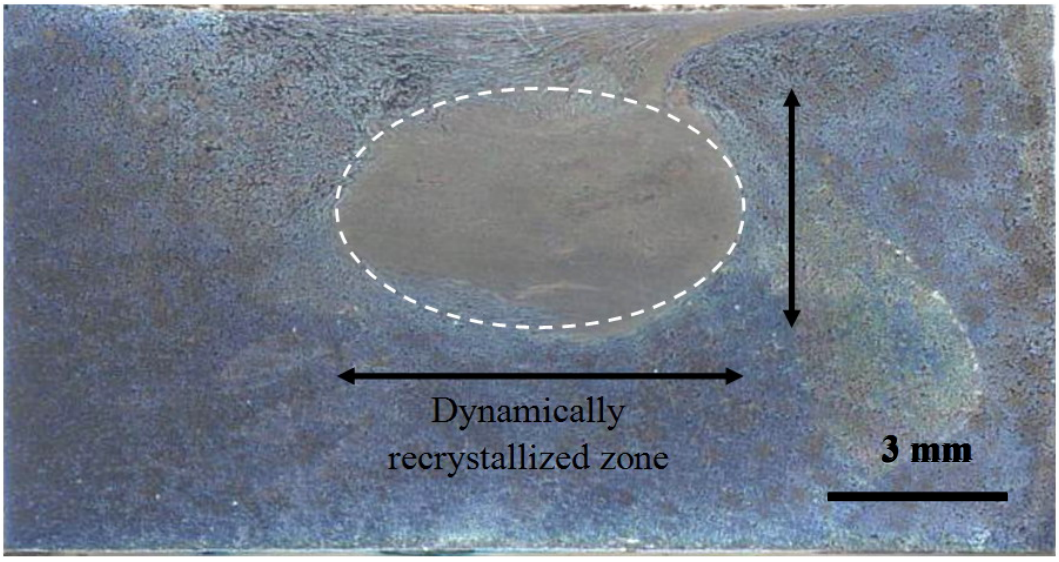

(a) Billet specimen FSPed at 1800 rpm 90 mm/min.

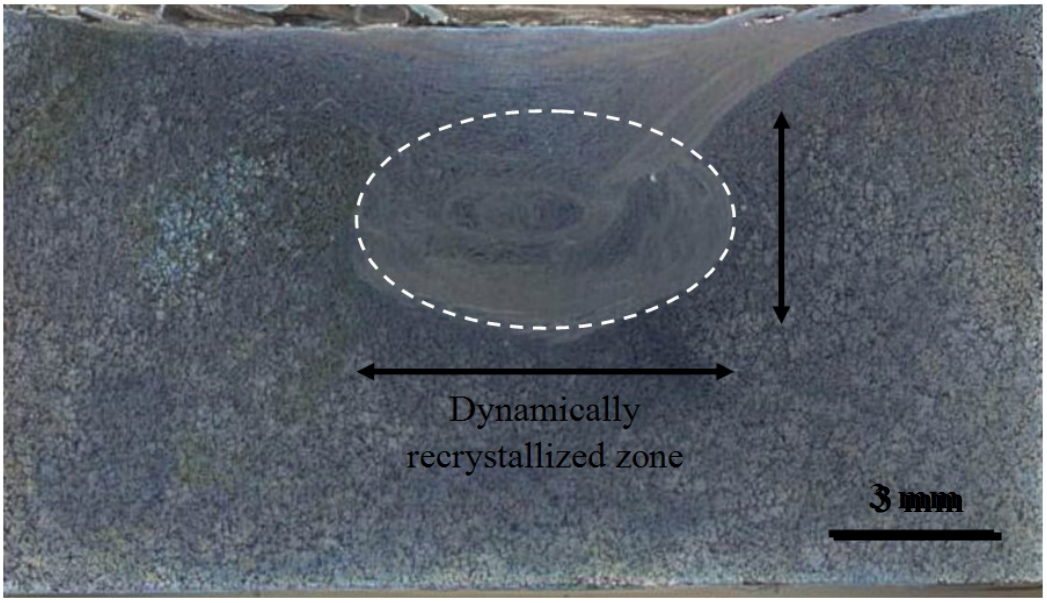

(b) Billet specimen FSPed at 800 rpm 200 mm/min.

Figure 3-4 The optical microscopy of the AZ31 alloy made by FSP: (a)-(b) cross-sectional view, (c)-(d) cross-sectional view at a higher magnification.

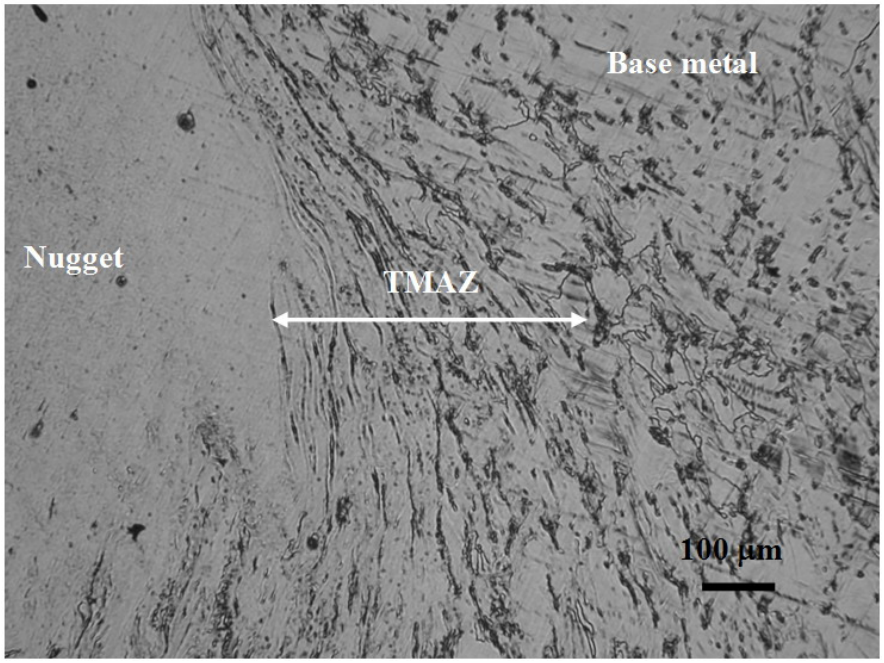

(c) Billet specimen FSPed at 1400 rpm 90 mm/min.

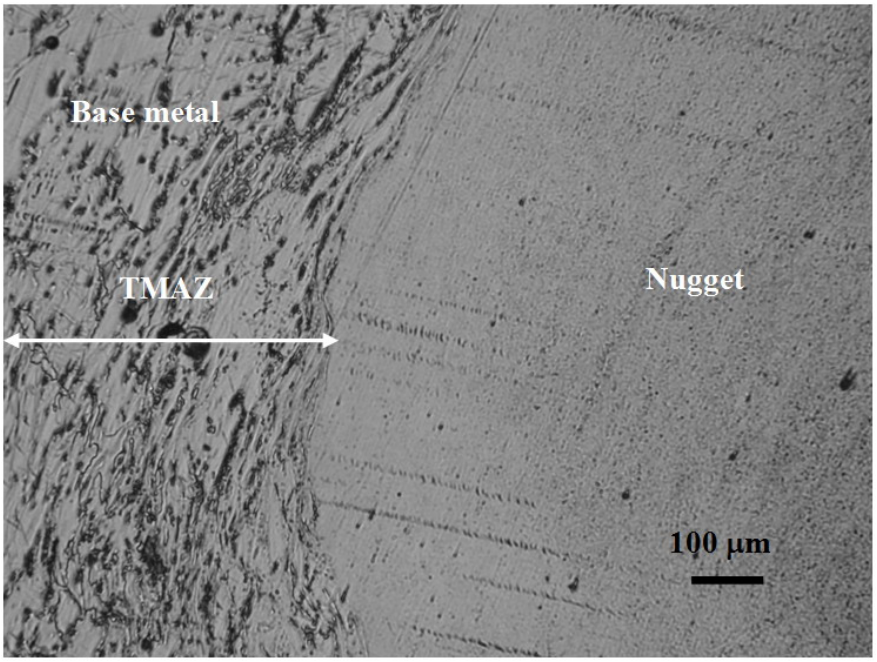

(d) Billet specimen FSPed at 1400 rpm 90 mm/min.

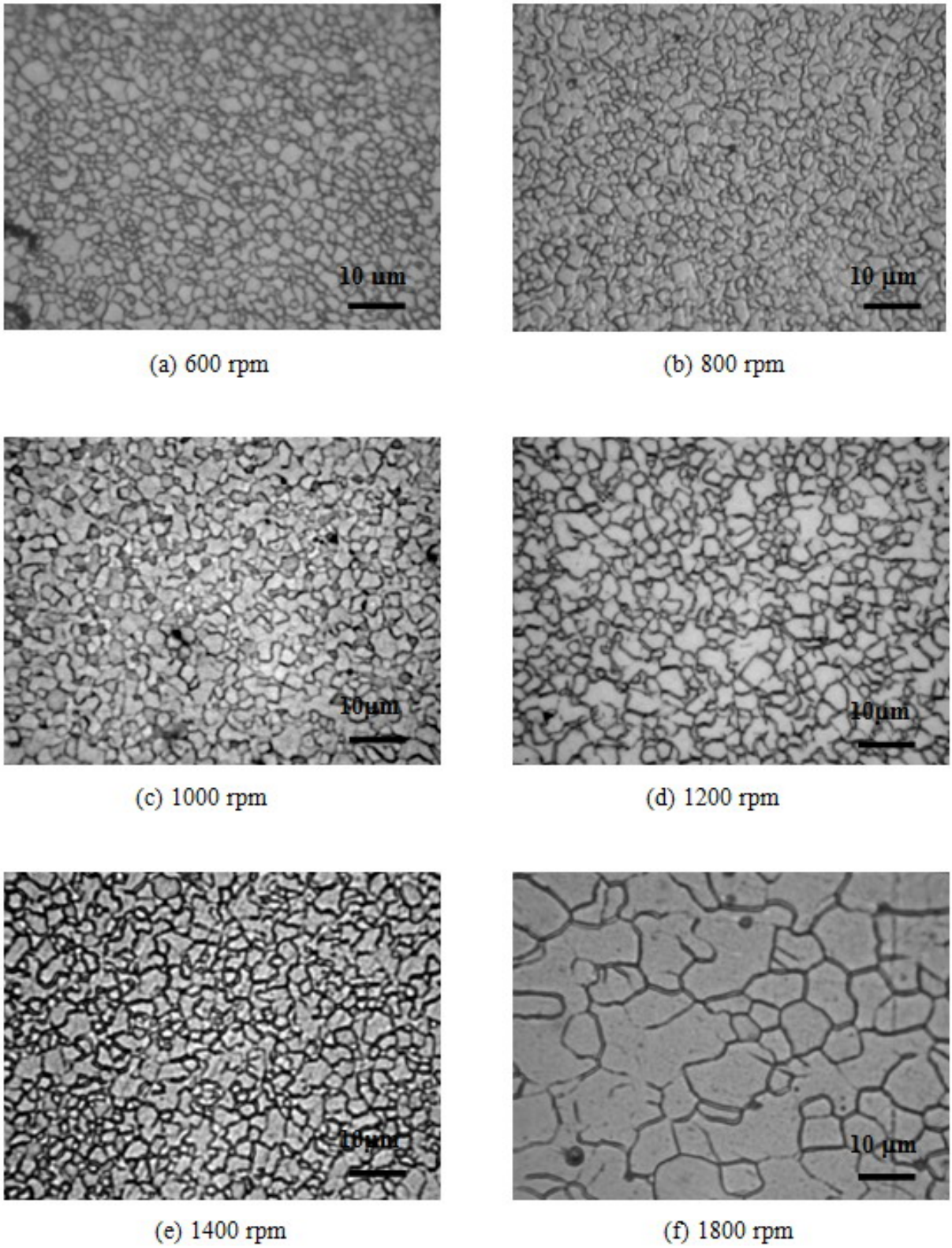

Figure 3-5 OM micrographs showing the variation of the recrystallized grain size in the nugget zone for the different rotational speeds under the same 90 mm/min advancing speed.

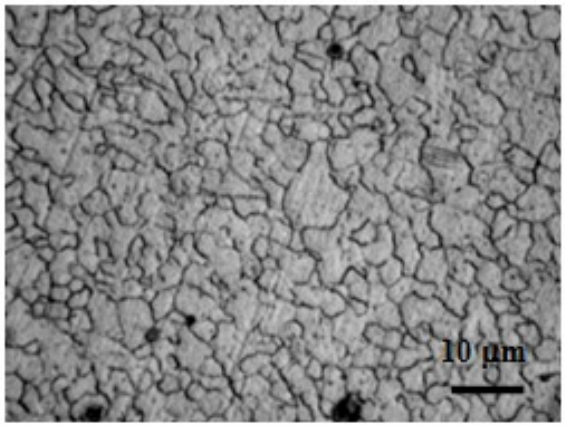

(a) 45 mm/min

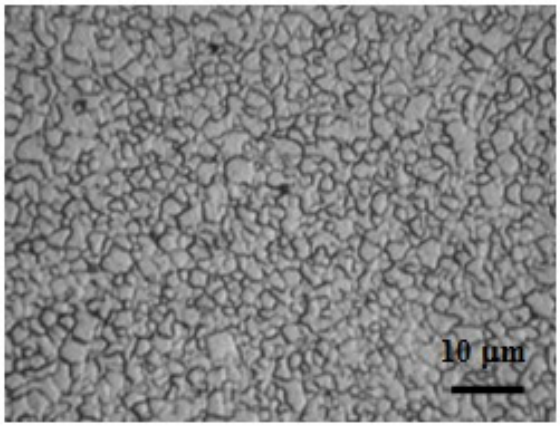

(b) 90 mm/min

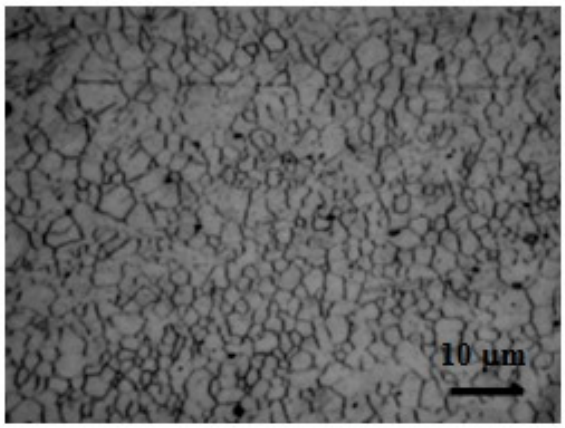

(c) 200 mm/min

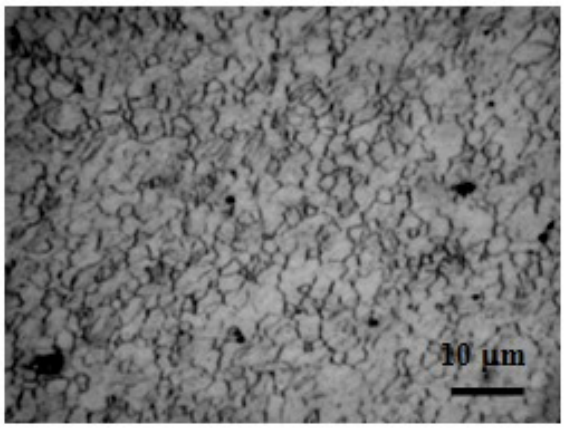

(d) 400 mm/min

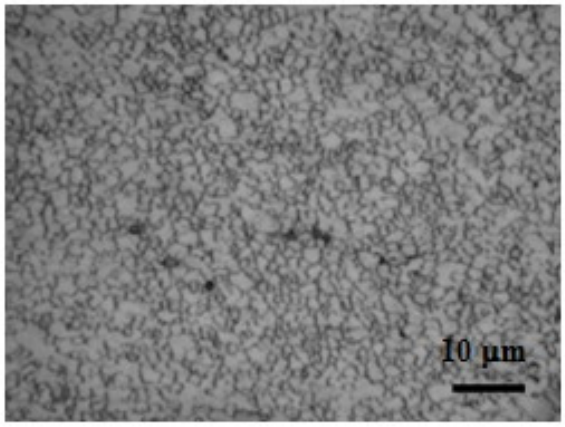

(e) 800 mm/min

Figure 3-6 OM micrographs showing the variation of the recrystallized grain size in the nugget zone for the different advancing speeds under the same 800 rpm rotational speed.

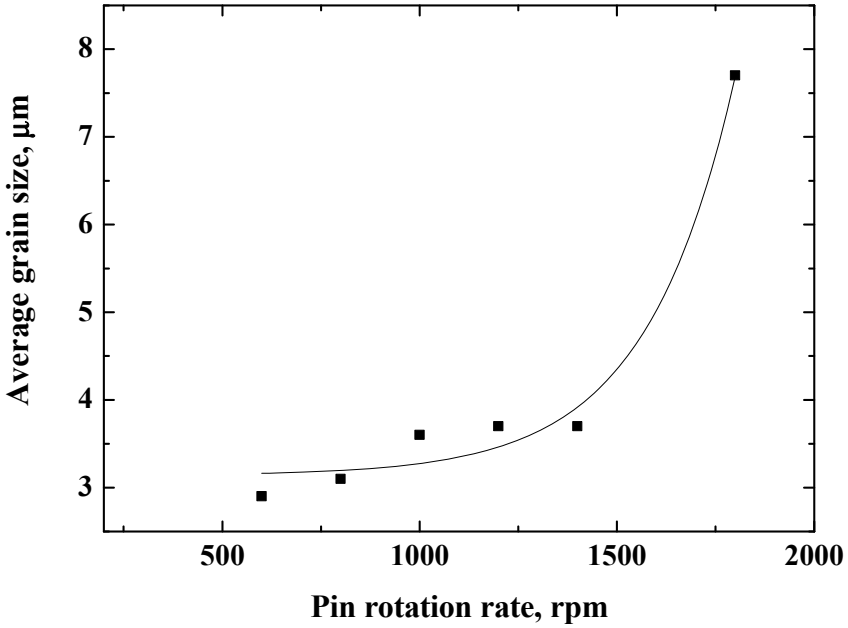

Figure 3-7 Variation of the average grain size as a function of pin rotation rate for the FSP AZ31 alloys under the same 90 mm/min advancing speed.

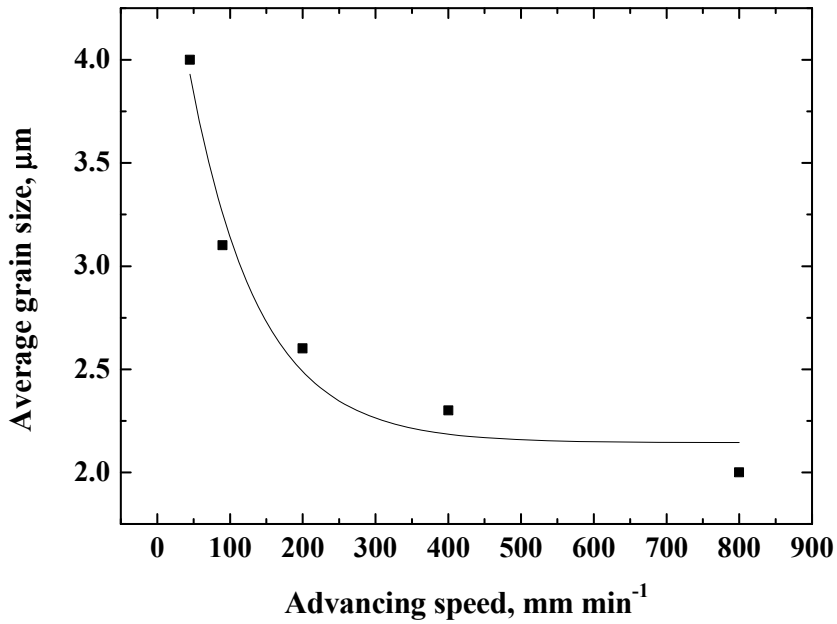

Figure 3-8 Variation of the average grain size as a function of advancing speed for the FSP AZ31 alloys under the same 800 rpm rotation rate.

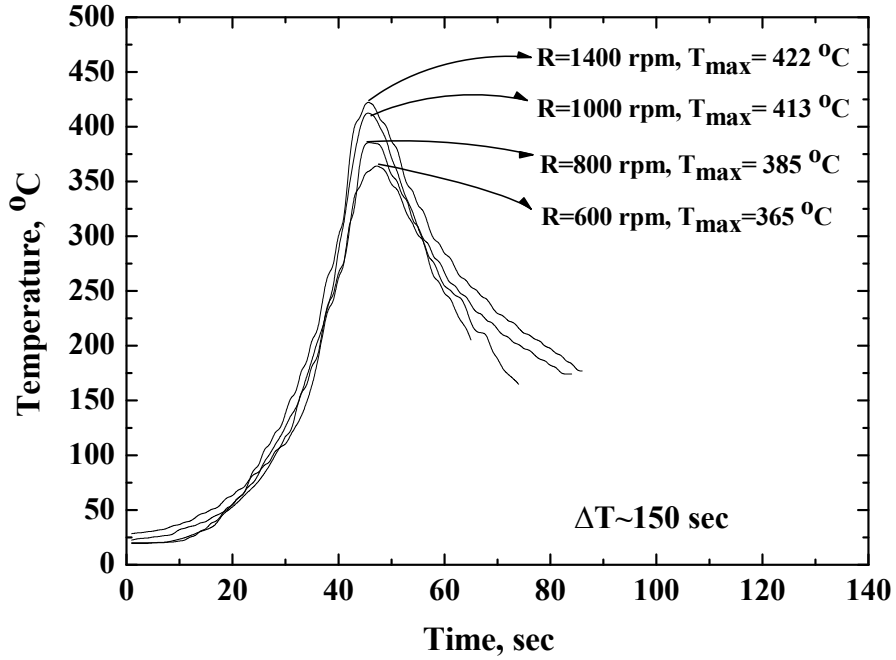

Figure 3-9 Typical temperature profiles measured by the inserted thermocouple into the pure AZ31 alloys under the same 90 mm/min advancing speed.

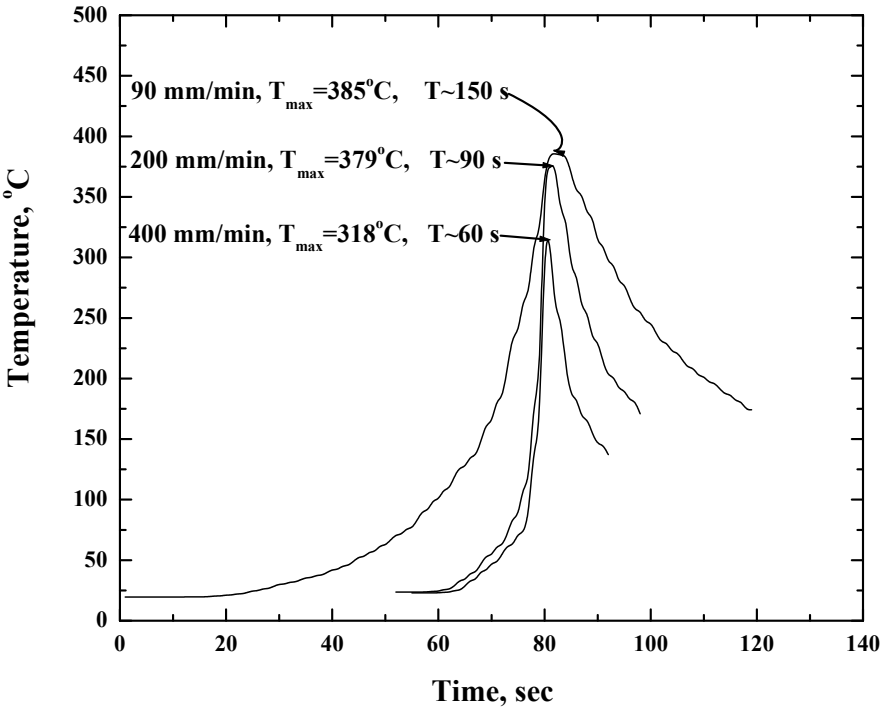

Figure 3-10 Typical temperature profiles measured by the inserted thermocouple into the pure AZ31 alloys under the same 800 rpm rotation speed.

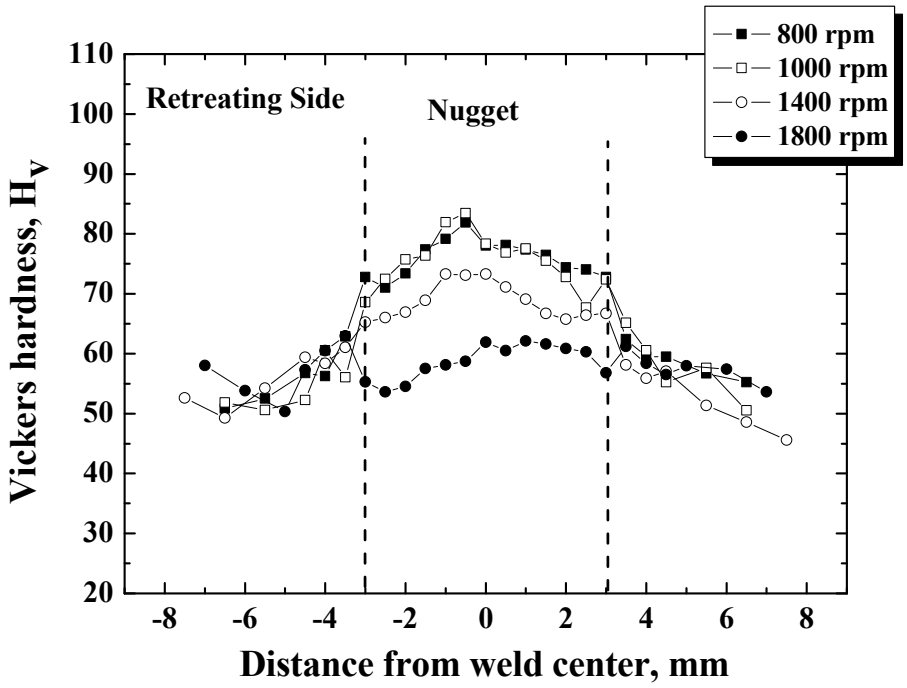

Figure 3-11 Typical microhardness variations in the central cross-sectional zones of FSP AZ31 alloys at 90 mm/min advancing speed.

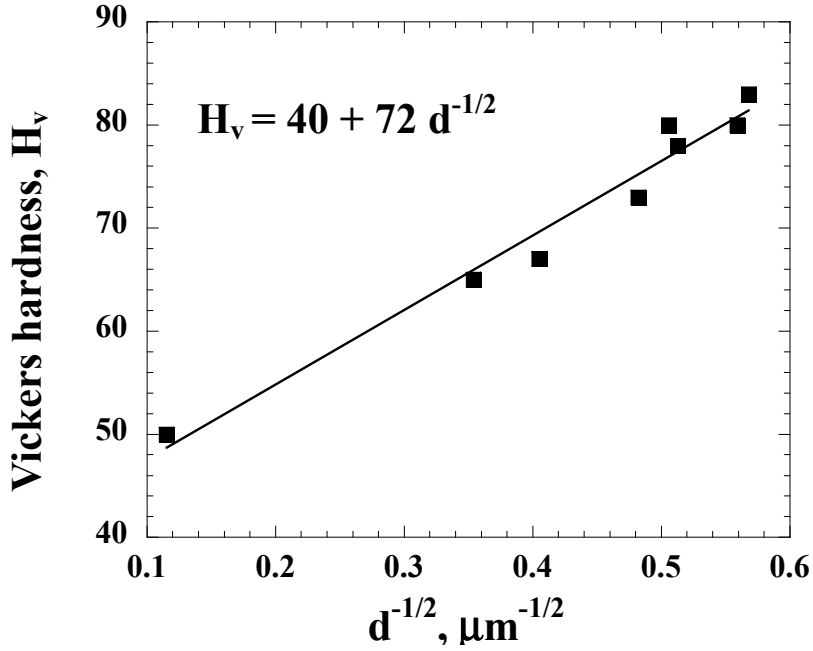

Figure 3-12 Plot for the Hall–Petch relationship for the grain size induced by FSP.

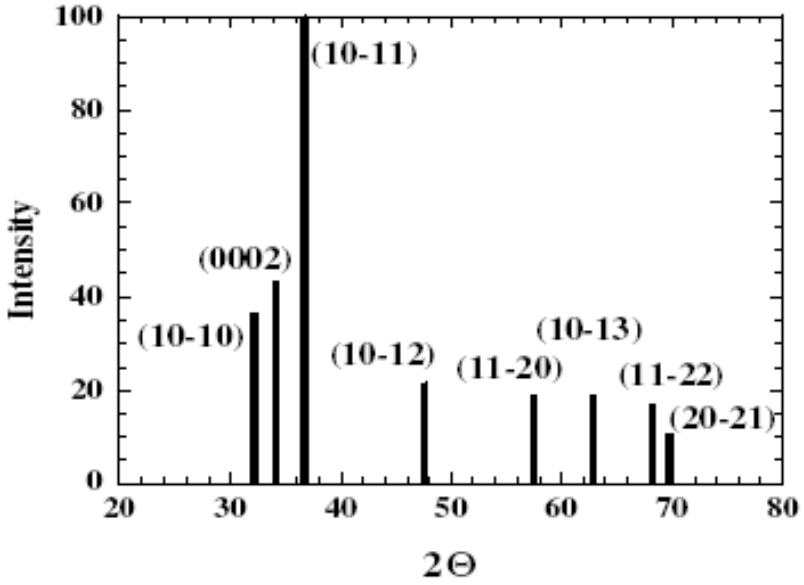

(a) Simulated X-ray diffraction for random Mg
using Cu Kα radiation

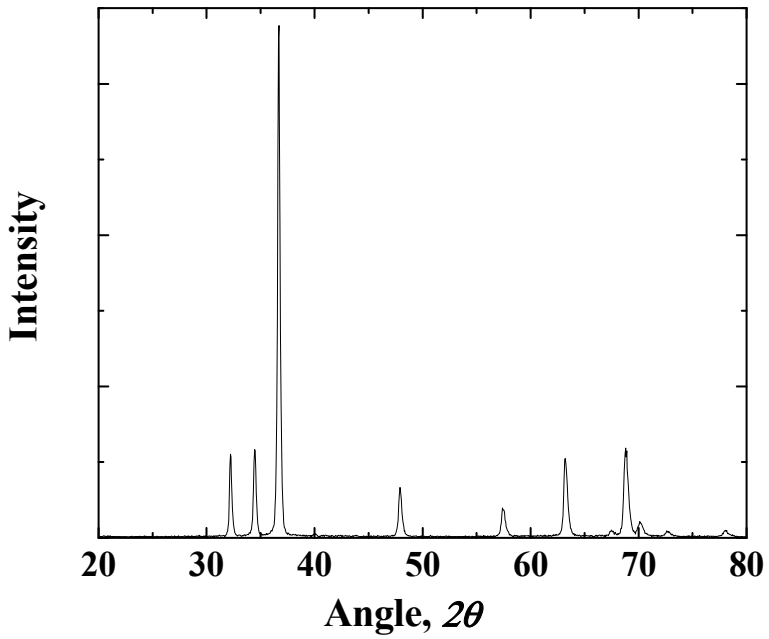

(b) X-ray diffraction for as-received AZ31 billet

Figure 3-13 X-ray diffraction for (a) random Mg, (b) as-received AZ31 billet.

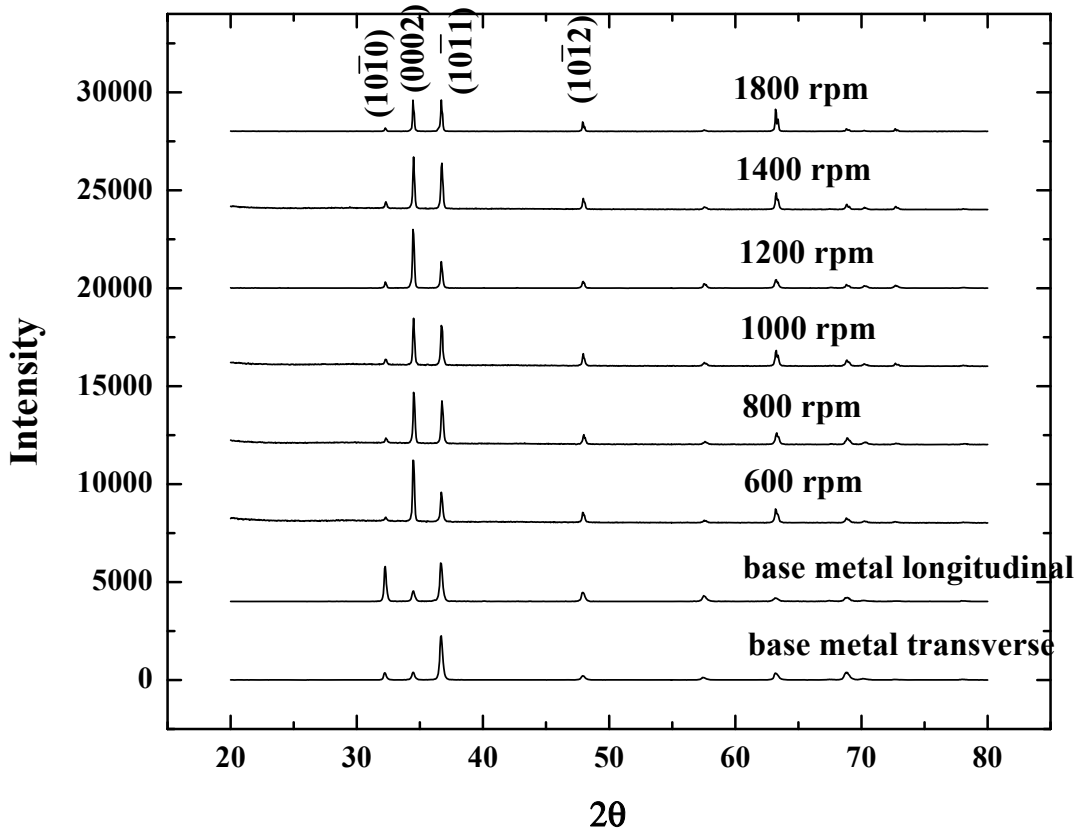

Figure 3-14 XRD patterns for modified AZ31 Mg alloys by FSP at 90 mm/min advancing speed.

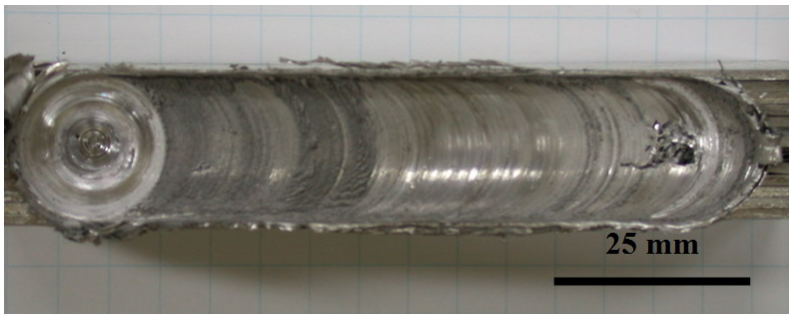

(a) $Mg_{70}Al_5Zn_{25}$ multi-element alloy FSP after 4 passes with 1500 rpm, 25 mm/min and 2^o tilt

(b) $Mg_{50}Al_5Zn_{45}$ multi-element alloy FSPed after 4 passes with 1500 rpm, 25 mm/min and 2^o tilt

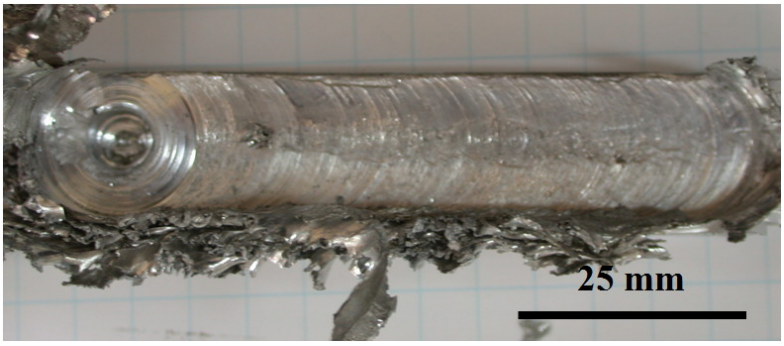

(c) $Mg_{37.5}Al_{25}Zn_{37.5}$ material FSPed after 10 passes with copper clamping kits and water cooled

Figure 3-15 The appearance of the FSPed specimens and nugget zone of intermetallic alloys.

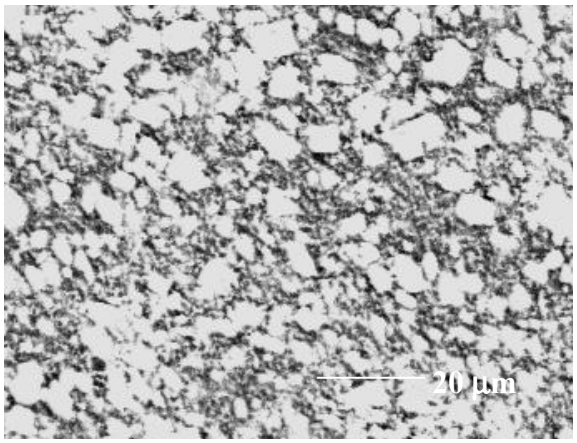

Fig. 3-16 SEM/BEI micrograph showing the phase dispersion in $Mg_{70}Al_5Zn_{25}$ after three passes with air cooling.

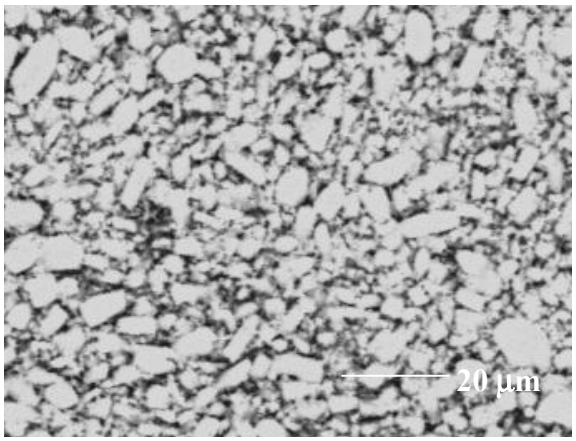

Fig. 3-17 SEM/BEI micrograph showing the phase dispersion in $Mg_{50}Al_5Zn_{45}$ after three passes with air cooling.

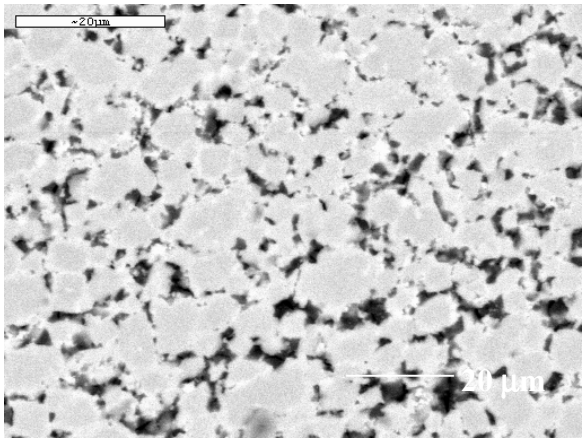

Fig. 3-18 SEM/BEI micrograph showing the phase dispersion in $Mg_{37.5}Al_{25}Zn_{37.5}$ after three passes with air cooling.

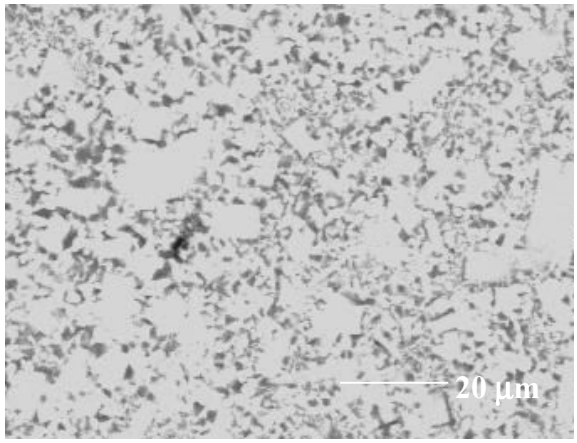

Fig. 3-19 SEM/BEI micrograph showing the phase dispersion in $Mg_{37.5}Al_{25}Zn_{37.5}$ after three passes with water cooling.

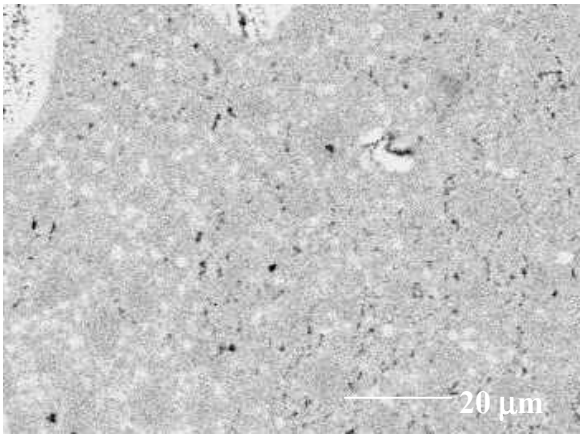

Fig. 3-20 SEM/BEI micrograph showing the phase dispersion in $Mg_{37.5}Al_{25}Zn_{37.5}$ after ten passes with water cooling.

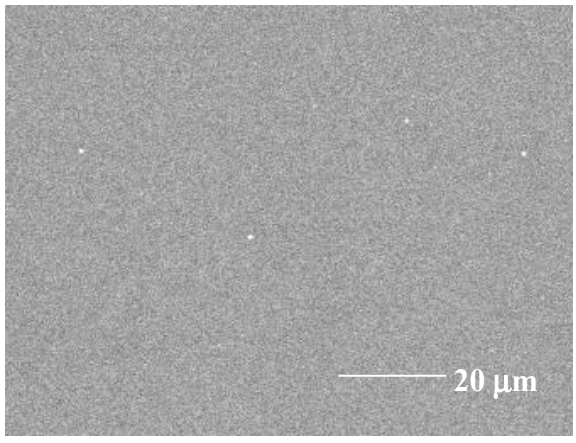

Fig. 3-21 SEM/BEI micrograph showing the complete amorphous phase in $Mg_{70}Al_5Zn_{25}$ fabricated by melt spinning.

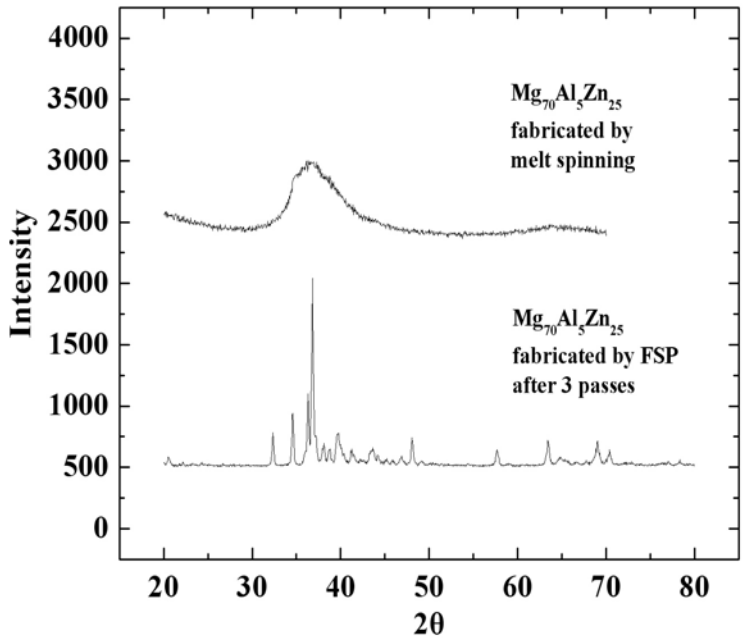

Figure 3-22 The XRD patterns for the $Mg_{70}Al_5Zn_{25}$ system fabricated by FSP and melt spinning.

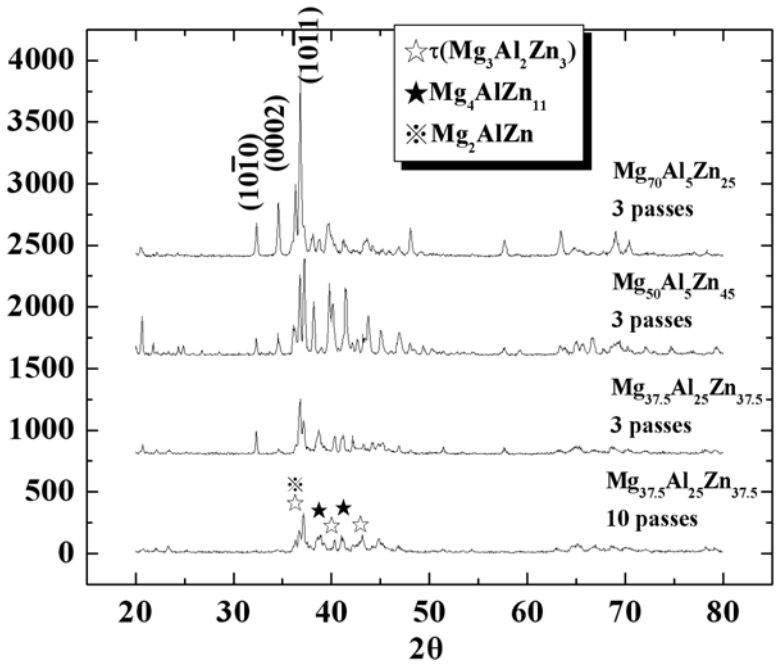

Figure 3-23 XRD patterns for $Mg_{70}Al_5Zn_{25}$, $Mg_{50}Al_5Zn_{45}$ and $Mg_{37.5}Al_{25}Zn_{37.5}$ after 3 or 10 passes.

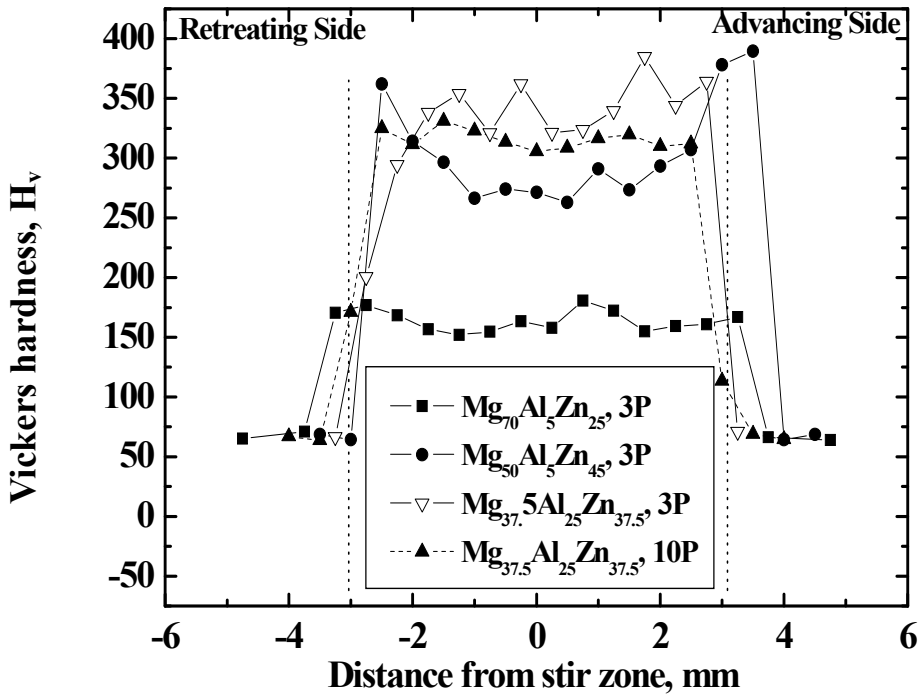

Figure 3-24 The variation of H_v along the transverse cross-sectional plane of the $Mg_{70}Al_5Zn_{25}$, $Mg_{50}Al_5Zn_{45}$ and $Mg_{37.5}Al_{25}Zn_{37.5}$ alloys after 3 or FSP 10 passes.

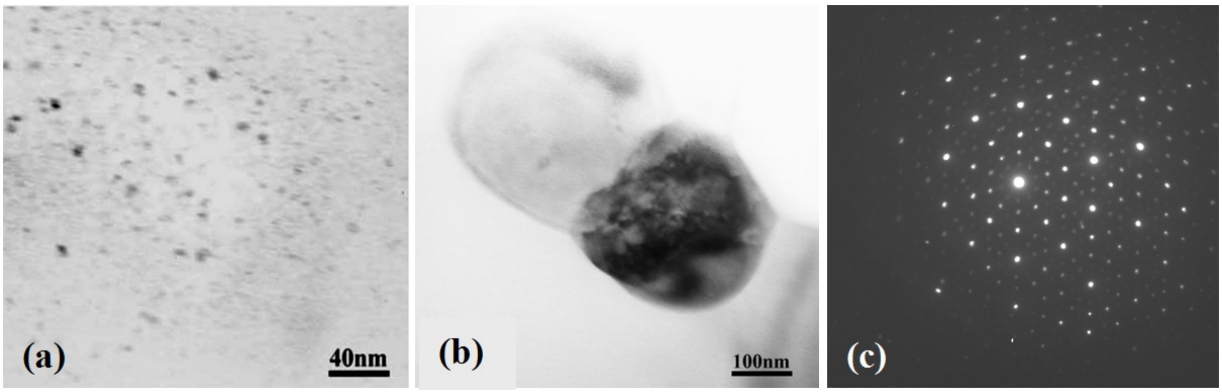

Figure 3-25 TEM micrographs showing (a) the nano-sized $Mg_3Al_2Zn_3$ τ phase in FSP $Mg_{50}Al_{20}Zn_{30}$ and (b) the icosahedral τ phase and (c) its diffraction pattern observed in FSP $Mg_{37.5}Al_{25}Zn_{37.5}$.

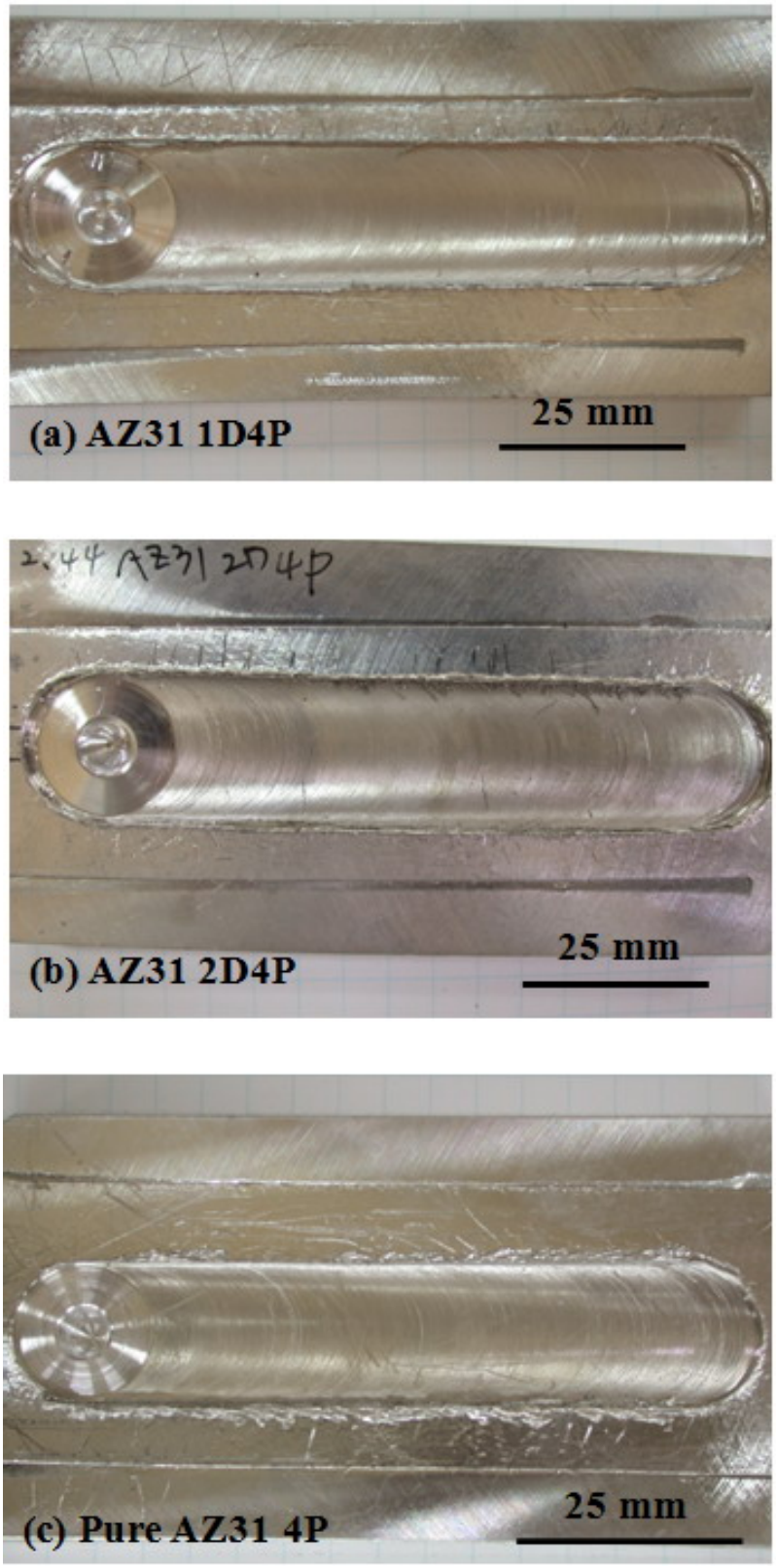

Figure 3-26 The appearances of the FSPed specimens under the 800 rpm rotational speed and 45 mm/min advancing speed.

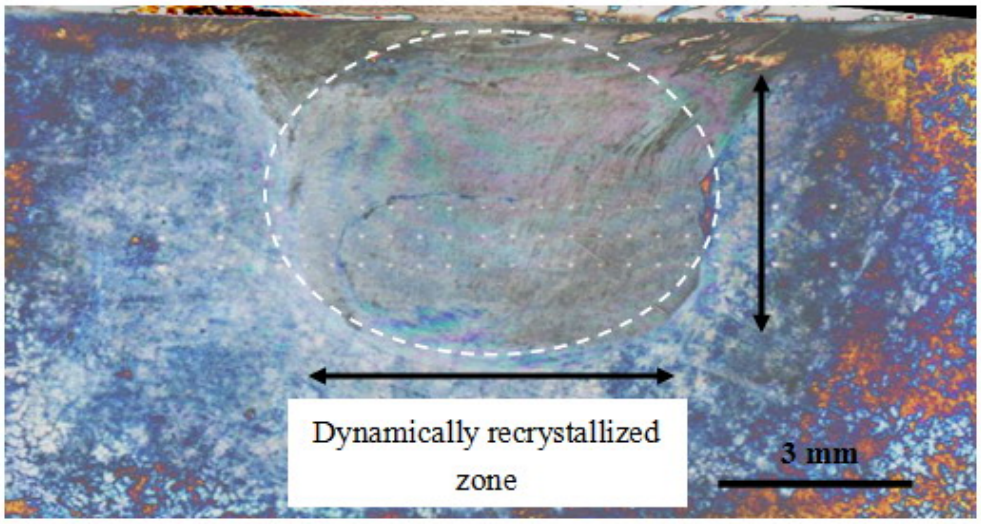

(a)

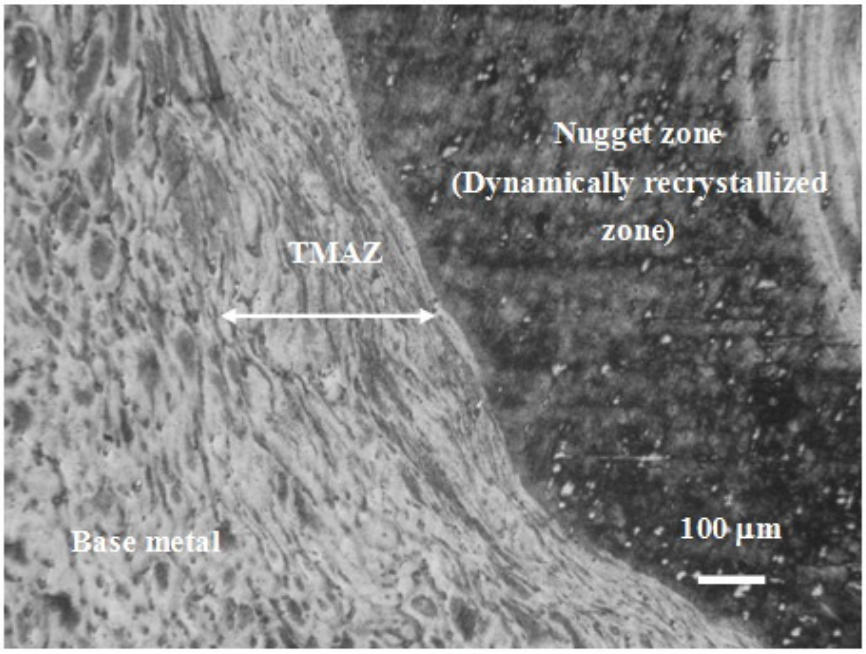

(b)

Figure 3-27 The OM micrographs of the 1D4P ZrO_2 composite sample made by FSP: (a) cross-sectional view, (b) cross-sectional view at a higher magnification.

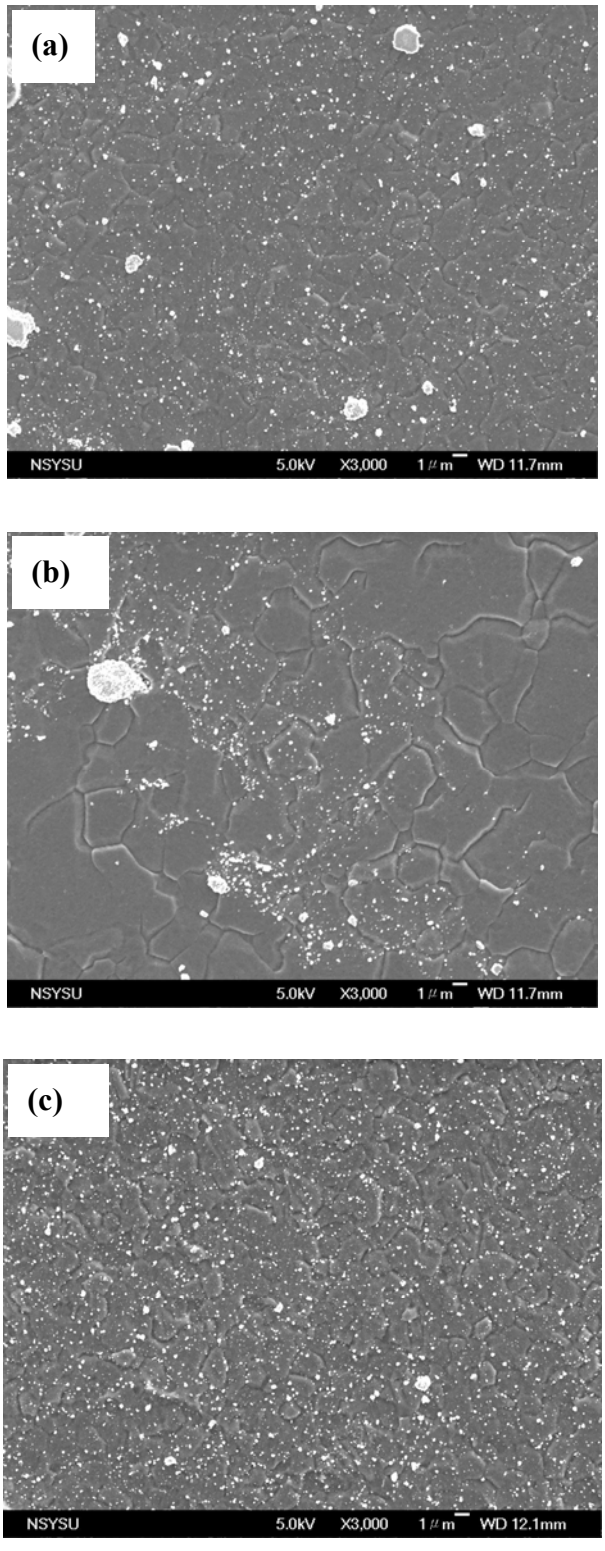

Figure 3-28 SEM/SEI images of the AZ31/10vol%ZrO_2 FSP composite showing (a) relatively homogeneous dispersion, (b) local inhomogenization of the nano-particle clusters within the stirred zone after one-pass FSP, and (c) the improvement of clustered ZrO_2 particles after four passes FSP.

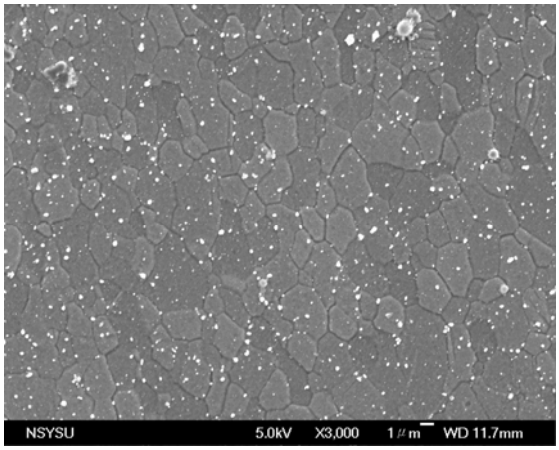

(a)

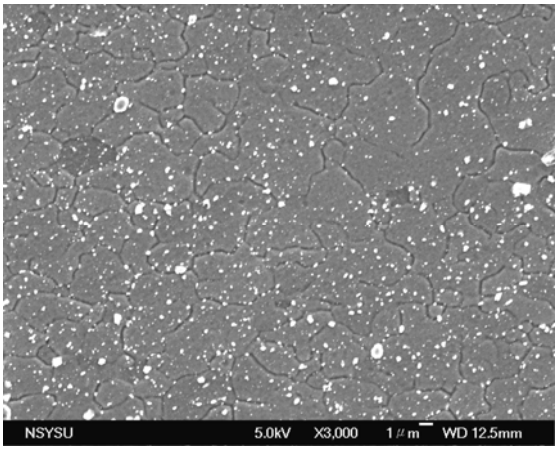

(b)

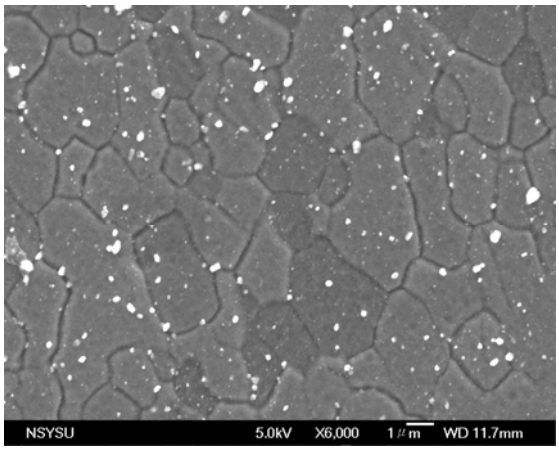

(c)

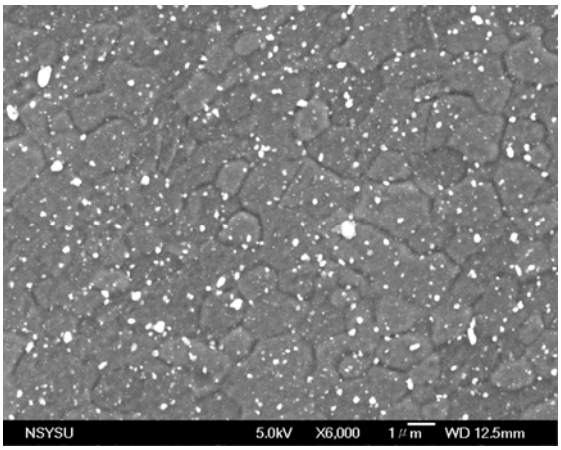

(d)

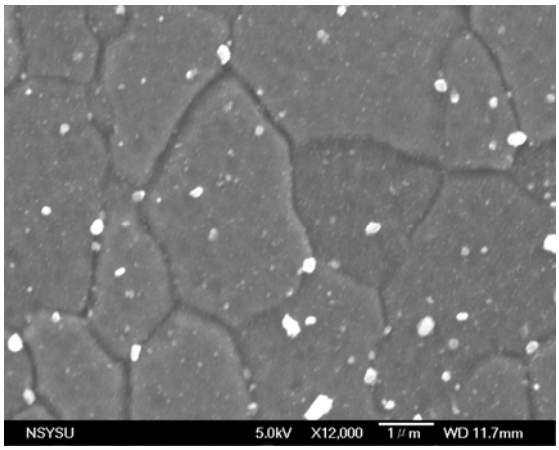

(e)

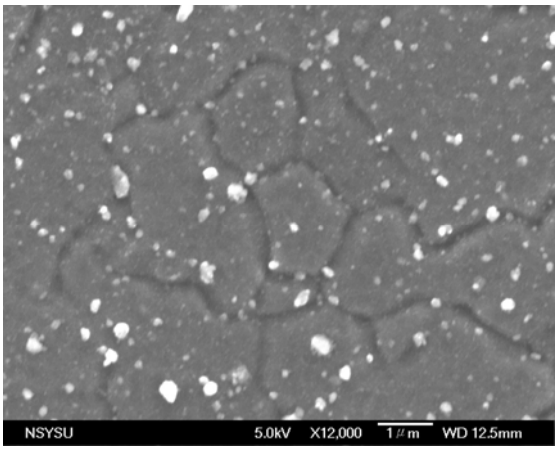

(f)

Figure 3-29 SEM/SEI images at different magnifications of the SiO_2 composite specimens with different volume fractions. (a), (c) and (e) 1G4P (~5 vol%), (b), (d) and (f) 2G4P (~10 vol%).

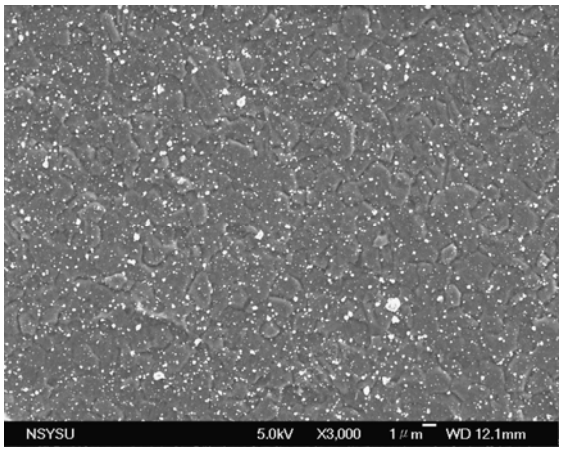

(a)

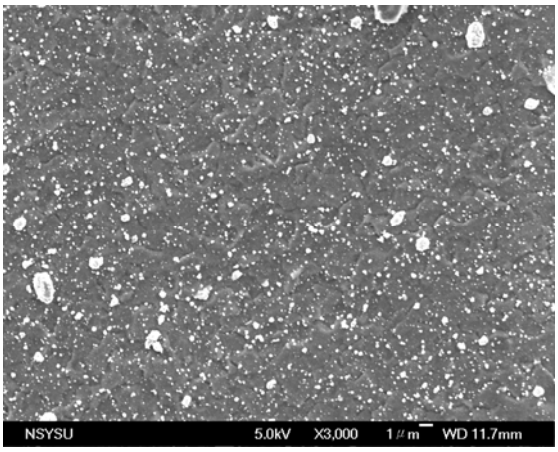

(b)

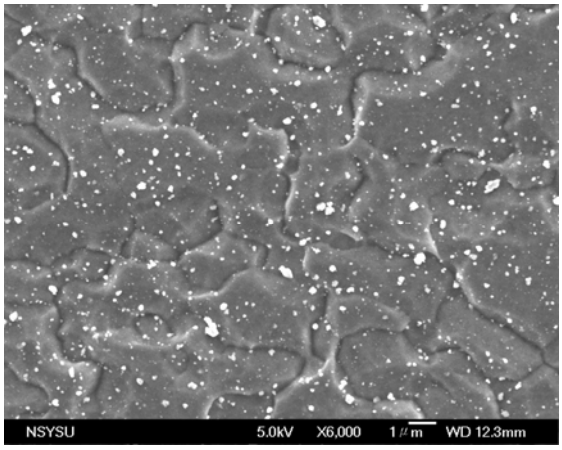

(c)

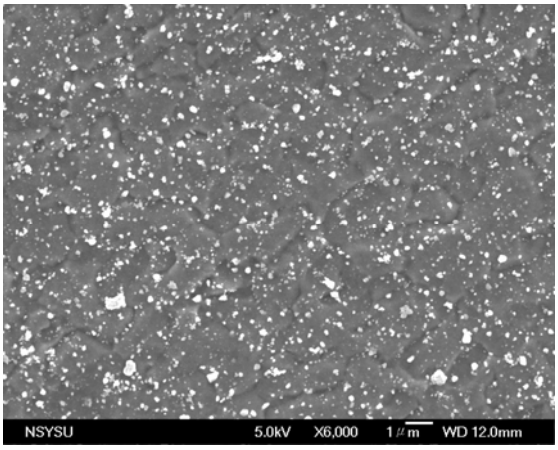

(d)

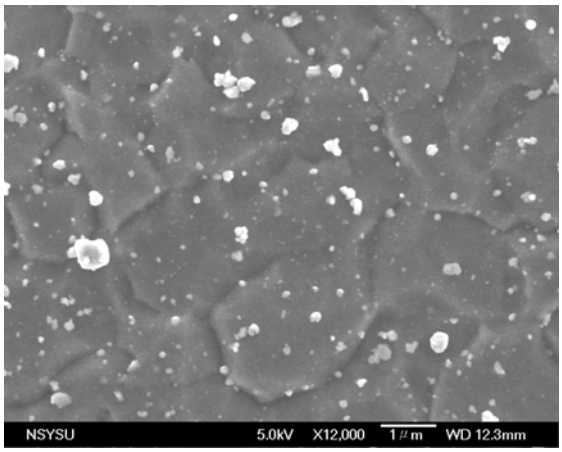

(e)

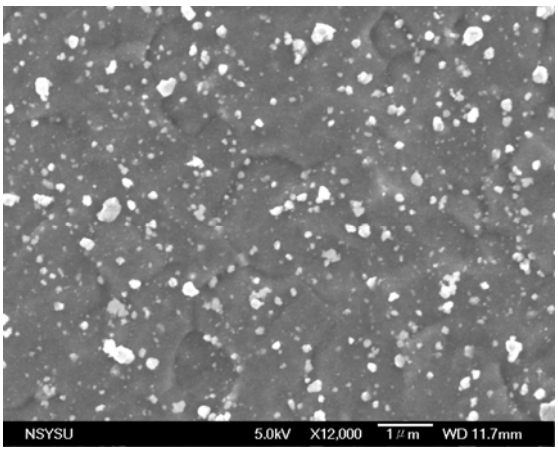

(f)

Figure 3-30 SEM/SEI images at different magnifications of the ZrO_2 composite specimens with different volume fractions. (a), (c) and (e) 1G4P (~10 vol%), (b), (d) and (f) 2G4P (~20 vol%).

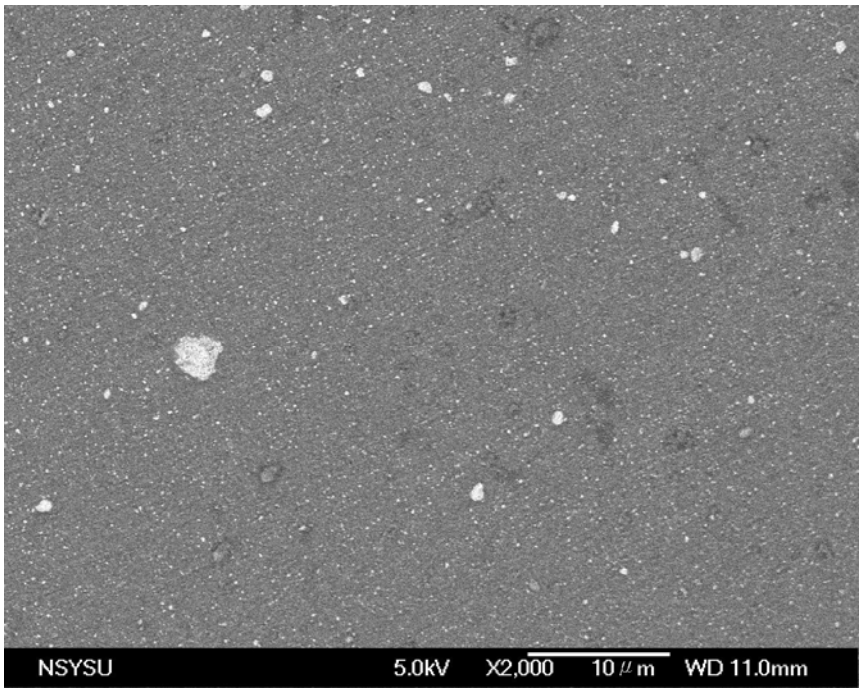

(a)

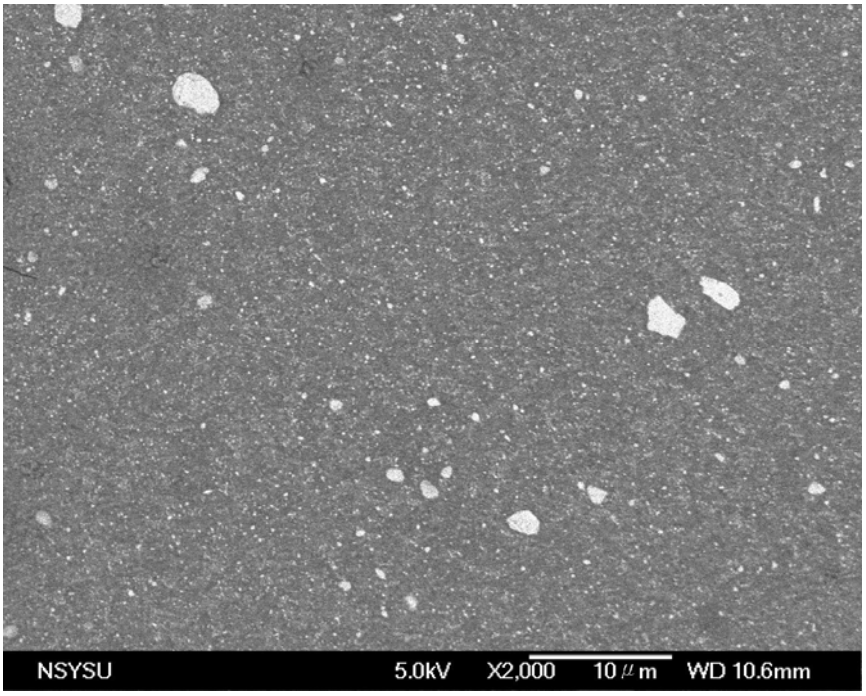

(b)

Figure 3-31 SEM/BEI images of ZrO_2 composite specimens with different volume fractions. (a) 1G4P (~10 vol%), (b) 2G4P (~20 vol%).

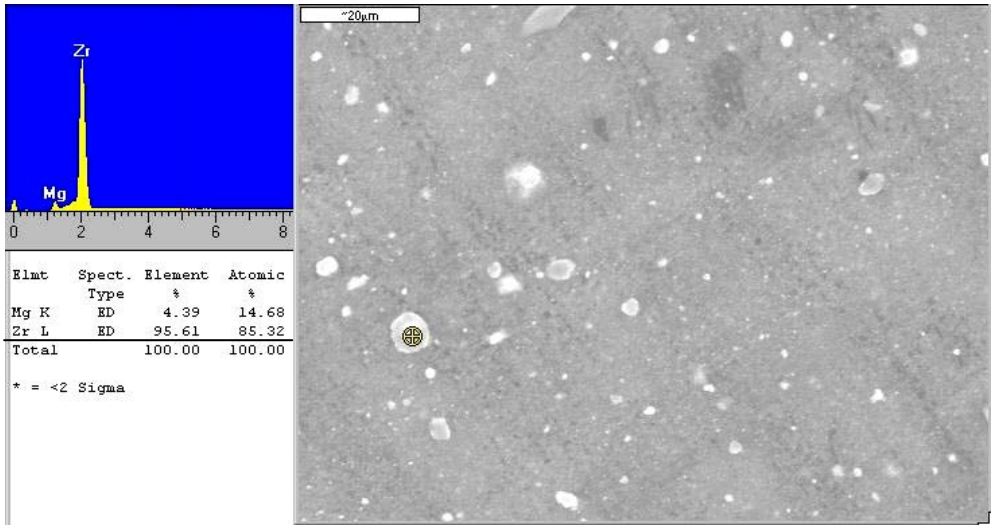

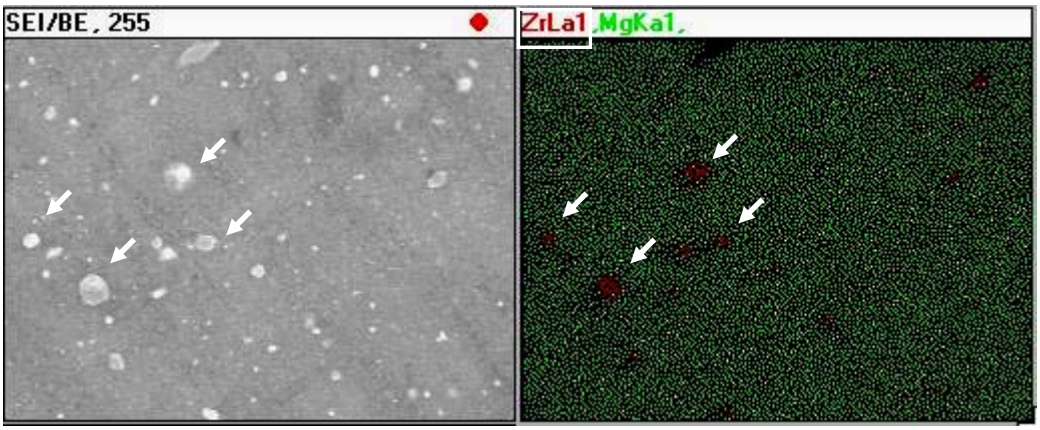

Figure 3-32 The SEM/EDS analysis of ZrO_2 2G4P (~20 vol%) composite specimens showing the clustered ZrO_2 particles.

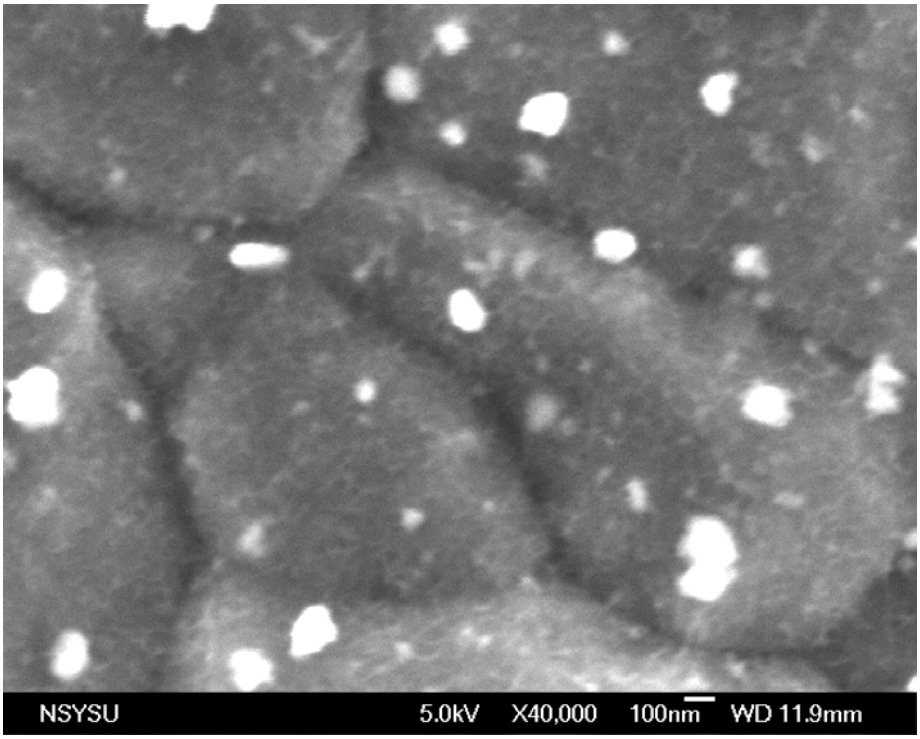

Figure 3-33 SEM photograph showing the clustered ZrO_2 located on grain boundaries or trip junctions and some ZrO_2 embedded into grains of the AZ31 matrix (1G4P).

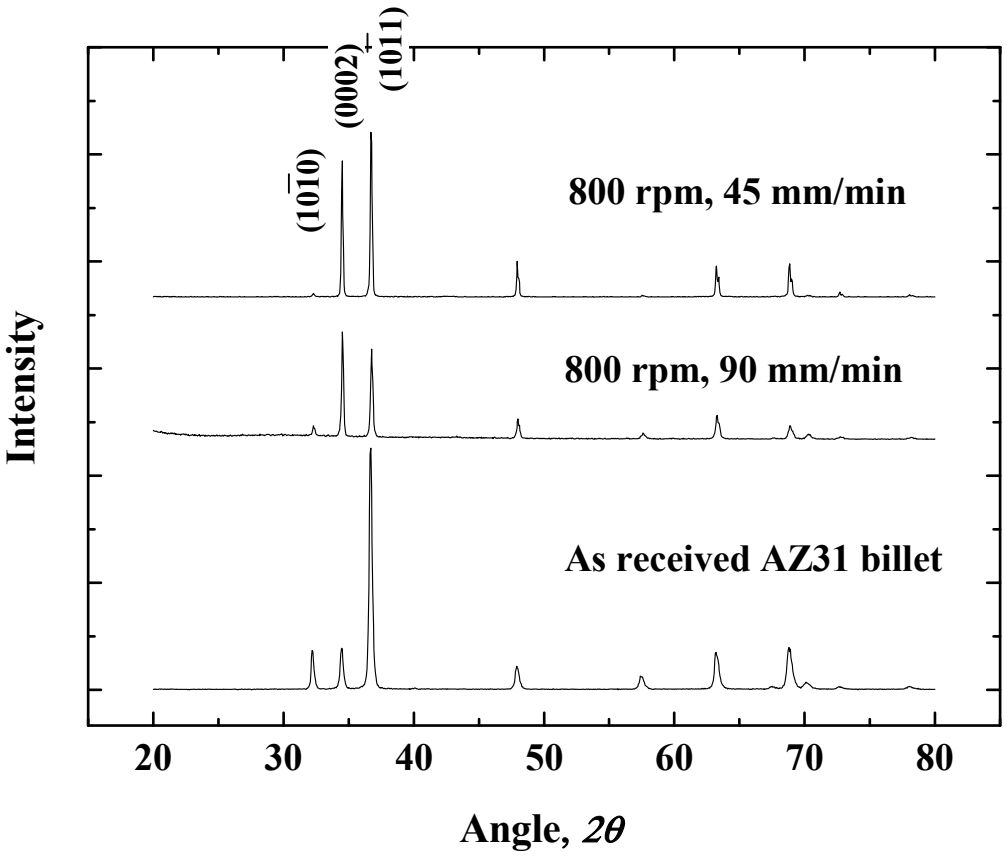

Figure 3-34 X-ray diffraction for modified AZ31 Mg alloy without any particle by FSP.

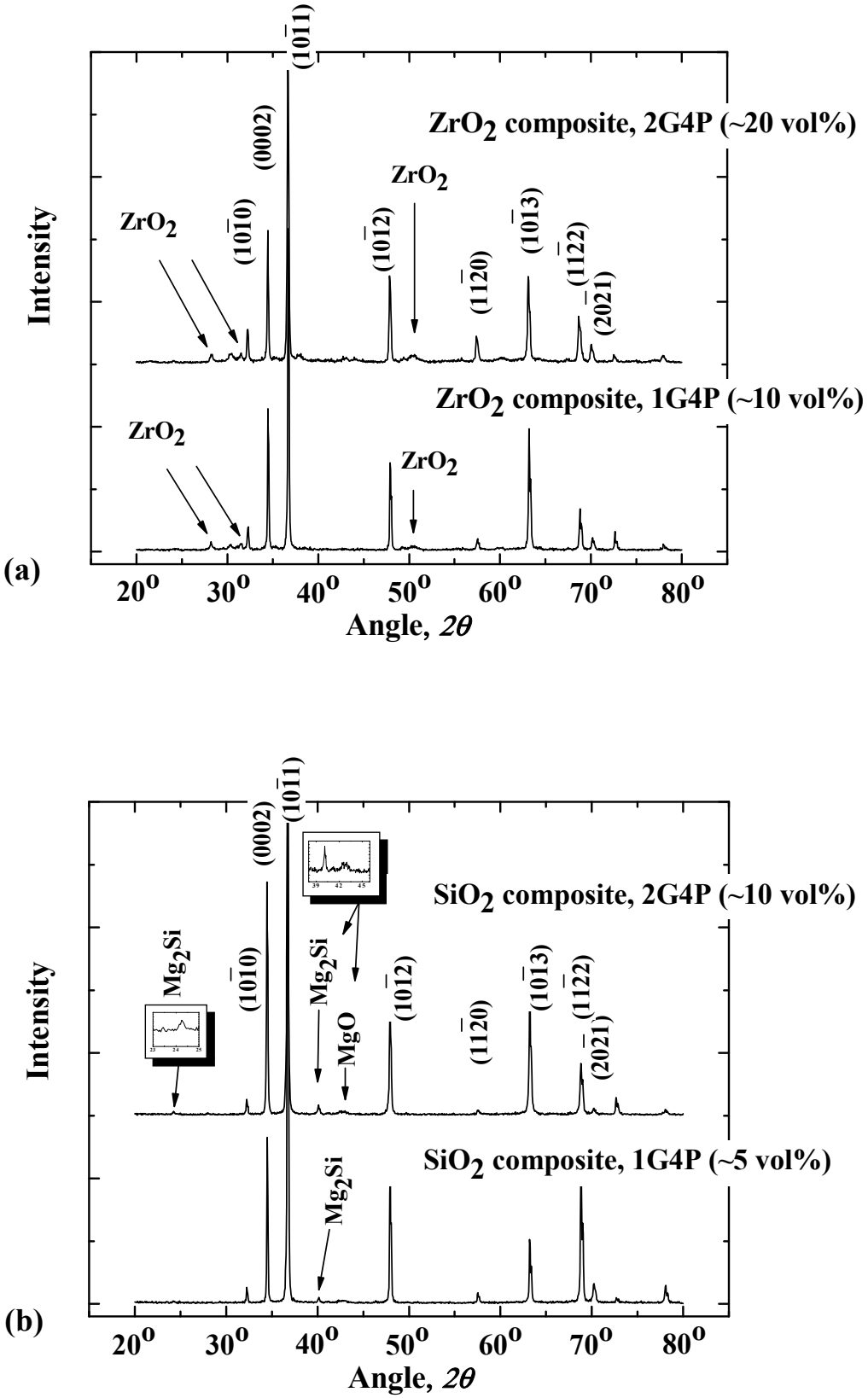

Figure 3-35 XRD patterns for (a) the Mg-AZ31/ZrO_2 and (b) the AZ31/SiO_2 composites.

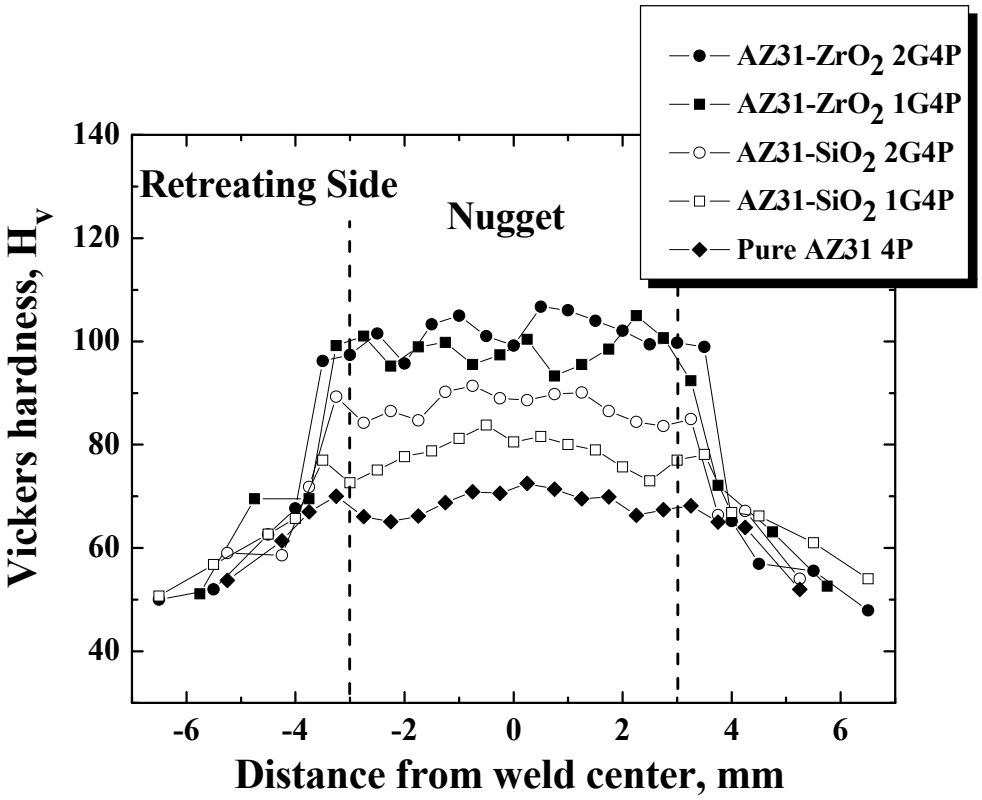

Figure 3-36 Typical variations of the microhardness (H_v) distribution in various FSP AZ31 composites and the FSP AZ31 alloy (no particles).

(a)

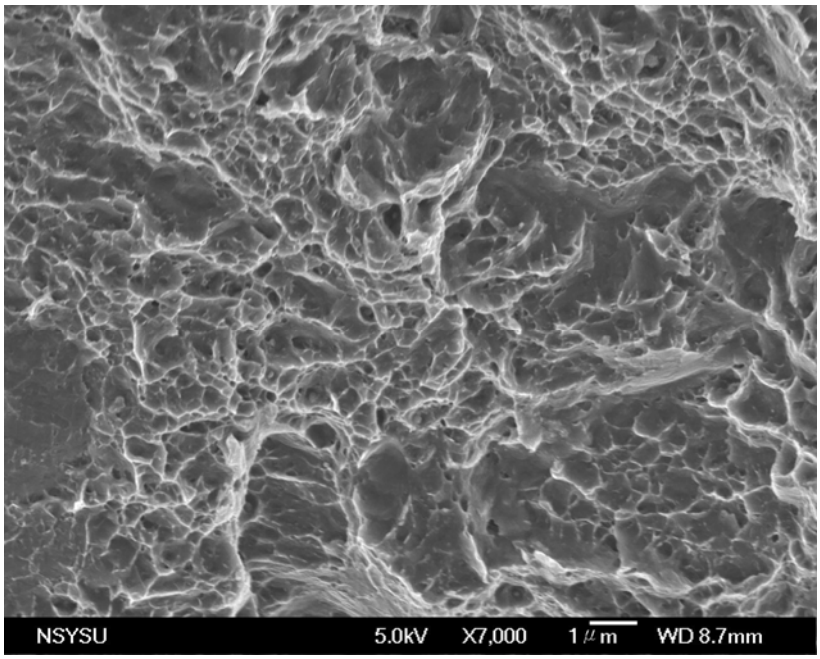

(b)

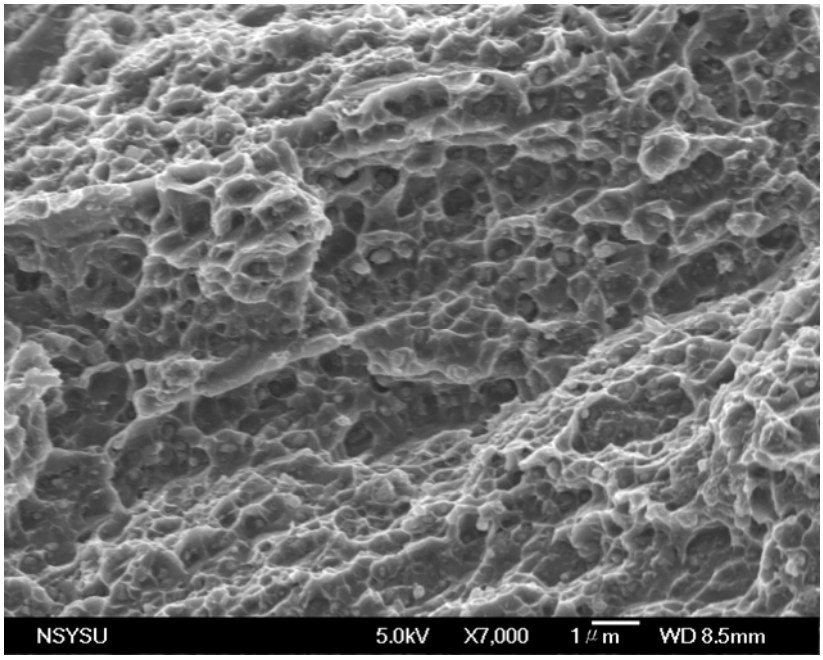

Figure 3-37 SEM/SEI fractographs of tensile samples: (a) the FSP AZ31 alloy, and (b) the FSP AZ31/10%ZrO_2 composite.

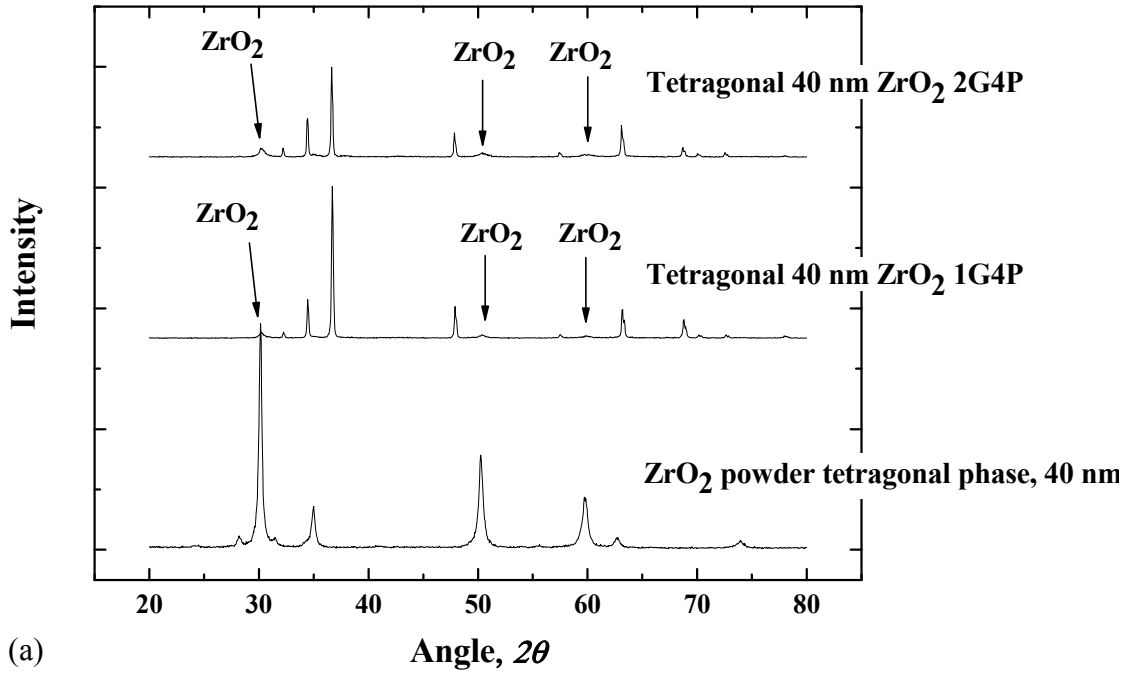

(a)

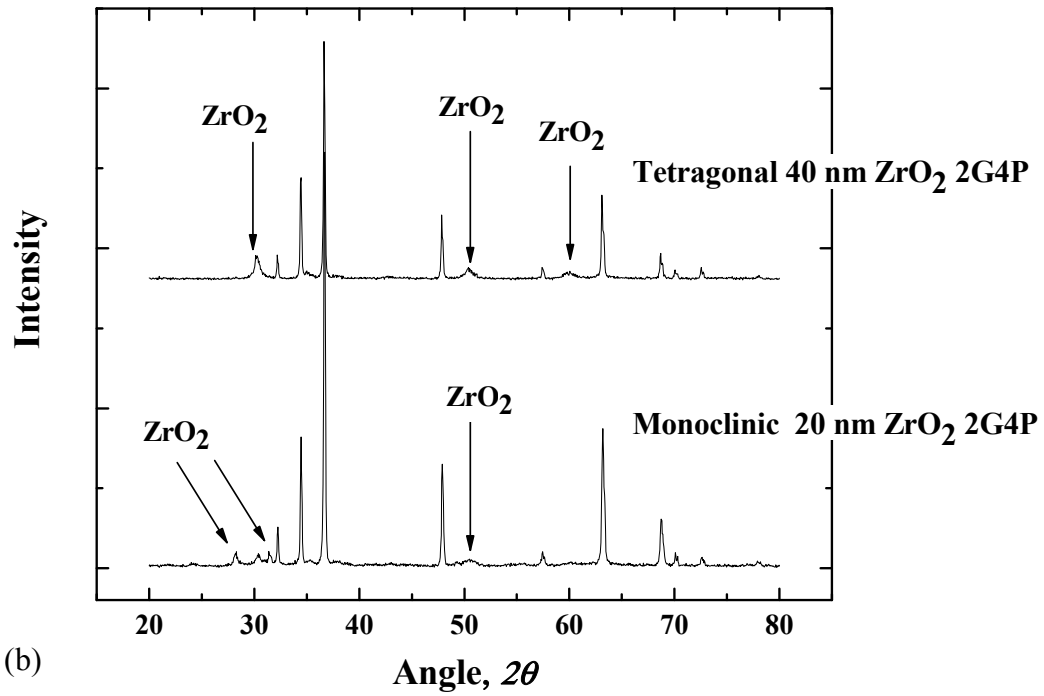

(b)

Figure 3-38 The XRD patterns for the transverse cross-sectional plane of the tetragonal phase ZrO_2 FSP composites.

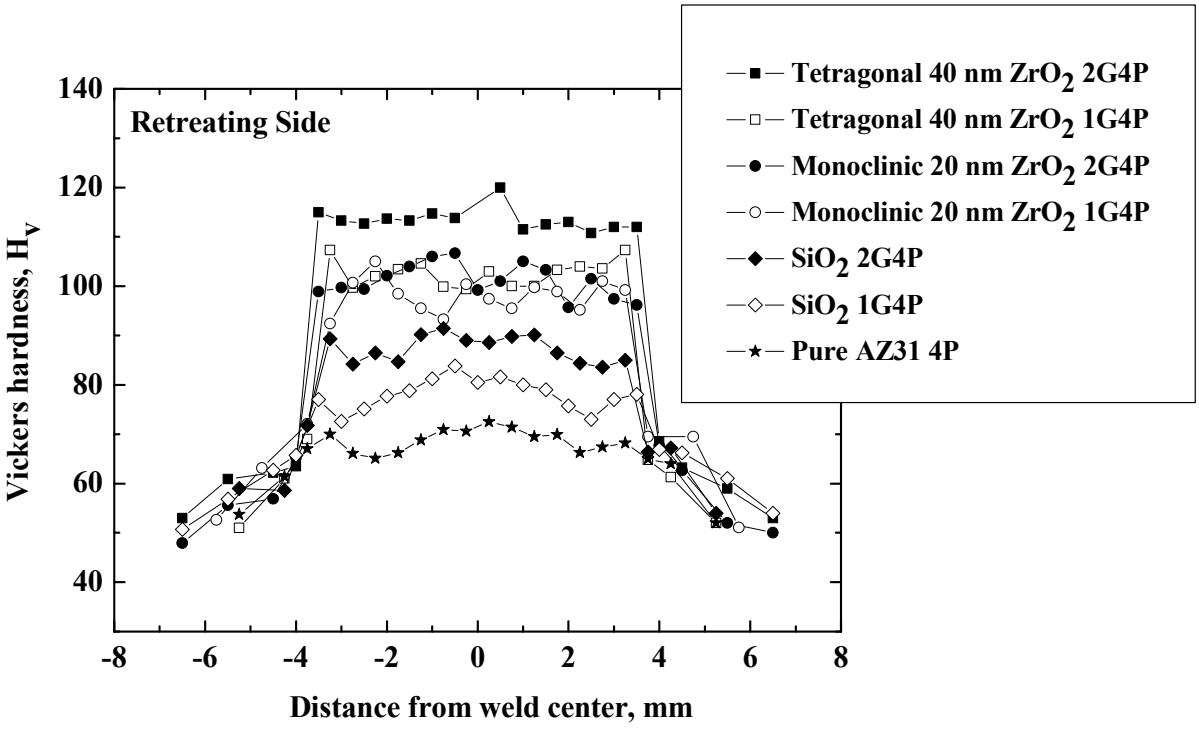

Figure 3-39 Vickers hardness variations measured along the central cross-sectional zones of the FSP samples.

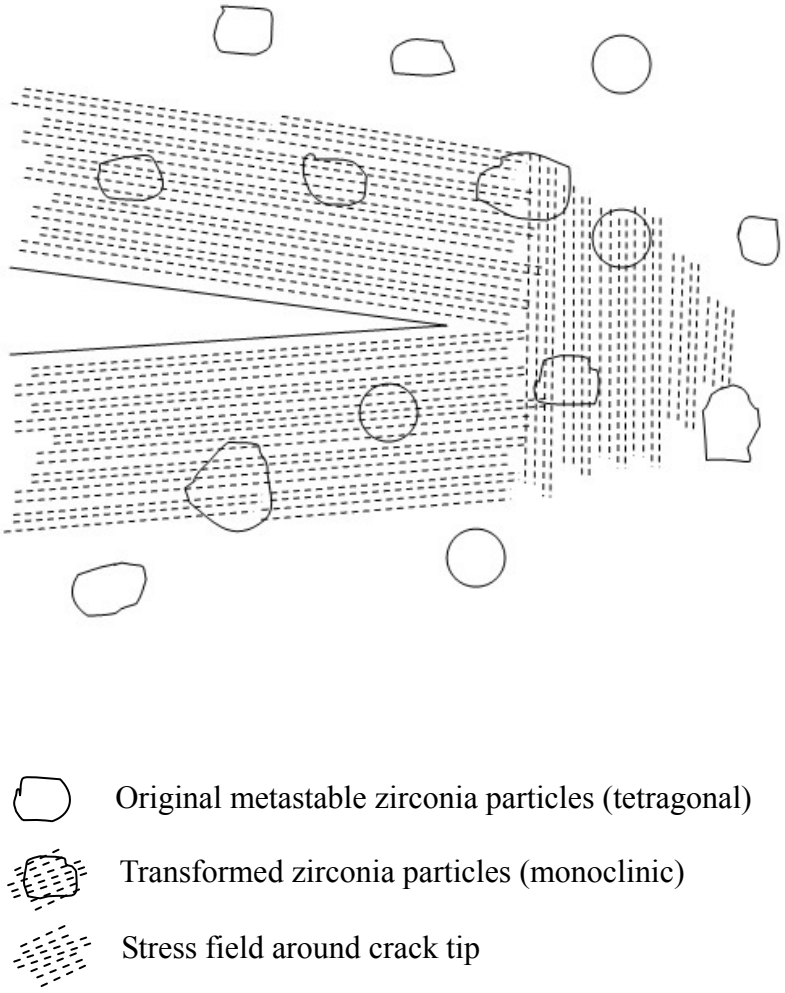

Figure 3-40 Stress-induced transformation of metastable ZrO_2 particles in the elastic stress field of a crack.

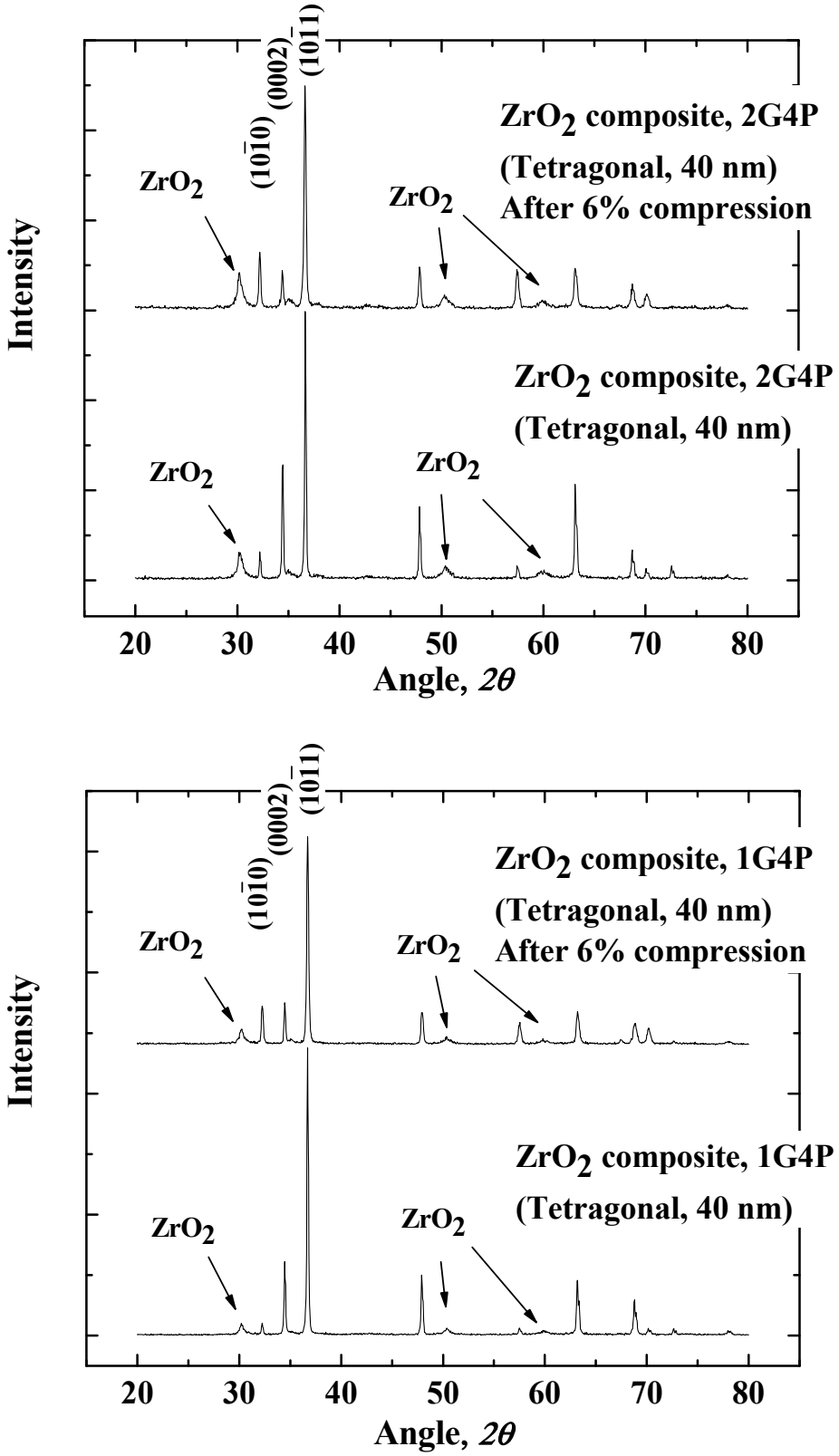

Figure 3-41 The XRD diffraction patterns of the 1G4P and 2G4P Mg/tetragonal phase ZrO_2 composites after 6% strain of subsequent compression along the normal direction.

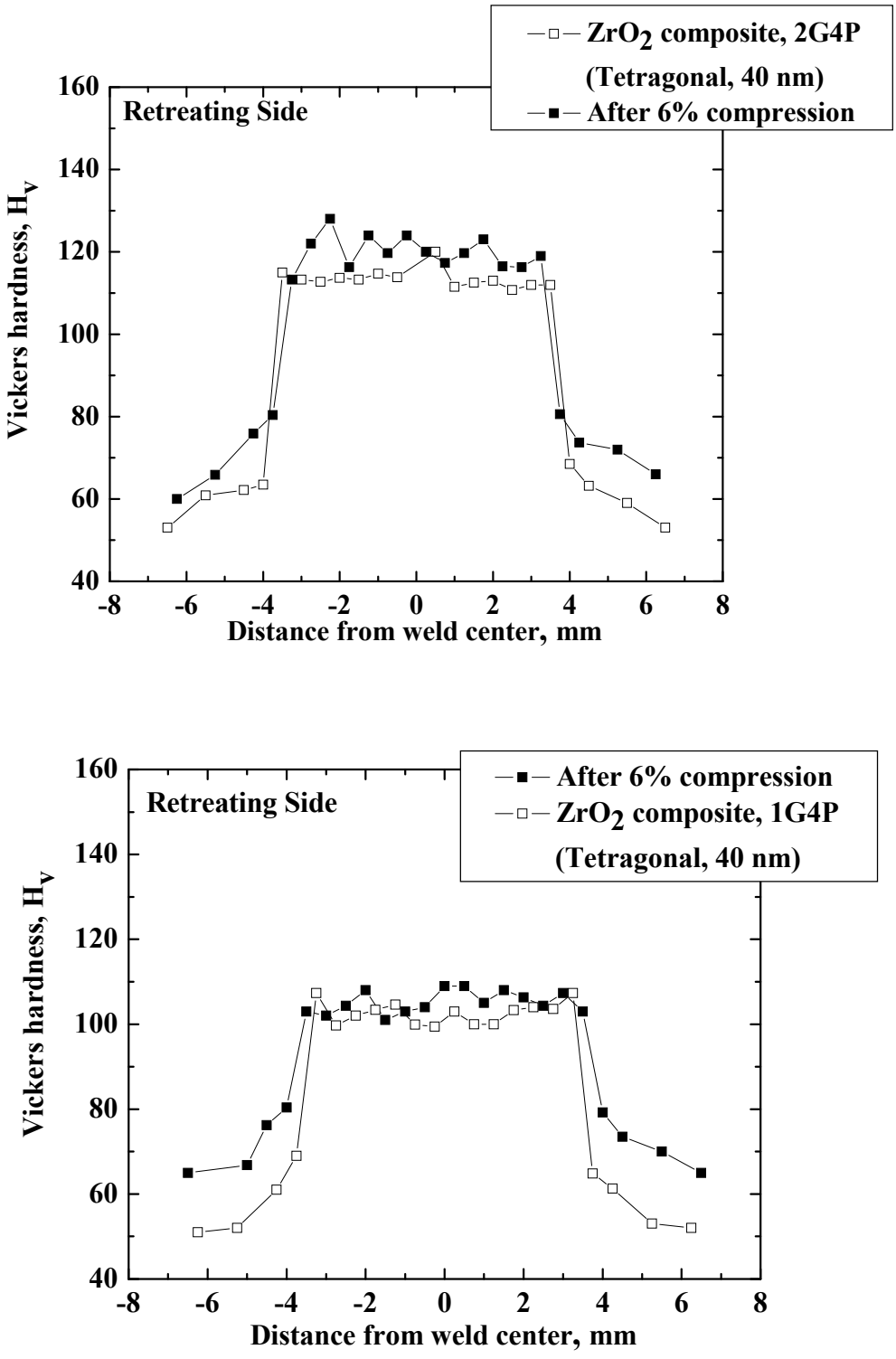

Figure 3-42 The hardness profiles for both 1G4P and 2G4P composites after 6% compression.

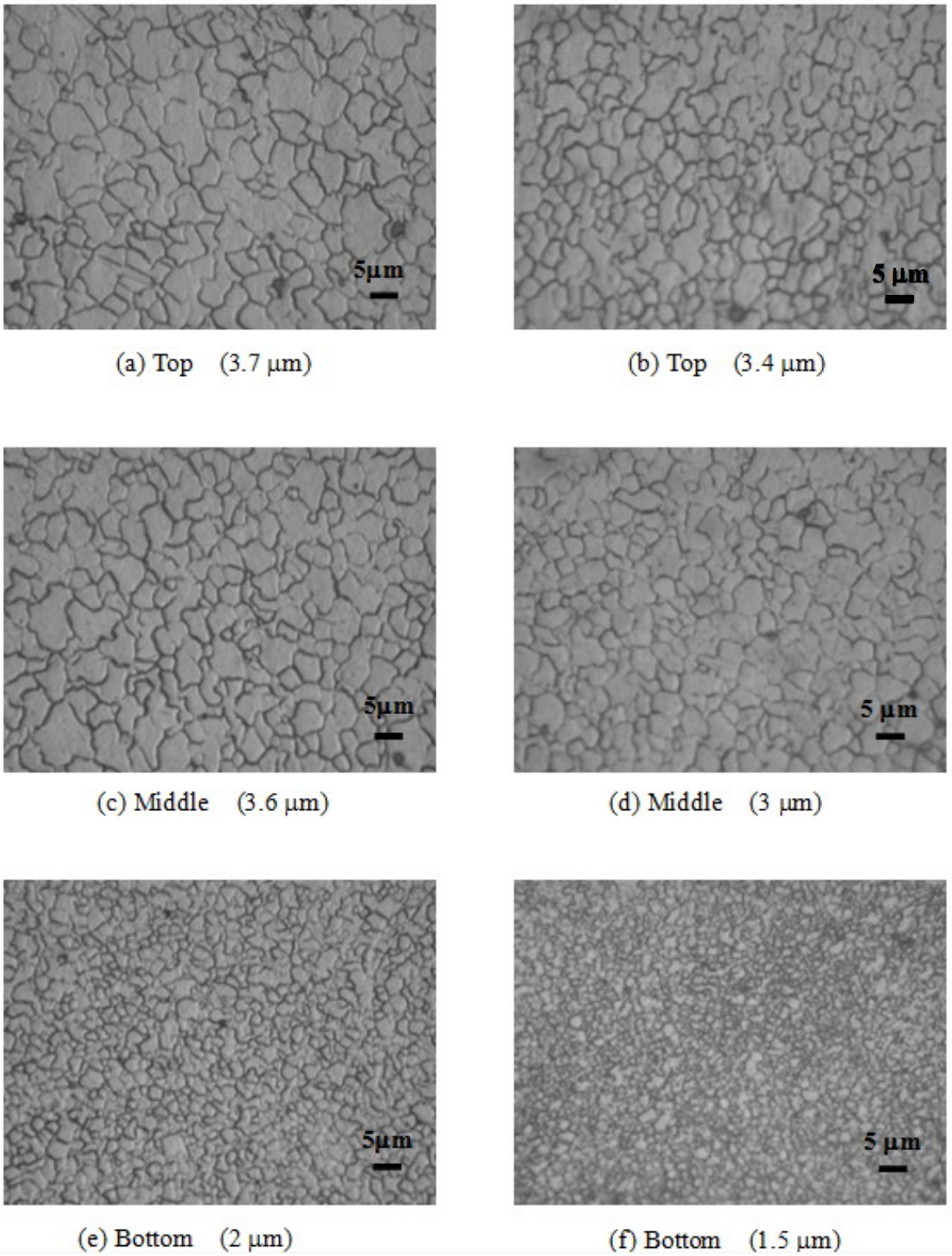

Figure 3-43 The stir zone microstructure of AZ31 billet FSPed at 800 rpm 90 mm/min (a),(c),(e) plate is 10 mm in thickness (ave. 3.1 μm); (b),(d),(f) plate is 7 mm in thickness (ave. 2.7 μm)

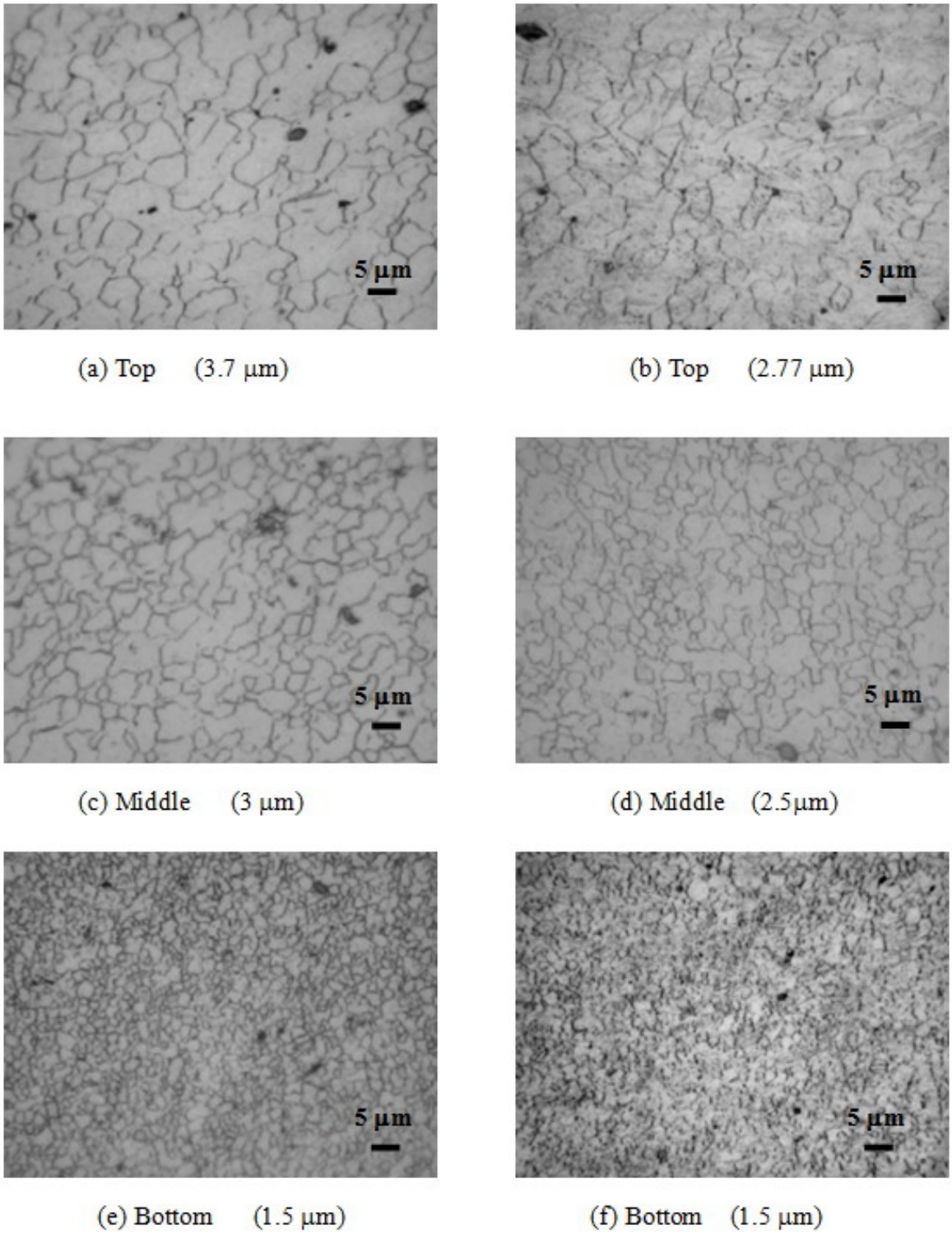

Figure 3-44 The stir zone microstructure of AZ31 billet FSPed at 800 rpm 400 mm/min (a),(c),(e) with steel back plate (ave. 2.8 μm) ; (b),(d),(f) with usual cooling facility (ave. 2.3 μm).

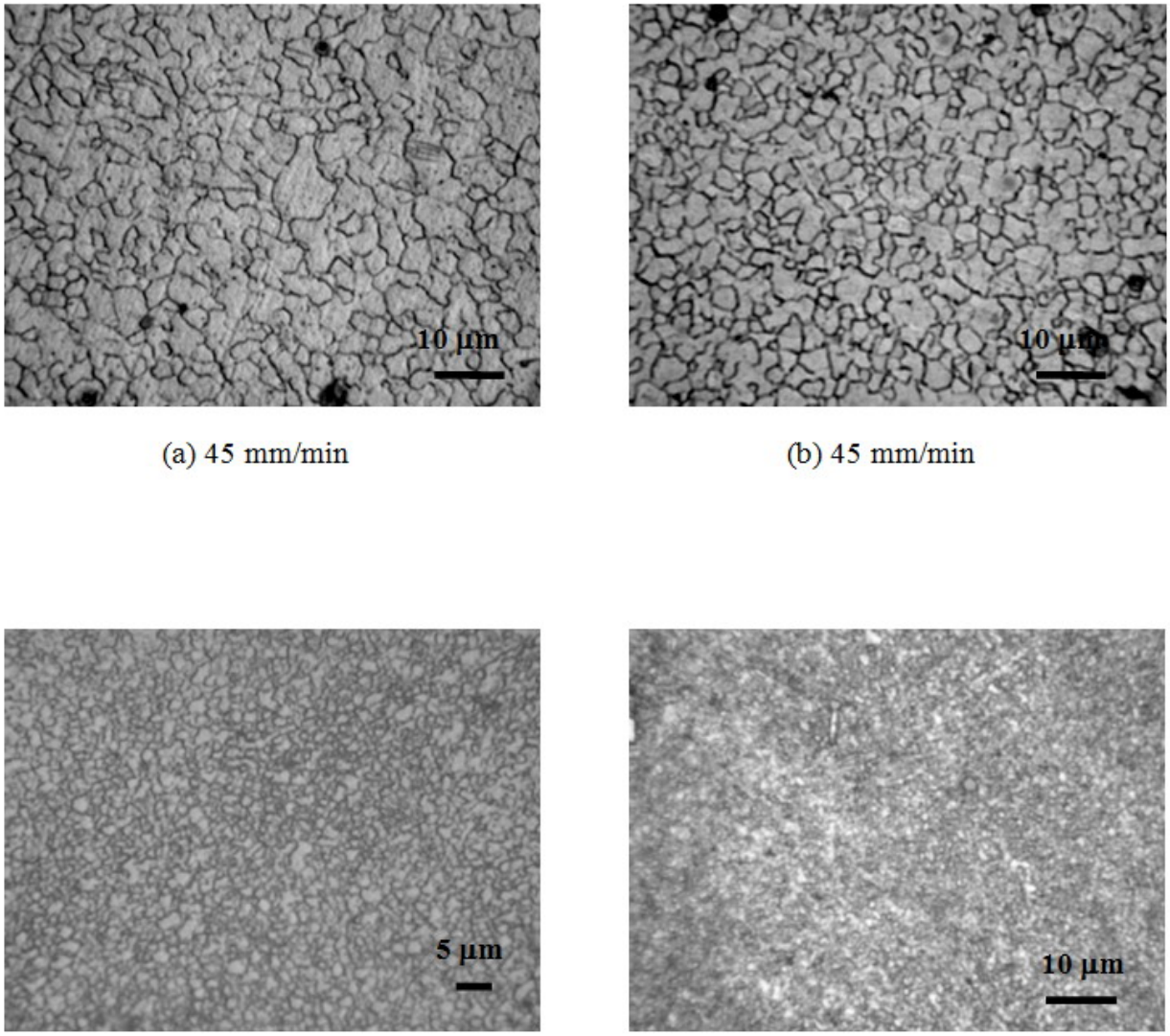

(a) 45 mm/min (b) 45 mm/min

(c) 90 mm/min (d) 90 mm/min

Figure 3-45 OM micrographs showing the variation of the recrystallized grain size in the nugget zone under the different cooling conditions as the same 800 rpm rotational speed. (a) and (c) without liquid nitrogen cooling, (b) and (d) with liquid nitrogen cooling.

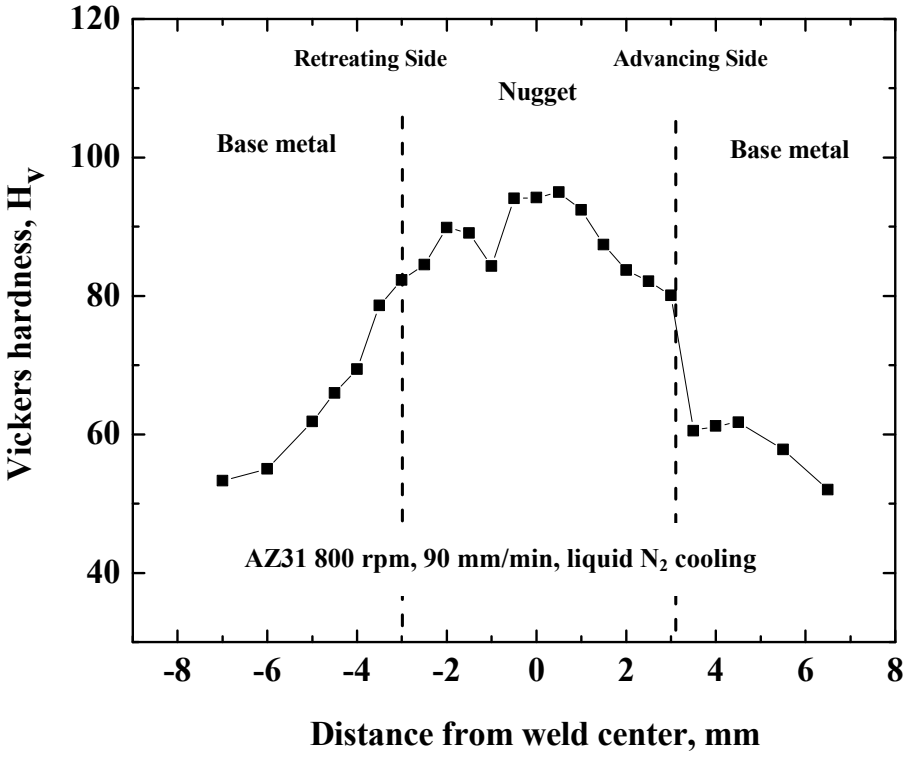

Figure 3-46 Hardness profile of AZ31 7 mm plate FSPed at 800 rpm 90 mm/min and cooled by liquid N_2.

(a)

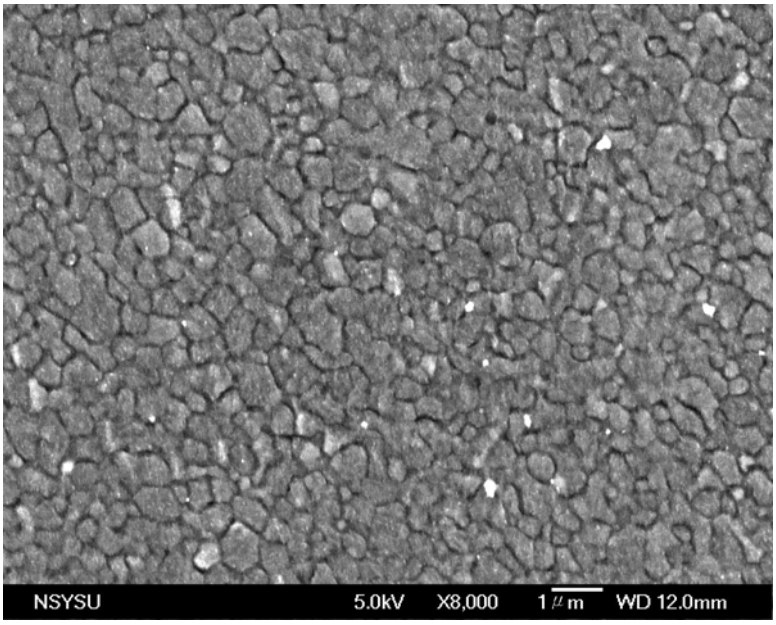

(b)

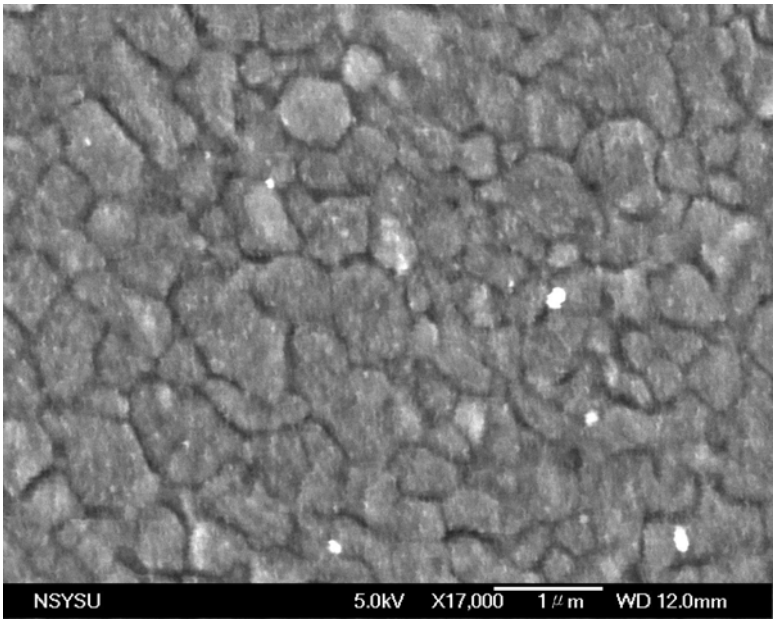

Figure 3-47 The SEM/SEI images for the pure AZ31 4 mm plate FSPed one pass with liquid N_2 cooling (~0.45 μm).

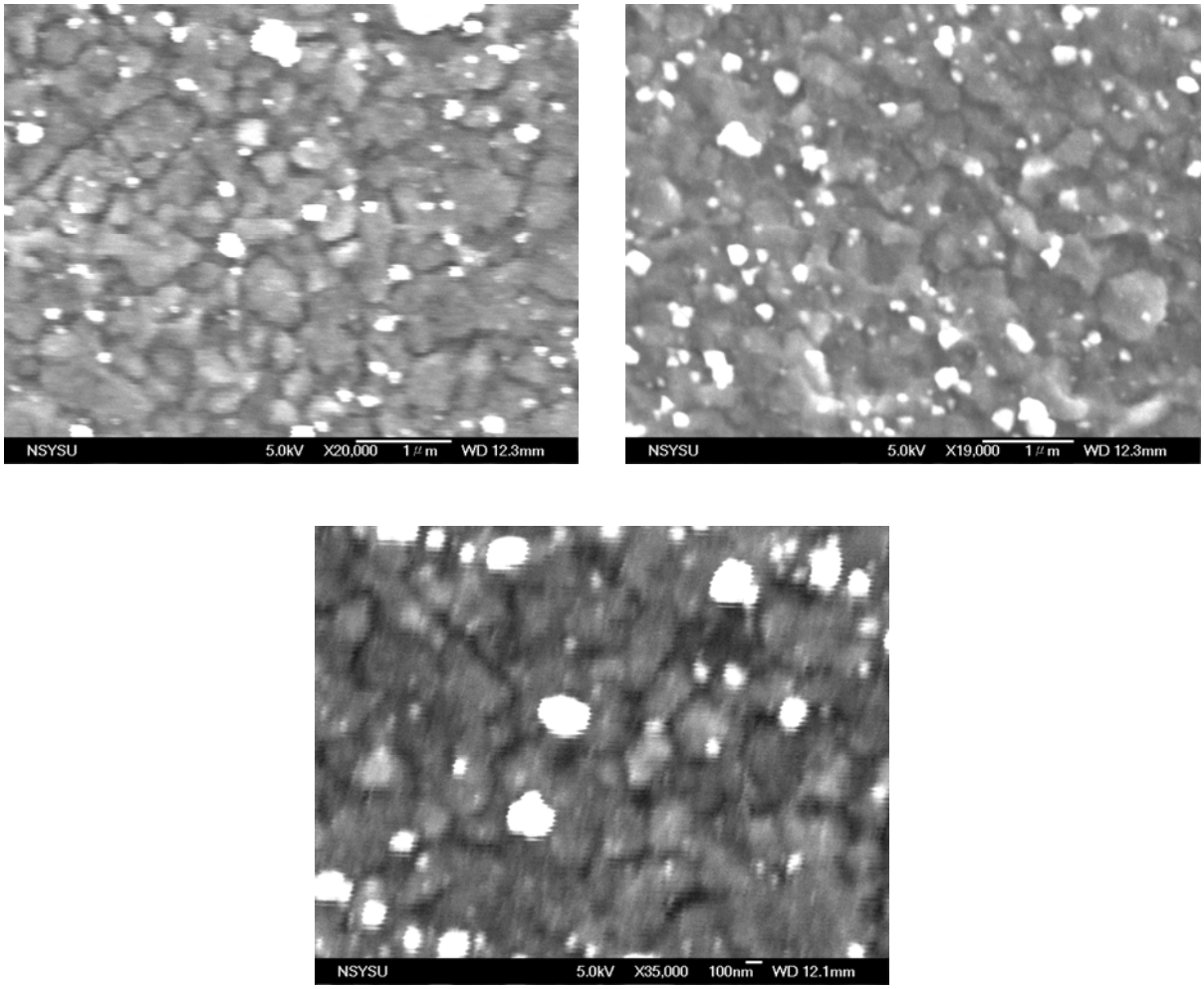

Figure 3-48 The SEM/SEI image for the AZ31/ZrO_2 2G4P FSPed with subsequent cooling process by the tool which has 3 mm pin in diameter and length and 10 mm shoulder in diameter.

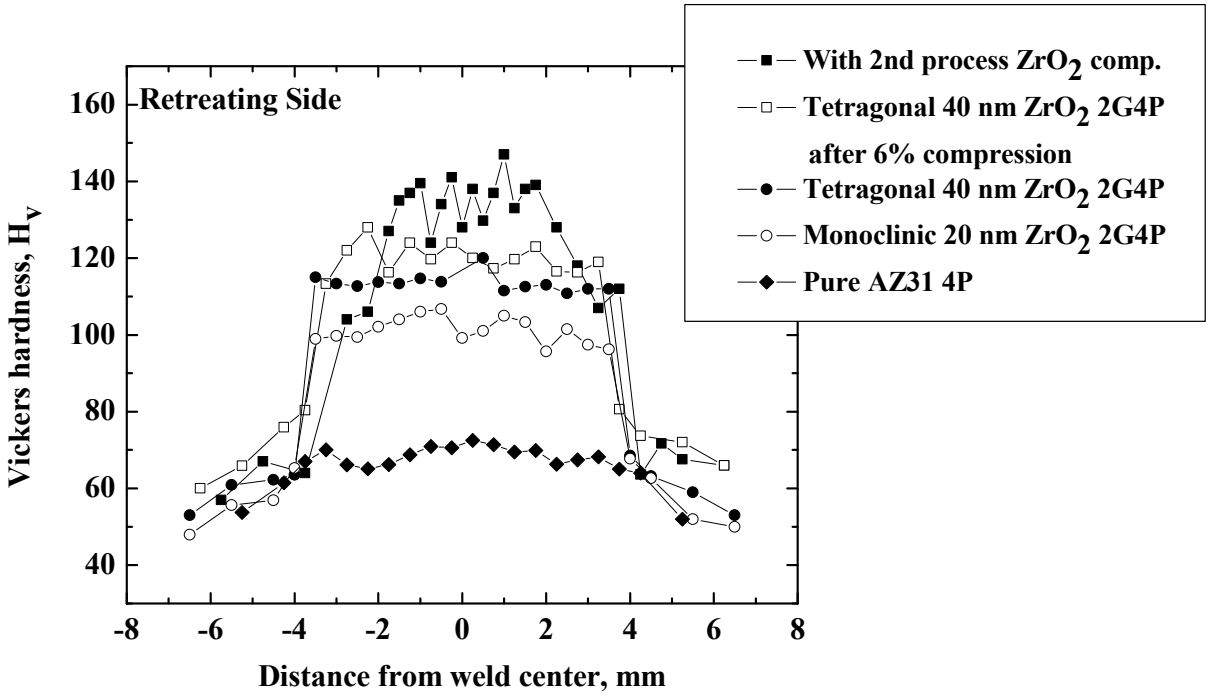

Figure 3-49 Hardness profiles of Mg-based composites made by FSP.

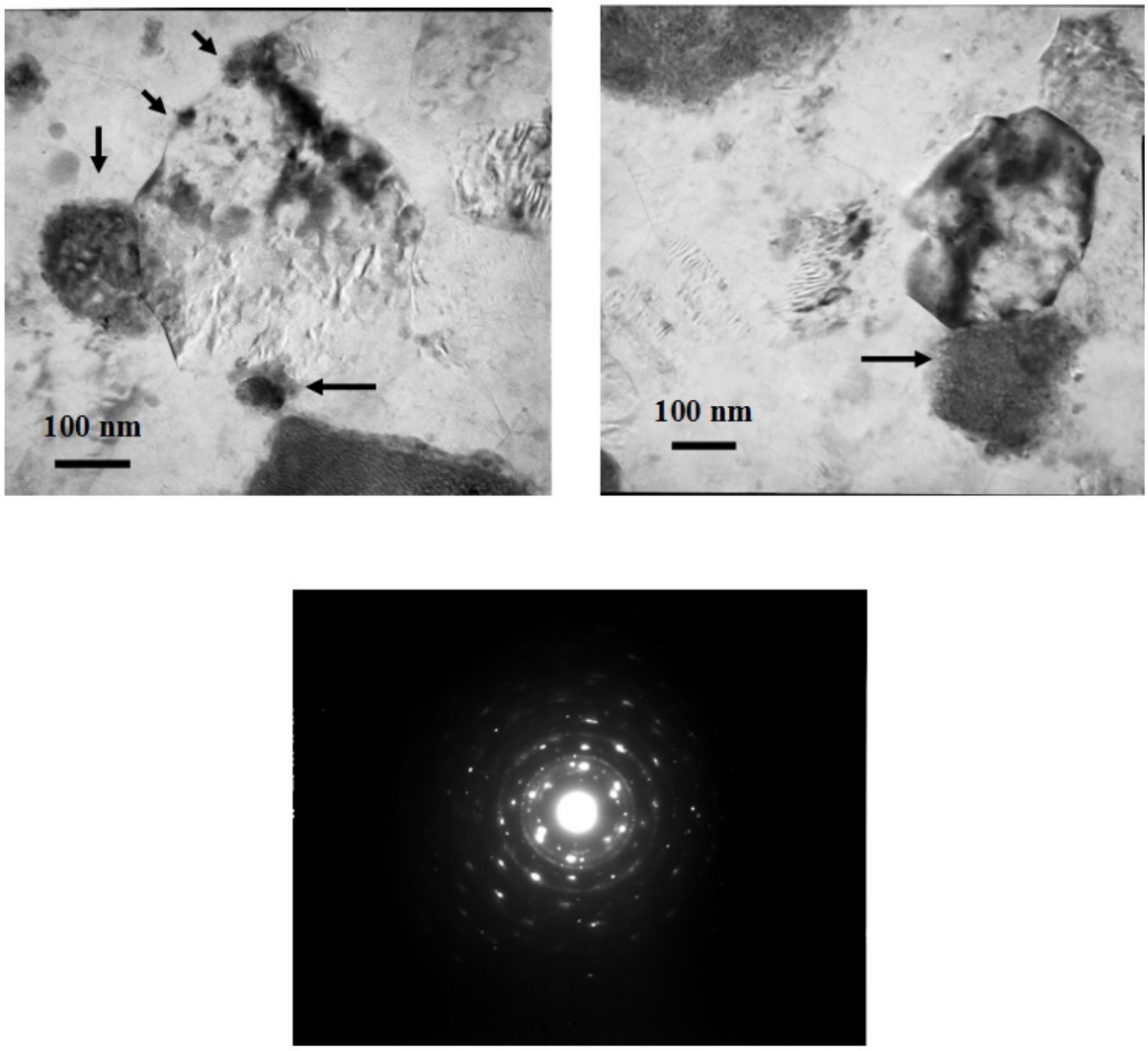

Figure 3-50 TEM observations for the Mg/ZrO_2 composite with subsequent cooling pass, together with a select area diffraction (SAD) pattern. Arrows indicate the ZrO_2 particles as the obstacles for the grain boundary migration.

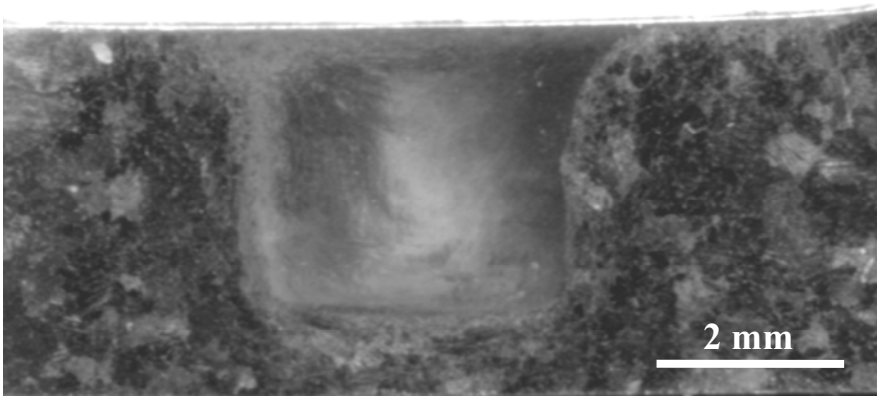

Figure 3-51 Macrograph of cross section of the single-pass FS Processed AZ31 alloy at an advancing speed is 28 mm/min.

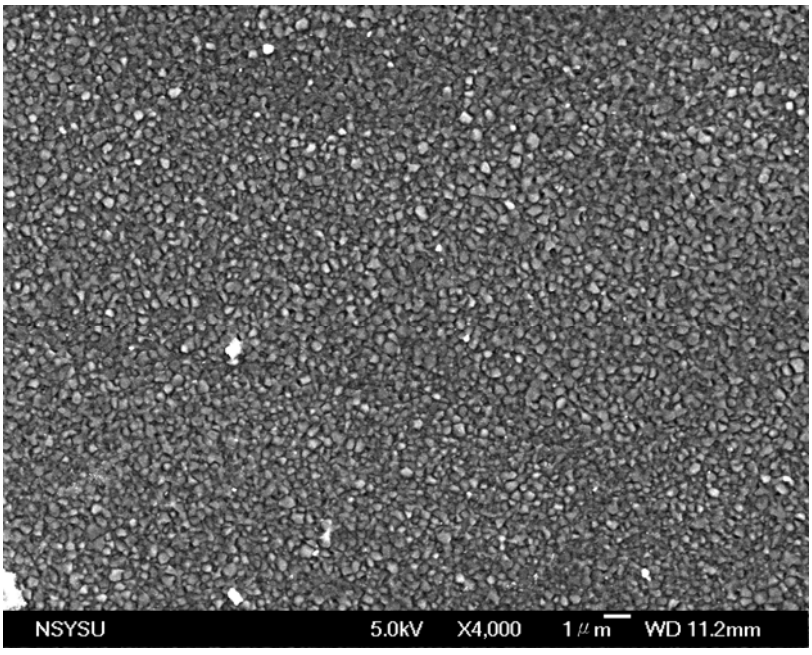

Figure 3-52 SEM micrograph at low magnification showing the uniform ultrafine grained structure in the AZ31 alloy after one-pass FSP at 28 mm/min with liquid N_2 cooling.

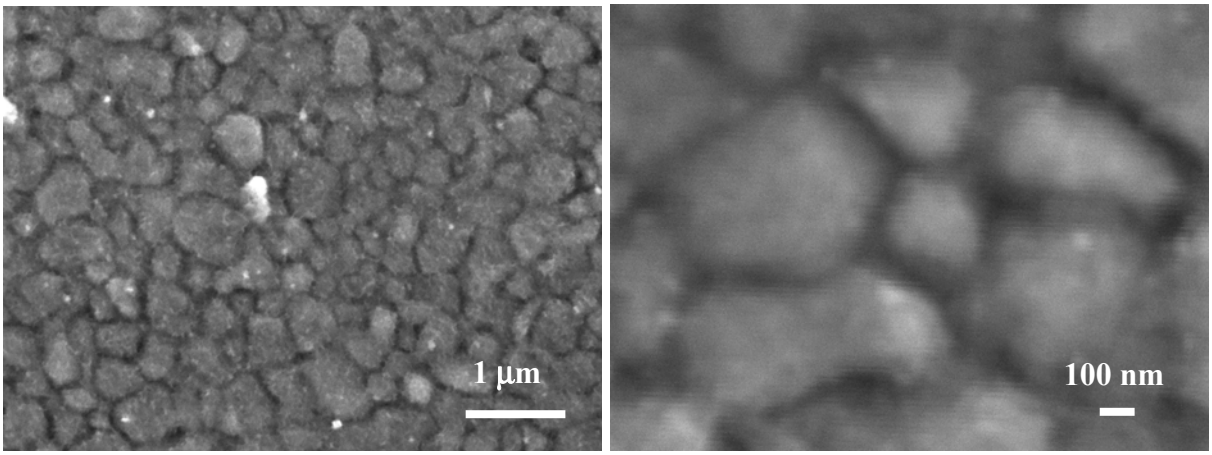

Figure 3-53 SEM micrographs for the FSP AZ31alloy at an advancing speed of 28 mm/min.

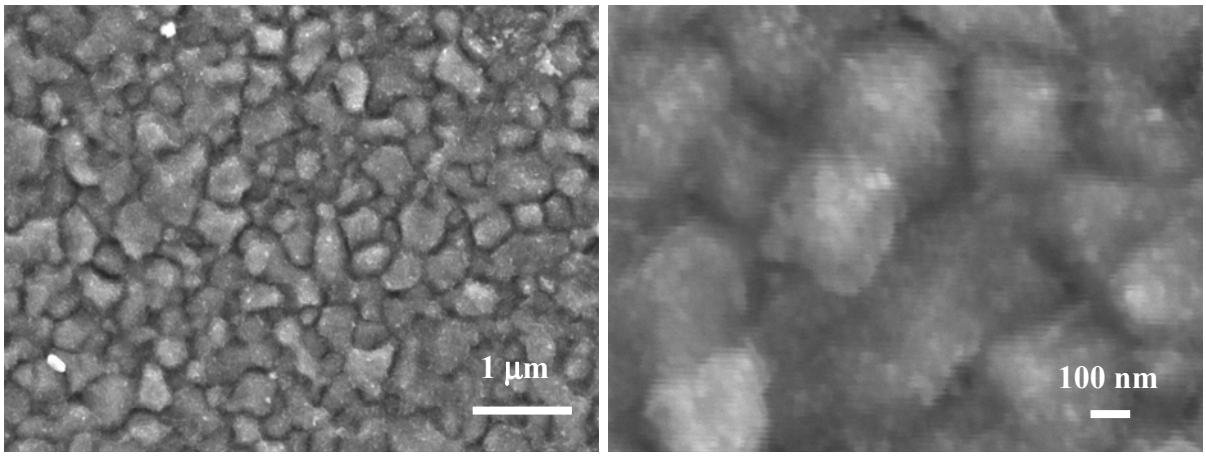

Figure 3-54 SEM micrographs for the FSP AZ31alloy at an advancing speed of 33 mm/min.

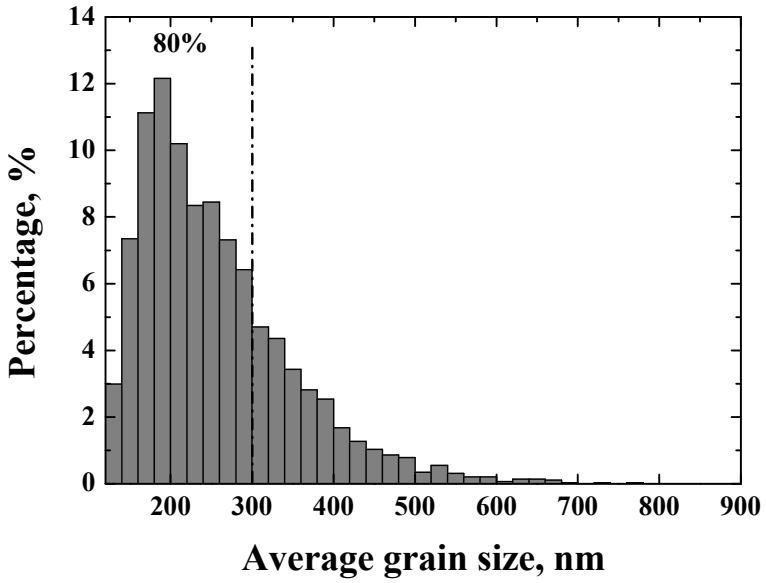

Figure 3-55 Grain size distribution chart of the ultrafine grained microstructure in FSP AZ31 alloys.

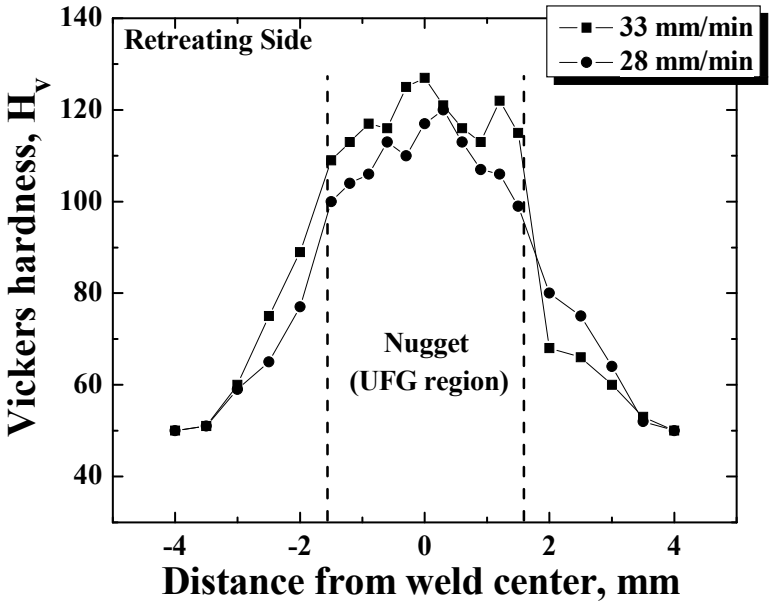

Figure 3-56 Microhardness (H_v) profile measured on cross-sectional planes for the FSP ultrafine grained AZ31 alloy.

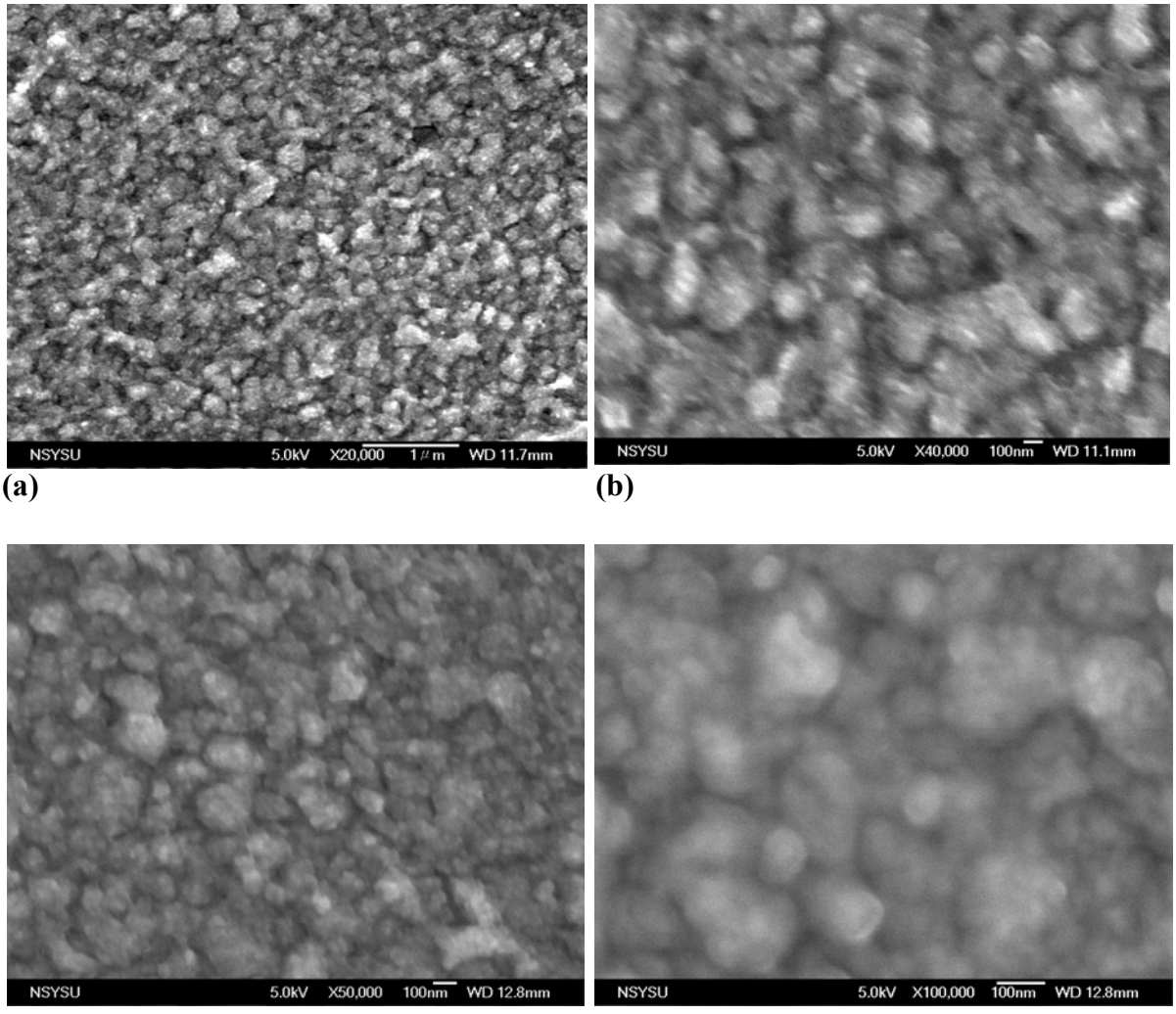

Figure 3-57 The SEM/SEI images of the grain structures in the AZ31 alloy after two passes FSP with the same advancing speed of 37 mm/min and the rotation rate of 1200 rpm at the first pass and 800 rpm at the second pass. The same pin tool size is used in both FSP passes.

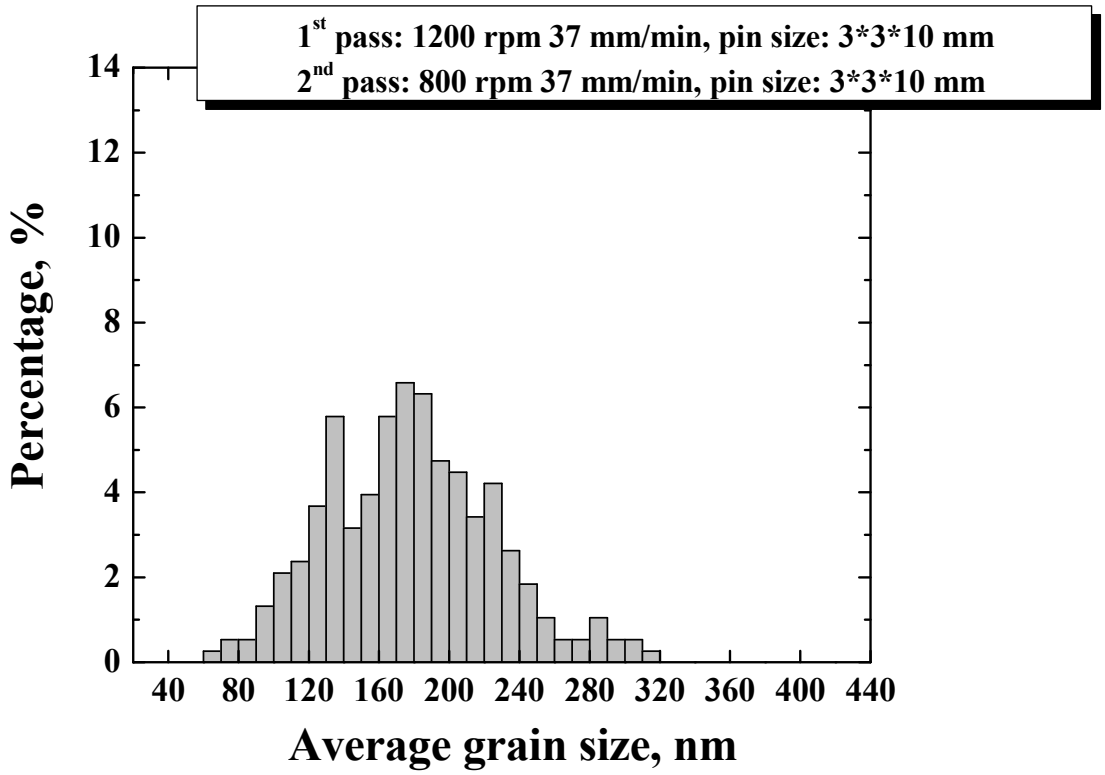

Figure 3-58 The grain size distribution of the ultrafine grained microstructure in FSP AZ31 alloys.

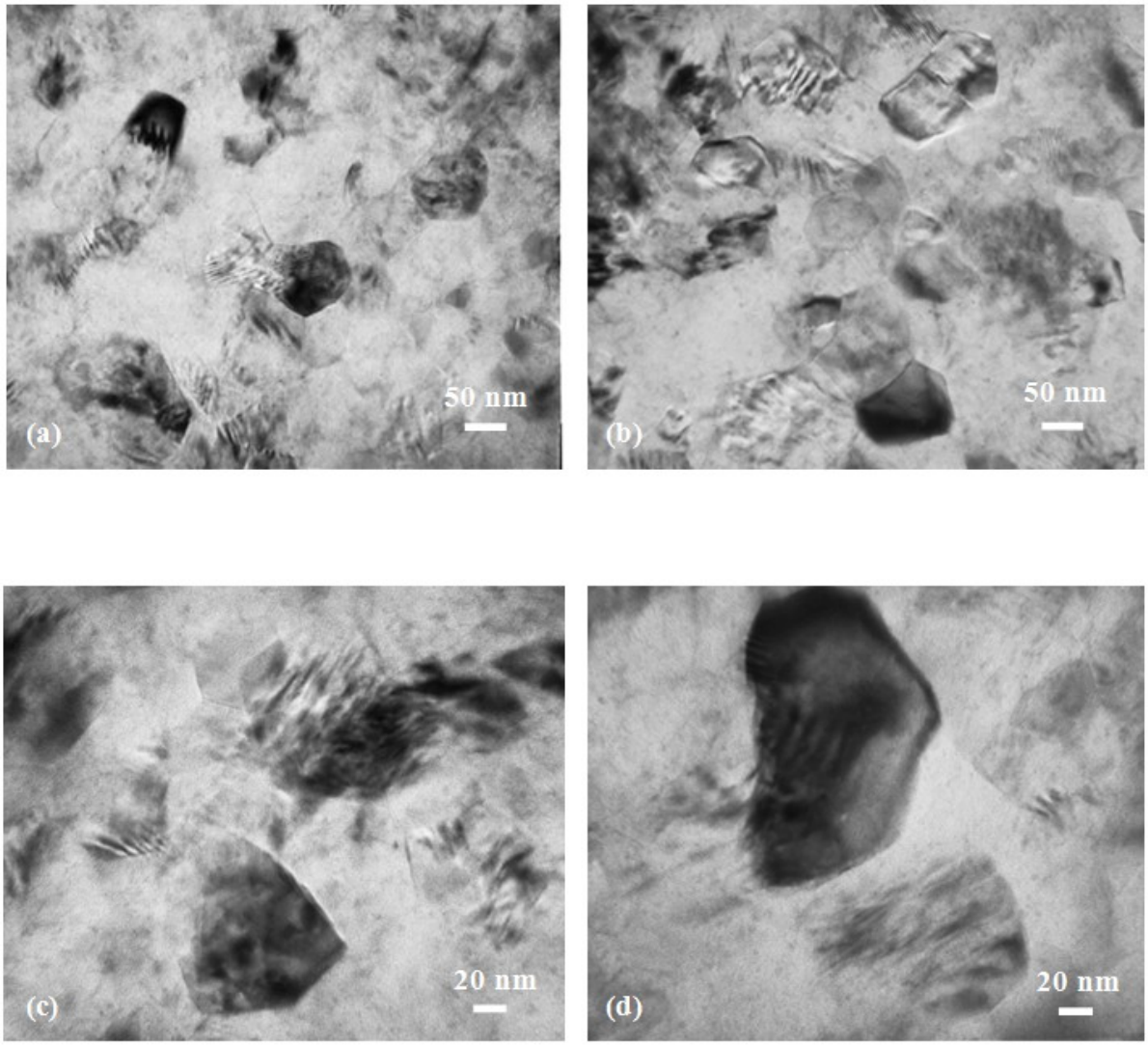

Figure 3-59　TEM observations for the two-pass FSPed AZ31 alloy in the as processed condition.

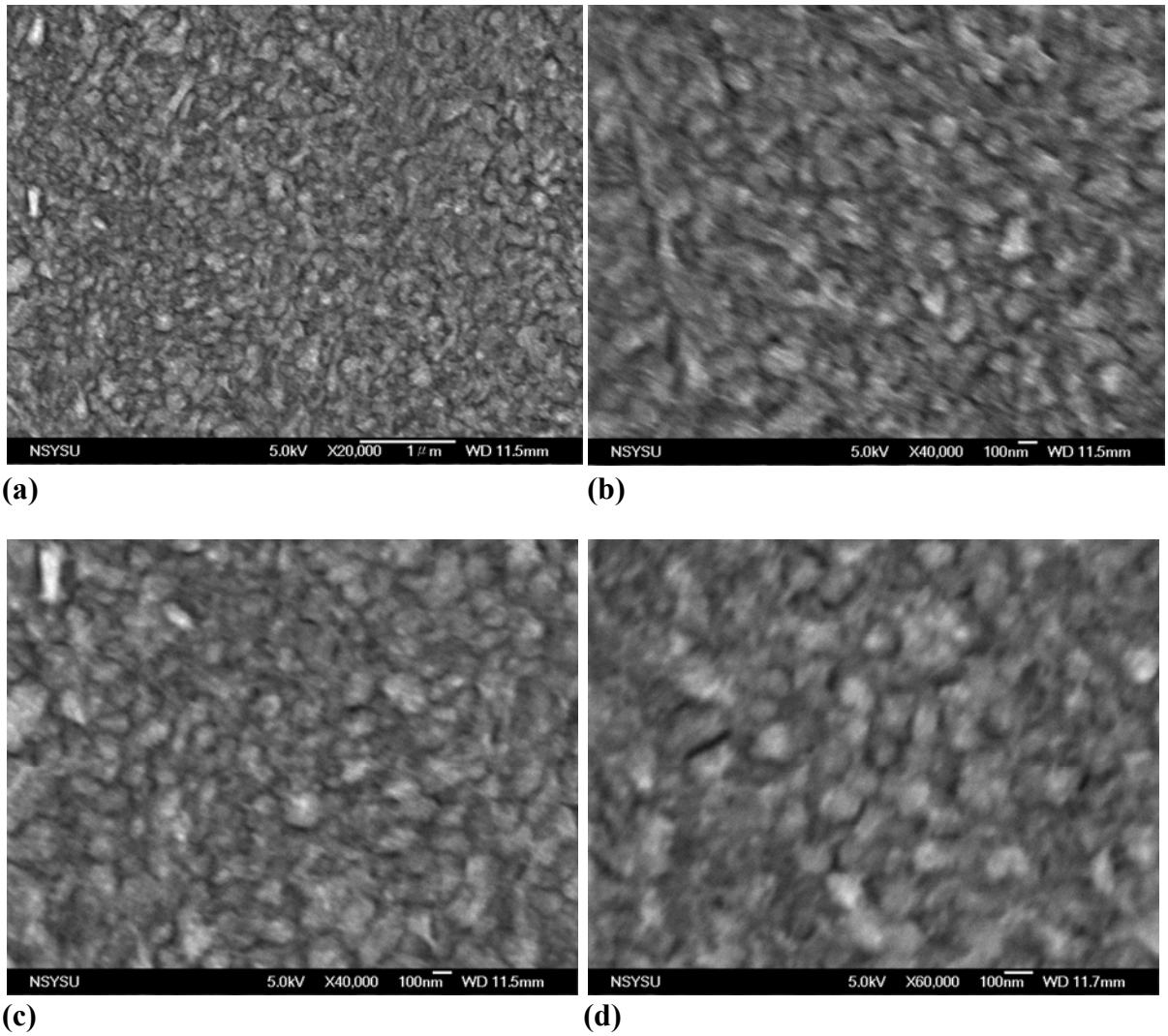

Figure 3-60 SEM/SEI images of the grain structures in the AZ31 alloys after two passes FSP with the same rotation rate and advancing speed of 1000 rpm and 37 mm/min, respectively. Smaller pin tool is used in the second pass.

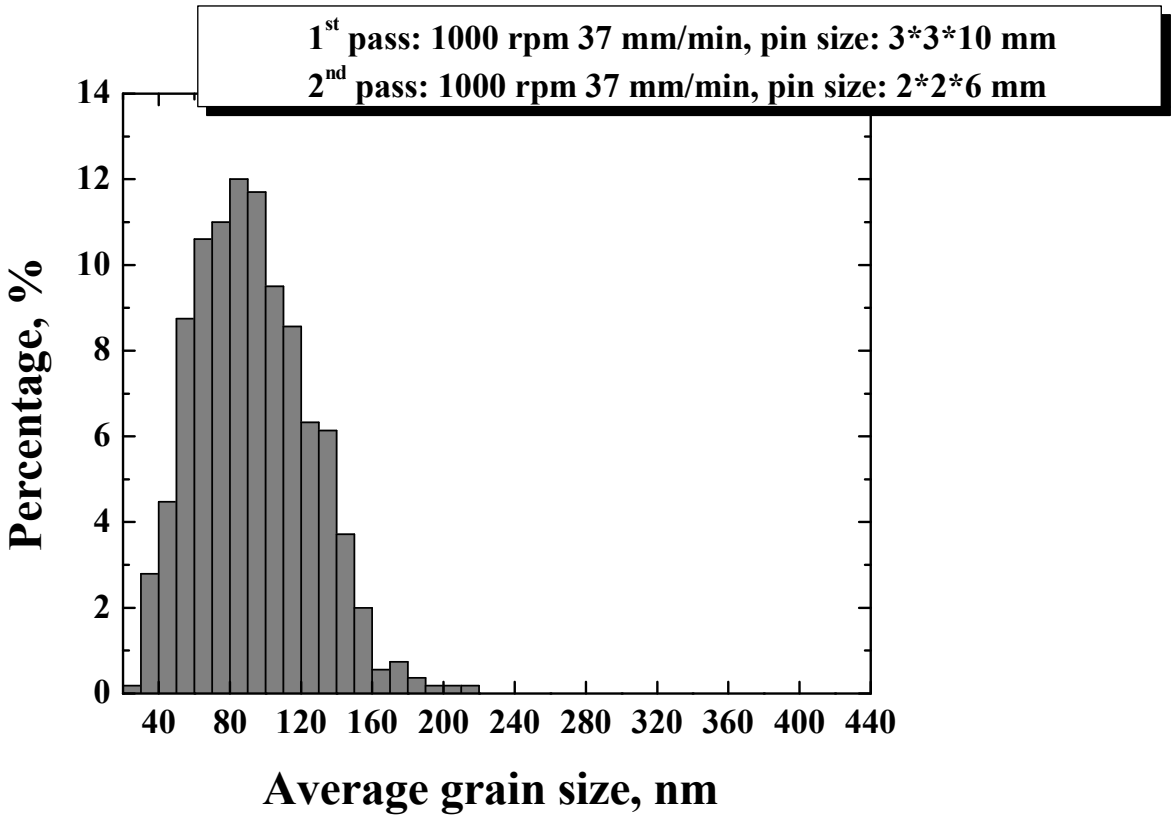

Figure 3-61 The grain size distribution of the nanometer grained microstructure in FSP AZ31 alloys.

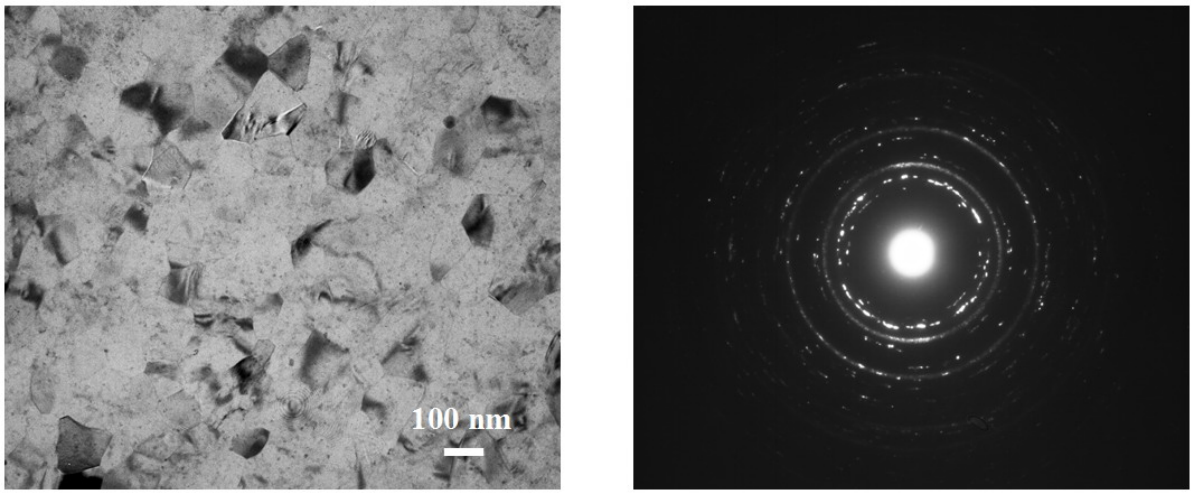

Figure 3-62　TEM observations for the two-pass FSPed AZ31 alloy in the as processed condition, together with a select area diffraction (SAD) pattern.

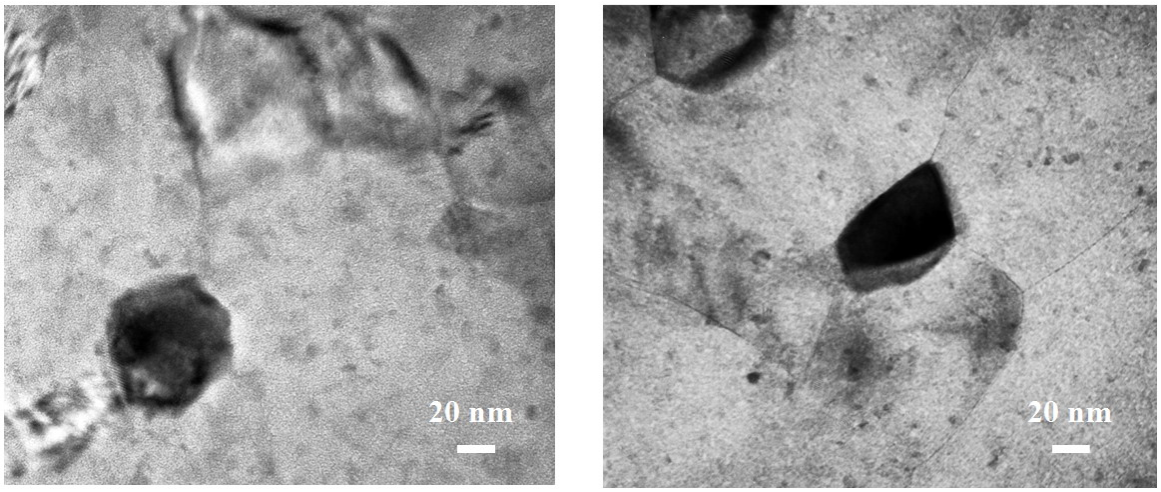

Figure 3-63　TEM observations for the two-pass FSPed AZ31 alloy in the as processed condition, showing the extremely fine nano-grains.

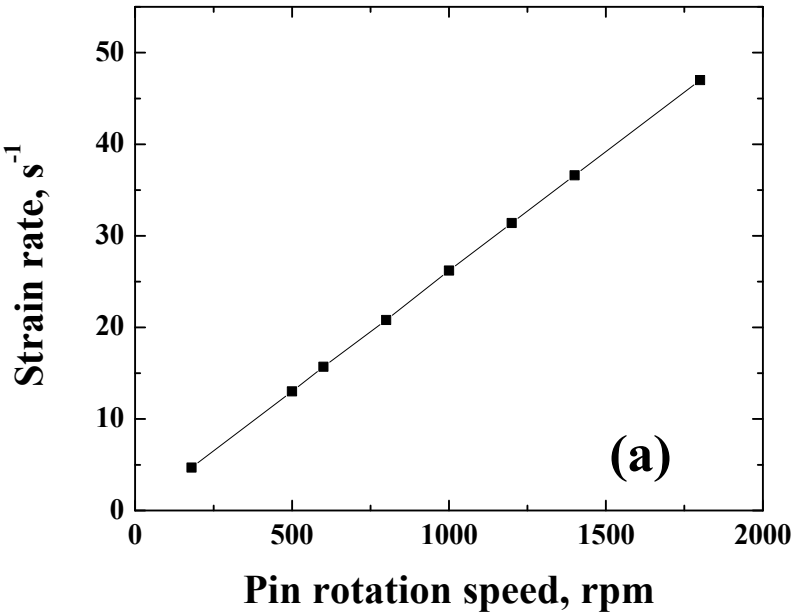

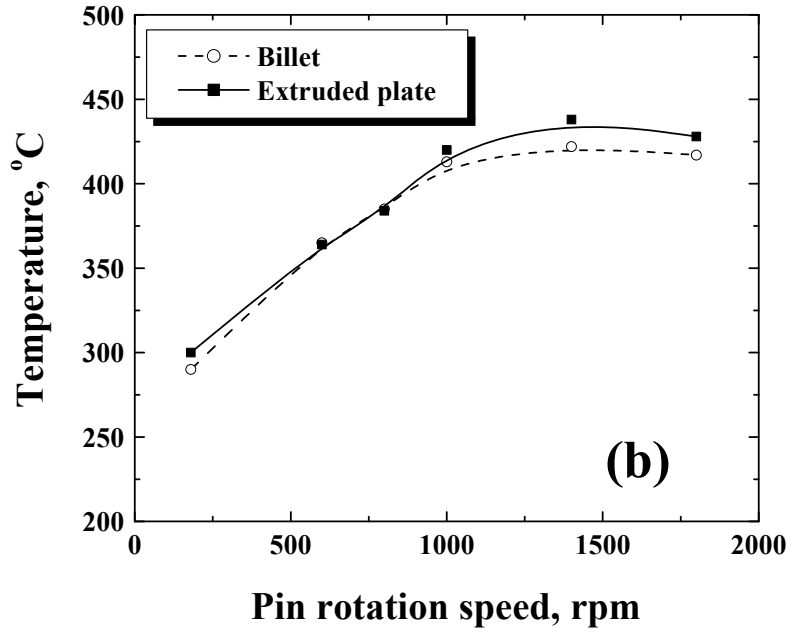

Figure 4-1 Variation of the (a) strain rate and (b) temperature as a function of pin rotation speed.

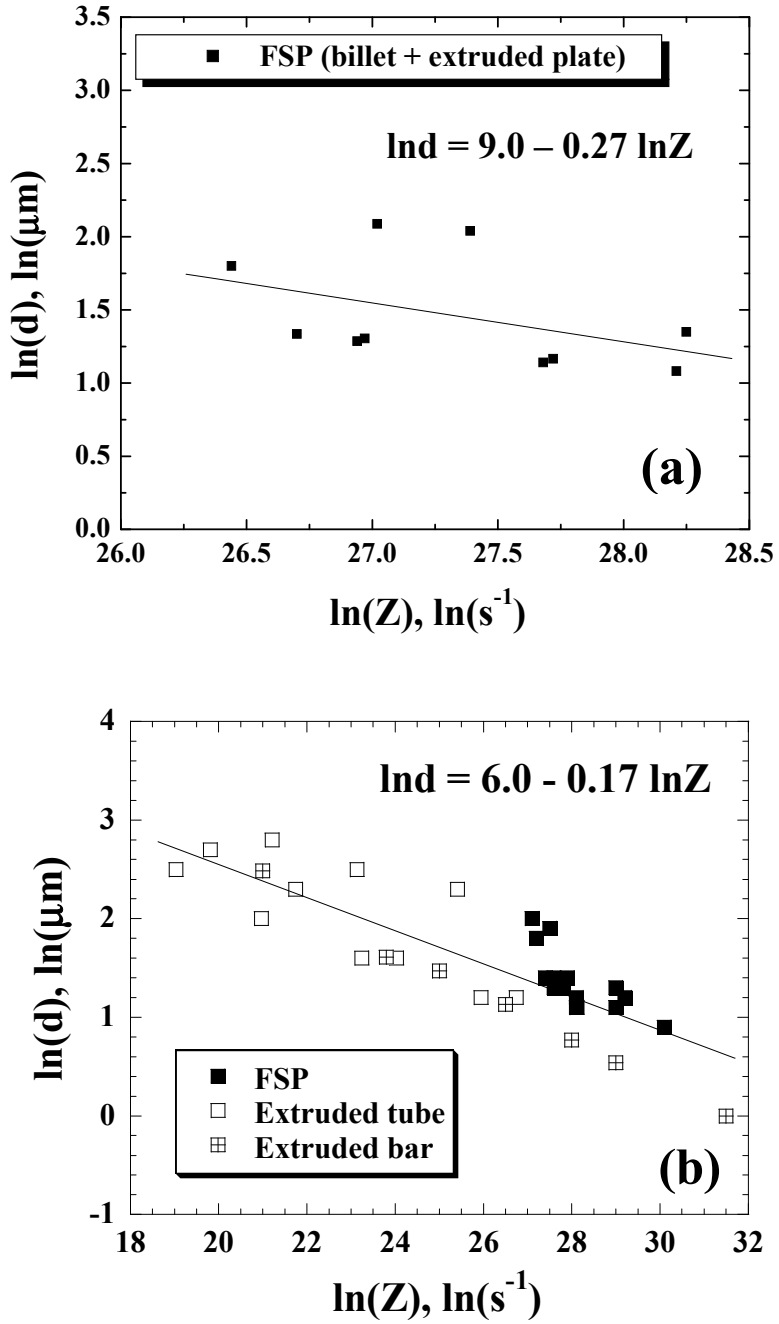

Figure 4-2 Plots for the relationship between the resulting grain size and Z-parameter in specimens processed by (a) FSP and (b) extrusion or tension. The data on FSP (solid square) are also included in (b) for comparison [170,171].

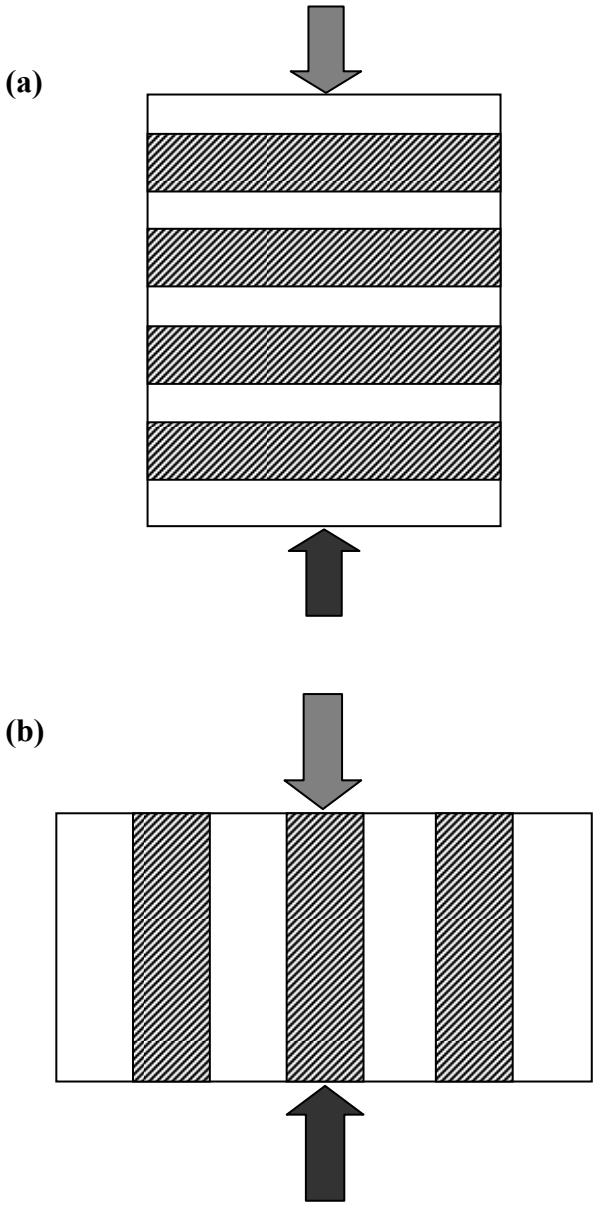

Figure 4-3 Schematic diagrams showing (a) the iso-stress and (b) the iso-strain models.

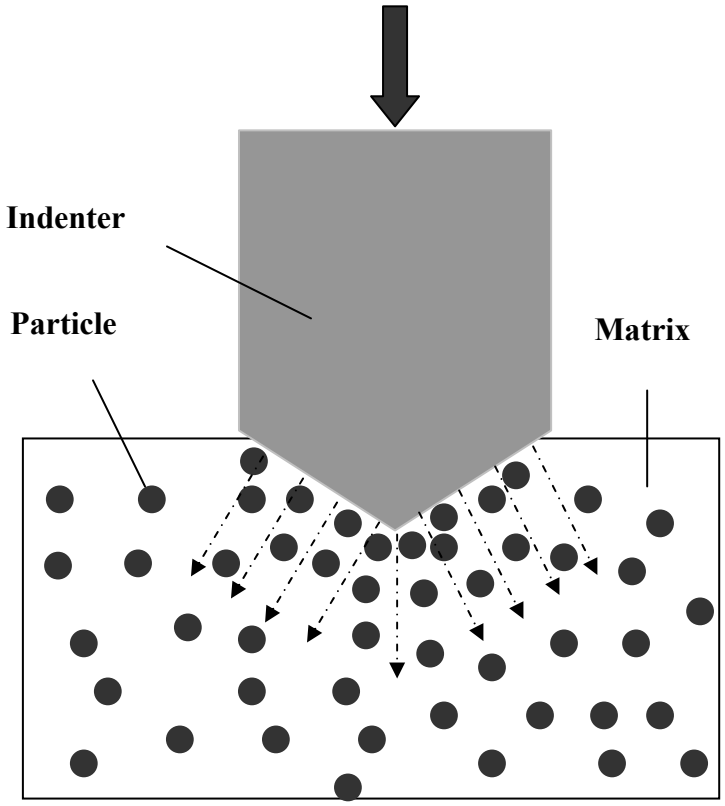

Figure 4-4 Schematic drawing of the load transfer direction under the indentation test.

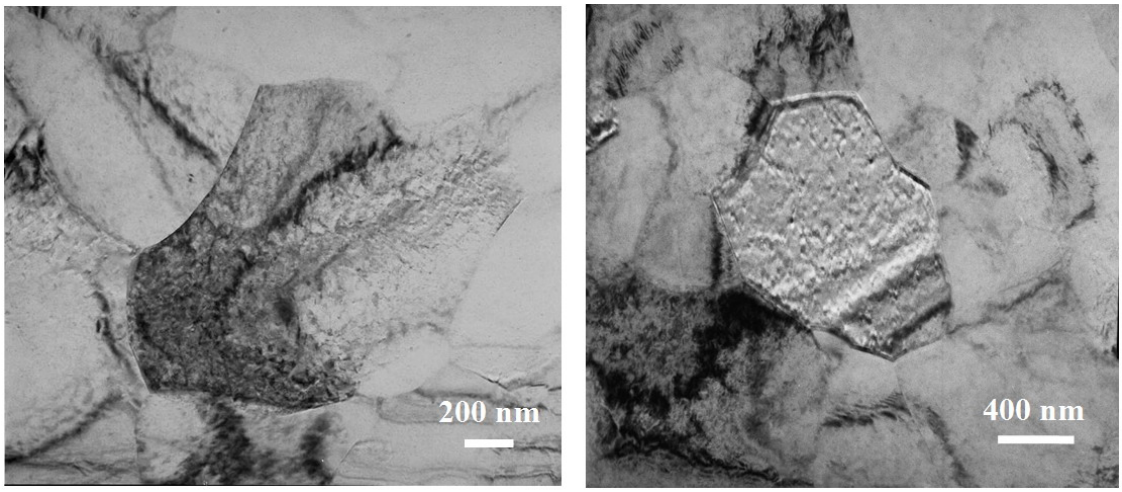

Fig.4-5 The TEM observations for the one-pass FSPed AZ31 alloy samples.

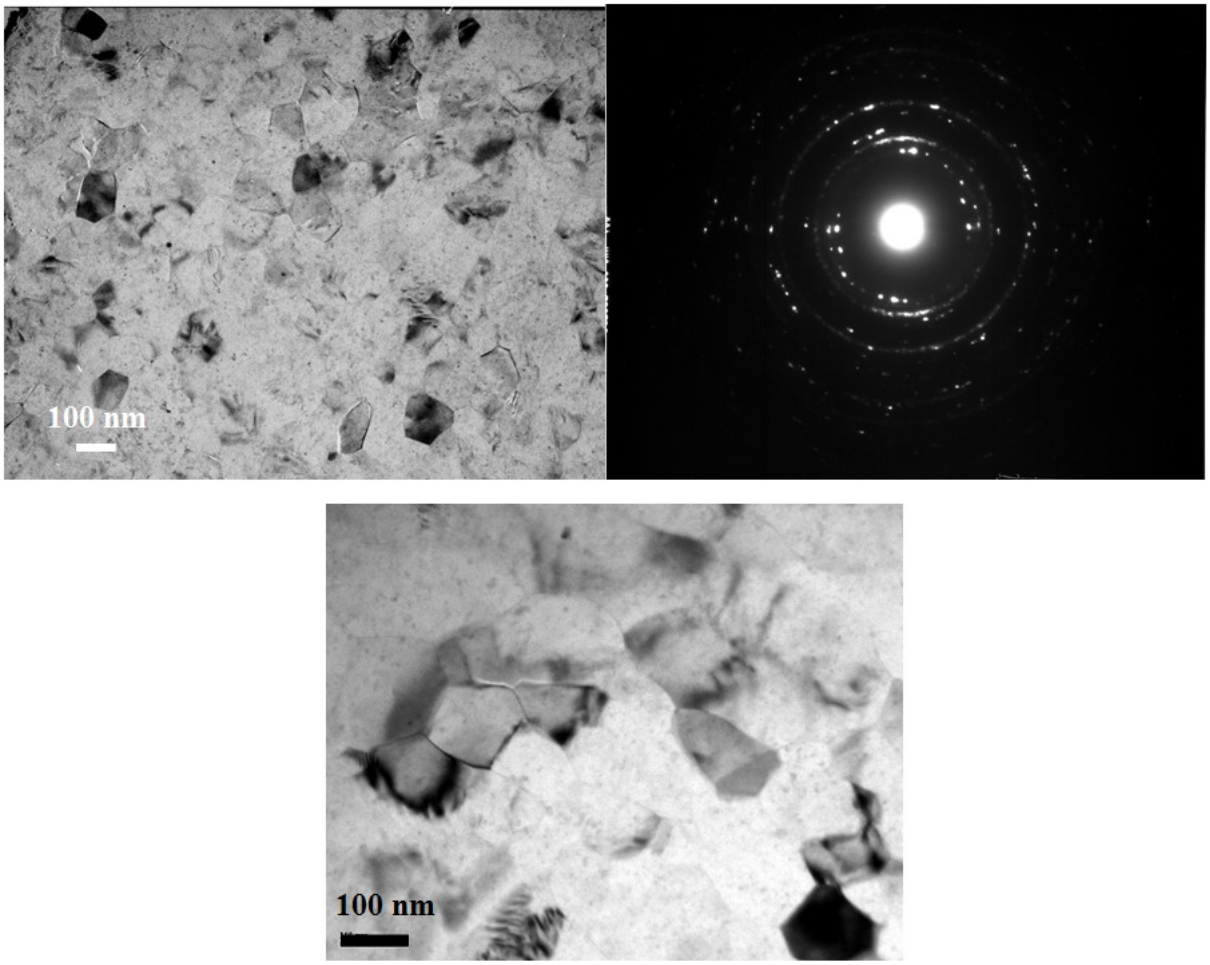

Figure 4-6 The typical microstructure of the two-pass FSPed AZ31 alloy in the as processed condition, together with a select area diffraction (SAD) pattern.

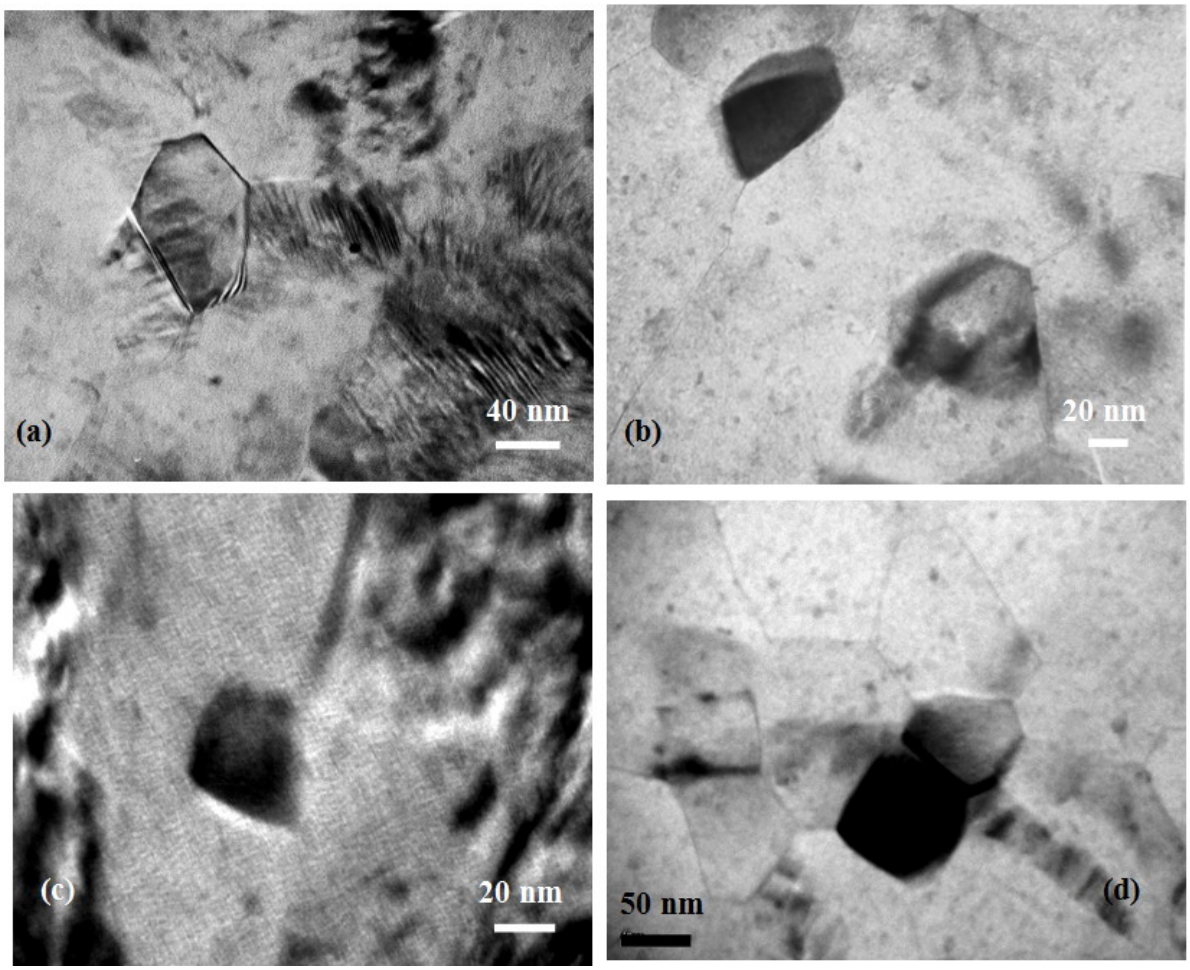

Figure 4-7 (a), (b), and (c) Strain-free nanometer grains formed along the subboundary and grain boundary through DRX; (d) equiaxed nano-sized grains formed by DRX within the nugget region.

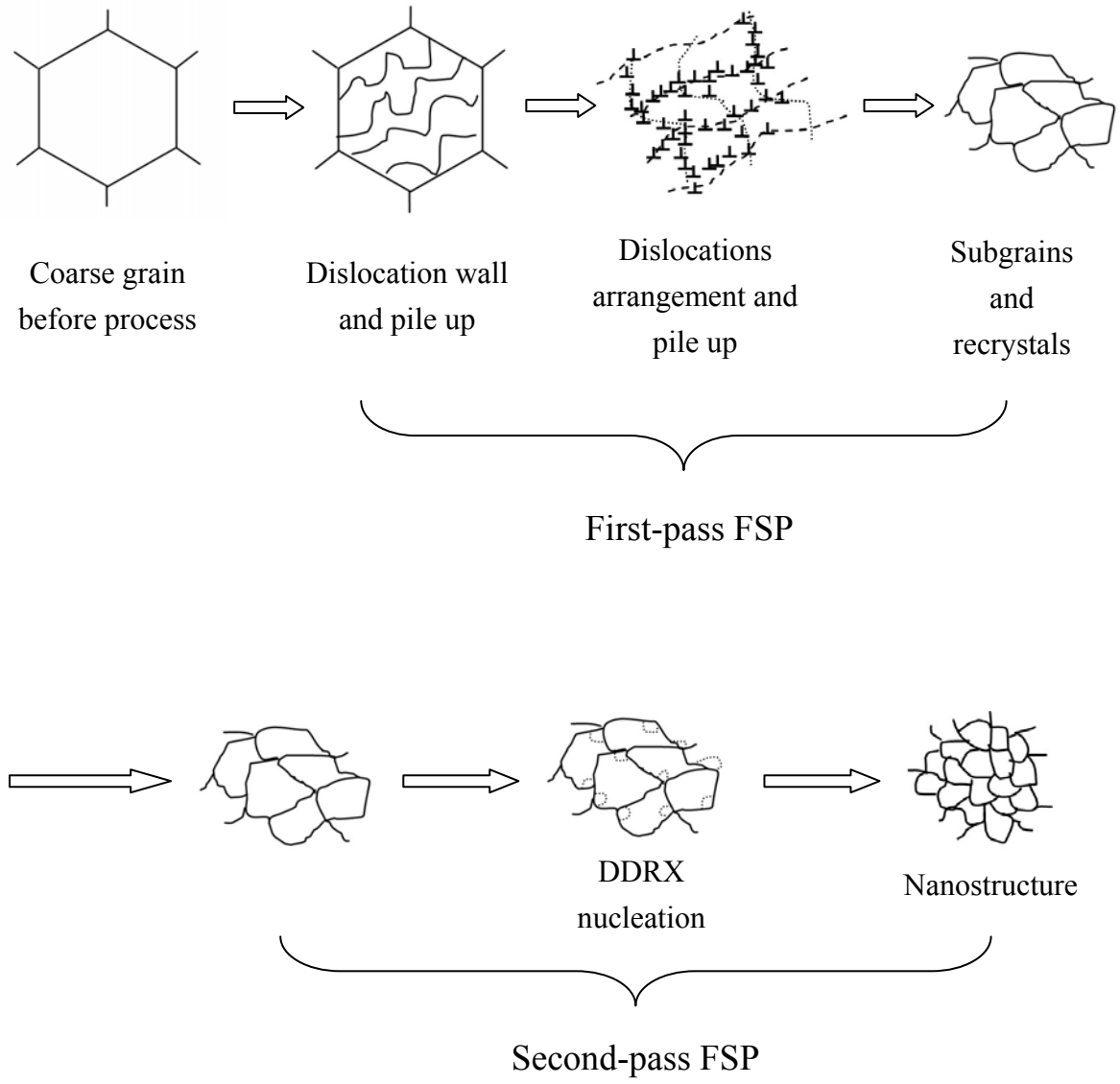

Figure 4-8 Schematic illustration of the grain refinement process of the two-pass FSPed AZ31 alloy.